

Soft Materials under Air Blast Loading and Their Effect on Primary Blast Injury

by

Christopher George Thom

A thesis
presented to the University of Waterloo
in fulfillment of the
thesis requirement for the degree of
Master of Applied Science
in
Mechanical Engineering

Waterloo, Ontario, Canada, 2009

© Christopher George Thom 2009

AUTHOR'S DECLARATION

I hereby declare that I am the sole author of this thesis. This is a true copy of the thesis, including any required final revisions, as accepted by my examiners.

I understand that my thesis may be made electronically available to the public.

Abstract

Injury from blast is significant in both military and civilian environments. Although injuries from blast are well-documented, the mechanisms of injury are not well understood. Developing better protection requires knowledge of injury mechanisms and material response to blast loading. The importance of understanding how soft materials such as foams and fabrics behave under blast loading is further apparent when one realizes the capacity for some of these materials, frequently used in protective ensembles, to increase the potential for injury under some conditions. The ability for material configurations to amplify blast pressure and injury has been shown experimentally by other researches, and numerically in this study.

Initially, 1-D finite element and mathematical models were developed to investigate a variety of soft materials commonly utilized in ballistic and blast protection. Foams, which have excellent characteristics in terms of energy absorption and density, can be used in conjunction with other materials to drastically reduce the amplitude of the transmitted pressure wave and corresponding injury.

Additionally, a more fundamental examination of single layers of fabric was undertaken to investigate to the effects of parameters such as fabric porosity and density. Shock tube models were developed and validated against experimental results from the literature. After the models were validated, individual fabric properties were varied independently to isolate the influence of parameters in ways not possible experimentally. Fabric permeability was found to have the greatest influence on pressure amplification. Kevlar, a ballistic fabric, was modelled due to its frequent use for fragmentation protection (either stand-alone or in conjunction with a hard ballistic plate).

The developed fabric and foam material models were then utilized in conjunction with a detailed torso model for the estimation of lung injury resulting from air blast. It was found that the torso model predicted both amplification and attenuation of injury, and all materials investigated as a part of the study had the capacity for both blast amplification and attenuation. The benefit of the models developed is that they allow for the evaluation of specific protection concepts.

By utilizing an approach which involved carefully validating models of soft materials under blast loading against experimental results, and then applying the validated models to more complicated scenarios such as protective concepts for the human body, insight has been gained into the behaviour of these materials when used as for blast mitigation. The techniques developed for predicting protection behaviour could be of great use to evaluators and designers of blast protection.

Acknowledgements

I would first like to express my gratitude to my supervisor, Duane Cronin, for his expertise and guidance throughout my studies. I feel fortunate to have been able to glean from his insight regarding research, academic life and B movies. I couldn't have asked for a better supervisor. Thank you.

This work would not have been possible without the sponsors of this research project, so I would like to acknowledge Martec Ltd., Allen-Vanguard and DRDC - Valcartier, and thank them for the opportunity to work on a project in such a fascinating and challenging area.

I would like to acknowledge the talented graduate students I have worked with at the University of Waterloo for their motivation, help and insight. In particular I would like to thank Christopher Salisbury for his guidance. I would also like to thank Ken Yuen, Steve DeMers and Karla Cassidy for all the laughs over the past few years.

I would like to express my appreciation for my friends, particularly those in the University of Waterloo Photo Club, who gave me something non-engineering related to discuss from time to time. In particular I would like to thank Ethan Wilding for all the coffee and entertaining discussions.

Angela, thank you for your support and for being understanding of my occasionally unusual working hours, particularly towards the end of this work.

Last but definitely not least, I would like to thank my family for all of the support and encouragement throughout this process. It is bittersweet completing this work and knowing that it came at the cost of quality time at home with the people I love.

for Dad

Table of Contents

List of Figures.....	xi
List of Tables.....	xxi
Chapter 1 Introduction.....	1
1.1 Motivation.....	1
1.2 Background.....	2
1.3 Research Objectives and Scope.....	3
1.4 Approach for Current Research.....	4
Chapter 2 Review of Blast Loading and Injury.....	6
2.1 Blast loading.....	6
2.2 Wave Propagation and Interaction with Boundaries.....	13
2.2.1 Interaction of Waves with Boundaries.....	14
2.2.2 Wave speed in a compressible porous medium.....	15
2.3 Blast Injury.....	16
2.4 Primary Blast Injury: Blast Lung Injury.....	18
2.4.1 Lung Anatomy.....	18
2.4.2 Lung Injury Description.....	21
2.4.3 Injury Mechanisms.....	24
2.5 Effect of Protection on Observed Blast Injury.....	27
2.6 Techniques for Estimation of Blast Lung Injury.....	28
2.6.1 Load Based Technique (Bowen Curves).....	29
2.6.2 Mathematical Model of the Torso.....	35
2.6.3 Physical Surrogates.....	39
2.6.4 Numerical Surrogates.....	46
Chapter 3 Modeling Background and Approach.....	49
3.1 Finite Element Overview.....	49
3.2 Simulation of Blast Loading.....	51
3.2.1 Uncoupled Loading.....	51
3.2.2 Coupled Loading.....	52

3.2.3 Arbitrary Lagrangian-Eularian (ALE) in Finite Element.....	53
3.2.4 Artificial Viscosity in Numerical Codes.....	56
3.2.5 Validation of the use of ALE to Simulate Shock Waves and Blast Phenomena	57
3.2.6 Simulation of Explosive Blast in ALE.....	58
3.3 Validation and Verification of Numerical Models	59
Chapter 4 Models for Injury Prediction Used in the Current Study	63
4.1 Modified Axelsson Model (Mathematical Model)	63
4.1.1 Modified Axelsson Model Verification	66
4.2 University of Waterloo Torso Model.....	69
4.2.1 Geometry.....	70
4.2.2 Material Properties.....	72
4.2.3 Boundary Conditions	74
Chapter 5 Foam Material Behaviour Under Blast Loading.....	77
5.1 Foam Material Behaviour	77
5.1.1 Rate Dependence of Foam Material Behaviour.....	83
5.2 Experimental Work (Literature)	87
5.2.1 Shock Tube Experiments on Foams.....	88
5.2.2 Blast Loading Experiments on Foams	90
5.2.3 Experiments on Foam and Rigid Plate Decouplers.....	91
5.3 Finite Element Model Development.....	92
5.3.1 Model Geometry	92
5.3.2 High Density Material Model	94
5.3.3 Low Density Polyethylene Foam (LDPE 45) Material Model	95
5.3.4 Rate Dependent Behaviour of LDPE 45 Foam	99
5.3.5 Low Density Polyethylene Foam Numerical Damping and Unloading Behaviour	101
5.3.6 Model of High Density Polyethylene Foam (HDPE 96)	104
5.3.7 Wave Speeds in LDPE 45 and HDPE 96 Material Models	105
5.4 Model Validation Results	107
5.4.1 Foam with Varied Thickness Under Blast Loading.....	107
5.4.2 Foam Coupled to High Density Material.....	116
5.5 Foam Parametric Study with Finite Element Model.....	120

5.5.1 Effect of Plate Mass	120
5.5.2 Effect of Foam Thickness	122
5.6 Foam Implementation with the Modified Axelsson Model To Investigate Injury	125
5.6.1 Validation of Foam Mathematical Model	127
5.6.2 Evaluation of the Differences in Behaviour Between Shock Tube and Blast Loading	128
5.6.3 Foam and Axelsson Model LD50 Predictions	132
5.7 Foam Implementation with Torso Model	133
5.7.1 Finite Element Torso Model Predicted Injury with Foam Protection	135
5.8 Discussion of Foam Results	137
Chapter 6 Single Layer Fabrics and their Behaviour in Blast	139
6.1 Single Layer Fabric Properties	139
6.2 Experimental Work (Literature)	140
6.3 Numerical Model of Single Layer Fabrics	144
6.3.1 Shock Tube Model for Fabrics	145
6.3.2 Fabric model	147
6.3.3 Finite Element Mesh refinement	152
6.4 Simulation of Shock Tube Tests	155
6.4.1 Parametric Study	160
6.5 Single Layer Fabric Implementation with the modified Axelsson Model	165
6.6 Validation of the Single Layer Fabric Mathematical Model	166
6.6.1 Fabric and Axelsson Model LD50 Predictions	167
6.7 Single Layer Fabric Implementation with Torso Model	169
6.7.1 Single Layer Fabric Torso Model Results	170
6.8 Discussion of Single Layer Fabric Results	171
Chapter 7 Multi-Layer Fabric Behaviour Under Blast Loading	174
7.1 Multi-Layer Fabric Transverse Behaviour	174
7.2 Shock Wave and Blast Loading of Multiple Layers of Fabric	178
7.3 Shock Wave Loading of Live Subjects Wearing Soft Ballistic Vests	183
7.4 Multi-Layer Fabric Finite Element Model	184
7.4.1 Multi-Layer Fabric Material Model	185

7.5 Parametric Study.....	188
7.6 Mathematical Model Implementation and Injury Prediction for Multi-Layer Fabrics.....	190
7.7 Multi-Layer Fabric Torso Model Implementation.....	192
7.7.1 Multi Layer Protection Results	193
7.8 Discussion of Results.....	195
Chapter 8 Conclusions, and Recommendations	198
8.1 Foam Conclusions.....	198
8.2 Fabric Model Conclusions	199
8.3 Multi-Layer Fabric Model Conclusions.....	200
8.4 Mathematical (Modified Axelsson) Model Conclusions	200
8.5 Finite Element Torso Model Conclusions	201
8.6 Recommendations.....	202
Bibliography	204

List of Figures

Figure 2.1 - Qualitative differences in maximum distance of threat propagation	7
Figure 2.2 - Friedlander curve	8
Figure 2.3 - Mach stem [Bulson,1997].....	11
Figure 2.4 - Shock tube vs. blast loading.....	12
Figure 2.5 - c) Complex blast wave b) Simple blast wave a) Idealized blast wave [Mayorga,1997]	13
Figure 2.6 - Sound speed versus apparent bulk density [Gibson, 1995]	16
Figure 2.7 - Respiratory System Anatomy [Wikipedia, 2007]	20
Figure 2.8 - X-Ray without contused lung [Wicky, 2000]	22
Figure 2.9 - X-Rays of a human blast victim [Rawlins,1978]	22
Figure 2.10 - Stained rat lung samples; control and exposed to injurious shock tube loading [Chavko et al., 2006].....	23
Figure 2.11 - Bowen injury prediction for the case of body being parallel to blast [Bowen, 1968]	30
Figure 2.12 - Bowen injury prediction for the case of body being perpendicular to blast [Bowen, 1968]	31
Figure 2.13 - Bowen injury prediction for the case of body being perpendicular to blast and against a reflecting surface [Bowen, 1968].....	32
Figure 2.14 - Comparison of LD50 curves for Bass study [Bass, 2006] and original Bowen curve [Bowen, 1968]	34

Figure 2.15 - Comparison of Bass [Bass, 2006], Gruss [Gruss, 2006] and Bowen [Bowen, 1968] LD50 curves for the case of body orientation parallel to blast	35
Figure 2.16 - Diagram of Axelsson mathematical torso model [Axelsson, 1994]	36
Figure 2.17 - Diagram of Stuhmiller torso model [Stuhmiller, 1996].....	38
Figure 2.18 - Probability of injury vs. normalized work [Stuhmiller, 1996].....	39
Figure 2.19 - Diagram of a BTB	40
Figure 2.20 - Severity of lung injury vs. thoracic wall peak acceleration for both shock tube and high explosive shock loading [Cooper, 1996]	42
Figure 2.21 - Effect of protective concepts on chest wall acceleration and severity of injury for porcine test subjects [Cooper, 1996].....	43
Figure 2.22 - MABIL thoracic surrogate [Ouellet, 2008b].....	44
Figure 2.23 - MABIL sternum acceleration vs. peak incident overpressure [Ouellet, 2008b].....	45
Figure 2.24 - MABIL sternum peak velocity vs. blast impulse [Ouellet, 2008b]	46
Figure 2.25 - 3D finite element torso model [Stuhmiller, 2006]	47
Figure 2.26 - Comparison of 3D finite element model results to experiments [Stuhmiller, 1997].....	48
Figure 3.1 - Hourglass deformation of a reduced integration point element.....	50
Figure 3.2 - Isometric advection of state variables in ALE algorithm: A) Initial configuration; B) After Lagrangian timestep; C) After ALE advection and remapping [Greer,2006].....	54
Figure 3.3 - Penalty coupling for fluid structure interaction in ALE [Greer, 2006].....	56
Figure 4.1 - Axelsson model diagram.....	64
Figure 4.2 - Original BTB pressure history from a single gauge [Axelsson, 1996].....	67

Figure 4.3 - Digitized first 6 ms of BTD pressure transducer data from [Axelsson, 1996]	68
Figure 4.4 - Comparison of predicted chest wall velocity from [Axelsson, 1996] compared to chest wall velocity predicted by current study.....	69
Figure 4.5 - A) High resolution image from Visible Human Project [NLM, 2004]; B) Torso slice model [Greer, 2006].....	71
Figure 4.6 - Pseudo 2D model of rib-cage (muscle and fat removed) [Greer, 2006]	72
Figure 4.7 - Torso model in ALE mesh [Greer, 2006]	75
Figure 5.1 - Comparison of (a) open and (b) closed cell structures [Mills, 2007].....	77
Figure 5.2 - Compression of a closed cell foam showing buckling of cell walls [Mills, 2007]	78
Figure 5.3 - Stress-Strain curve for a foam, showing: 1) Pre-buckling, 2) Post-buckling, 3) Densification stages in compression. (Features exaggerated)	79
Figure 5.4 - Stress Strain behaviour of closed celled polyethylene foam at various foam densities [Gibson, 1988]	80
Figure 5.5 - Illustration of the effect of strain rate on foam stress-strain behaviour [Ouellet, 2006]	83
Figure 5.6 - Effect of strain rate on plateau stress for LDPE45 foam, experimental and proposed fit from [Nerenberg, 1998], and a logarithmic fit to experimental data.....	84
Figure 5.7 - Foam cell air and polymer temperatures vs. time. Cell diameter of: a) 0.1mm and b) 1.0mm [Mills, 2007]	85
Figure 5.8 - Quasistatic and high rate compressive Stress-Strain behaviour of a 34 kg/m ³ LDPE foam [McArthur, 2003].....	86
Figure 5.9 - Differences in air flow in and out of a foam under air shock wave loading with and without an impermeable front face	89

Figure 5.10 - Blast chamber used by both the Nerenberg and Ouellet studies [Nerenberg, 1998]	91
Figure 5.11 - 1D models of: A) Foam without high density material, B) Foam with high density material	93
Figure 5.12 - Diagram showing cell wall material and air being considered in series	96
Figure 5.13 - Contribution of solid cell wall and enclosed air to stress strain behaviour of a foam	98
Figure 5.14 - Quasi-static stress strain behaviour for LDPE45 foam (experimental and theoretical)	99
Figure 5.15 - Stress strain behaviour from experimental work [Nerenberg, 1998], compared to calculated quasi-static behaviour, and the stress strain behavior used in simulations for the non-rate dependent model.....	101
Figure 5.16 - Effect of addition of wave dispersing and energy absorbing parameters to foam material model. A) No dispersion (No Hysteresis, Low Damping); B) No Hysteresis, Damping Added; C) Hysteresis, Low Damping; D) Hysteresis and damping added. All compared against data from [Nerenberg, 1998] for 100mm of LDPE 45 foam loaded by 170g at a 1m distance.....	103
Figure 5.17 - Comparison of experimental quasi-static and high rate stress-strain data to the stress-strain behaviour predicted in the current study for HDPE 96 foam	105
Figure 5.18 - Sound speed versus apparent bulk density for a porous material (polyethylene) ..	106
Figure 5.19 - Experimental pressure histories for various thicknesses of LDPE 45 foam loaded by 170g of C4 at 1m [Nerenberg, 1998]	108
Figure 5.20 - Comparison of experimental results from [Nerenberg, 1998] and numerical results from the current study for: A) Baseline loading without foam, B) 20mm LDPE 45 foam, C) 60mm LDPE 45 Foam, D) LDPE 45 Foam. All loaded by 170g of C4 at 1m.	109

Figure 5.21 - Wave diagram for 100mm of LDPE 45 foam under blast loading from 170 g of C4	111
Figure 5.22 - Comparison of experimental results from [Nerenberg, 1998] and numerical results from the current study for: Baseline loading (left) and 20mm HDPE96 foam (right). Both loaded by 170g of C4 at 1m.....	112
Figure 5.23 - Comparison of experimental results from [Nerenberg, 1998] and numerical results from the current study for: Baseline loading (left) and 20mm LDPE45 foam with 1.5mm steel plate (right). Both loaded by 170g of C4 at 1m.....	113
Figure 5.24 - Comparison of experimental results from [Nerenberg, 1998] and numerical results from the current study for: Baseline loading (top left), 20mm LDPE45 foam (top right), and 40mm LDPE45 (bottom). Both loaded by 325g of C4 at 1m.....	114
Figure 5.25 - Comparison of experimental results from [Nerenberg, 1998] and numerical results from the current study for: Baseline loading (top left), 20mm HDPE96 foam (top right), and 60mm HDPE96 foam (bottom). Both loaded by 325g of C4 at 1m.	115
Figure 5.26 - Comparison of experimental results from [Nerenberg, 1998] and numerical results from the current study for: Baseline loading (left) and 20mm LDPE45 foam with 1.5mm steel plate (right). Both loaded by 325g of C4 at 1m.....	116
Figure 5.27 - Experimental set up for blast testing of foam decouplers [Ouellet, 2008].....	117
Figure 5.28 - Experimental data showing 12.7mm of LDPE45 foam with various high density materials mounted on the front face. Loaded by 250g of C4 at 1m distance. [Ouellet, 2008]	117
Figure 5.29 - Comparison of numerical results to experimental results [Ouellet, 2008] for A) Baseline loading (no protection), B) 12.7mm LDPE45 with 5mm UHMWPE plate, C) 12.7mm LDPE45 with 4mm aluminum plate, D) 12.7mm LDPE45 with carbon fibre plate	118

Figure 5.30 - Wave diagram for a 4mm Aluminum and 12.7mm LDPE 45 sample Loaded by 250g C4 at 1m.....	119
Figure 5.31 - 13mm of HDPE 96 foam faced with plates of varied areal density.....	121
Figure 5.32 - 25mm of LDPE 45 foam faced with plates of varied areal density	122
Figure 5.33 - Varied thicknesses of HDPE 96 foam faced with 4mm of aluminum (AD = 5.6kg/m ²).....	123
Figure 5.34 - Varied thicknesses of LDPE 45 foam faced with 4mm of aluminum (AD = 5.6kg/m ²).....	123
Figure 5.35 - Peak back wall pressure vs. plate areal density for various thicknesses of LDPE 45	124
Figure 5.36 - Peak back wall pressure Vs. plate areal density for various thicknesses of HDPE 96	125
Figure 5.37 - Foam and high density material model diagram.....	126
Figure 5.38 - Validation against experimental data [Ouellette, 2008] for 1D model of foam with high density materials with an A.D. of: A) Loading; B) 4.8 kg/m ² ; C) 5.6 kg/m ² ; D) 9.5 kg/m ² ;.....	127
Figure 5.39 - Pressure and integral of pressure (impulse per unit area) for 12.7mm LDPE 45 foam faced with a 4.8kg/m ² plate; loaded by 250g C4 at 1m	129
Figure 5.40 - Effect of increasing foam thickness or plate areal density on pressure and integral of pressure (impulse per unit area) for 12.7mm LDPE 45 foam faced with a 4.8kg/m ² plate; loaded by 250g C4 at 1m	130
Figure 5.41 - Effect of increasing foam thickness or plate areal density on pressure and integral of pressure (impulse per unit area) for 12.7mm LDPE 45 foam faced with a 4.8kg/m ² plate; loaded by a 3 bar pulse wave.	131

Figure 5.42 - Foam model combined with Axelsson torso model.....	132
Figure 5.43 - Torso model with 30mm of foam and 10mm hard plate protection	134
Figure 5.44 - Predicted lung injury results from the finite element torso model with various foam and high impedance material protection concepts.	136
Figure 5.45 - Percentage severe lung injury for foam protection concepts	136
Figure 6.1 - Fabric orientation and descriptions used in curren study.....	140
Figure 6.2 - Diagram of shock tube apparatus with fabric sample	141
Figure 6.3 - Pressure time histories for various fabrics with 6mm stand-off, 2.21 bar baseline reflected overpressure [Hattingh, 2001]	142
Figure 6.4 - Variation of shock strength and the resulting pressure amplification by fabrics [Hattingh, 2001].....	143
Figure 6.5 - Effect of varied air gap width (stand-off) on pressure amplification for various fabrics [Hattingh,2001].....	144
Figure 6.6 - Side view of shock tube model	146
Figure 6.7 - Fabric and shock tube model	149
Figure 6.8 - Numerical fabric model geometries for various permeabilities.....	151
Figure 6.9 - Fabric air permeability numerical Results	151
Figure 6.10 - Mesh Refinement Results, with dotted box showing element size used in most simulations	153
Figure 6.11 - Mesh refinement results, pressure time history behind non-permeable fabric at various element sizes	154

Figure 6.12 – Air flow through hole in: a) permeable fabric (muslin), b) non-permeable fabric (aramid). From numerical model with added symbols for clarity.	156
Figure 6.13 - Reflected Pressure History on Back Wall behind Satin: Averaged, Behind Fabric Hole, and Behind Fabric	157
Figure 6.14 - Reflected pressure history on back wall behind satin, cotton and muslin. experimental results from Hattingh and Skews [Hattingh, 2001].....	158
Figure 6.15 - Pressure time histories without fabric sample. Load case used for muslin, cotton and satin cases.....	159
Figure 6.16 - Predicted back wall pressure amplification for various fabrics	160
Figure 6.17 - Pressure traces 6mm from the back wall for 3.92, 3.32 and 2.25 bar reflected pressures (without fabric)	161
Figure 6.18 - Back wall pressure time histories for fabrics of varying permeabilities, back wall pressure without fabric: 3.92 bar (reflected), stand-off: 3mm	161
Figure 6.19 - Back wall pressure history for fabrics of varying areal densities, back wall pressure without fabric: 3.92 bar (reflected), stand-off: 3mm, no permeability	162
Figure 6.20 - Pressure amplification vs. areal density for fabrics with varied permeabilities, stand-off: 3mm, back wall pressure without fabric: 3.92 bar (reflected).....	163
Figure 6.21 - Back wall pressure amplification for various permeabilities under varied shock tube loads, stand-off: 3mm, areal density: 150g/m ²	164
Figure 6.22 - Back wall pressure amplification vs. stand off for fabrics of various permeabilities, areal density 150g/m ² , back wall pressure without fabric: 3.92 bar (reflected).....	165
Figure 6.23 - Fabric and air gap model diagram.....	166

Figure 6.24 - Validation of 1D mathematical model for a plate with air gap against experimental data [Ouellet, 2008]	167
Figure 6.25 - Fabric model combined with Axelsson torso model.....	168
Figure 6.26 - Geometries used in torso model simulations with a fabric and air gap	169
Figure 6.27 - Predicted lung injury results from the finite element torso model with fabric concepts having a 10mm stand-off.	170
Figure 6.28 - Percentage of lung severely injured as determined by peak dynamic pressure for fabric with an air gap	171
Figure 7.1 - Transverse Stress-Strain behaviour for Kevlar KM2 fabric from [Raftenberg, 2004]	176
Figure 7.2 - Transverse compression test and unloading of 30 layers of Kevlar 29 fabric [Yu, 1985].....	177
Figure 7.3 - Transverse loading and unloading of a single Kevlar fibre [Cheng, 2005]	178
Figure 7.4 - Average peak pressure ratio [Gibson, 1995].....	179
Figure 7.5 - Overpressure amplification for two different fabrics: A) Fabric with density below minimum sound speed; B) Fabric with density above minimum sound speed [Gibson, 1995]	180
Figure 7.6 - Change in pressure amplification for various load cases and varied number of layers of Kevlar 29 [Yu, 1985].....	181
Figure 7.7 - Effect of multi-layer fabric on transmitted blast pressure [Gibson, 1995]	182
Figure 7.8 - Effect of a soft ballistic apron on peak pressure when loaded by 250g of C4 at 0.65m. digitized from [Nerenberg, 2000]	183
Figure 7.9 - 1D multi-layer fabric model configuration	184

Figure 7.10 - Experimental loading and unloading behaviour for a Kevlar 29 fabric [Yu, 1985], fit to data to smooth results, and results of single element test with hysteresis implemented	186
Figure 7.11 - Speed of sound versus apparent bulk density for a porous media using Kevlar parameters from the current study.	187
Figure 7.12 - Results from numerical simulation of various thicknesses of multi-layer Kevlar loaded by 250g of C4 at 1m (loading from [Ouellet, 2008])	188
Figure 7.13 - Peak pressure results for various thicknesses of Kevlar under: A) 25 bar, 0.65 ms duration blast load (fit to data from [Ouellet, 2008]); B) 63 bar, 0.37 ms blast load (fit to data from [Nerenberg, 2000]); C) 4.5 bar Shock Tube Loading	189
Figure 7.14 - Pressure time history behind 20mm and 30mm of Kevlar loaded by 250g of C4 at 1m. Predictions from 1D finite element models (dashed lines) and the mathematical models (solid lines)	191
Figure 7.15 - Model used in multi-layer fabric protection simulations	193
Figure 7.16 - Predicted lung injury results from the finite element torso model with multiple layer soft ballistic protection.....	194
Figure 7.17 - Percentage of lung severely injured as determined by peak dynamic pressure for multi-layer fabric concepts	195

List of Tables

Table 2.1 - Expected Injuries to Unprotected Victims at Relative Distances from HE in Open Air [Wightman et al., 2001]	17
Table 2.2 - Percent Contusion of Rat's Right Lung from Experiment and FEA [Stitzel, 2005]....	25
Table 2.3 - Comparison of Various Metrics for Predicting Lung Injury [Gayzik, 2007].....	26
Table 2.4 - Axelsson Model Parameters [Axelsson et al., 1996].....	37
Table 2.5 - Injury levels corresponding to ASII and inward chest wall velocity [Axelsson et al., 1996]	37
Table 4.1 - Axelsson Model Parameters[Axelsson, 2006]	64
Table 4.2 - Bone Properties for Torso Model [Greer, 2006]	73
Table 4.3 - Soft Tissue (Muscle and Fat; Heart and Blood) Properties for Torso Model [Greer, 2006]	73
Table 4.4 - Lung Properties used for Torso Model [Greer, 2006].....	74
Table 5.1 - High Density Plate Elastic Material Properties	95
Table 5.2 - Comparison of peak backwall pressures from Experiment [Nerenberg, 1998] and Current Study	110
Table 5.3 - Comparison of Experimental [Ouellet, 2008] and Numerical Peak Back Wall Pressures behind 13mm of LDPE 45 Foam Faced with Various Plates	118
Table 5.4 - Summary of Modified Axelsson Model Results for Foams.....	133
Table 6.1- Fabric parameters for experiments and numerical simulations. Experimental results from Hattingh and Skews [Hattingh, 2001].....	150

Table 6.2 – Grid Convergence Indices for permeabilities investigated in convergence study	153
Table 6.3 - Range of Values for Parametric Study	160
Table 6.4 - Summary of Modified Axelsson Model Results for Fabric with an Air Gap	168
Table 7.1 - Constants for Fabric Constitutive Model [Raftenberg, 2004].....	175
Table 7.2 - Number of Layers and Areal Density for the Thicknesses Examined in the Multi-Layer Fabric Parametric Study	190
Table 7.3 - Summary of Modified Axelsson Model Results for Multi Layer Fabric Concepts ..	192

Chapter 1

Introduction

1.1 Motivation

Explosives are an increasingly common threat to military forces and civilian first responders. Explosive devices have the potential to cause injury in a number of modes, the prevalence of each mode depends on the device itself, the environment in which it is located, the victim's location relative to the explosive, and any protective equipment the individual may be wearing. Injuries can include primary blast injury (caused by the transmission of a shock wave through the body), secondary blast injury (resulting from high velocity fragments), tertiary blast injury (blast wind causing a loss of balance or throwing the subject into objects in the surrounding environment), as well as other injuries including burns, chemical, biological or other toxic threats. The focus of the current study is primary blast injury.

Primary Blast Injury (PBI), or blast lung, involves damage to air-containing organs such as the lungs, gastro-intestinal tract, and tympanic membrane (ear drum), and is the result of interaction between the body and pressure wave generated by an explosion. Although the relative occurrence of different forms of blast injury does depend on the specific situation, PBI has been recognized and observed as a significant form of injury [Mellor, 1992]. Frykberg [Frykberg, 1988] reported that 47% of 305 fatalities in terrorist bombings in Northern Ireland were found to have blast lung. Studies by Bowen [Bowen, 1968] and Bass [Bass, 2006] have provided an estimate of human tolerance to air blast, with loading described by the peak pressure and positive phase duration. While the tolerance of unprotected animals has been evaluated [Bowen, 1968] (and the tolerance of humans estimated), the effect of protection under blast loading has not been investigated to the point that effective estimates of injury can be made.

It has been shown that high-impedance materials used in many forms of personal protection may reduce PBI, while low-impedance materials, such as ballistic fabrics may enhance PBI in some cases [Young, 1985; Phillips, 1988; Cooper, 1991]. There is a need to understand the potential

effect of blast amplification by soft materials, as well as the fundamental injury mechanism within the lungs, in order to improve protection from blast while maintaining protection from fragments.

1.2 Background

Work by Axelsson [Axelsson, 1996], Stuhmiller [Stuhmiller, 1996] and Greer, [Greer, 2006] has focused on the development of models to predict lung injury from blast loading. While these models have been applied to predicting free field injury with some success, they have not been applied to predicting the effect of protection on injury.

Experiments undertaken by Cooper et. al. [Cooper, 1991] showed that some materials may attenuate blast waves, while others like soft foams can amplify blasts. Makris et. al. [Makris, 1996], and Nerenberg et. al. [Nerenberg, 2000; Nerenberg, 1997] demonstrated that soft materials are capable of both amplifying and attenuating peak pressures under blast loading, depending on material thickness, properties and loading. Further work by Young [Young, 1985] using human volunteers has shown that fabric-based protection can amplify the overpressure in a blast scenario. However, the limitations of live human testing meant that only small blast overpressures could be used (18.6 kPa) and pressure measurements could only be taken in the esophagus. An increase in lung injury with fabric vests has also been observed using sheep, where increased injury (based on weight of the injured lung) and risk of mortality was observed for animals wearing cloth ballistic vests as compared to those not wearing cloth ballistic vests [Phillips, 1988].

Skews and Hattingh et. al. [Hattingh, 2001; Skews, 2006] have undertaken shock tube tests to investigate fabric materials, and focused on the pressure amplification at a surface oriented normally to the direction of propagation of the planar shock wave (the surface is referred to as the back wall throughout this study). In their work, Skews and Hattingh utilized fabric samples and a controlled stand-off from the back wall. These studies considered fabrics of varying density and porosity (muslin, cotton, and satin) and air shock waves of varying pressure ratios (the ratio of pressure of the shocked and unshocked air). Muslin resulted in the lowest amplification of blast pressure (1.1 times), having the lowest density as well as the highest permeability. For the

materials considered, satin had the highest amplification of blast pressure (2 times), with the highest density as well as the lowest permeability of the three samples. Aramid fabric was investigated in another study using a similar approach [Skews, 2006] and produced a peak pressure amplification of 4.5 times at the back wall. The pressure trace exhibited multiple steps over time, resulting from the multiple reflections of the transmitted shock-wave between the fabric and back-wall. As the fabric was accelerated towards the back wall there was a decrease in volume between the back wall and fabric, and a corresponding increase in pressure measured at the back wall, where the fabric acted as a “moving piston” [Hattingh, 2001].

Work by Gibson [Gibson, 1995], Phillips [Phillips, 1988], and Nerenberg [Nerenberg, 2000] has shown that multiple plies of ballistic fabric can amplify the peak pressure of the transmitted blast wave. Work by Makris [Makris, 1996] has also shown that the blast wave may be attenuated if the number of layers of soft ballistic fabric is sufficient.

Similarly, a number of researchers have investigated the effect of foam materials, which modify the blast pressure-time history. As with single and multi-ply fabric protection concepts, foam materials have the capacity to both amplify and attenuate blast waves.

While experimental work has shown the relative effect (amplification or attenuation) of blast waves, there has been little to explain the mechanism behind amplification. Many researchers have chosen to use relations developed in acoustics in order to offer impedance mismatching as an explanation for changes in blast loading with protection. These descriptions fall short, however, as they do not account for the ability for the material thickness or the magnitude of blast loading, both of which have been shown to have an effect of the attenuation or amplification of blast by soft materials.

1.3 Research Objectives and Scope

The study documented here was focused on modeling blast interaction with low-impedance materials, and prediction of the corresponding pressure attenuation or amplification, which is

related to blast injury. Because so called “low-impedance” materials encompass a range of materials, efforts were focused on developing models which predict the behaviour of foams and fabrics under blast loading, two materials commonly used in personal protection systems. Work was also done on examining the effect of air gaps on protection effectiveness.

The objective of this work was to develop an understanding through numerical simulation of the mechanism of blast amplification and attenuation. In addition to understanding the effect on the blast wave as it was transmitted through the protection, it was also desirable to understand what effect protection would have on injury. Protection models were developed such that they could be integrated with pre-existing injury models, namely those developed by Axelsson [Axelsson, 1996] and Greer [Greer, 2006]. The desire to integrate the material models with both mathematical and finite element representations of the human torso necessitated the development of mathematical and finite element protection models. The models developed could be used for the evaluation of protection and the determination of the range of threats which a protective concept could protect against, as well as the design of protective concepts for a particular threat. Limitations of both numerical models and the use of soft materials for blast protection were identified and are discussed in this document.

1.4 Approach for Current Research

The goal of this research was to simulate materials used in protection under blast loading. As a part of this study, experiments from literature were used to validate the material models used for modeling protection.

It should be noted that since the experimental studies were carried out separately, with various methods and motivations, it was important to consider the type of loading applied (shock or blast wave) and the implications with respect to the results. Though all of the studies were unique, they all focused on comparing the pressure time history of a reflecting back-wall (either in the form of a wall at the back of the instrumented section of a shock tube, or a flat plate oriented normally towards a spherical charge).

Before modeling protection with a torso model to evaluate injury, the effect of these materials on blast loading transferred to the human body had to be understood. Examining the pressure produced behind the materials when struck by a shock or blast wave is a useful, and experimentally measured means of both validating the models used, but also method for gaining insight into the mechanism of blast amplification or attenuation by protective systems.

The approach taken for each type of material was as follows:

- 1) Investigate experimental shock tube or blast studies for material in question through literature
- 2) Determine mechanical properties of materials through literature
- 3) Develop and implement material model
- 4) Validate material model by numerically reproducing experiments from #1, using a simplified shock tube model
- 5) Undertake studies to determine what the effect of various material parameters would be on blast attenuation or enhancement
- 6) For select cases, evaluate what the effect of the material/protection concept has on lung injury determined through the UW Torso Model

In addition to the use of finite element models, a mathematical model, based on the Axelsson Torso model [Axelsson, 1996], was produced in order to further support the results obtained using FEA.

A description of the materials of interest follows, along with a review of experimental works which contribute to the understanding of each material's behaviour under blast or shock tube loading. The experimental results were also used to validate numerical models described in the same chapters.

Chapter 2

Review of Blast Loading and Injury

The effects of blast interaction with structures, soft materials, and injury are complex multidisciplinary phenomenon. The goal of this review is to introduce the relevant topics and how they related to blast injury, and the modification of blast injury through the use of protective concepts utilizing soft materials.

2.1 Blast loading

Blast loading is characterized by a rapid increase in pressure, with a limited duration. Combustion of a material can occur through deflagration or detonation. Deflagration is combustion process where propagation occurs at a velocity lower than the wave speed of the combustion material. Detonation is a class of combustion where the reaction propagates as a shock wave (above the wave speed in the material). The potential sources of blast loading are varied. Examples of materials which are typically associated with explosions include low explosives, such as gunpowder (when confined), as well as high explosives (HE) such as TNT, RDX, PETN and HMX [Bulson, 1997]. Nuclear devices and thermobaric weapons (such as Fuel/Air Explosive bombs) each have their own unique characteristics and behaviours as well. Dispersed vapour or dust can combust and, when confined, cause explosions. Surprisingly, relatively benign materials such as flour can deflagrate under the “wrong” conditions [Bulson, 1997; Smith, 1994]. This study focuses on high explosives, as HEs are a common source of blast loading, and are particularly potent sources of energy because they combust through detonation.

In high explosives, detonation is achieved through the propagation of a stress wave, created by a detonator, through the explosive material. The stress wave causes detonation of the explosive, leaving a high pressure gas as it travels through the material. Conversely, dust and vapour explosions typically occur through high rate combustion, and for these explosions a shock wave may only occur if the explosives are confined in a vessel which fails suddenly and catastrophically

[Meyers, 1994]. Thus, the release of energy of a high explosive is typically much more sudden than a low explosive.

In all cases with HE, the detonated explosive products release energy at such a rate that a shock-wave is produced in the locally surrounding air. This shock wave can travel much further and faster than the explosive products themselves, which manifest themselves as a visible fireball. In many cases, the explosive is encased in a material which produces fragments. The blast wave can also accelerate fragments from the environment, such as rocks and debris, and propel them at high velocities. The fragments resulting from a blast can travel much further than the blast wave and fireball. The typical distance that various threats travel is qualitatively shown in Figure 2.1. This work focuses purely on the blast wave (mid field), and does not examine the effect of fragmentation (secondary blast injury) or the fireball.

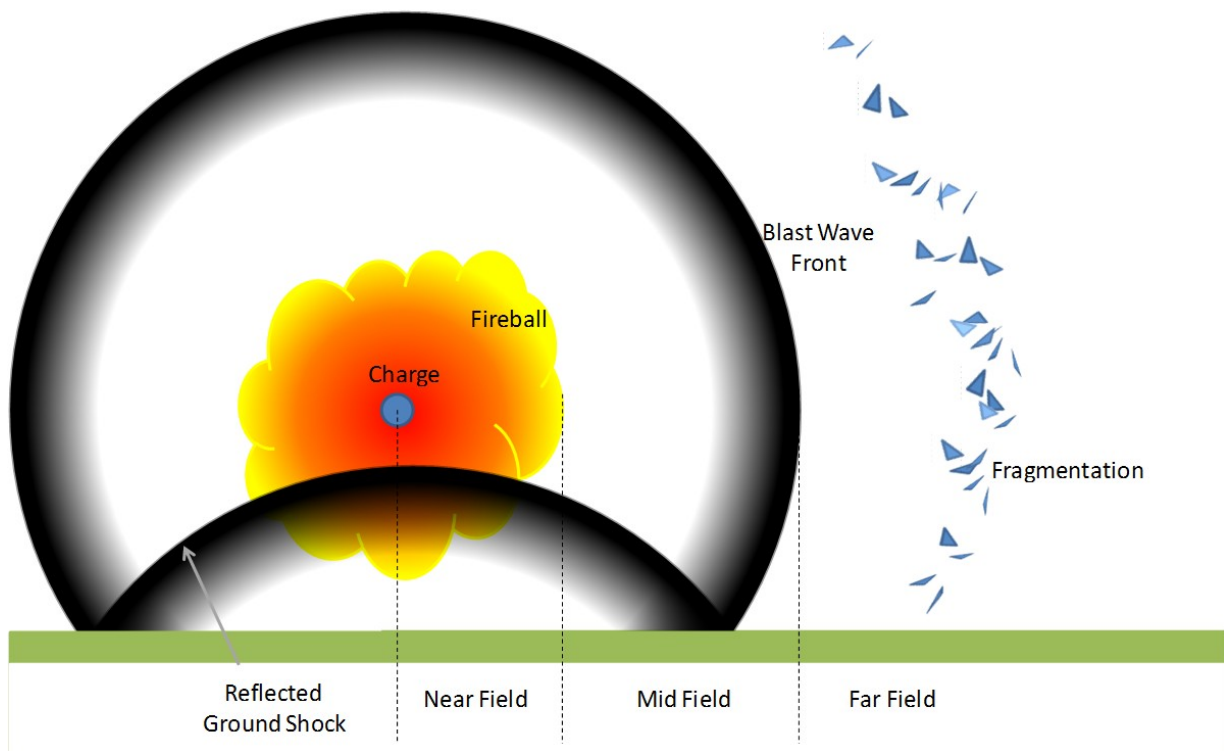


Figure 2.1 - Qualitative differences in maximum distance of threat propagation

In the case of the detonation of a spherical charge, a spherical shock-wave will be produced. The pressure time profile of shock waves resulting from high explosives and nuclear air blasts can be characterized by a Friedlander curve for the mid to far field. The curve, as shown in Figure 2.2, assumes an instantaneous increase in pressure up to a peak value, followed by an exponential decay in pressure over time. Eventually an overpressure of 0 is reached, and the duration from the pressure peak to zero pressure is called the positive phase duration. The positive phase is followed by a negative phase. The positive phase is generally considered to be the most significant source of loading with respect to injury.

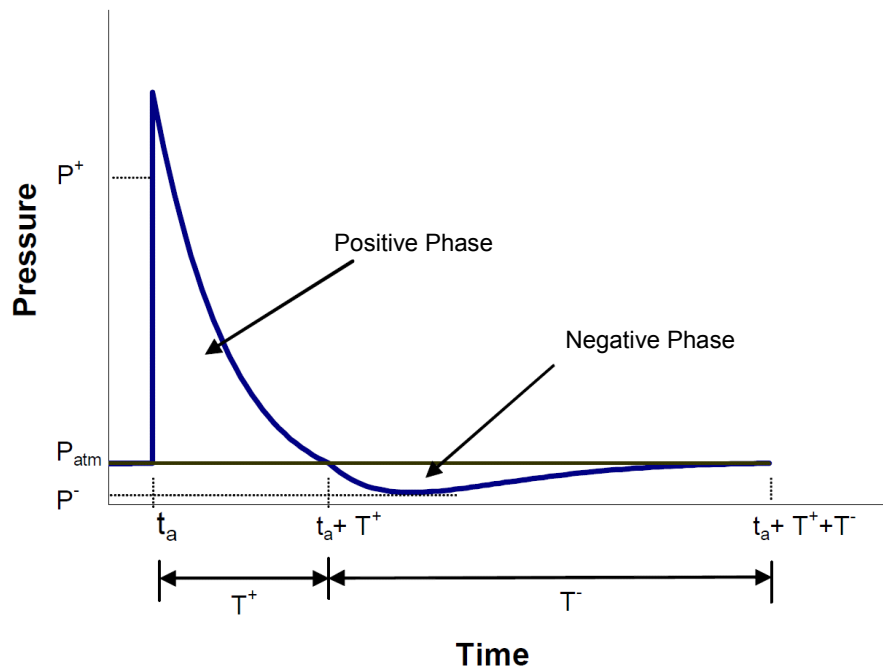


Figure 2.2 - Friedlander curve

The positive phase of the Friedlander curve is defined mathematically as follows [Smith., 1994]:

$$P(t - t_a) = P^+ \left[1 - \frac{t - t_a}{T^+} \right] e^{-\frac{b(t-t_a)}{T^+}} \quad (2.1)$$

Where t is the time, t_a is the arrival time, P is the pressure at the given time, P^+ is the Peak Pressure, T^+ is the positive phase duration, and b is a wave form parameter. P^+ , T^+ and b are determined using empirical data.

For an explosive charge of a given size and shape the pressure-time history seen by an observer will depend on their location relative to the charge. Pressures near a blast are of shorter duration, but higher peak pressure than those at a further distance away. The reduction of loading can be quite drastic with small changes in distance from the explosive. If we consider an explosive of given mass at $t=0$ (detonation), the energy released by the explosive is contained within a sphere of radius equal to the charge radius. As time progresses and the blast wave propagates spherically away from the charge, the volume defined by the spherical shock front and containing the energy released by the charge increases cubically as shock distance increases [Bulson,1997]. These scaling laws [Bulson,1997] can be described as:

$$p = \frac{KE}{r^3} \quad (2.2)$$

Where p is the peak pressure, K is a non-dimensional parameter, E is the instantaneous energy released by the explosive, and r is the distance from the charge center where the pressure is to be determined.

Curve fits to empirical blast data have been produced by a US Army ballistic research lab project [Kingery, 1966] which are used in a weapon effects calculation program named CONWEP [Hyde, 1988]. CONWEP utilizes a database which allows the calculation of, among other parameters, the pressure time history at a given distance away from a charge of TNT of a given size [Hyde, 1988].

Different high explosives have different energy outputs, but TNT is considered to be the baseline with which other explosives can be compared. For example Composition B has an energy output of 1,240 cal/g while TNT has an output of 1,000 cal/g, thus 1 gram of composition B is considered to be equivalent to 1.24 grams of TNT [Meyers,1994; Wharton,2000]. Using this equivalence it is possible to use the data from CONWEP to determine blast loading for a variety of explosives.

It is important to distinguish some common points of confusion regarding blast data. First, there are two pressures which are commonly quoted in literature. Incident pressure (P_i) which is also referred to as static or side-on pressure, but will be referred to as incident in this thesis. This is used in some work relating to the assessment of injury from blast. Incident pressure is often referred to as side-on pressure because it is the pressure that is seen on a surface whose normal is oriented perpendicular to the direction of fluid flow. A different measure of pressure is reflected pressure (P_r), which is the incident pressure, plus the dynamic/stagnation pressure associated with interaction with a body. Reflected pressure is also referred to as face-on pressure, and corresponds to the pressure actually applied to the front face of a body in a blast environment. In this work, reflected pressure is the value of greatest interest, however loading is often defined in terms of incident pressure, since incident pressure does not is not affected by the geometry and stiffness of the body being loaded.

The reflected pressure (in terms of incident pressure) on a flat, infinite, rigid plate struck by a planar shockwave moving normal to the rigid plate can be given by the following equation [Bulson,1997; Smith, 1994]:

$$\frac{P_r}{P_i} = 2 \frac{7P_{atm} + 4P_i}{7P_{atm} + P_i} \quad (2.3)$$

It can be shown from this equation that the reflected pressure under the above described circumstances will be 2-8 times the incident pressure, however the above relation is not applicable at distances extremely close to the source of blast, due to the assumption of air behaving as a real gas (at extremely close ranges there are gas dissociation effects) [Smith, 1994]. Reflected pressures on differently oriented, shaped or non-rigid walls will not generally follow the above relation. Deformable structures may have lower reflected pressures than a rigid wall for example [Monti,1970]. Also, obliquely reflecting shock waves typically have reflected pressures lower than normally reflecting shock waves. There does exist a critical angle of incidence, however, near which the reflected pressures actually exceed those described in the equation above. In air, this angle ranges between 40° and 55°.

For a blast which occurs above ground, the reflection of a spherical blast wave off of the ground results in the formation of a mach stem. A mach stem is a reflected shock wave which travels at a higher velocity than the original shockwave and results from the merging of the incident blast wave with the reflected wave from the same blast. The height of the mach stem depends on the original blast wave shape and distance of the charge from the ground. The mach stem is illustrated in Figure 2.3 below, and occurs when the angle of incidence of the shock wave exceeds 45 degrees.

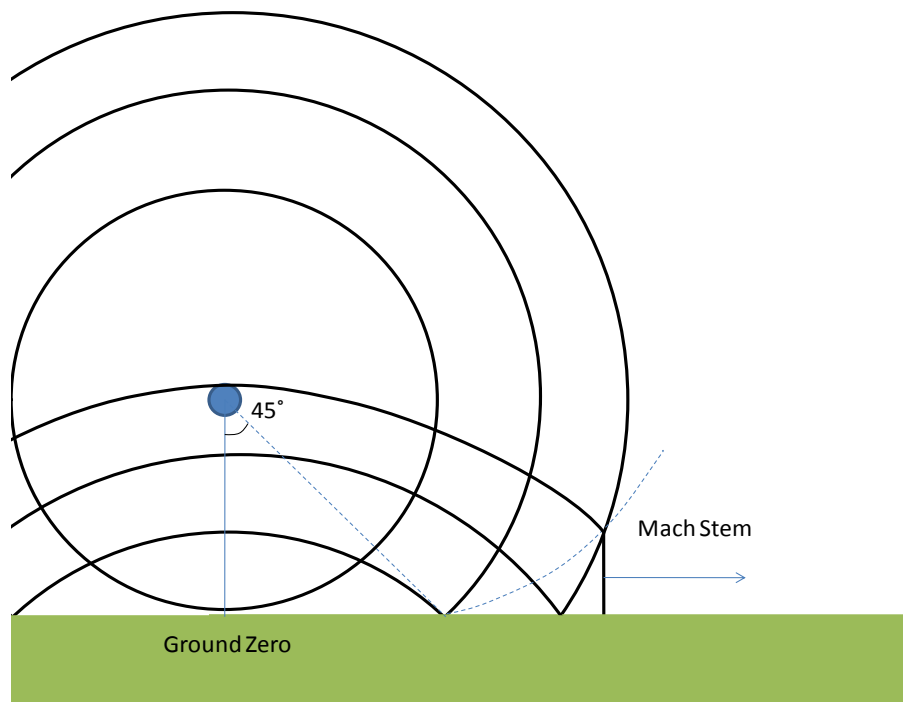


Figure 2.3 - Mach stem [Bulson,1997]

A second point to clarify is the difference between shock-tube loading and blast loading since data of both types is used in experimental blast testing and for validation of models produced for this work. Blast loading consists of finite duration shock wave, which exhibits a behaviour similar to the Friedlander curve. Shock tube loading consists of a shock wave with a relatively square pressure-time profile, a fast rise time (like blast loading), and duration much longer than the typical blast loading. Figure 2.4, below shows the difference graphically.

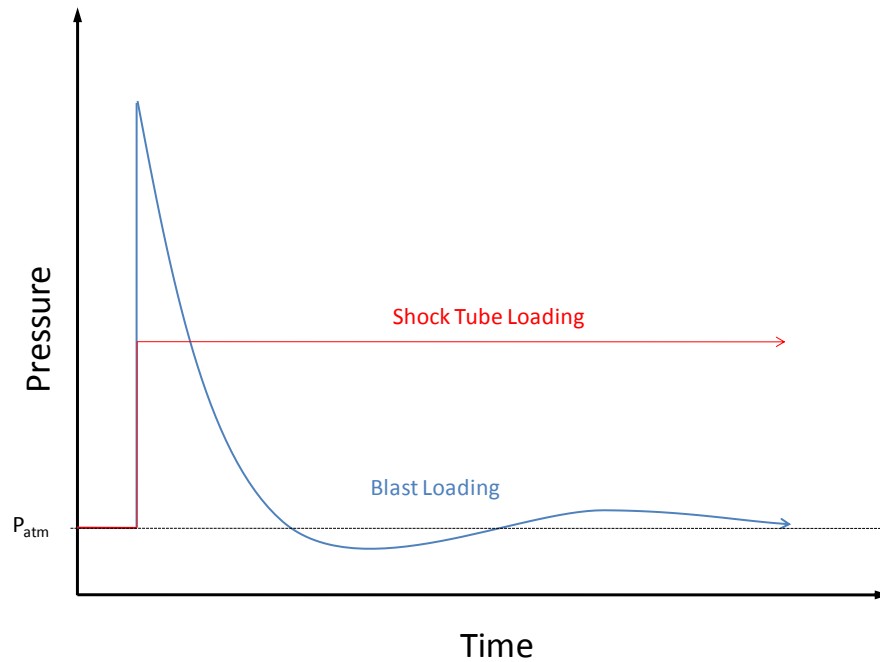


Figure 2.4 - Shock tube vs. blast loading

The Friedlander curve was described earlier in this chapter and shown in Figure 2.2. The typical Friedlander curve is applicable only to “Simple Blast”. As its name implies, “Complex Blast” has a more complicated pressure-time profile; primarily due to reflections of the blast wave off of walls or other structures in the blast field. An example of a complex blast profile is shown in Figure 2.5c. Often, complex blast waves appear to be the result of super-position of Friedlander curves, though for very confined environments, the pressure trace can be extremely noisy due to reflections. Sources of reflection can include walls, floors and ceilings, and as such explosions which occur or propagate to the interior of buildings or vehicles are complex in nature.

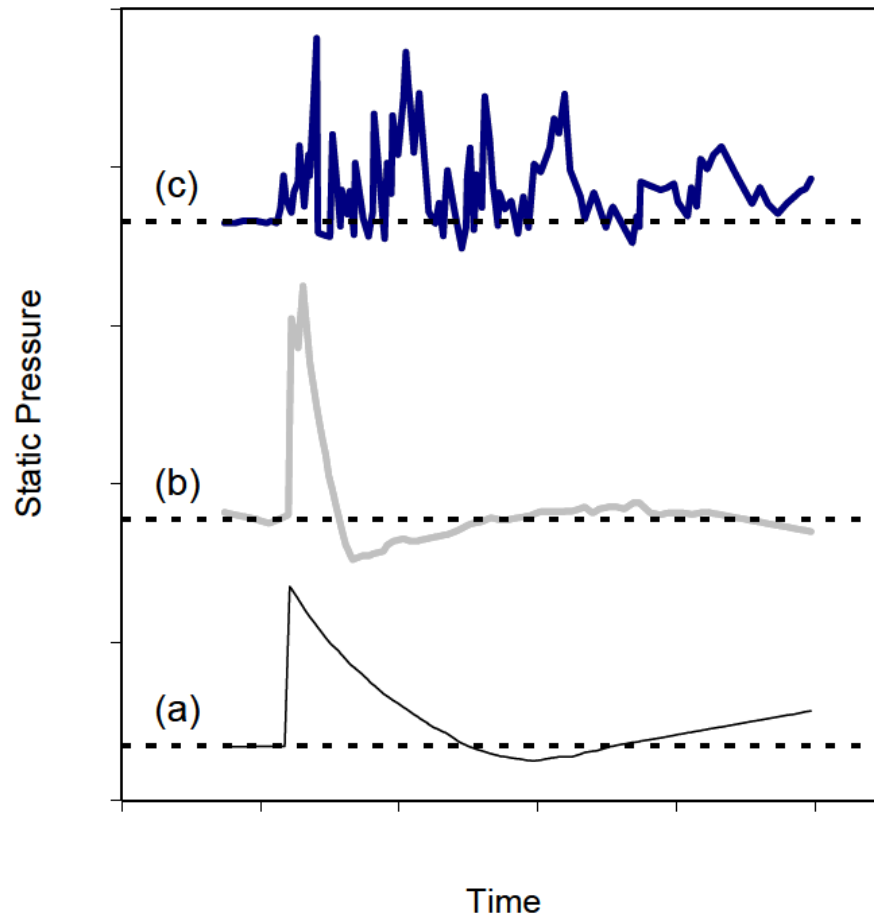


Figure 2.5 - c) Complex blast wave b) Simple blast wave a) Idealized blast wave [Mayorga,1997]

2.2 Wave Propagation and Interaction with Boundaries

The application of force to a body is a dynamic process, however, at low rates the dynamic effects, though present, may not be significant to the overall response. Stresses are transmitted through an elastic body at a speed, c , which can be determined, knowing the material's stiffness, E , and density, ρ , by [Meyers, 1994]:

$$c = \sqrt{\frac{E}{\rho}} \quad (2.4)$$

The above speed is referred to as the elastic wave speed. If loading is applied to at a rate and magnitude sufficient enough to cause particle velocities within the material to exceed the elastic wave speed, then a shock wave is formed.

2.2.1 Interaction of Waves with Boundaries

A topic of wave interaction of interest is the transmission of a wave from one material to another. When a wave arrives at an interface between two materials, a reflected and transmitted wave are produced. The magnitude of the transmitted and reflected waves are dependent on the impedances of the materials on each side of the interface. The impedance can be defined as the product of elastic wave speed and density of a material [Meyer, 1994]. It should be noted that while this calculation of impedance is fine for elastic waves, it serves only as an estimate for calculations involving shock waves.

The ratio of reflected stress to incident stress at an interface can be defined as [Meyer, 1994]:

$$\frac{\sigma_r}{\sigma_i} = \frac{c_2\rho_2 - c_1\rho_1}{c_2\rho_2 + c_1\rho_1} \quad (2.5)$$

While the ratio of reflected stress to incident stress at an interface can be defined as [Meyer, 1994]:

$$\frac{\sigma_t}{\sigma_i} = \frac{2c_2\rho_2}{c_2\rho_2 + c_1\rho_1} \quad (2.6)$$

Where c_1 and ρ_1 are the elastic wave speed and density of the material through which the disturbance is initially passing, and c_2 and ρ_2 are the elastic wave speed and density of the material on the other side of the interface.

From the above equations, if a wave travelling through a material of very high impedance strikes a material of low impedance, the wave transmitted to the low impedance material may be significantly attenuated. Combining materials with sufficiently dissimilar impedances creates what many researchers refer to as a "stress wave decoupler" [Cooper, 1996], which under the right circumstances, can nearly isolate the low impedance material from the high impedance material.

Foams and fabrics, having both low densities and a low stiffness, are examples of materials with very low wave impedance values. Metals, ceramics, and other high density, relatively rigid materials, have relatively high impedance values.

The equations described in this section work well, however material non linearity can limit their applicability in circumstances where large deformations or high pressures occur.

2.2.2 Wave speed in a compressible porous medium

The propagation of waves in a compressible porous medium is more complex than the calculation of wave speed in a linear elastic solid. Gibson, building off of work by Rudinger on the dynamic behaviour of gas-particle mixtures [Rudinger, 1965], showed that the sound speed in a porous material containing air (c) can be calculated as [Gibson, 1995]:

$$c^2 = \frac{c_a^2}{\left[1 + \left\{\frac{\rho_b}{\rho_a} / \left(1 - \frac{\rho_b}{\rho_s}\right)\right\}\right] \left(1 - \frac{\rho_b}{\rho_s}\right)^2} \quad (2.7)$$

Where ρ_b is the apparent bulk density of the material, ρ_a is the density of air, ρ_s is the density of the solid phase of the porous material and c_a is the speed of sound in air.

When the above is used to plot sound speed versus apparent bulk density, it can be shown that porous materials such as foams and textiles have bulk densities which put them near the minima of the sound speed vs. density curve (Figure 2.6).

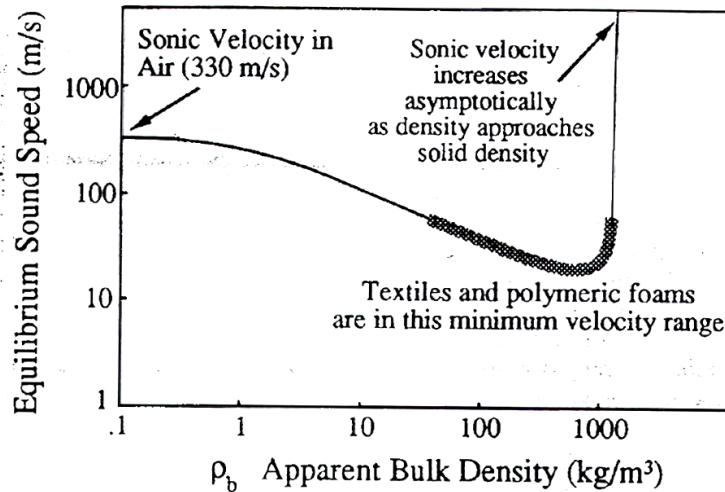


Figure 2.6 - Sound speed versus apparent bulk density [Gibson, 1995]

The above behaviour applies to a few of the materials which were investigated as a part of this research (foams and fabrics).

2.3 Blast Injury

The types of injury resulting from blast are categorized as primary, secondary, tertiary and (in some literature) quaternary blast injury [DePalma et al., 2005; Adler et al., 1988].

Primary blast injury (PBI) is considered to be injury which results from the impact and transmission of a shock or blast wave through the human body, typically affecting air containing organs. Injury of the lungs (blast lung), intestines or gastrointestinal tract (blast gut) and rupture of the tympanic membrane (ear drum) are the traditional PBIs observed. More recently, traumatic

brain injury (TBI) and mild traumatic brain injury are being investigated as a form of PBI [Trudeau et al., 1998].

Secondary blast injuries result from ballistic impact of fragments with the human body. This type of injury is the most common of blast related injuries. While current armour systems are capable of stopping fragmentation, most do not offer complete coverage of the human body. Explosive Ordnance Disposal (EOD) suits offer complete coverage to reduce the risk of fragmentation injury.

Tertiary blast injury is caused by the interaction of the human body with any surrounding surfaces or structures after a blast event. The pressures applied by blast loading can accelerate a subject such that the body is thrown or limbs flail, resulting in impact with environmental objects and causing injury. Tertiary blast injury may also result from the sudden loading causing loss of balance, the subsequent fall causing injury.

Quaternary blast injury generally includes burns, chemicals and other toxic effects resulting from the fireball and detonation products.

The charge size, and distance of a subject to the source of a blast will determine the types of injuries sustained. Table 2.1 shows the types of injuries that might occur at varied distance from a blast threat.

Table 2.1 - Expected Injuries to Unprotected Victims at Relative Distances from HE in Open Air [Wightman et al., 2001]

Injury Type	Distance relative to explosive							
	Close							Far
Total Body Disruption	X							
Burns and Inhalation Injuries	X	X						
Toxic Inhalations	X	X	X					
Tramatic Amputations	X	X	X	X				
PBI of the Lung and Bowel	X	X	X	X	X			
Tertiary Blast Injuries	X	X	X	X	X	X		
Ear Drum Rupture	X	X	X	X	X	X	X	
Secondary (Fragment) Injuries	X	X	X	X	X	X	X	X

Primary blast injury in the form of lung injury is sometimes referred to as blast lung injury (BLI), and will be the focus of this study.

2.4 Primary Blast Injury: Blast Lung Injury

Although the relative occurrence of different forms of blast injury does depend on the specific situation, PBI has been recognized and observed as a significant form of injury [Mellor,1992]. Traditionally, the lungs are considered the organ most susceptible to PBI next to the tympanic membrane [Mayorga,1997; Argyros,1997]. Frykberg [Frykberg, 1988] reported that 47% of 305 fatalities in terrorist bombings in Northern Ireland were found to have blast lung.

Further investigation of cases where humans had been exposed to blast was undertaken in another study [Mellor,1992]. In this study, of 828 servicemen exposed to blast, there were 216 fatalities. Of these fatalities: 24 occurred from chest injury (PBI) without any other sign of injury; 46 occurred as a result of a combination of head and chest injury, and 86 occurred as a result of combined secondary (fragmentation) injury and head or chest injuries. It is also worth noting that 90% of the injured servicemen wore soft ballistic armour.

Results from controlled animal studies [Irwin, 1997; Irwin, 1998; Yelveton, 1996] under blast and shock tube loading have shown blast lung injury tends to have a lower threshold for injury than blast gut injury (both being forms of PBI).

2.4.1 Lung Anatomy

The function of the lung is as an organ for gas exchange between the atmosphere and the human body. Oxygen is absorbed (inspiration/inhalation) and carbon dioxide is expelled (expiration/exhalation) through the lungs in the respiratory process. Air is drawn in through the oral and/or nasal cavity during respiration, and down into the trachea. The trachea splits into left and right primary bronchi, which further separate into bronchi that serve each of the 5 lobes of the

lung: the right superior, right middle, right inferior, left superior, and left inferior lobes. Within each lobe, the bronchus branches out into bronchioles, which supply air to alveolar sacs via alveolar ducts. The alveolar sacs, containing multiple alveoli, are where gas exchange takes place between the air occupying the lung and the human body. The alveoli are covered by a system of capillary's which are connected to the pulmonary veins and arteries. The pulmonary veins and arteries carry oxygen rich and oxygen starved blood to and from the heart/circulatory system. The alveoli allow the lung to have a large surface area for gas exchange, and give the lung its sponge like structure. Any reduction in available surface area, either by flooding of alveolar sacs with fluid or collapse of the lung, results in reduced effectiveness of the respiratory system, and possibly death. A diagram of the respiratory system including details at the alveolar sac level is provided in Figure 2.7.

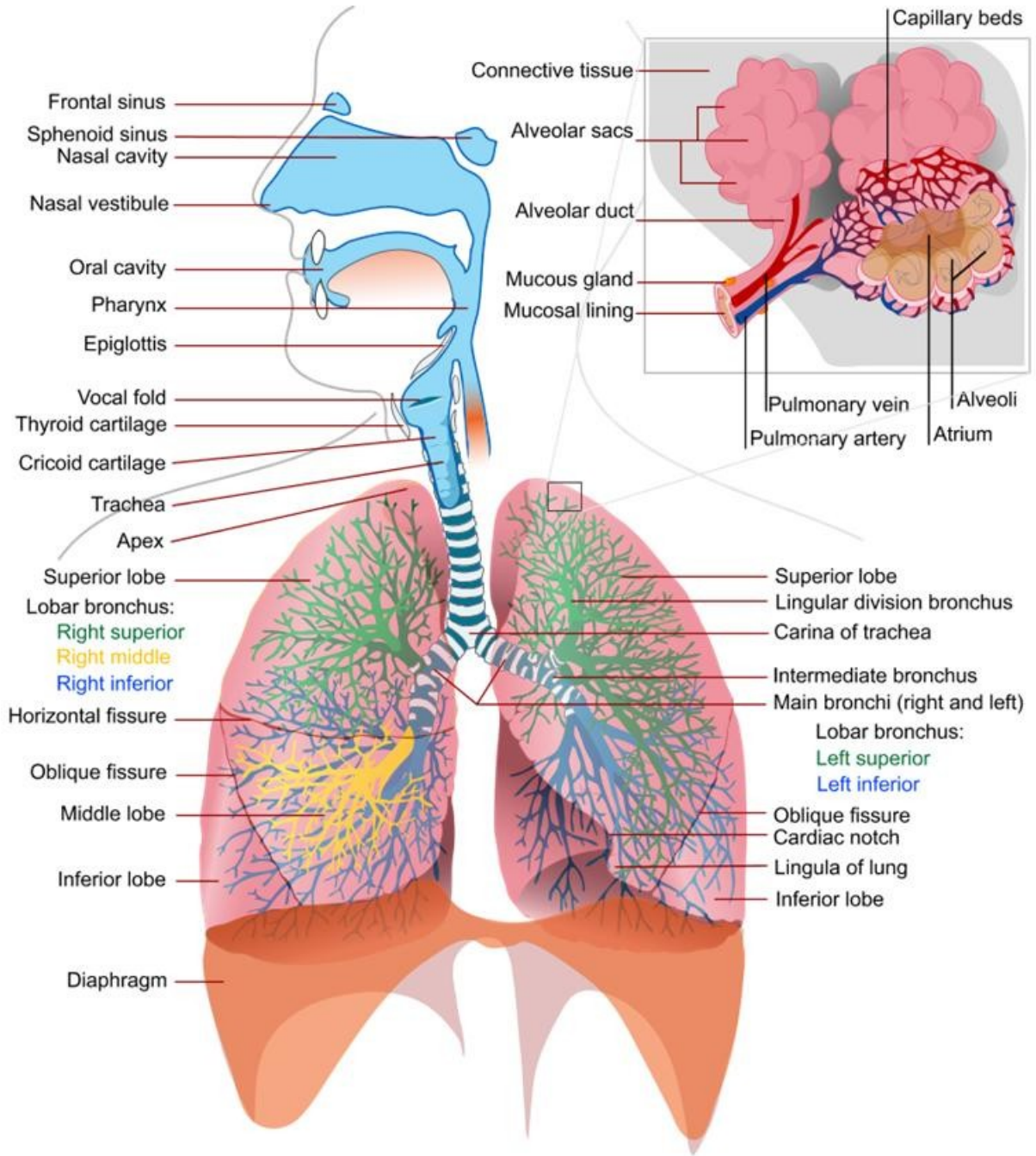


Figure 2.7 - Respiratory System Anatomy [Wikipedia, 2007]

2.4.2 Lung Injury Description

The pathology of lung injury includes pulmonary contusions (bruising), with or without laceration. The contusion manifests itself as hemorrhage and can be observed through petechiae and/or ecchymosis (purple spots or colouring) [Mayorga, 1997] and are primarily observed medially next to the heart, laterally along the rib cage, and at the posterior lung/air interface (the section of the lung near the spine) [Mayorga,1997; Zuckerman,1940]. Lung contusion in blast is observed along intercostal spaces (between ribs), as opposed to contusion resulting from blunt trauma, which is typically seen directly behind the ribs [Adler, 1988]. The previous observation suggests the ribs offer some protection from blast injury, and that the mechanism may not be the same as lung injury observed in different loading conditions.

Hemorrhage into alveolar spaces can cause the lungs to fill with fluid, and reduces the capacity of functioning lung because the area of the alveolar/air interface is reduced. Pulmonary oedema, which also results from damage to the lung, also results in an increase of fluid in the lungs. An X-Ray of a healthy lung is shown in Figure 2.8 while Figure 2.9 shows an X-Ray of a blast victim directly after hospital admittance, as well as after 40 hours of recovery [Rawlins, 1978]. The higher density (lighter) areas on the X-ray show the contused lung.

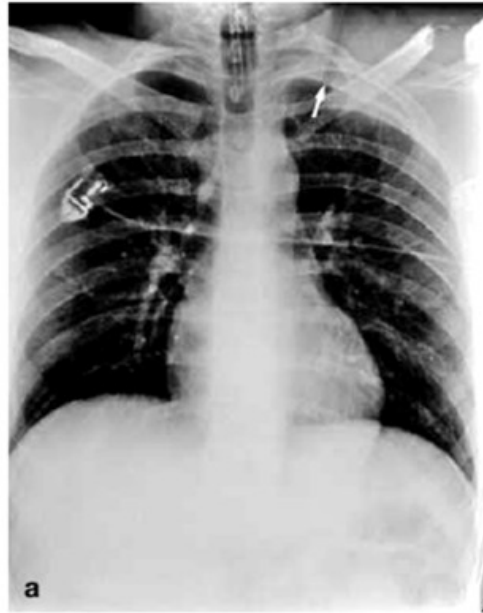
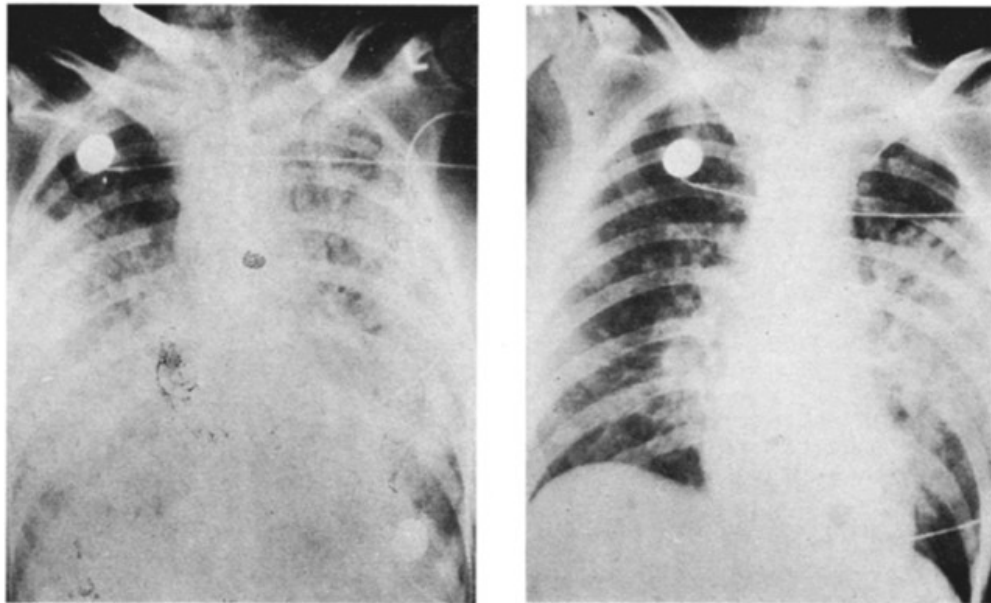


Figure 2.8 - X-Ray without contused lung [Wicky, 2000]



Chest X-Ray of Blast Victim

Subject after 40 hrs of Recovery

Figure 2.9 - X-Rays of a human blast victim [Rawlins,1978]

Lung contusion can also be observed at the tissue level, as shown from samples of rats exposed to blast loading (Figure 2.10)[Chavko et al., 2006]. The lung is initially a very high volume of air,

with a large alveolar surface area (to increase oxygen absorption). The injured lung sample has much less air-alveolar interface present, with much of the lung volume again being occupied with fluid.

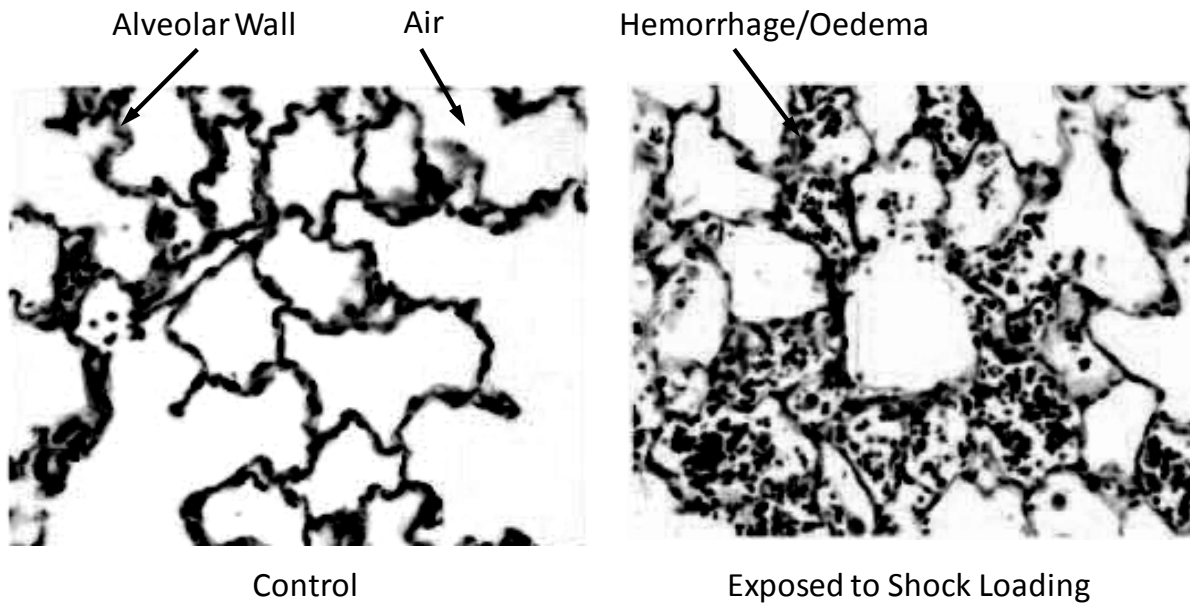


Figure 2.10 - Stained rat lung samples; control and exposed to injurious shock tube loading [Chavko et al., 2006]

Another critical result of injury to the lungs is the risk of air embolism after pulmonary contusion. It is suspected that air embolisms (air bubbles which enter the blood stream and cause blockages of vessels or arteries) are the primary cause of instantaneous death from PBI and may be associated with very aggressive blast loading. Unfortunately, air embolisms are difficult to detect and locate (the air bubbles can dissolve in the blood with time), and as such it is uncertain how frequent or significant they are. They have been observed post-mortem in blast casualties, and one particularly interesting case study reports “When the aorta was opened in order to take a cuff of aorta with the artery, air escaped with a loud hiss, accompanied by foamy blood.” [Freund, 1980]. Examination of case studies where air embolisms have been confirmed shows that they do not occur without pulmonary contusion also being present [Mayorga, 1997; Argyros, 1997].

2.4.3 Injury Mechanisms

The specific mechanism of lung injury and damage to alveoli has not been determined, however there have been 4 mechanisms proposed, some of which are specific to shock type loading [Wightman, 2001; Treadwell, 1989; Ho, 2002].

The first proposed mechanism is spallation [Wightman, 2001; Treadwell,1989]. Spallation can occur when a shock wave reaches the interface of two media. If the acoustic impedance of the material through which the shock is initially propagating is higher than that of the subsequent material at the interface, a tensile wave is formed in the higher impedance material with magnitude depending on the difference between impedances (see Section 2.2.1). If the magnitude of the created tensile wave is of high enough magnitude, high impedance material may be ejected into the low impedance material. In application to lung injury, alveolar tissue or fluid would act as the ejecta, and air within the lungs would behave as a low impedance material, causing oedema (a swelling of tissue caused by an accumulation of fluid).

The second proposed mechanism is implosion [Wightman, 2001; Treadwell,1989]. As the shock wave travels through the lung, the lung compresses and the gas within the alveoli decreases in volume, storing the potential energy. As the shock wave passes the high pressure gases within the lung are allowed to quickly expand, resulting in the alveoli “exploding”, causing lacerations. This could also result in the introduction of air into the blood stream through bronchioles.

The third proposed mechanism is that of differences in accelerations of various materials within the lung [Wightman, 2001; Treadwell, 1989]. The accelerations from a blast wave are so violent, that the differences in inertia between lung components such as the bronchioles and the alveoli could cause shearing forces and damage at the interface [Mellor, 1992].

The fourth proposed mechanism is pressure differential between lung components [Wightman, 2001; Treadwell, 1989]. One of the characteristics of a blast wave is a discontinuity in pressure. While the shock wave is transmitted through the body, the high pressure behind the shock front

could cause blood and other fluids to be forced through alveolar walls. Pressure differentials could also cause shearing injury of tissues as a result of different displacements.

To date, no experiments have confirmed or disproven any of the above theoretical mechanisms behind lung injury. It is likely that lung injury results from a combination of these mechanisms [Ho, 2002], or that the mechanism experienced depends on the nature of the loading experienced by a given volume of the lung.

Because blast lung injury consists of contusion and oedema, injuries which continue to develop after tissue damage, investigations into the mechanism and development of the injury would be properly done through live subject testing. It is difficult (if not impossible) to instrument the lung non-intrusively in order to determine the mechanism behind injury. Without full knowledge of the mechanism behind blast lung injury, it is difficult to infer what the tolerable limits of the lung are in terms of loading. At the tissue level principal strain [Stitzel, 2005] and the product of principal strain and strain-rate [Gayzik, 2007] have been proposed as possible parameters which could have thresholds assigned to them to estimate lung injury numerically. The proposed metrics are based on experiments and subsequent simulation of pendulum impacts to rat lungs in vivo.

Work by Stitzel suggests first principal strain as a metric to be used in FEA for determining the volume of injured lung, as well as intensity of the injury (based on the number of days after injury that the lung remains contused). Volumes of contused lung were determined from impact experiments using Positron Emission Tomography (PET), after which FEA was used in order to determine the first principal strain thresholds summarized below in Table 2.2.

Table 2.2 - Percent Contusion of Rat's Right Lung from Experiment and FEA [Stitzel, 2005]

Days After Impact	1	7	28
Percent Contused Lung from Experiment	93%	62%	8.6%
Percent Contused Lung from Finite Element	93%	62%	8.6%
First Principal Strain Threshold	0.035	0.088	0.35

A study by Gayzik [Gayzik, 2007] used Computer Tomography (CT) scans to determine “High Radiography” (HR) lung volume (which consists not only of contused lung, but also could include collapsed alveoli and hemothorax), and compared the accuracy of various metrics from FEA calculations (Table 2.3). Statistical comparisons via a registration score, calculated by comparing the dimensions of the experimental HR volume and the numerically predicted HR volume, were used for comparing the metrics. The study found that the product of maximum principal strain and strain rate within the lung was the best metric for predicting lung injury.

Table 2.3 - Comparison of Various Metrics for Predicting Lung Injury [Gayzik, 2007]

Rank	Metric	24 hour post-impact threshold	Reg. Score	Reg. Score (Percent Increase)
1	Max principal strain · strain rate	28.5	0.320	
2	Max principal strain	0.154	0.338	6%
3	Max principal strain rate	304	0.345	8%
4	Max shear strain rate	367	0.346	8%
5	Max shear stress	7.10	0.349	9%
6	Triaxial mean strain rate	58.3	0.382	19%
7	Max shear strain	0.210	0.390	21%
8	Max shear strain · rate	48.9	0.396	23%
9	Octahedral shear stress	6.00	0.401	25%
10	Triaxial mean strain	0.0242	0.493	53%
11	Triaxial mean strain · strain rate	0.700	0.540	67%

Work by Yuen, et al. [Yuen, 2008] examined the lung response of a 50th percentile male numerical surrogate to vehicle side impact conditions. As a part of Yuen’s study, strain, strain rate and strain multiplied by strain rate were examined as potential metrics for estimating lung injury. It was found that strain rate did not converge numerically, and was highly dependent on mesh density. Strain, while converging with increasing mesh density, did not account for rate effects of loading and under-estimated high velocity impact injuries. Dynamic pressure was determined to be an appropriate metric for predicting lung injury, due to its convergence with increased mesh density, and ability to capture transient effects and properly predict the high-velocity injury. The threshold

values for strain and strain rate based metrics for the study by Yuen were different from those by Gayzik and Stitzel, due to differences in lung material models and mesh densities.

It has been shown in one study of patients with pulmonary contusion (not from blast) [Wagner, 1989], that patient with 18% or less of lung volume reduction from contusion (determined through Computed Tomography) did not require ventilation. On the other extreme, patients with 28% or more of their lung air space filled with fluid required ventilation. While this does not offer much in terms of quantitative data, it does offer some qualitative information regarding the severity of contusion. The results from Wagner [Wagner, 1989] are in line with another study [Miller, 2001] where 20% lung contusion, as determined through CT, was considered to be a critical volume, across which incidence of acute respiratory distress syndrome (ARDS) increases dramatically. In the study by Miller, 78% of patients developed ARDS when 20%-30% of their lung was contused by volume; compared to 16% of patients developing ARDS when contused lung was in the 10%-20% range.

2.5 Effect of Protection on Observed Blast Injury

It has been shown in various studies that soft ballistic protection, such as vests made from Kevlar, may increase the severity of lung injury resulting from shock and blast waves. Work using human volunteers [Young, 1985] has shown that fabric-based protection can amplify the overpressure in a blast scenario. However, the limitations of live human testing meant that only small blast overpressures could be used (18.6 kPa) and pressure measurements could only be taken in the esophagus. An increase in lung injury with fabric vests has also been observed using sheep, where increased injury (based on lung weight) and risk of mortality was observed for animals wearing cloth ballistic vests as compared to those not wearing cloth ballistic vests [Phillips, 1988].

In order to investigate protection concepts aimed at mitigating PBI, work done by Cooper et al, [Cooper, 1996; Cooper, 1991; Cripps, 1996] focused on the use of low impedance materials. The results of animal tests using only foam and rubber for protection had shown that these materials actually increase the likelihood of injury from blast. The explanation offered by the

experimentalist is that the soft materials increase the “coupling” of the blast loading to the torso. It is also suggested that the foams and rubber materials change the frequency of the loading such that it is nearer the frequency of resonance of the rat’s thoracic wall (reported to be 0.35-0.8kHz in [Cooper et al., 1991]).

This finding by Cooper is contrary to earlier work [Zuckerman, 1940] which found that foams could be used to reduce lung injuries in rats. This contradiction suggests that the differences in material thickness, properties, or loading could result in different results and thus soft materials have the potential to both mitigate and exacerbate blast injury.

Further investigations into foams and rubber materials by Cooper [Cooper, 1991; Cooper, 1996] have shown that by mounting a high density material onto the front face of the foam (that is, the face that is struck by the blast wave), it is possible to reduce the level of injury from blast in live animal subjects. Cooper attributes the reduction of injury to “stress-wave decoupling”, which is achieved by mounting material with a high acoustic impedance (for example, a metal or ceramic) onto a material with low acoustic impedance (for example, foam or rubber).

Based on the experiments described, and the current materials used in protection, four materials have been identified that are particularly relevant to attenuation of blast injury: single layers of fabric, multiple layers of fabric (soft ballistic vests), foams (for attenuation), and high density materials (such as ceramic used in ballistic plates).

2.6 Techniques for Estimation of Blast Lung Injury

Numerous studies have been undertaken in order to develop techniques that can be used to estimate lung injury. Animal testing has been relied upon in a number of studies, particularly earlier studies in order to investigate the effects of varied blast loading on injury, and estimate the tolerance of mammals to blast loading. It is costly and difficult to conduct biological tests on living subjects, and so most tests where animals have been exposed to blast loading have been used in order to aid the development of injury criteria and models to predict injury.

The injury estimation techniques that have been developed can be categorized as being load based, mathematical models of the torso, physical surrogates of human or animal subjects, and numerical (finite element) surrogates. It will be seen that no consensus has been made as to the metric that best correlates, and makes physical sense to correlate, to lung injury.

2.6.1 Load Based Technique (Bowen Curves)

This section describes techniques for estimating injury that use the applied loading to estimate injury directly. These techniques do not require the use of a model (mathematical or finite element), but attempt to estimate injury resulting from a given blast loading (defined either by peak pressure and duration, or charge size and distance).

Studies by Bowen [Bowen, 1968] used animal test data to estimate human tolerance to blast in terms of the peak pressure and positive phase duration of the loading. The experiments were carried out on monkeys, swine, goats, dogs, cats, steers, rats, hamsters, rabbits, mice and sheep. The use of a range of animal sizes allowed the development of mass scaling laws which were applied in order to predict the human tolerances. The tolerance curves produced by this study (Figures 2.10-12) are commonly used when determining the likelihood of blast lung injury under given loading conditions. Each curve represents a probability of "lethal dose" (LD). A blast load which falls on the LD50 curve has a lethality of 50%.

Note that the values used by [Bowen, 1968] are side-on overpressure values (static gauge pressure) and do not represent the pressures actually applied to the human body. Explosives were used to produce loadings of short durations, however shock tubes were also used to produce long duration shock loads. In all cases, animals were against a reflecting surface, resulting in an increased blast loading due to the reflection of the shock wave off of the reflecting surface.

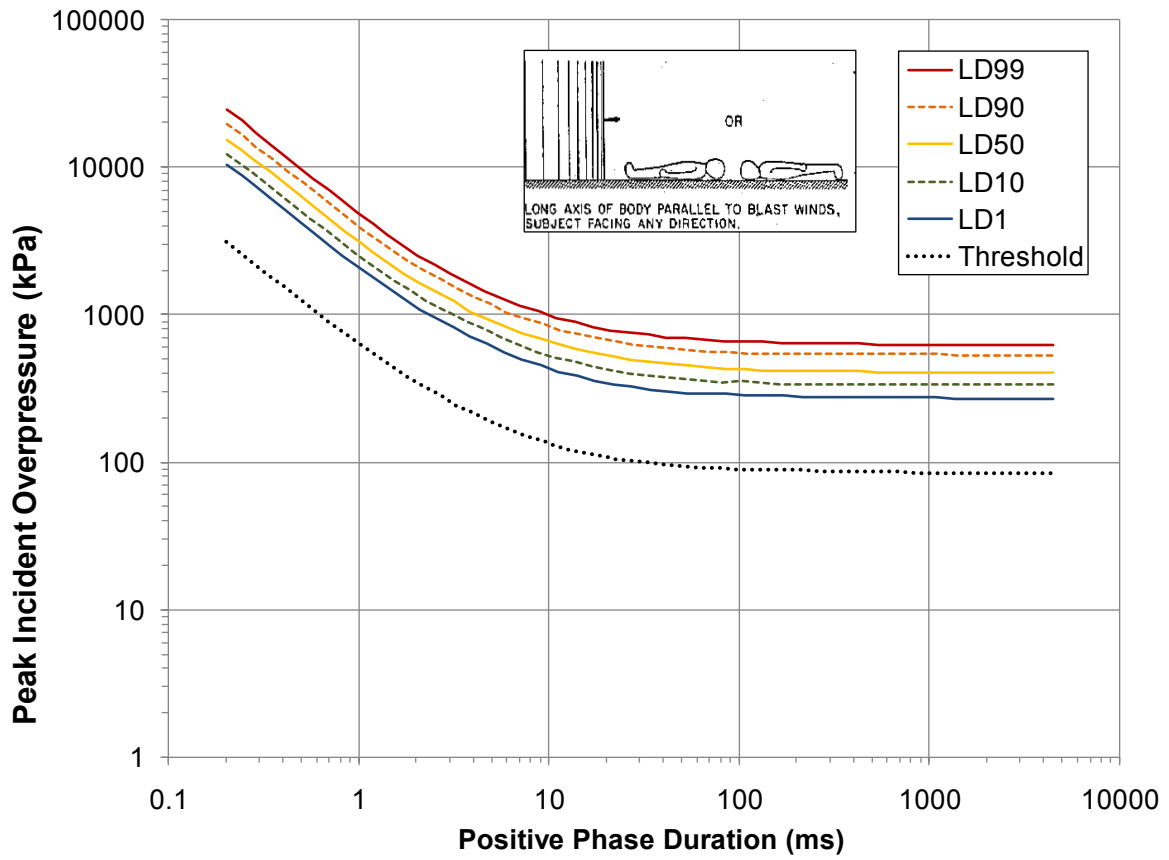


Figure 2.11 - Bowen injury prediction for the case of body being parallel to blast [Bowen, 1968]

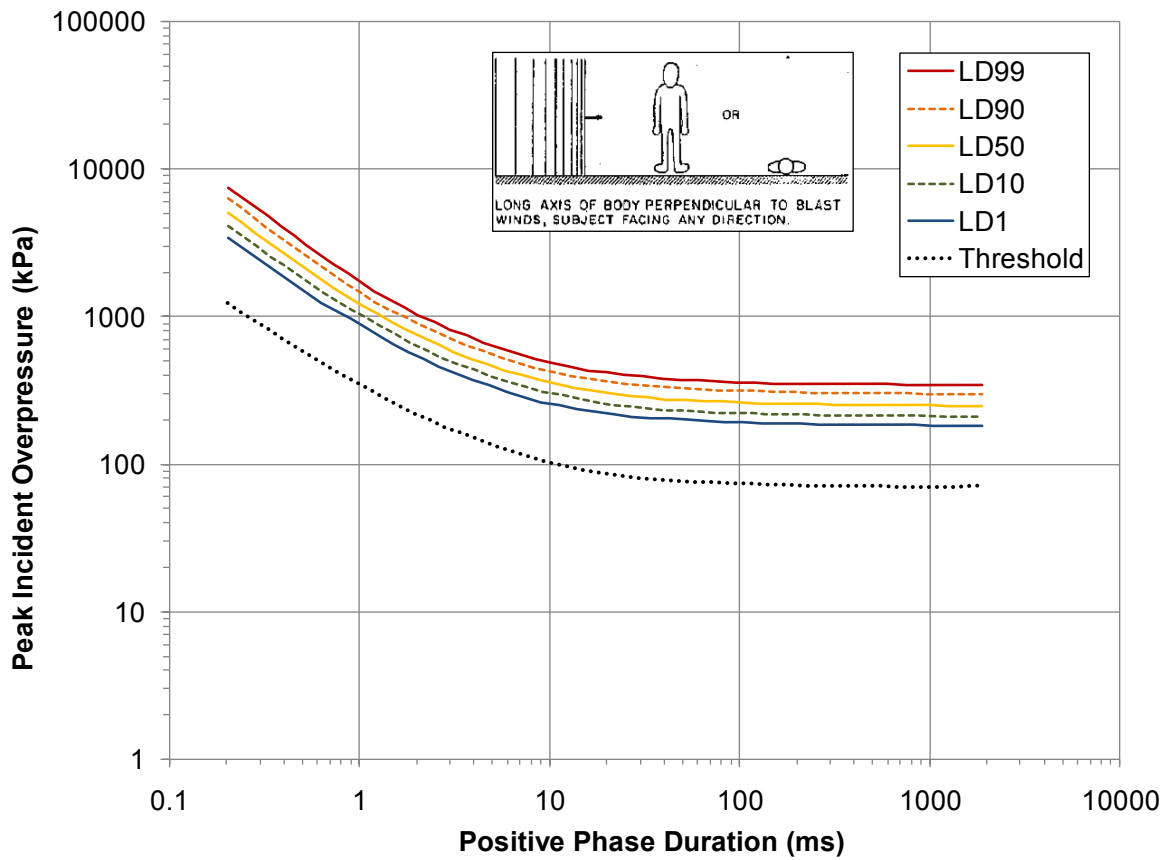


Figure 2.12 - Bowen injury prediction for the case of body being perpendicular to blast [Bowen, 1968]

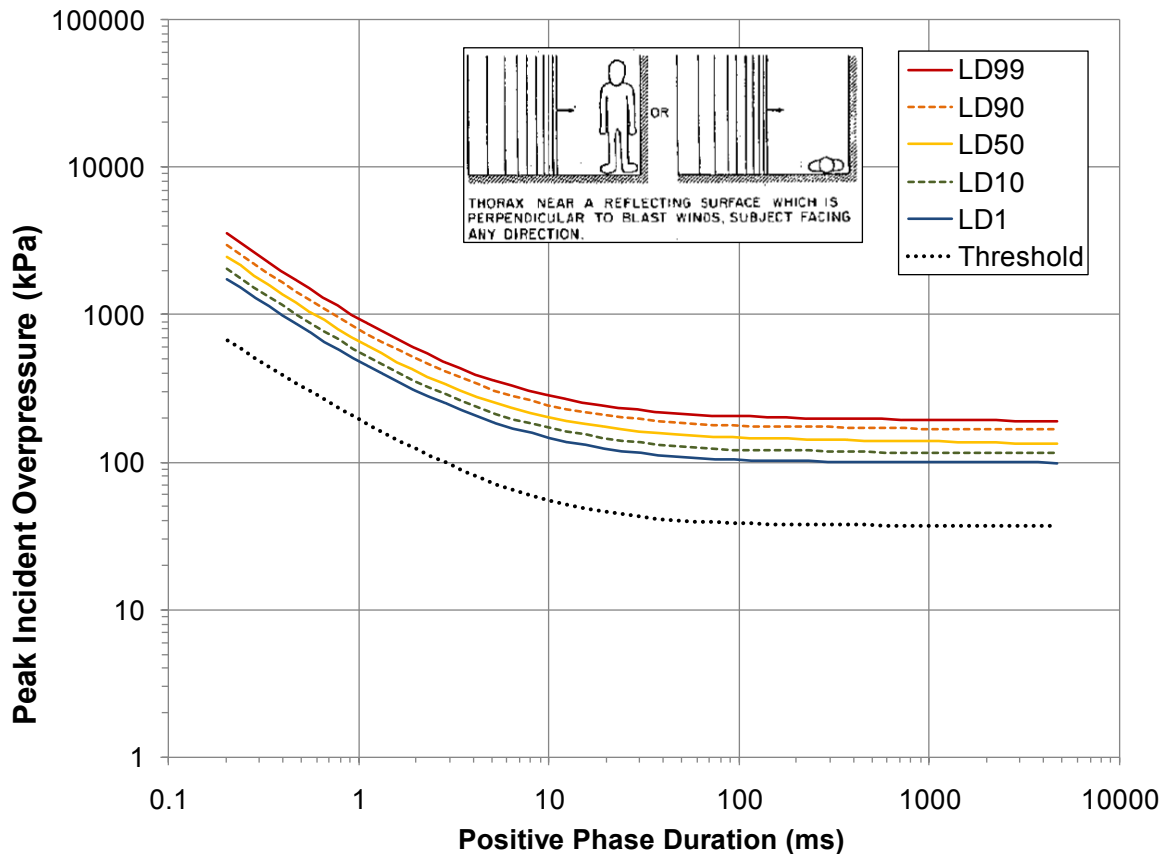


Figure 2.13 - Bowen injury prediction for the case of body being perpendicular to blast and against a reflecting surface [Bowen, 1968]

A limitation of the original Bowen data [Bowen, 1968] is that while pressures were measured, duration was estimated based on the peak pressure, and empirical correlations between peak pressure, duration, charge size, and distance. Also, the curves which predict injury from free field blast pressure do so through a few assumptions. For example, Figure 2.11 (injury prediction for a body laying parallel to the direction of blast propagation) was generated by assuming similar injury will result from a given loading, whether resulting from reflected pressure (what was measured in experiments) or free field pressure (what is assumed in Figure 2.11) . Figure 2.13 represents the loading scenario closest to the original experiments.

Due to increased interest in blast injuries, the original curves by Bowen were re-evaluated, and adjustments have been proposed [Bass, 2006; Gruss, 2006] using the knowledge gained regarding

blast since the publication of Bowen's original results. These adjustments affect the lower duration region of the Bowen curves. Unfortunately, the adjustments suggested by Gruss are contrary to those suggested by Bass et al.; that is, Gruss suggests that the Bowen curves are overly conservative, while the Bass results suggest that the Bowen curves under-estimate the injury during low duration blasts under certain loading conditions.

The Bass curves are based on an assessment of various blast studies done prior to 2006, including data from the original Bowen studies [Bass, 2006]. A total of 1129 animal experiments from the literature were used by Bass et al. to estimate tolerances for short duration (<30ms) blasts. Differences between the Bass and Bowen curves are visible in the "Perpendicular" and "Parallel" cases (shown in Figure 2.14 and Figure 2.15, respectively). A particular difference, aside from the larger pool of data from which Bass et al constructed their curves, is that while Bowen scaled over pressures based on ambient pressures (based on long duration, shock tube, results), Bass et al. consider this unjustified for short duration blasts, and thus did not scale pressures based on ambient conditions.

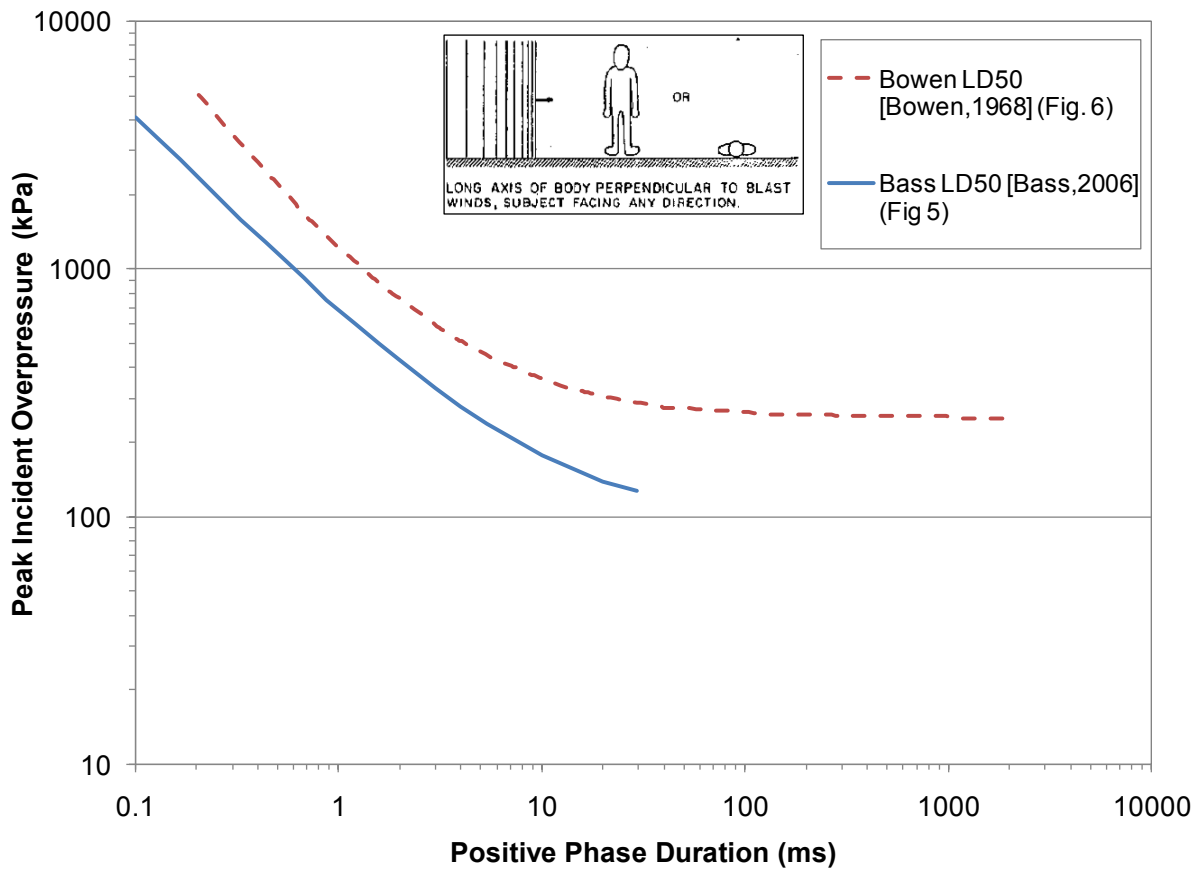


Figure 2.14 - Comparison of LD50 curves for Bass study [Bass, 2006] and original Bowen curve [Bowen, 1968]

Work by Gruss [Gruss, 2006] applied a correction to the Bowen curves based on more recent explosives data. The empirical data for relating charge size and placement to peak pressure is relatively unchanged between the Gruss and Bowen studies. Conversely, the more recent data for positive phase duration suggests that at short durations Bowen was underestimating the positive phase duration of blast loading. An example comparing the Gruss and Bowen curves is shown below in Figure 2.15. Also note the Bass curve, which deviates from the original Bowen LD50 curve at durations over 3ms.

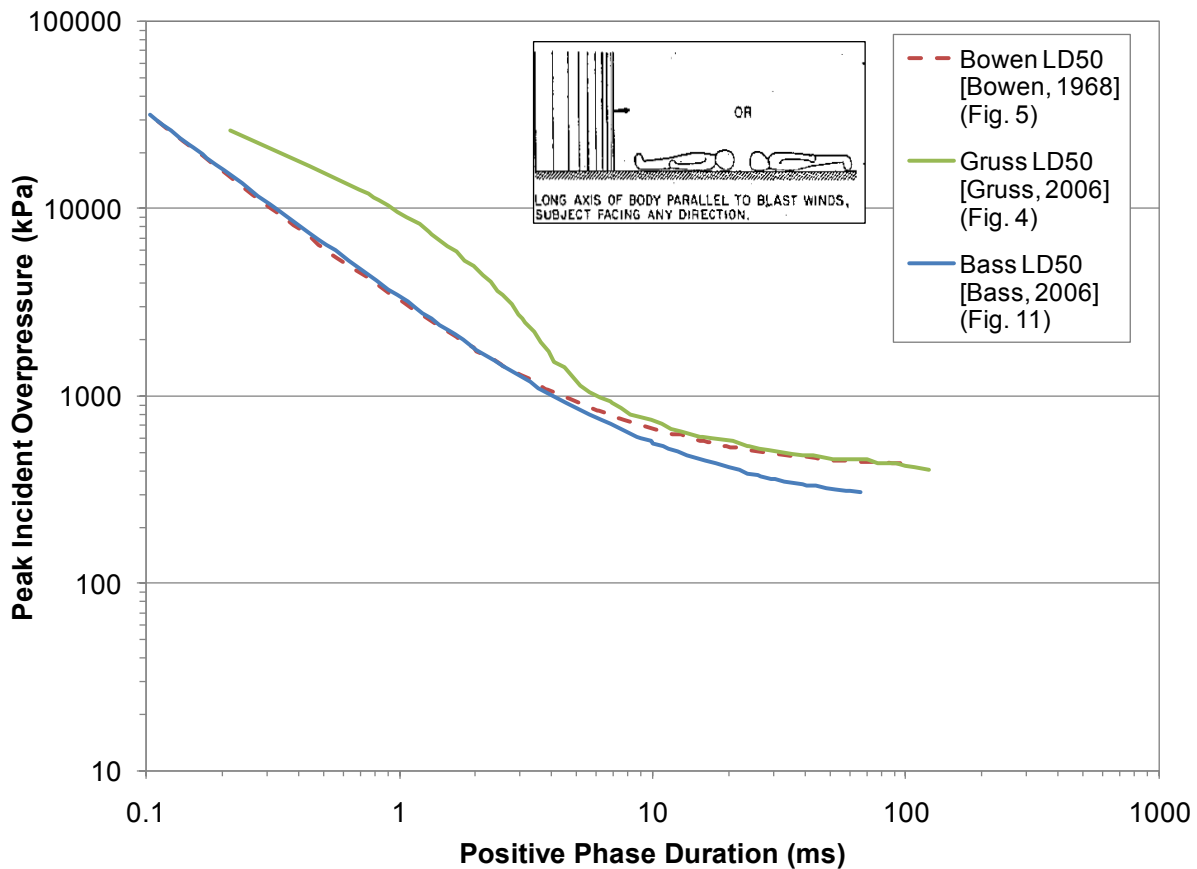


Figure 2.15 - Comparison of Bass [Bass, 2006], Gruss [Gruss, 2006] and Bowen [Bowen, 1968] LD50 curves for the case of body orientation parallel to blast

Given the uncertainty in these recent developments, the more conservative curves (as proposed by [Bass, 2000]) are more appropriate for use in this study. These curves were used in the validation of a model for injury developed at the University of Waterloo and used for the current study.

2.6.2 Mathematical Model of the Torso

At the torso level, chest wall velocity has been proposed to correlate with lung injury [Axelsson, 1996]. A mathematical model, representing the stiffness and damping characteristics of the human torso, was developed in order to estimate injury under a given loading, including simple and complex load cases. The pressure developed in the gaseous volume of lung was the intended

metric for injury evaluation using this model (which effectively makes the metric chest wall displacement). Axelsson found that chest wall velocity was a better correlate to injury and thus this is the result used for estimating injury using the model.

The Axelsson model treats the thorax as a spring, mass, damper system. A diagram illustrating this is presented in Figure 2.16 [Axelsson, 1994].

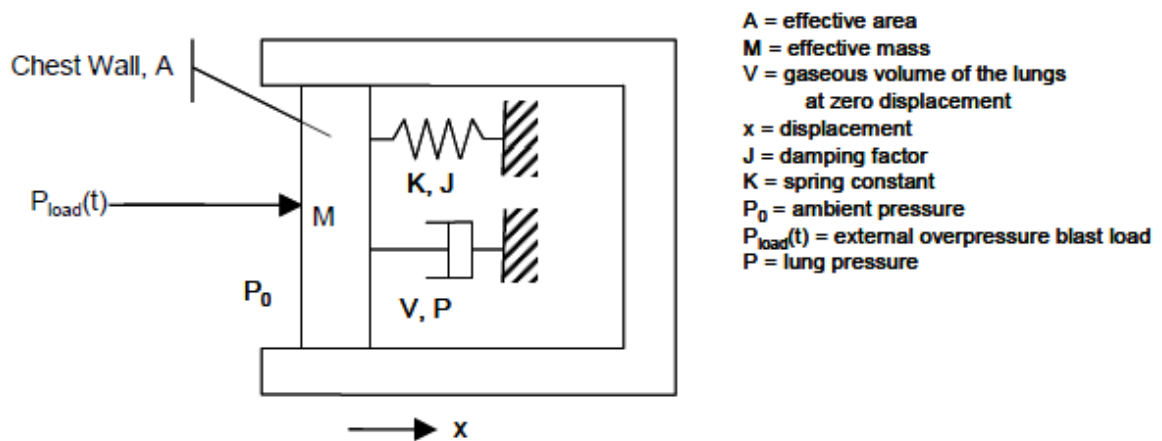


Figure 2.16 - Diagram of Axelsson mathematical torso model [Axelsson, 1994]

Displacement of the chest wall produces a pressure in the closed chamber (meant to represent the lung). The pressure produced in this chamber also resists movement of the chest wall. The mathematical model is presented below [Axelsson et al., 1996].

$$M \frac{d^2x}{dt^2} + J \frac{dx}{dt} + Kx = A \left[p(t) + P_0 - \left(\frac{V}{V - Ax} \right)^{\gamma} P_0 \right] \quad (2.8)$$

It should be noted that by modelling this way, Axelsson did not capture any of the associated wave phenomenon, and thus this model presumed that chest-wall kinematics dominate lung injury from blast. The parameters for the model are given in Table 2.4 below.

Table 2.4 - Axelsson Model Parameters [Axelsson et al., 1996]

Parameter	Units	70kg Body	Scaling Factor
M	kg	2.03	$(m/70)$
J	Ns/m	696	$(m/70)^{2/3}$
K	N/m	989	$(m/70)^{1/3}$
A	m ²	0.082	$(m/70)^{2/3}$
V	m ³	1.82E-03	$(m/70)$
g	-	1.2	-

Experimental studies on sheep in an enclosure were used by Axelsson to validate this model for complex blast scenarios. In total, 177 sheep were exposed to this complex blast loading. It was found that the pressure in the lungs predicted by the model did not correlate well with the injuries seen in experiments. Inward chest wall velocity was found to correlate and thus the chest wall velocity from the Axelsson model was selected by Axelsson for use in predicting injury. The proposed correlation between chest wall velocity and injury level is shown in Table 2.5.

Table 2.5 - Injury levels corresponding to ASII and inward chest wall velocity [Axelsson et al., 1996]

Injury Level	ASII	Chest Wall Velocity (m/s)
No Injury	0.0-0.2	0.0-3.6
Trace to Slight	0.2-1.0	3.6-7.5
Slight to Moderate	0.3-1.9	4.3-9.8
Moderate to extensive	1.0-7.1	7.5-16.9
>50% Lethality	>3.6	>12.8

A similar approach was undertaken by Stuhmiller et al. [Stuhmiller, 1996]. Instead of modelling the thorax as a mass/spring/damper system, a model which took into account the bulk pressure and compression waves developed by chest wall compression was developed (Figure 2.17).

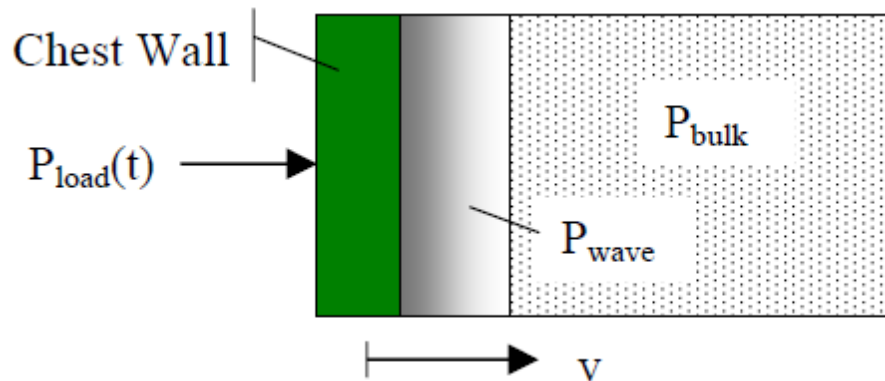


Figure 2.17 - Diagram of Stuhmiller torso model [Stuhmiller, 1996]

While a general description of the approach taken by the researchers is given, published information on the Stuhmiller model was not specific (constants or formulation are not available) [Stuhmiller, 1996]. The model was implemented in an injury prediction program, the most recent being Injury 8.2 (L3 Communications/Jaycor, 2006). The model takes pressure traces from experimental or numerical blast scenarios, and estimates the percentage of lung injury. The model calculates the normalized work which is “...total work done to produce the wave [in the lung model] divided by the volume of the lung and the ambient pressure” [Stuhmiller, 2006]. The relationship of normalized work to lung injury is shown below (Figure 2.18).

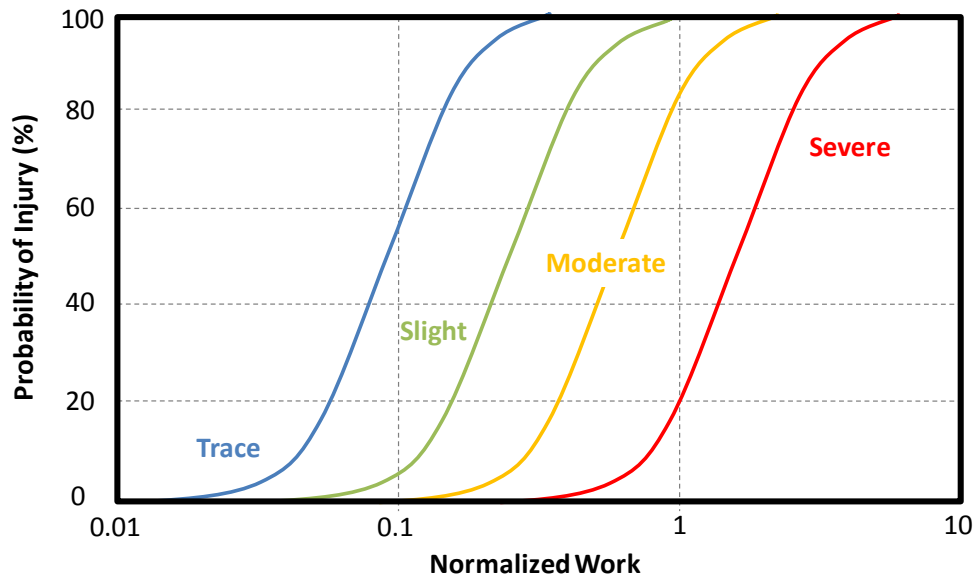


Figure 2.18 - Probability of injury vs. normalized work [Stuhmiller, 1996]

It is interesting to note that it was found that the compressive wave strength in Stuhmiller’s lung model increased linearly with increasing chest wall velocity [Stuhmiller,1997], which lends validity to Axelsson’s injury criterion based on chest wall velocity for predicting injury.

2.6.3 Physical Surrogates

Physical surrogates are desirable for experimental studies because of the difficulty and cost associated with live animal testing. Some surrogates like the Blast Test Device (BTD) are used to provide inputs into models for injury prediction, while others like the thoracic rig [Cooper, 1996] and the Mannequin for the Assessment of Blast Incapacitation and Lethality (MABIL) [Ouellet, 2008b] use the kinematics of the surrogate to predict injury directly (chest wall acceleration, for example).

The inputs to both the Axelsson and Stuhmiller models are the reflected pressure, side-on pressure, and the pressure seen at the back of a body as measured by four pressure transducers. Blast Test Devices (BTDs) are commonly used in experiments to acquire the required pressure measurements

for calculating injury using the Stuhmiller or Axelsson models, and represent a simple physical surrogate of the body.

A BTD is a hollow cylinder with 4 pressure gauges mounted as shown in Figure 2.19 below. The cylinder is kept as rigid as possible. The BTD described by Axelsson [Axelsson, 1996] and used for his work was a 0.305m diameter hollow cylinder. The pressure transducers were located at the circumference, and at half of the longitudinal length of the cylinder. The cylinder was placed such that the pressure transducers were 1.22m off of the ground during the experiments.

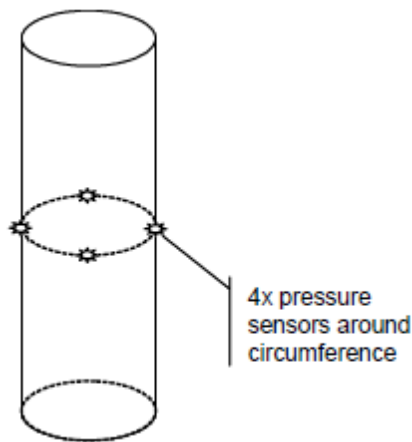


Figure 2.19 - Diagram of a BTD

The Axelsson model uses the pressure readings from all four pressure sensors around the BTD circumference, uses each pressure trace as an input to his model and then averages the results for use in estimating injury. The result is the average peak value of inward chest wall velocity. There are some obvious weaknesses to this approach (applying averaged pressure trace data to a 1-D model), however, this averaging approach was taken due to the use of this model in evaluating complex blast. If only one gauge was used to calculate chest wall velocity, some of the waves resulting from reflections might not be measured.

The Stuhmiller model also uses all 4 pressure traces in a single injury calculation. The results are dependent on orientation, and thus different results can be obtained from the model by choosing

different traces to be the front/centre pressure trace. Thus, from a single set of BTD data it is possible to predict injury when the subject is facing the blast, 90 degrees to the blast, and facing away from the incident blast wave. However, the significance of each pressure trace, and how it is used in the model, has not been published.

A limitation of the BTD as a surrogate is that it does not deform when struck by a blast wave, and thus the reflected pressure as measured by transducers is likely over predicted compared to what would be seen on a deformable cylinder. More importantly, the geometry of the BTD is cylindrical with a smaller diameter than the human torso, and the relatively slender geometry of the BTD could result in lower reflected pressure measurements than if they were taken from a torso. The significance of the above limitations has not been determined in any studies. The Axelsson and Stuhmiller models are calibrated to BTD results, and thus using data from BTD experiments is the only recommended means of using these models.

Another surrogate has been proposed by Cooper [Cooper, 1996], and was designed to be a deformable physical surrogate of a porcine test subject (pig). The surrogate consisted of a rounded, hollow, rectangular tube of Rubber, with two steel and aluminum end plates. During experimental evaluation of the rig, lead loaded PVC had to be added to the surrogate in order to tune the response to more closely represent the porcine subjects it was meant to imitate.

The metric used when evaluating the results from the above rig was the peak acceleration of the thoracic wall. This was based on a previous study using both shock tube and explosive data [Cooper,1996], where severity of lung injury, determined by lung weight after blast loading, was correlated to peak acceleration of the thoracic wall (Figure 2.20). For the live animal tests, a peak chest wall velocity of 10,000 m/s² was considered to be the threshold value, below which, the incidence of injury is “low” and above which the incidence is higher. The surrogate designed by Cooper is tuned to allow use of the same 10,000 m/s² threshold.

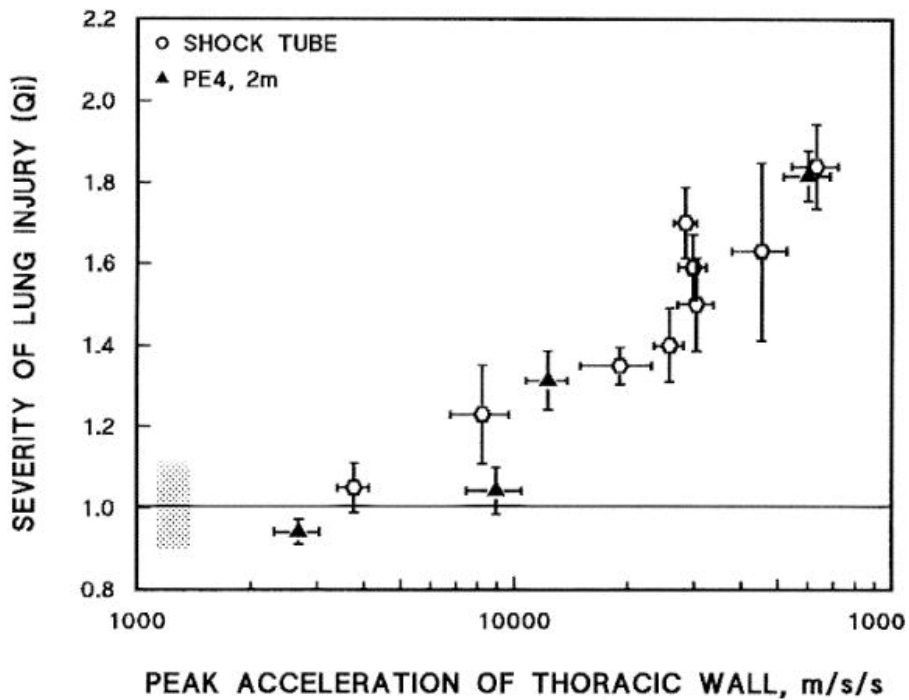


Figure 2.20 - Severity of lung injury vs. thoracic wall peak acceleration for both shock tube and high explosive shock loading [Cooper, 1996]

The purpose of the Cooper rig was to evaluate protective concepts. As discussed previously, soft armors were found to exacerbate lung injury, while combinations of hard and soft materials were found to attenuate blast injury. Peak acceleration of the thoracic wall is the only metric in the literature that shows sensitivity to protection concepts used and their effect on lung injury. This is illustrated in Figure 2.21 below. Note that textile armor alone increases peak thoracic wall acceleration and severity of lung injury, and stress wave decouplers reduce both chest wall acceleration and lung injury [Cooper, 1996].



Figure 2.22 - MABIL thoracic surrogate [Ouellet, 2008b]

The surrogate has accelerometers mid torso, one at the height of the sternum, and another located in the abdomen. While the surrogate is not tuned to reproduce “biofidelic” response (I.E., response that is comparable to that of a human torso) it is useful in that it can be used to evaluate protective concept designs that could potentially be used by soldiers in the field.

Like the Cooper surrogate, acceleration was found to be a good metric when protection was added to the torso (Figure 2.23).

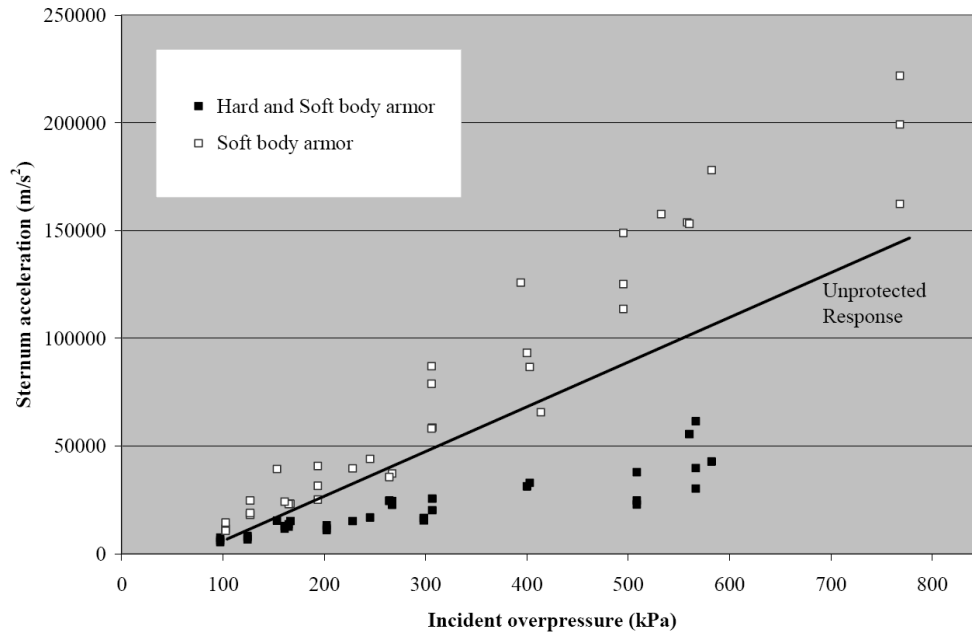


Figure 2.23 - MABIL sternum acceleration vs. peak incident overpressure [Ouellet, 2008b]

Velocity was also investigated as a metric for use with MABIL to evaluate protection (Figure 2.24), however this metric did not seem to predict an amplification of injury with the use of soft body armor. It will be shown later that care must be taken in assuming soft materials always amplify blast injury; however, for the loading and thickness of soft ballistic of material seen here, amplification should be expected.

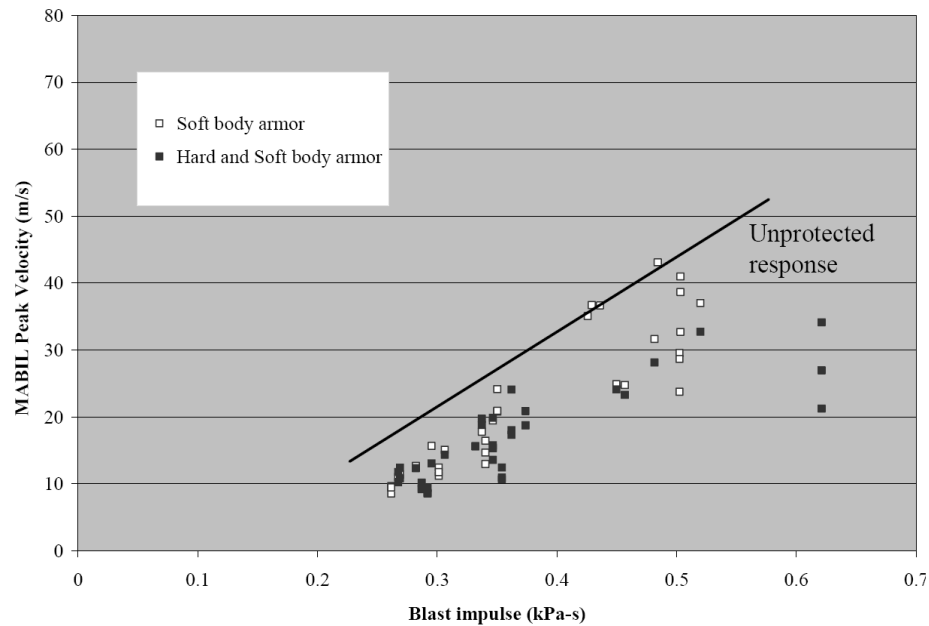


Figure 2.24 - MABIL sternum peak velocity vs. blast impulse [Ouellet, 2008b]

2.6.4 Numerical Surrogates

The mathematical models and experimental surrogates described above are useful, in that they build from correlations between loading and the behavior of the thoracic wall, and the kinematics of the thoracic wall are correlated to a probability of lung injury. The short coming of these models and surrogates is that they do not predict lung injury at the local level, nor have they been fully validated for complex loading and protection. More complicated finite element models have the potential to provide a more detailed evaluation of lung injury. An additional benefit of numerical models is that they can facilitate parametric studies and, potentially, aid as protection design tools.

A model developed by L3/Jaycor, as a continuation of the Stuhmiller studies, utilizes the finite element method to estimating lung injury [Stuhmiller, 2006; Stuhmiller, 1997]. The model was a 3-dimensional model of the torso (Figure 2.25).

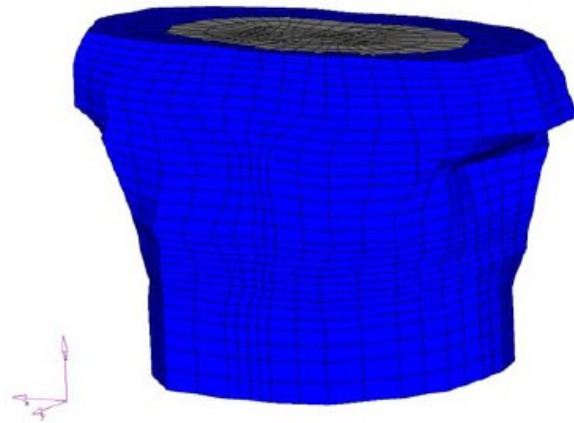
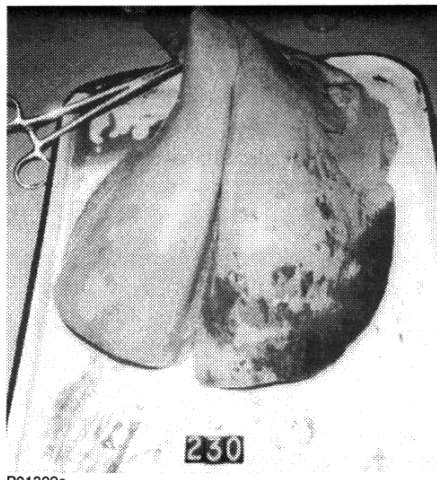


Figure 2.25 - 3D finite element torso model [Stuhmiller, 2006]

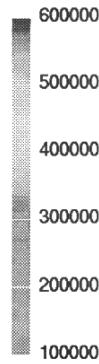
It is worth noting that in a paper containing validation results [Stuhmiller, 1997], maximum pressure of the lung elements was being used as a criteria for predicting lung contusion. While it was not explicitly stated, it appears a threshold pressure of approximately 60kPa was used in their model for predicting visibly contused lung (Figure 2.26). A few limitations of their model include a failure to model rigid structures of the torso (such as ribs and sternum), as well as a course mesh, which could make the results and predictions somewhat model dependent.



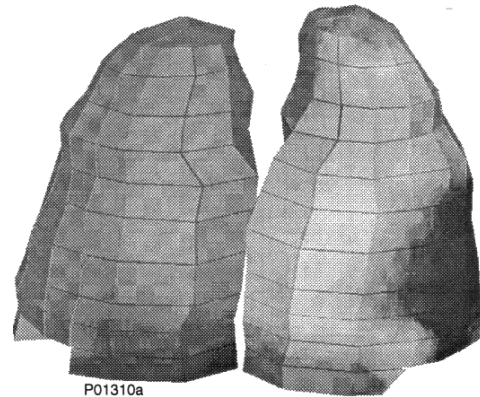
P01309a

(a) Pathology photograph

Maximum Pressure
dyne/cm²

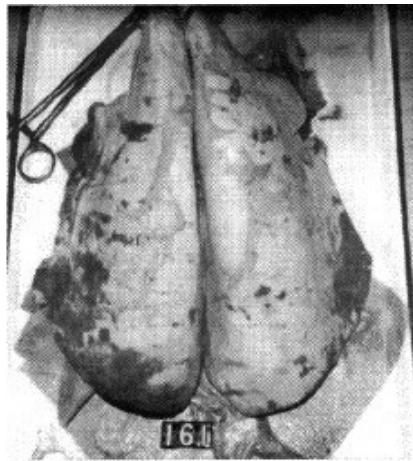


DYNA3D CALCULATION WITH SEVERE INJURY LOADING



P01310a

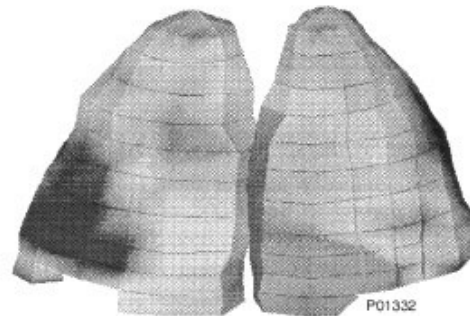
(b) FEM simulation



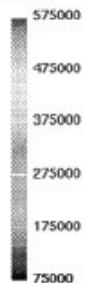
P01317

(a) Pathology photograph

DYNA3D SIMULATION OF COMPLEX WAVE LOADING



Maximum Pressure
dyne/cm²



P01332

DORSAL VIEW

(b) FEM simulation

Figure 2.26 - Comparison of 3D finite element model results to experiments [Stuhmiller, 1997]

A finite element model developed by the University of Waterloo takes a different approach than that taken by [Stuhmiller, 2006; Stuhmiller, 1997]. The University of Waterloo finite element model for predicting blast lung injuries (herein to be referred to as the UW Thorax Model) focuses on detailed modeling of a pseudo 2D section of the human torso. This model will be used as a part of the current study as a tool for evaluating protection numerically. The details of the UW Torso model will be covered in Section 4.2.

Chapter 3

Modeling Background and Approach

The purpose of this study was to investigate personal protection, using models which could eventually be implemented with a finite element model of the human torso for evaluation of injury. As such, an overview of finite element, and the simulation of blast loading is provided. An overview of the modelling approach taken in this study will also be described.

3.1 Finite Element Overview

A comprehensive review of finite element formulations will not be presented in this thesis. It is, however, useful to give an overview of the differences between implicit and explicit finite element formulations, where the explicit formulation was used for this work.

FEA requires numerical time integration in order to calculate displacements. Implicit formulations assume a constant average acceleration during each time-step, and require an inversion of the structural stiffness matrix. Explicit formulations assume a linear change in displacement between time steps, and do not require the stiffness matrix to be inverted. In explicit time integration schemes, the velocity and acceleration at t_n is calculated using governing equations and then the displacement at t_{n+1} is determined.

Implicit finite element formulations are unconditionally stable, allowing relatively large time steps while explicit formulations have a stability condition, where the time step must be less than the time it takes for a dilation wave to travel across an element. As a result, the time step size in explicit calculations is necessarily very small; however, the calculations associated with explicit formulations are computationally cheap compared to the solution of equations involved in implicit analysis.

The a simplified relation for the minimum time step is [Hallquist, 2006]:

$$\Delta t = \frac{L}{c} \quad (3.1)$$

Where Δt is the time step, L is the characteristic element length, and c is wave speed. The details of calculation of the element length and wave speed depend on the element formulation and material model used.

Explicit finite elements generally have a very small time step, and a large quantity of calculations are made, so a computationally undemanding element formulation is typically used, which is a reduced integration element. The disadvantage of these elements is that they can exhibit a zero energy deformation mode, sometimes called the “hourglass” mode, which can easily propagate through elements (Figure 3.1). Other element formulations can have zero energy modes, however they are suppressed when more than one element is involved in the model.

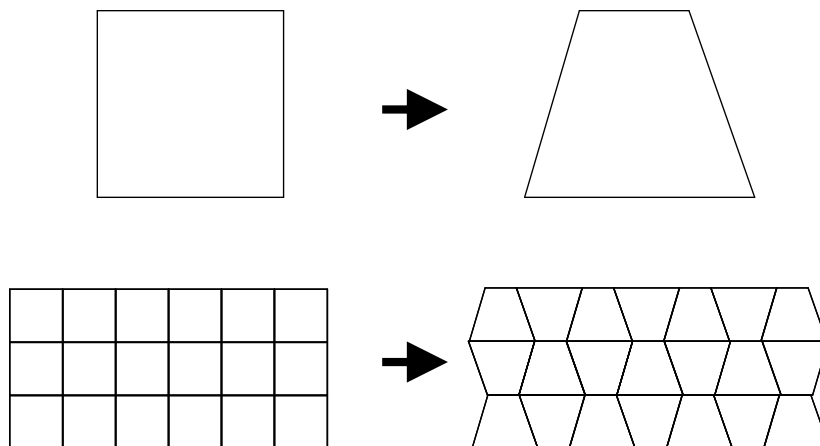


Figure 3.1 - Hourglass deformation of a reduced integration point element

Hourglassing can be addressed by introducing stiffness or viscous based hourglass controls to elements, reducing localized (point) loading as much as possible, or by replacing some reduced integration elements with higher order elements which do not exhibit hourglassing.

Explicit FEA codes are preferable to implicit codes for some of the following types of problems, where implicit codes may not be appropriate due to the dynamic nature of the problem, convergence issues, or calculation time:

- High speed dynamic events
- Complex contact problems
- Geometric and material non-linearity
- Material degradation and failure

The problem of blast loading of soft materials and the human body is a problem involving high speed dynamic events, with large deformations, non-linear materials and contact. This type of problem is much better suited for explicit analysis than implicit analysis. For this work, the LS-DYNA explicit code (Livermore Software Technology Company) was used.

3.2 Simulation of Blast Loading

There are several methods available for the simulation of blast loading in finite element codes. They all have advantages and disadvantages relative to one another in terms of accuracy and computational cost. The methods can be described as either coupled or un-coupled.

3.2.1 Uncoupled Loading

Uncoupled loading is applied by prescribing a pressure-time to the elements in a FE model. In the case of blast loading, this would be done by applying the expected pressure-time (Friedlander) curve. As mentioned previously, the pressure applied is the reflected pressure, as measured by a pressure transducer mounted flush with the reflecting surface. While it would be possible to determine and apply the pressure-time loading manually, some FE solvers use the same databases as CONWEP [Hyde, 1988; Bannister, 1997] in order to determine the pressure time loading on a

element, based on a charge mass (TNT equivalent) and location. The benefit of the use of the integrated blast loading versus manually prescribed pressures is that as the distance of the element from the charge changes, so does loading (this might be considered a semi-coupled solution). While the integrated blast loading solutions in FE codes have typically been limited to single uncased explosives, the options available are being updated, and recently some packages include the ability to determine loading from multiple sources, as well as varied explosive devices.

The advantage of the above approaches is that they offer computational time savings compared to fully coupled solutions. The disadvantages are reduced accuracy of loading due to the lack of full coupling of the fluid and structure. The level of inaccuracy depends on the geometry and rigidity of the structure being loaded. Rigid structures, with geometries which do not result in significant changes in loading from clearing effects can be loaded using uncoupled methods quite reasonably [Bulson, 1997; Bannister, 1997]. If the structure is very deformable, the pressure applied might be over-estimated, and if the geometry is such that the blast wrapping around the object causes significant loading, uncoupled methods are not appropriate. Another disadvantage of using loading based on the CONWEP database is that the empirical data within the database is only valid for the mid to far field. Near field results do not account for interactions with the contact surface of the explosive.

3.2.2 Coupled Loading

Coupled loading requires full modelling of the structure being loaded, as well as the fluid or gas which is loading the structure. This is sometimes referred to as fluid-structure interaction. In terms of air blast loading, a coupled simulation models the structure struck by the shock wave, but also includes simulation of the shock wave in the air which strikes the torso. Fully coupled simulations are useful, in that they provide a level of detail that uncoupled approaches cannot. A fully coupled blast simulation will predict how the shock wave interacts with a target structure, and the loading takes into account the stiffness, deformation and translation of the structure. The deformation and translation of the structure then also influences the surrounding air.

Fully coupled simulations also allow the option of calculating complex blast loading. By simulating the entire flow field including walls and other obstacles, the resulting shock wave reflections are produced and the appropriate loading is applied to all bodies in the flow field.

This level of accuracy is not without a price, however. The entire flow field must be modelled with sufficient accuracy, and in order to reproduce shockwaves, the mesh density must be quite high (small element size). Thus, it quickly becomes computationally prohibitive to undertake fully coupled simulations.

A method that has been proven a viable means of simulation shock and blast waves with full coupling to Lagrangian structures is an arbitrary Lagrangian-Eularian (ALE) formulation; this approach is investigated in this study.

3.2.3 Arbitrary Lagrangian-Eularian (ALE) in Finite Element

Lagrangian element formulations are typically associated with solid analysis. Each element is of constant mass, the nodes of the element translate to produce deformations and stresses and the material stays within element boundaries. The benefit of Lagrangian formulations are the relative ease of implementation, improved accuracy, and the availability of a wide variety of material models (which follows from the widespread use of this formulation). A disadvantage of Lagrangian formulations is that they may produce erroneous results if the mesh is heavily distorted. Excessive mesh distortion is typically a result of either poor initial geometry or large deformations.

Eularian formulations are also widely used, primarily in computational fluid dynamics, where finite difference/volume formulations are used. In these formulations, nodes do not translate, and the mass of a material within a given volume is not constant as it is in a Lagrangian formulation. The advantage of this formulation is that large deformations can be simulated. The disadvantage of the Eularian formulation is that it cannot simulate interaction of fluids with deformable structures.

An Arbitrary Lagrangian-Eulerian formulation overcomes the weaknesses of the Lagrangian formulation, and bestows some of the benefits of the Eulerian formulation. Each step of an ALE simulation begins with the calculation of Lagrangian deformations and state variables. Depending on the frequency of advection desired, the results are then remapped either every step, or at some specified interval of iterations in order to reduce computational cost. The remapping of element boundaries requires an advection process, which involves the transport of element state variables from one element to another. The variables transported are dependent on the material models or equation of states used. In the case of an equation of state (typically used for fluids), density, internal energy and shock viscosity are transported. The largest weakness of this process is the fact that advection is carried out across elements isometrically, and as such advection only occurs through element faces (Figure 3.2).

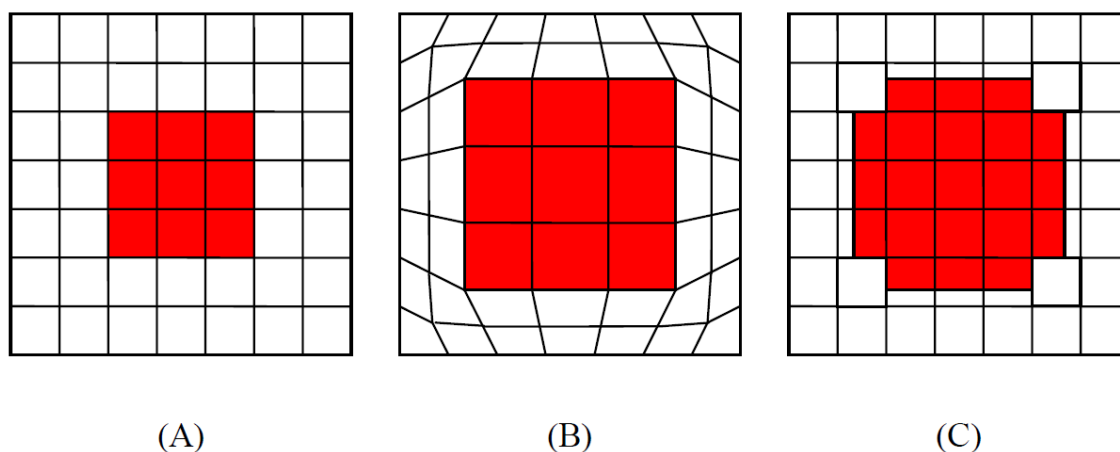


Figure 3.2 - Isometric advection of state variables in ALE algorithm: A) Initial configuration; B) After Lagrangian timestep; C) After ALE advection and remapping [Greer,2006]

Eulerian calculations exist as a subset of an ALE formulation, where all deformation is handled through advection, and the mesh is always fully remapped to its original geometry (as per Figure 3.2). On the other extreme, if no advection is allowed, the mesh cannot be remapped and the simulation behaves as a traditional Lagrangian calculation. This subset of the ALE formulation is the one typically used for fluid simulations, and thus are utilized in this study.

To summarize, the procedure for an ALE calculation is typically as follows , where the steps not required by the Eulerian subset are italicized below:

1. Perform a Lagrangian Time Step.
2. Perform an Advection Step.
 - a. Identify nodes to move.*
 - b. Move boundary nodes.*
 - c. Move interior nodes. (using smoothing algorithm)*
 - d. Calculate the transport of element centered (state) variables.
 - e. Calculate the momentum transport and update the velocity.

For simulations involving fluid flow, the use of ALE is possible, however it is important to treat it as an Eulerian calculation (with full advection) in order to prevent extreme mesh distortions, which may occur in all but the completely remapped calculations.

Coupling Lagrangian solid elements to ALE material elements is achieved through a penalty coupling method. After the Lagrangian time step described above, the movement of the ALE fluid mesh relative to the Lagrangian solid is used to apply a penalty coupling force to both the Lagrangian solid's nodes and the ALE material's nodes (which at this stage of the routine is being treated as a Lagrangian solid). The magnitude of this force is proportional to the displacement of the ALE element (during the lagrangian time step) to the Lagrangian solid part (Figure 3.3). If a low penalty factor is defined, or the ALE fluid mesh is much higher in density than the Lagrangian solid mesh, leakage can occur. If the penalty factor is too low, it can be increased to control leakages. Having ALE and Lagrangian solid meshes of similar densities also aids in coupling, but situations where the ALE mesh is higher in density than the Lagrangian can be dealt with by adding quadrature points. Quadrature points act as additional locations on the Lagrangian solid element surface that are checked against the ALE mesh for coupling. Situations where the Lagrangian mesh is higher in density than the ALE fluid mesh will result in an uneven distribution of coupling forces.

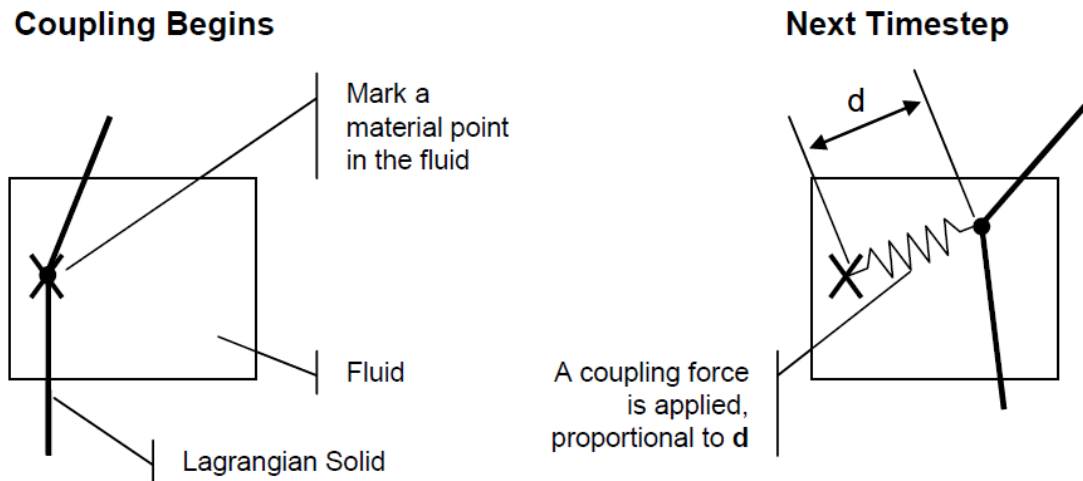


Figure 3.3 - Penalty coupling for fluid structure interaction in ALE [Greer, 2006]

3.2.4 Artificial Viscosity in Numerical Codes

Artificial bulk viscosity is implemented in a number of numerical codes to allow the resolution of discontinuities which can result from the compression of a material which exhibits increasing stiffness with decreasing volume. The use of an artificial viscosity in numerical codes allows the solution of problems involving shock-waves without producing spurious, high frequency oscillations in the shocked region [Meyers, 1994], and was originally implemented by VonNeumann and Richtmeyer [VonNeumann, 1950]. The viscosity implemented by VonNeumann and Richtmeyer added a viscous pressure contribution which was proportional to the product of the element length strain rate squared. This meant that the viscous contribution was small except when changes in strain rate were very large, and thus should only be active in the region of a shock wave. Use of the quadratic artificial viscosity does not totally eliminate spurious oscillations in the shocked region, and as such some code utilize an additional term in the artificial viscosity which is proportional to the product of element length and strain rate in order to aid in the damping of these oscillations. The addition of a linear term to the artificial viscosity was originally proposed by Landshoff [Landshoff, 1955]. While the quadratic term is only active in the shocked region, the linear term is active wherever strain rates are non zero.

In one dimensional simulations the determination of the characteristic element length is straight forward. In 2D and 3D simulations the square root of the area and the cube root of the volume are used respectively; this is done for computational efficiency. The disadvantage of this approach is that erroneous viscosity values can be calculated for elements which have non-ideal aspect ratios 1:1(:1) as a result of either poor meshing or large deformations.

The values of the linear and quadratic terms of the artificial bulk viscosity are well accepted and based off of the initial work by Landshoff [Landshoff, 1955]. Unless otherwise stated, these values were 1.5 and 0.6 for this study [Hallquist, 2006]. Exceptions were the foam and multi-layer fabric material models, discussed later, which instead utilize damping parameters for stability.

3.2.5 Validation of the use of ALE to Simulate Shock Waves and Blast Phenomena

Shock waves are differentiated from elastic and acoustic waves in that they exhibit a discontinuous change in pressure, density and temperature across the shock front. Blast waves, being a subset of shock waves, also exhibit this behaviour.

A study by Salisbury [Salisbury, 2004] validated the use of ALE to reproduce waves in a shock tube. The study involved the modeling of both the high pressure driver section, and the low pressure shock tube. At the beginning of the simulation, the air from the high pressure region was allowed to expand into the low pressure region at such a rate that a shock wave was produced in the original low pressure region, and an expansion wave was observed in the original high pressure region. These were compared to experimental results, and the results were found to be in excellent agreement.

It was found that the element size must be smaller than 5mm to properly resolve the shock front in the 1m long, 0.1m wide tube (the study was two-dimensional). It was also shown that if the elements were created so faces were 45° to the direction of shock propagation, the isometric advection resulted in less accurate pressure-time histories.

3.2.6 Simulation of Explosive Blast in ALE

Two common methods exist for creating blast loads using the ALE formulation. The first involves modelling the explosive using an appropriate equation of state; the second involves manually prescribed boundary conditions in order to produce a blast wave.

The most thorough (and computationally expensive) option is to model the explosive and the surrounding air in its entirety. A Jones-Wilkins-Lee (JWL) equation of state with a high explosive material model can be used to model most HE charges. The computational cost of this method results not only from having to mesh the area of interest, but it is also necessary to have a high mesh density near and around the explosive and in areas where there is interaction with Lagrangian bodies. The final complication of this method is that in order to accurately reproduce a spherical shock front, the mesh must be spherical (3D) or cylindrical (2D) in order to prevent distortion from the ALE advection algorithm. The divergent mesh can result in an extremely coarse mesh at distances further away from the explosive.

An alternative method to blast simulation in ALE is to use elements which can be prescribed an internal energy (temperature) time curve. It is possible to define this curve such that as the pressure time history downstream of these elements is the same as what would be experienced in blast loading. The advantages of this method are that it simplifies the geometry of the air mesh and it reduces the volume of air that must be meshed (as the ambient elements can be placed nearer the body of interest than the actual explosive would be). It is possible to reproduce a variety of pressure-time profiles (not just Friedlander curves), and as such shock tube loading, characterized by a step pressure-time curve, can be simulated. The disadvantage of this method is that the blast wave is assumed to be planar rather than spherical, and determining the location of the load producing elements and the temperature time curve is needed in order to obtain the proper pressure time history. This method has been validated in studies done at the University of Waterloo reproducing BTD test results [Cronin, 2004; Salisbury, 2004b; Salisbury, 2004c; Greer,2006].

3.3 Validation and Verification of Numerical Models

The validation and verification of numerical models is an important part of the modelling process. The process typically involves a check for mesh convergence, as well as a comparison to available experimental data. Regardless of the level of accuracy achieved when compared to experimental results, mesh convergence studies should be conducted in order to ensure that the solution obtained contains a minimum or acceptable level of numerical error.

It should be noted that regardless of the method used, mesh convergence studies only provide information about numerical error, but do not provide an estimate of error resulting from erroneous assumptions in modeling of geometry, boundary conditions, or material properties. The only way to evaluate these factors is a comparison against experimental (or for simple models, analytical) results, and this comparison should ideally be made after the level of numerical error has been determined via mesh convergence study.

A few methods exist for verifying mesh convergence. One, useful in static finite element calculations, is to compare the value of a state variable at one node or element to the state variables of surrounding nodes or elements. If the gradient is below a certain level (determined through experience and the level of accuracy desired), the mesh is considered fine enough to capture the desired details for the calculation [ASME, 2006].

The other method has been proposed by Roache [Roache, 1998; ASME, 2006] and involves the use of multiple calculations of varied mesh density. The approach is well defined such that it can be performed in a consistent manner. Richardson extrapolation is used in order to extrapolate the calculated numerical results to determine an estimate of the result at “zero” mesh density. From this estimate, the error of calculations at various mesh sizes can be determined.

Richardson extrapolation requires that the modeller know the order of convergence of the results. If the modeller knows with confidence the order of convergence of a given problem, results from calculations using only two different mesh sizes are required to perform an extrapolation. The

more rigorous approach involves calculation using three mesh sizes, which allows the determination of the order of convergence of the given problem. The order of convergence is given by [Roach, 1998]:

$$p = \ln\left(\frac{f_3 - f_2}{f_2 - f_1}\right) / \ln(r) \quad (3.2)$$

Where p is the order of convergence, f_3 , f_2 and f_1 are the results from calculations at fine, medium and coarse meshes, and r is the grid ratio. The grid ratio is the ratio of the grid/mesh characteristic length from one mesh to another; for example if the size of elements is reduced by half in the X, Y and Z coordinates from medium to fine meshes, and coarse to medium meshes, r is “2”. It should be noted for transient calculations, the time-step should also obey the same ratio as the element lengths (i.e., in the previous example the time-step of the medium mesh would be half that of the fine mesh).

The error of the Richardson extrapolation can be calculated as [Roach, 1998]:

$$E_{12}[Fine\ Grid] = \left(\frac{f_2 - f_1}{f_1}\right) / (r^p - 1) \quad (3.3)$$

The Richardson extrapolation error is modified by a safety factor (F_S), which is based on experience (suggested values are given in [Roach, 1998]. The safety factor is larger for calculations involving only two meshes ($F_S=3$), and smaller for those involving three meshes ($F_S=1.25$), which follows from the increased confidence in the results from the three mesh approach [Roach, 1998]. The result of multiplying the Richardson extrapolation error and the safety factor is what Roach refers to as the “Grid Convergence Index” (GCI) and it is this value that he proposes researchers use as a means of evaluating the numerical error in their calculations.

$$GCI_{12} = F_S E_{12} \quad (3.4)$$

The caveat of Richardson extrapolation is that the results must all exist in the asymptotic regime, that is, the solution with reduced mesh size is asymptotically approaching a given value. Roache provides a means of checking the results to ensure this is satisfied [Roach, 1988].

$$GCI_{23} = r^p GCI_{12} \quad (3.5)$$

Where GCI_{23} is defined as:

$$GCI_{23} = F_S \left(\frac{f_3 - f_2}{f_2} \right) / (r^p - 1) \quad (3.6)$$

If equation (3.5) is satisfied, the results exist in the asymptotic range. The value GCI_{12} is of interest.

As mentioned previously, Richardson extrapolation allows the estimation of a “zero” element size solution. This estimate is achieved by estimating the error in the finest mesh calculation, and using the order of convergence to determine the error from the fine mesh solution to the zero mesh solution. This error is then added to the fine mesh solution to provide the estimate of a solution at a grid spacing/element size of “0”. The error estimate is defined [Roach, 1988] as:

$$f_{h=0} = f_1 + \frac{f_1 - f_2}{r^p - 1} \quad (3.7)$$

Ultimately the level of acceptable error is left up to the researcher, and the acceptable error in terms of a “good” fit is not standardized. Consideration has to be given to the sensitivity of the metric used for estimating error, and its significance on the desired outcome. For example, the modification of a wave as it is transmitted through a soft material might be evaluated based on the peak pressure transmitted. The nature of this metric for the current study, as will be shown later, is quite sensitive, however, there are other metrics (such as time of arrival of peak and overall curve shape) which might be more significant. For this study the metric of most importance would be that which is best correlated to lung injury. Furthermore, for a broad study such as this, it may be

acceptable to merely identify the relative effects of protection rather than exactly matching the pressure time history behind the protection.

Chapter 4

Models for Injury Prediction Used in the Current Study

The model used for injury prediction as a part of the current study will be described in this chapter. These models were later implemented with protection as described in later chapters. The purpose of this chapter is to familiarize the reader with the implementation and validation of the injury prediction models utilized.

A mathematical model based on the work by Axelsson [Axelsson, 1996] was used to aid in determining cases of interest for protection studies. This was followed by a implementation of protection with a finite element model of the human torso developed at the University of Waterloo. The modified Axelsson model allows a quick calculation and determination of cases of interest, while the finite element model allows for more detailed analysis.

A variety of protection cases were chosen for implementation with the Axelsson and finite element models. The cases considered include: fabric with air gap, foam and a high density material, and multiple layers of ballistic fabric. The cases were selected as they involve material configurations which have shown the capacity to both amplify and attenuate shock loading, and they are materials used in protective clothing. The implementation of protection with the injury models is discussed in sections following the current chapter.

4.1 Modified Axelsson Model (Mathematical Model)

The model described in this section was based on the model developed by Axelsson [Axelsson, 2006]. This model is shown in Figure 4.1 below.

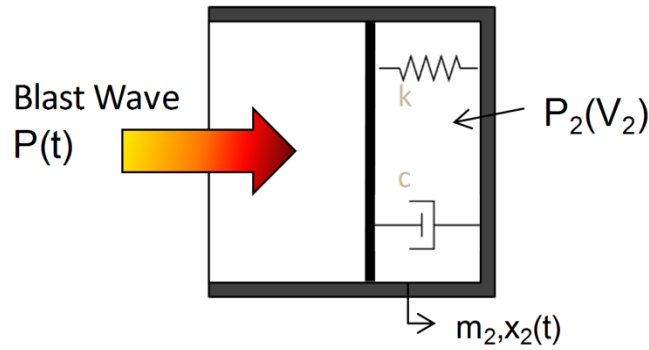


Figure 4.1 - Axelsson model diagram

The same mathematical model and parameters as defined by Axelsson were used as described in Table 4.1 and Equation (4.1) below.

$$m_2 \ddot{x}_2 + J \dot{x}_2 + K x_2 = A \left[P(t) + P_0 - \left(\frac{V}{V - A x_2} \right)^g \right] P_0 \quad (4.1)$$

Table 4.1 - Axelsson Model Parameters [Axelsson, 2006]

Parameter	Units	70-kg Body
m ₂	kg	2.03
J	Ns/m	696
K	N/m	989
A	m ²	0.082
V	m ³	1.82E-03
g	-	1.2

Axelsson's implementation of the model involved taking BTD pressure time histories, averaging results from all four channels [Axelsson, 1996]. The averaging of the results was necessary to account for complex blast loading given the 1-D nature of the model. Unfortunately, given the nature of the model, this means of reducing the data is not representative of the actual physical behaviour; loading of the side and front of the torso simultaneously should result in a stiffer chest wall behaviour, however averaging the pressure traces suggests the opposite is true.

For this study, pressure measurements were not averaged, and only the wave which would strike the front of the torso was considered. This, combined with the current study's use of the Bass curves [Bass, 2006] rather than the original Bowen curves [Bowen, 1968], means results from this study are not directly comparable to Axelsson's results, nor can it be used to examine complex blast loading cases where the waves loading the body come from various directions. Fortunately, Axelsson [1996] provided experimental BTD pressure traces, as well as results from his model which were used for verification (to be described in Section 4.1.1). This model can still be used for comparison against a "Baseline" mathematical model of the torso without protection.

As mentioned in Section 2.6.2, the parameter proposed by Axelsson for evaluating lung injury was chest wall velocity. It was also observed during literature review that most researchers examining the effectiveness of protection have found correlation with peak acceleration or peak pressure rather than chest wall velocity. All 3 of these parameters were evaluated in this research in order to determine their sensitivity to blast protection concepts.

The differential equations defined for each model above were solved through numerical integration using Microsoft Excel. Numerical integration was done using a first order Runge-Kutta method (Euler's method). The integration method used was chosen for its ease of implementation. The time step was set to a sufficiently small value such that the calculation would remain stable, thus preventing numerical artefacts such as the inversion of the element (negative volume). If the time step was too coarse, it would be possible for the front face of a protective concept to travel "through" the torso or back wall, resulting in an error in calculation analogous to a negative volume error in a finite element code. Consideration was also given to the error which could be produced through use of Euler's method of integration, and the time step was made sufficiently small such that no effect on results was observed. The integration was conducted as shown below in Eqns (4.2)-(4.3).

$$x_{t+h} = x_t + \dot{x}_t h \quad (4.2)$$

$$\dot{x}_{t+h} = \dot{x}_t + \ddot{x}_t h \quad (4.3)$$

Where \ddot{x} was determined differently depending on the model for which a solution was being determined (fabric and air gap, foam and high density material, multi-layer fabric and high density material and/or the Axelsson torso model). Details of each implementation are not provided, though the equations describing the individual components of the systems have been provided.

For determining the loading of the model, equation (2.1) was used to produce a Freidlander pressure curve, which was compared against experiments. The reflected pressure was used as this is most representative of what loads the protection or torso. It should be noted, however, that the stiffness, velocity or displacement of the loaded face was not accounted for in this model (the loading was uncoupled as mentioned previously).

4.1.1 Modified Axelsson Model Verification

The implementation of the Axelsson model utilized in this study was verified against data provided in [Axelsson, 1996] where pressure traces from two out of four BTM pressure transducers was provided. The pressure data used as a part of the verification is shown in Figure 4.2.

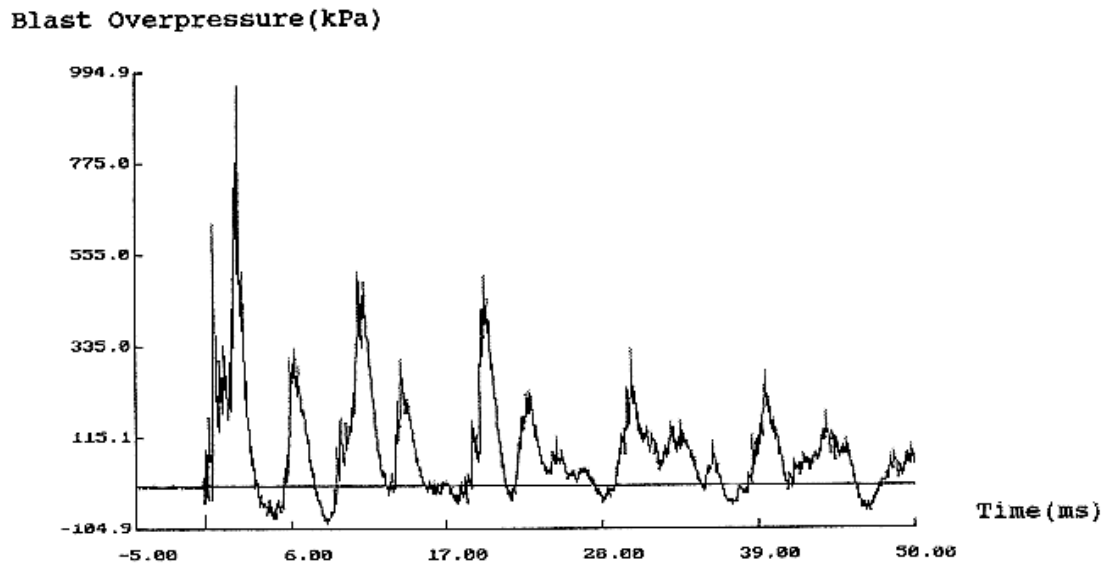


Figure 4.2 - Original BTM pressure history from a single gauge [Axelsson, 1996]

The data was digitized by using digitizing software (Engauge Digitizer). The data was output at 1×10^{-3} ms intervals. Only the first 6 ms were digitized, as this was all that was necessary to capture the first peak in chest wall velocity. Because of the image quality of the graph used, and the small quantity of data needed (6ms of a 50ms pressure trace), the digitization is a likely source of error in results. The digitized data is shown in Figure 4.3

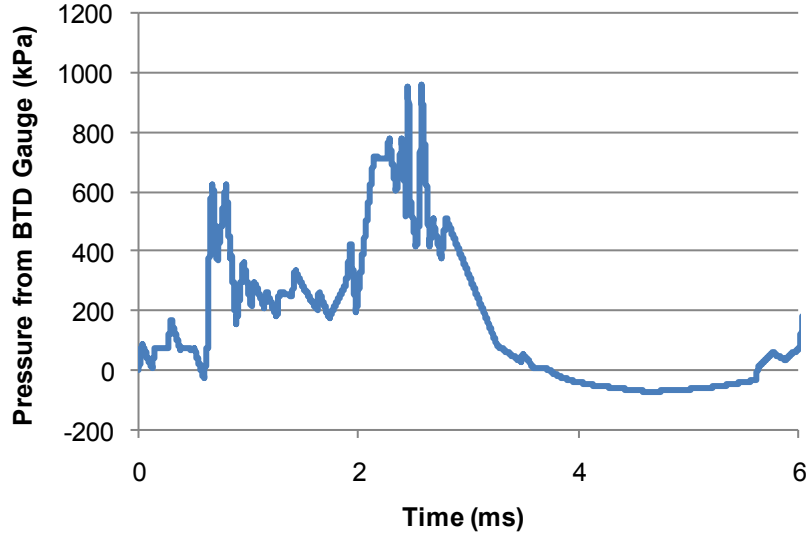


Figure 4.3 - Digitized first 6 ms of BTM pressure transducer data from [Axelsson, 1996]

The chest wall velocity was calculated using the mathematical model and compared to results provided in [Axelsson, 2006]. The traces match well (Figure 4.4), suggesting the implementation of Axelsson's model had been properly reproduced. Small error was evident, however this is likely due to the digitizing of the data from [Axelsson, 2006]. The simple integration scheme used in the current study's implementation of the mathematical model could also be a source of error, though the use of a sufficiently small time step should have minimized this error. The first peak in chest wall velocity from the digitized results of [Axelsson, 1996] was 14.8 m/s, compared to 15.4 m/s from the current study (4.23% error).

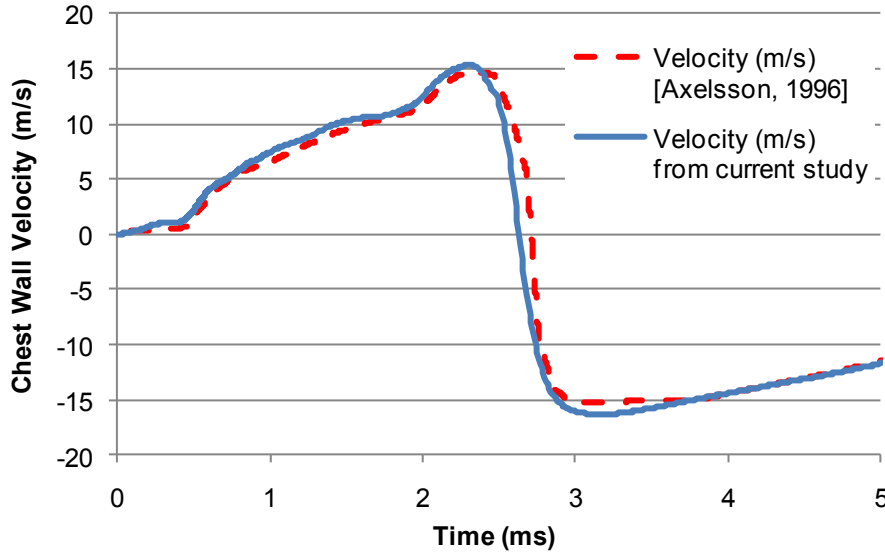


Figure 4.4 - Comparison of predicted chest wall velocity from [Axelsson, 1996] compared to chest wall velocity predicted by current study

The peak intrathoracic pressure (determined by the reduction of volume of an airspace caused by the chest wall displacement) was calculated in the work by Axelsson to be 3486 kPa, while it was calculated in this study to be 3450 kPa, yielding an error of 1.03%.

4.2 University of Waterloo Torso Model

A finite element model of the human torso was developed at the University of Waterloo [Greer, 2006]. The goal of the work was to develop a numerical surrogate which could be used to estimate lung injury not only for free field (simple) blast loading, but also for complex blast loading. Also, the model was developed to be used as a tool for evaluating protective designs. The model was developed using the explicit finite element code LS-DYNA (Livermore Software Technology Company, Livermore, CA) This work was undertaken as an M.A.Sc. project by Alexander Greer [Greer, 2006].

The University of Waterloo torso model was utilized in this study to investigate the effect of personal protective equipment and soft materials on blast lung injury. The material models that were utilized for the protective materials will be described in Chapters 5, 6 and 7.

4.2.1 Geometry

A 2D slice of the human torso was developed properly capture stress-wave propagation through the torso. A high mesh density was required and a full 3D model would be computationally prohibitive and thus was not pursued. The geometry of the model was based on data from the visible human project [NLM, 2004], which is a collection of high resolution images of a sectioned, 50th percentile, male cadaver. A mid-sternal section was chosen, as this represents a plane approximately half way through the lung (Figure 4.5).

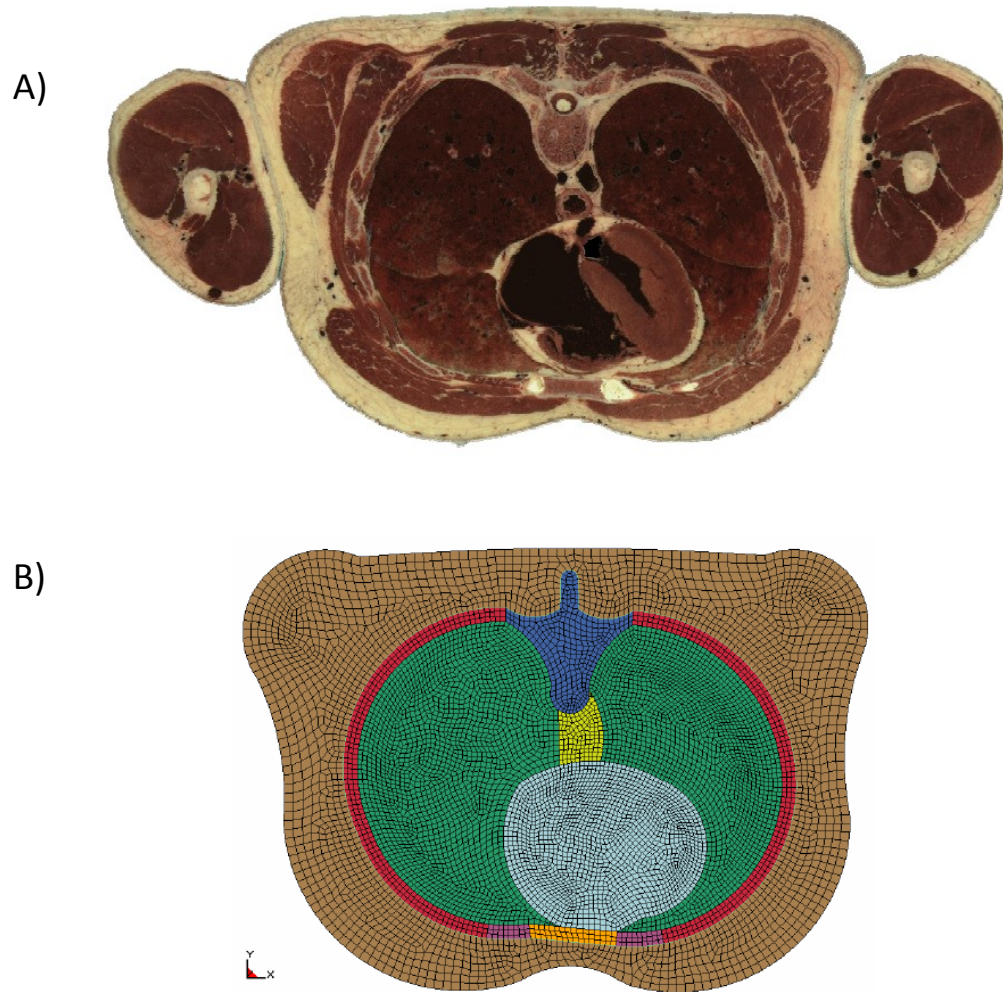


Figure 4.5 - A) High resolution image from Visible Human Project [NLM, 2004]; B) Torso slice model [Greer, 2006]

The model actually has multiple elements through thickness in order to allow modelling of both rib material and inter-costal tissue (Figure 4.6). This pseudo 2D approach was required in order to prevent the thoracic cage from behaving in an overly stiff manner (if ribs were modelled without intercostal tissue).

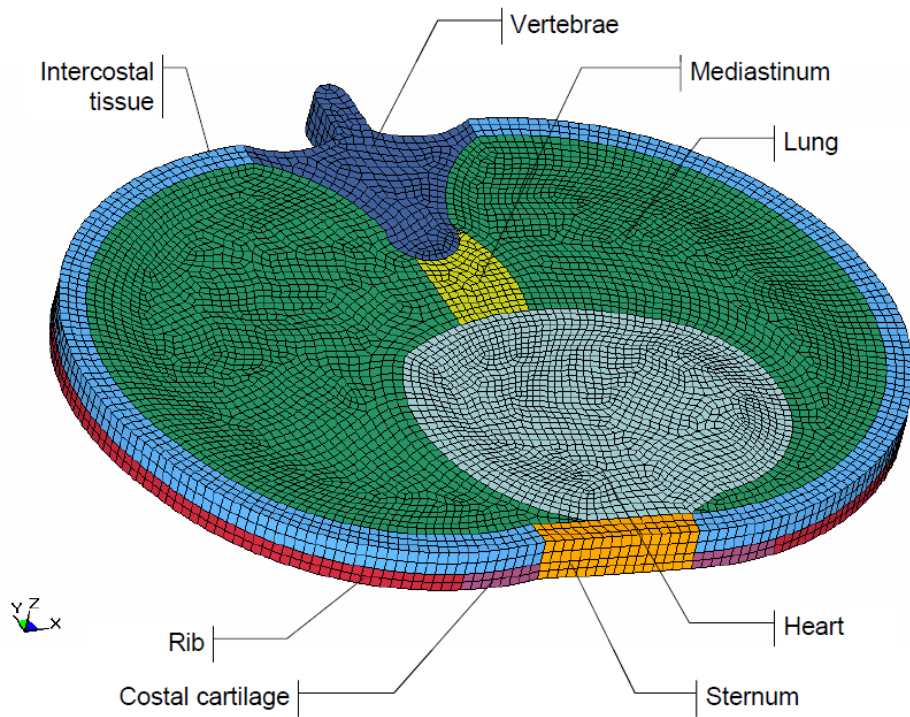


Figure 4.6 - Pseudo 2D model of rib-cage (muscle and fat removed) [Greer, 2006]

Geometry for a bovine (sheep) torso was also produced as a part of the above project and used to by Greer to validate the modelling approach using animal test results.

4.2.2 Material Properties

Material models and properties were selected based on data from literature. The materials were modelled as continua, with properties based on the measured overall behaviour of the material. Cortical and cancellous bone; fat and muscle; heart tissue and blood; lung tissue and air are modelled as continuous materials, with properties being based on the rule of mixtures.

The properties for cortical and cancellous bone were calculated using literature values. Various values of stiffness for each type of bone were reported in literature, so the approach taken by Greer was to average all literature values for cortical and cancellous bone. After determining the

properties of the two types of bone, the rule of mixtures was applied to calculate the properties of the ribs, sternum, and vertebrae. Properties for costal cartilage are based on those of Yamada [Yamada, 1970]. An elastic material model was found to be appropriate for modelling all of the above mentioned bone and cartilage structures, as the deformation of bone was found to be linear within the range of deformations seen in the torso under blast loading. The values used in the human torso model are given in Table 4.2 below.

Table 4.2 - Bone Properties for Torso Model [Greer, 2006]

Human	Density (kg/m³)	Young's Modulus (GPa)	Poisson's Ratio	Calculated Sound Speed (m/s)
Cortical	1907	15.26	0.367	3730
Cancellous	1216	0.57	0.392	971
Ribs	1561	7.92	0.379	3073
Sternum	1354	3.51	0.387	2248
Vertebrae	1644	9.68	0.376	3282
Costal Cartilage	1281	0.049	0.400	286

Soft tissue (muscle and fat) is made primarily of water (73%) and as such, when determining an equation of state for tissue in order to ensure proper shock transmission properties, it was decided to use the same equation of state as water. A Mie-Gruneison equation of state was utilized initially, however the lack of deviatoric strength resulted in unrealistic deformation of the tissue in initial studies. In order to overcome this weakness, a simplified hyperelastic model was used. This model includes rate sensitivity, which is quantified through the use of uniaxial stress-strain curves at various strain rates. The compressive curves at various strain rates were obtained from literature by Van Sligtenhorst et al. [Van Sligtenhorst, 2003] and McElhaney [McElhaney, 1966], and the tensile curve (only available at quasi-static strain rates) was based on work by Yamada [1970]. The properties of the soft tissue are shown below in Table 4.3.

Table 4.3 - Soft Tissue (Muscle and Fat; Heart and Blood) Properties for Torso Model [Greer, 2006]

Material	ρ (kg/m³)	Sound Speed (m/s)	Bulk Modulus (N/m²)
Soft Tissue	1000	1500	2.2×10^9

The behaviour of the heart and its contained blood were assumed to be the same as the above soft tissue model, and so the same properties and material model were used.

Because the lung can experience large deformations under blast loading, it was important to model it in such a way that captures the non-linear behaviour, and so an EOS which properly describes the behaviour of porous lung was required. The Gruneison EOS was created, with the speed of sound and shock vs. particle velocity curve being based on relations for water with air bubbles [Wilbeck, 1978]. The lung tissue was assumed to have the same EOS parameters as water and thus the rule of mixtures was used in order to produce an air/water mixture which had density equal to that of lung (200 kg/m^3) from the literature [Bowen, 1968]. The lung was modeled this way as being 80% air, and 20% tissue (having the same EOS as water). This is a representative porosity for lung, as it is 10-30% tissue [Greer, 2006]. Further work prompted a change in the dynamic viscosity value used in the lung tissue model. The value used in [Greer, 2006] was $1.0 \text{ Pa}\cdot\text{s}$, however, it had been changed for the current study to $3.0 \text{ Pa}\cdot\text{s}$ based on work by D'yachenko [D'yachenko, 2006]. The resulting properties used in the material model are shown in Table 4.4.

Table 4.4 - Lung Properties used for Torso Model [Greer, 2006]

Material	ρ (kg/m³)	Dynamic Viscosity (Pa·s)	C (m/s)	S_1
Lung	200	3.0	30.1	1.295

4.2.3 Boundary Conditions

The method by which load is applied to the torso model is one of the features that makes it particularly powerful as a blast injury evaluation tool. Because fully coupled fluid/structure simulation was developed as a part of the model, it would be possible to consider the effects of complex blast environments on the blast loading which reaches the torso, and the resulting injury. This was done as a part of the project where the model was initially developed [Greer, 2006].

The UW Torso model utilized the ALE algorithm, just as the shock tube models described previously. The boundary conditions should be discussed since this is a 2D case and thus slightly

more complicated than the 1D cases previously described. Because the model is an ALE model, there are the Lagrangian torso parts, which occupy the same volume as the ALE part (Figure 4.7).

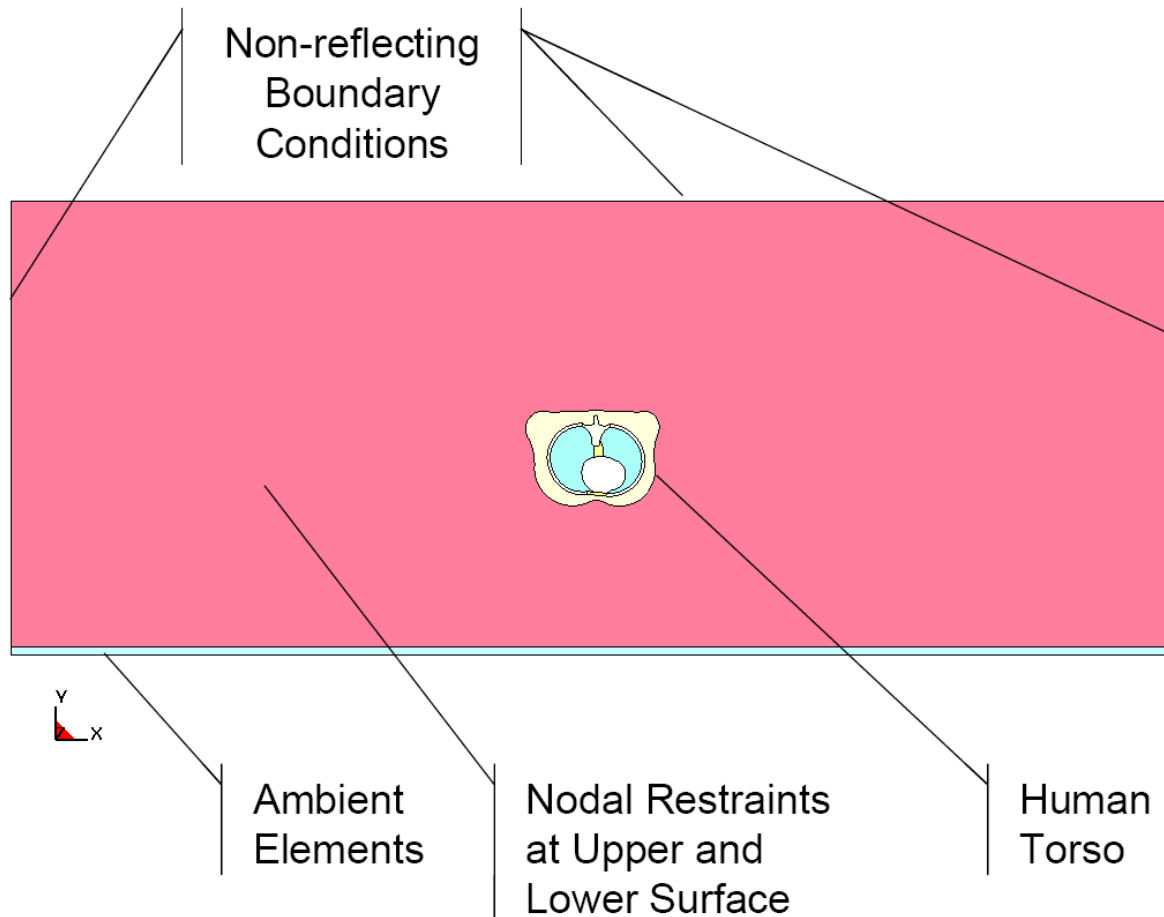


Figure 4.7 - Torso model in ALE mesh [Greer, 2006]

As with the simpler 1D shock tube and blast models used for evaluating material models, loading was applied through boundary elements where pressure and density vary with time. In the torso model, the boundary elements exist along an entire face of the ALE model to produce a planar shock wave.

The nodes on the faces of the ALE and torso meshes which were in-plane with the torso slice were prescribed boundary conditions and symmetry was assumed such that the torso model is being considered as an infinite tube being struck by a planar shock wave.

The Lagrangian torso part was coupled to the ALE air mesh, as the protection models were coupled to air meshes in the previous chapters. Special consideration was made for the space occupied by the lungs in the model. Like a low density foam, an ALE air material would contribute to the stiffness of the lungs when compressed. To prevent this added stiffness, the ALE mesh occupying the same volume as the lungs was given a nearly massless, zero stiffness material model and properties (vacuum).

The sides and back of the ALE mesh were prescribed a non-reflecting boundary condition, which prevented the reflection of waves back “into” the model when they reach the boundary. The ALE mesh was made quite a bit wider than the torso in order to ensure that the boundary conditions would not affect the flow of the shock and clearing effects around the torso.

Chapter 5

Foam Material Behaviour Under Blast Loading

5.1 Foam Material Behaviour

Foams are low density materials that exhibit non-linear behaviour and are commonly used in energy absorbing applications. Foam structures can be categorized as open or closed cell (Figure 5.1). The cells of a closed cell foam are defined by walls of solid material, which prevent air from escaping the cell. Conversely, open celled foam structure is more skeletal, with air being able to move from cell to cell (with some resistance determined by the geometry of the foam structure).

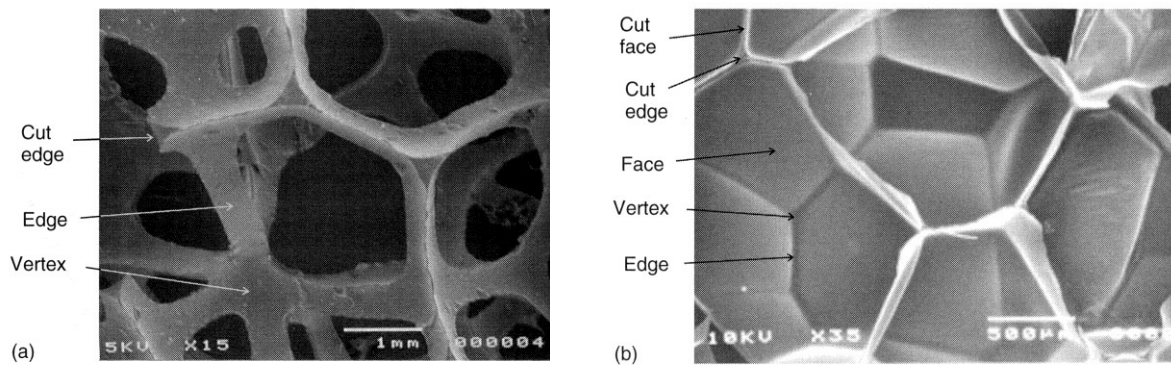


Figure 5.1 - Comparison of (a) open and (b) closed cell structures [Mills, 2007]

For open and closed cell foams, the stress-strain curve can be considered as 3 sections. Initially there is linear stress-strain behaviour, which is associated with the behaviour prior to buckling of the foam structure. This is followed by the post-buckling stress-strain behaviour of the foam. In the case of open cell foams, eventually the foam becomes so compressed that the cell walls start to come in contact with one another and densification begins. After the foam has fully densified and no air remains within the cells, the stress-strain behaviour becomes that of the material which comprises the cell walls.

Closed cell foams exhibit similar behaviour to open cell foams. They exhibit cell wall buckling (Figure 5.2) instead of the buckling of beam like structures seen in open celled foams.

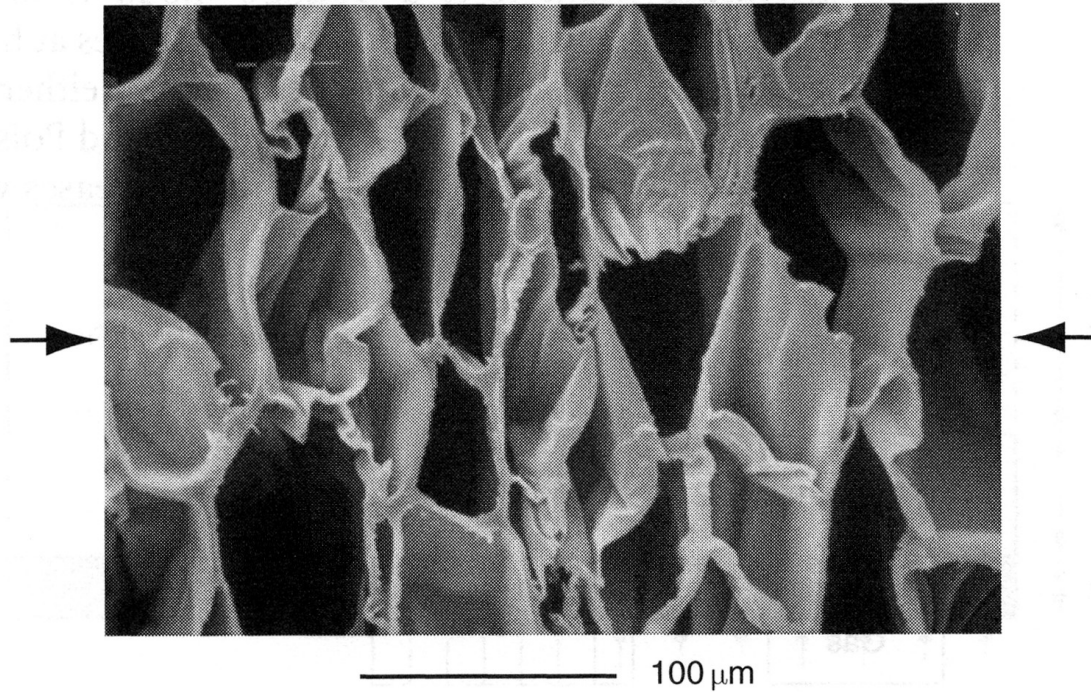


Figure 5.2 - Compression of a closed cell foam showing buckling of cell walls [Mills, 2007]

The post buckling behaviour is somewhat different, in that full densification is not possible (unless the cells rupture). Instead, as the cells are compressed, the air pressure increases within the cells (asymptotically as volume approaches zero). An illustration of foam compressive stress-strain behaviour is shown in Figure 5.3 below.

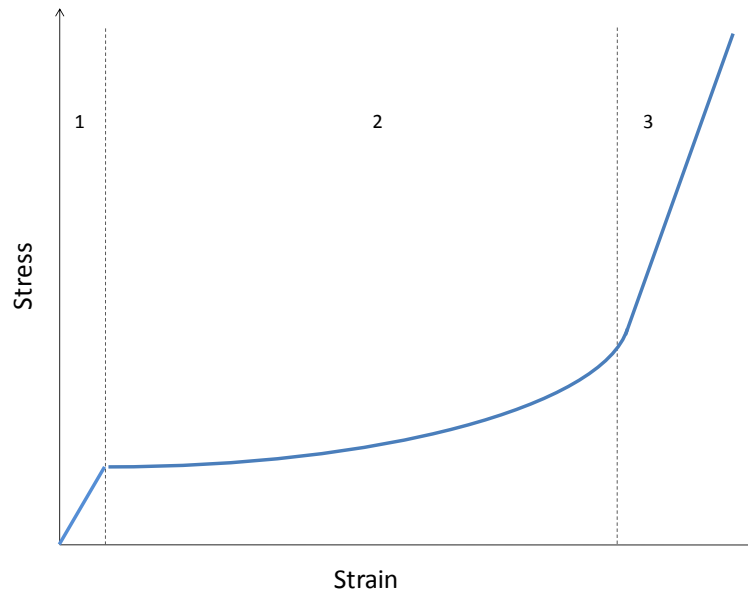


Figure 5.3 - Stress-Strain curve for a foam, showing: 1) Pre-buckling, 2) Post-buckling, 3) Densification stages in compression. (Features exaggerated)

For both open and closed cell foams, quasi-static stress-strain behaviour is based on two variables: the properties of the material used in the solid phase of the foam, and the density of the foam in question. Gibson and Ashby [Gibson, 1988] , provide a great deal of information on the characterization of foams under quasi-static compression, particularly a means of calculating the static stress-strain behaviour of a foam based on the modulus of elasticity and density of the solid phase, and the foams density. These relations are both theoretically and empirically based from compressive tests, such as those shown in Figure 5.4, which compare stress strain curves of polyethylene foams of various densities.

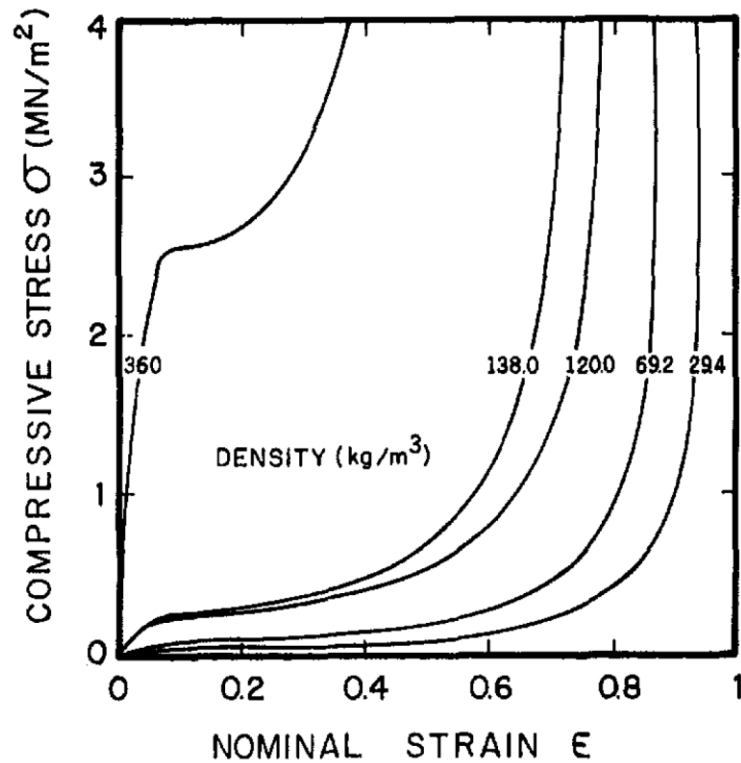


Figure 5.4 - Stress Strain behaviour of closed celled polyethylene foam at various foam densities [Gibson, 1988]

In general, for the same material being foamed, the plateau stress increases and the densification strain decreases with increasing density of the resulting foam.

Gibson and Ashby [Gibson, 1998] provide two means of determining the behaviour of a foam, one is theoretically based and the other is empirically based. Their theoretical results suggest:

$$\frac{\sigma_{el}^*}{E_s} = 0.05 \left(\frac{\rho^*}{\rho_s} \right)^2 \quad (5.1)$$

$$\frac{\sigma^*}{E_s} = \varepsilon \left(\frac{\rho^*}{\rho_s} \right)^2 \quad \text{when } 0 < \varepsilon < \varepsilon_{el} \quad (5.2)$$

$$\frac{\sigma^*}{E_s} = \varepsilon_{el} \left(\frac{\rho^*}{\rho_s} \right)^2 + \frac{p\varepsilon}{E \left(1 - \varepsilon - \frac{\rho^*}{\rho_s} \right)} \text{ when } \varepsilon_{el} < \varepsilon < 1 \quad (5.3)$$

Gibson and Ashby also provide empirically based stress-strain relations [Gibson, 1998]:

$$\varepsilon_D = 1 - 1.4 \frac{\rho^*}{\rho_s} \quad (5.4)$$

$$\frac{\sigma^*}{\sigma_{el}^*} = 1 \text{ when } \varepsilon \leq \varepsilon_D \left(1 - \frac{1}{D} \right) \quad (5.5)$$

$$\frac{\sigma^*}{\sigma_{el}^*} = \frac{1}{D} \left(\frac{\varepsilon_D}{\varepsilon_D - \varepsilon} \right)^m \text{ when } \varepsilon > \varepsilon_D \left(1 - \frac{1}{D} \right) \quad (5.6)$$

Ben-Dor [Ben-Dor, 1996] state that if the stress-strain relations proposed by Gibson and Ashby are used, the curves which are published in their book [Gibson, 1998] are not reproduced. The curves, as described by Ben-Dor "... are far from being horizontal as they should have been had they been actually drawn using [equation (5.5)] which simply implies that $\sigma = \text{constant}$ inside the plateau regime." [Ben-Dor, 1996]

This suggests a mistake may have occurred in Gibson and Ashby's communication of the empirically based stress-strain relations for foams. Rather than attempting to infer the intended formulae, these relations were not considered for this study.

A further limitation of Gibson's proposed stress-strain relations was that as the foam approaches densification, the foam's stiffness should approach that of the polymer of which it is made. Gibson and Ashby's equations (both theoretical and empirically based) result in an asymptotic increase in stress at densification strain. Ben-Dor [Ben-Dor, 1996] also recognized this shortcoming of Gibson and Ashby's equations and proposed the following relation for closed cell foams:

$$\sigma = E^* \varepsilon \text{ when } 0 < \varepsilon < \varepsilon_{el} \quad (5.7)$$

$$\sigma = \sigma_{el} + \frac{p_0(\varepsilon - \varepsilon_{el}) \left(1 - \frac{\rho^*}{\rho_s}\right)}{\left(1 - \varepsilon - \frac{\rho^*}{\rho_s}\right) \left(1 - \varepsilon_{el} - \frac{\rho^*}{\rho_s}\right)} \text{ when } \varepsilon_{el} < \varepsilon < \varepsilon_D \quad (5.8)$$

$$\sigma = \sigma_{el} + \frac{p_0(\varepsilon_D - \varepsilon_{el}) \left(1 - \frac{\rho^*}{\rho_s}\right)}{\left(1 - \varepsilon_D - \frac{\rho^*}{\rho_s}\right) \left(1 - \varepsilon_{el} - \frac{\rho^*}{\rho_s}\right)} + \frac{E_S(\varepsilon - \varepsilon_D)}{1 - \varepsilon_D} \text{ when } \varepsilon_D < \varepsilon < 1 \quad (5.9)$$

$$E^* = E_s \left[\varphi^2 \left(\frac{\rho^*}{\rho_s}\right)^2 + (1 - \varphi) \frac{\rho^*}{\rho_s} + \frac{\frac{p_0}{E_s} (1 - 2\nu^*)}{1 - \frac{\rho^*}{\rho_s}} \right] \quad (5.10)$$

$$\varepsilon_{el} = \frac{0.03 \left(\frac{\rho^*}{\rho_s}\right)^2 \left[1 + \left(\frac{\rho^*}{\rho_s}\right)^{\frac{1}{2}}\right]^2 + \frac{p_0 - p_{atm}}{E_s}}{\varphi^2 \left(\frac{\rho^*}{\rho_s}\right)^2 + (1 - \varphi) \frac{\rho^*}{\rho_s} + \frac{\frac{p_0}{E_s} (1 - 2\nu^*)}{1 - \frac{\rho^*}{\rho_s}}} \quad (5.11)$$

The disadvantage of Ben-Dor's model is that it assumes that at densification, all gas has been evacuated from the foam cells. This assumption is correct for open celled foams, but in closed cell foams there is still air present even at densification. In a closed cell foam we would expect the air to be compressed until its stiffness matches that of the solid phase of the foam, at which point the solid phase begins undergoing compressive strain.

5.1.1 Rate Dependence of Foam Material Behaviour

Foams are rate dependent [Ouellet, 2004; Ouellet, 2006; Gibson, 1988; McArthur, 2003; Nerenberg, 1998], and are shown to exhibit stiffer behaviour as strain-rate increases (Figure 5.5). Since foams consist of two phases (the solid cell walls and the air gas) the contributions to strain rate sensitivity of each should be explored.

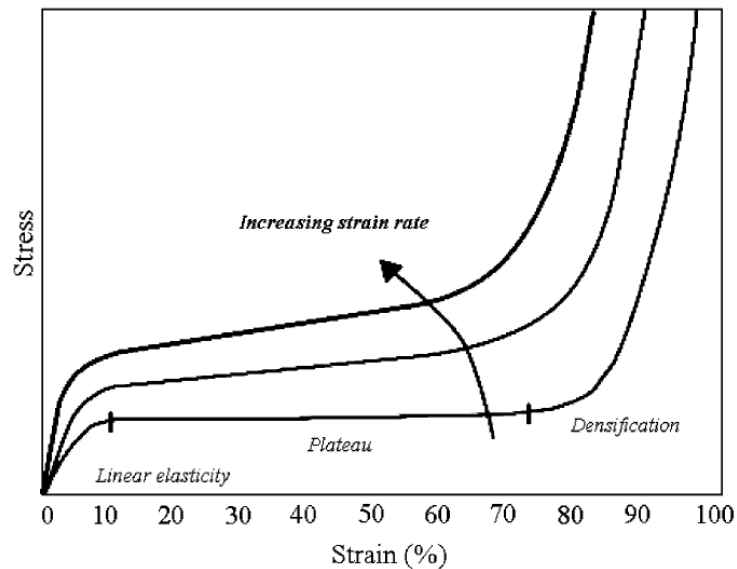


Figure 5.5 - Illustration of the effect of strain rate on foam stress-strain behaviour [Ouellet, 2006]

For both open and closed cell foams, the solid phase of the foam will exhibit a rate sensitivity dependent on the stress strain behaviour of the solid material under various strain rates. There are no analytical means of evaluating this for the wide variety of materials used in foams. Gibson and Ashby suggest that the rate dependence of the foam is entirely based on the rate dependence of the material which has been foamed [Gibson, 1988], and the example given, the plateau stress of a foam is shown to vary linearly with the logarithm of the strain rate. This trend may not continue at high strain rates seen in blast loading, in fact, work by Ouellet, [Ouellet, 2006] shows that at strain rates above 1000/s, foam crush stress (defined as stress at 50% strain) begins to increase quickly with increasing strain rate. This could be the result of a change in the strain-rate dependence of the

solid phase of the foam at high strain rates, and/or a change in the contribution of the gas pressure to the foam stiffness; since the strain values used are 50%, the air contribution cannot necessarily be neglected.

As a part of their research, Nerenberg [Nerenberg, 1998] used high rate testing to aid in the characterization of foams. The plateau stress from Nerenberg, as well as a logarithmic fit are shown in Figure 5.6 below.

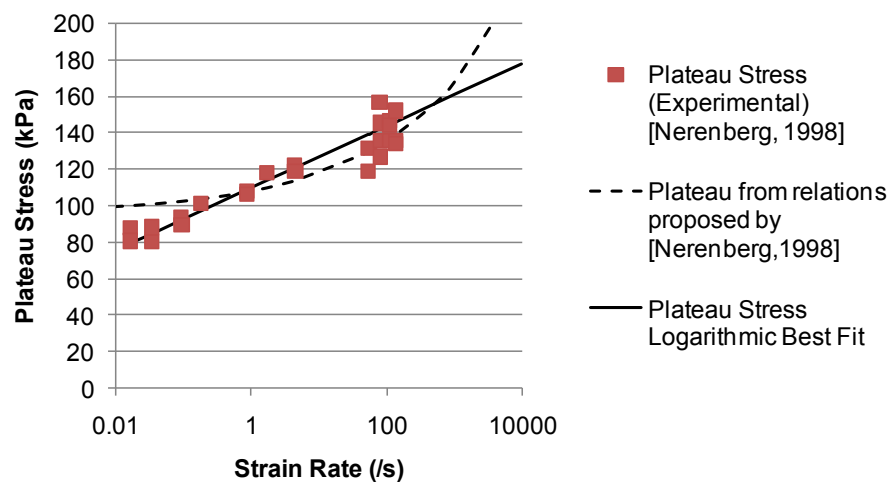


Figure 5.6 - Effect of strain rate on plateau stress for LDPE45 foam, experimental and proposed fit from [Nerenberg, 1998], and a logarithmic fit to experimental data

The rate dependent model utilized by Nerenberg suggests an increase in plateau stress with strain rate that is more drastic than what would be estimated based on the trend of the available data at various strain rates. Nerenberg's estimates deviate from the predicted trend because his model attempted to match foam initial stiffness (E^*) to experimental results, from which plateau stress was determined as a by-product.

The gas phase (air) has a contribution which depends (as mentioned previously) on whether the foam is closed or open cell. For closed cell foams, the contribution of air has traditionally considered to be independent of strain rate or foam geometry [Gibson, 1998]. The idea of a constant contribution from air has been based on the assumption that the air is being compressed

isothermally, even at high strain rates. Gibson et al justify this by suggesting that the solid phase of the foam absorbs heat generated by the compression of the air [Gibson, 1988]. For polymeric foams this assumption requires further investigation, as polymers typically have low thermal conductivity values [Gibson, 1988], and at high strain rates the polymeric solid phase is likely to be increasing in temperature itself, particularly under high rate deformation. Work by Mills and Gilchrist [Mills, 1997] shows (using a numerical model) how high rate compression of the air contained within a foam cell could increase the air phase temperature under impact loading and approach adiabatic compression. The model is an effort to predict the behaviour of a foam, with a cross sectional area of 0.025m^2 and a thickness of 50mm , when a 5 kg mass impacts at a velocity of 7 m/s . While it is the most thorough investigation of thermal effects in foams under high rate loading to date, accounting for heat transfer from the air to the solid phase, the effect of temperature increase in the polymer due to high rate deformation is not considered, nor is the effect of thermal softening. The strain rate and maximum compressive strain were approximately 50 s^{-1} and 70.5% respectively; neither of these values approach those in foams under blast loading. The temperature rise was found to depend on cell size, with the increased surface area of smaller cells resulting in faster heat transfer between the air and foam cell walls (Figure 5.7).

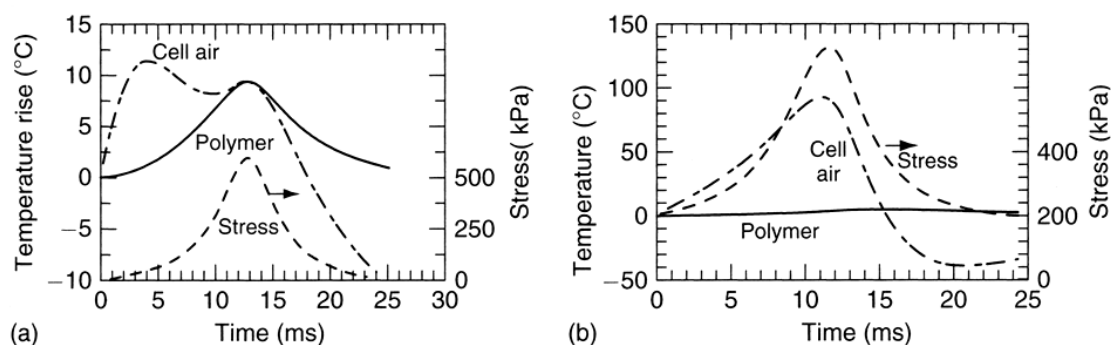


Figure 5.7 - Foam cell air and polymer temperatures vs. time. Cell diameter of: a) 0.1mm and b) 1.0mm [Mills, 2007]

High strain rate tests of closed cell polyethylene foams [McArthur, 2003] demonstrate the dramatic change in high strain behaviour, which makes it appear as though the material is densifying at a lower strain (Figure 5.8).

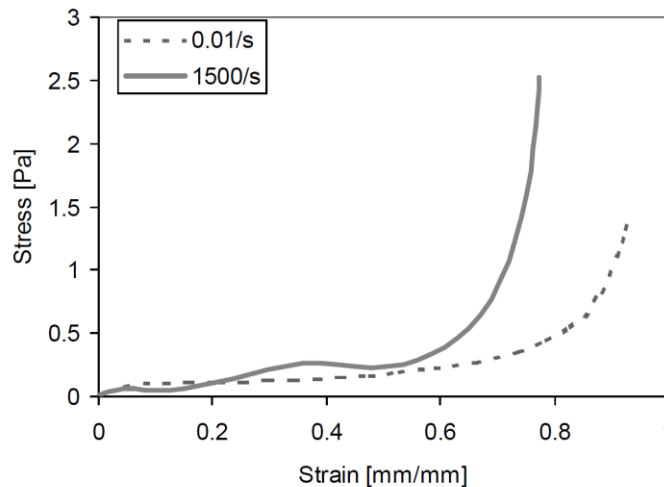


Figure 5.8 - Quasistatic and high rate compressive Stress-Strain behaviour of a 34 kg/m³ LDPE foam [McArthur, 2003]

For open cell foams the contribution of air to the stiffness of a foam is more complicated. At extremely low strain rates, the air has ample time to escape from foam cells. There is no contribution to the foam stiffness from air under quasi-static strain rates. At higher strain rates, the air has a viscous contribution to the stiffness of the foam. If one imagines that the foam is compressed at an extremely high rate, a pressure is generated in the foam cells from the air. This high pressure is required in order to produce flow through foam pours. At high strain rates, the air must be evacuated from the foam a higher rate yielding higher pressures in the foam cells and thus a higher contribution to foam stiffness.

The viscous contribution of air to an open cell foam does not depend only on strain rate, but also on the area available for air to escape from. The available “breathing” area of a foam is dependent on geometry and boundary conditions. Another contributor to the viscous contribution from air is the foam cell size which determines the size of the orifices that air can flow through in the foam.

It might be expected that at some extremely high strain rate, and/or low breathing area of the foam, an open celled foam's behaviour would approach that of a closed cell foam, due to an increased contribution of the air to foam stress-strain behaviour. This assumption is used in analysis of data from Ouellet [Ouellet, 2008] in Section 5.4.2.

While geometry independent material characterization should be possible for closed cell foams under high rates of deformation, it presents a problem for open cell foams. Samples used in material characterization (Hopkinson bar tests, for example) are typically of different geometries than the foams being modelled. Furthermore, in the case of blast loading, the boundary conditions for the air phase are different. In material tests two sides are blocked by the surfaces applying compressive loads (the platens); in blast tests the back is blocked by a rigid wall, but the front face is open, allowing air movement in and out of the foam.

5.2 Experimental Work (Literature)

Foams have been a material of interest under shock and blast loading, as they have been shown capable of both attenuating and amplifying peak pressures under shock loading [Ben-Dor, 1994; Lagutov, 1997; Skews, 1991; Seitz, 2006; Gubaidullin, 2003; Ouellet, 2006; Ouellet, 2008; Nerenberg, 1998]. Because of the differences in load duration, trends from shock tube loading may not be the same as those seen in blast loading. Shock tube loading does offer insight into how shock waves interact with the materials, and can be used for validating numerical models before proceeding with blast loading if necessary.

Fortunately, some blast data exists for foams and very detailed studies have been undertaken using shock tubes. Results from both types of loading will be reviewed.

5.2.1 Shock Tube Experiments on Foams

When shock tube loading is of infinite duration (or of duration exceeding the time for equilibrium in the material to be reached), a layer of foam located at the back wall of a shock tube will amplify the peak pressure observed at the back wall [Ben-Dor, 1994; Lagutov, 1997; Skews, 1991; Seitz, 2006; Gubaidullin, 2003; Ouellet, 2006]. Of course, assuming an infinite duration pulse pressure, no attenuation is possible because stresses at the front and back of the foam must eventually reach equilibrium, meaning the minimum possible pressure applied by the foam to the plate on which it is mounted is the pressure applied to the foam by the shock tube loading. As the physical length of the foam increases, the peak pressure also increases [Seitz, 2006]. Additionally, it was found that foam density was a parameter which influenced the magnitude of amplification, with higher density foams causing higher peak pressures. Again, this is a trend unique to long load durations.

Work by Ouellet [Ouellet, 2006] showed a foams with a low and high plateau stresses amplifying shock tube pressures. Even a foam which was not compressed past its elastic, pre-buckling, strain showed a slight amplification of pressure, though this was likely a result of impedance mismatch (see section 2.2.1).

As discussed in Section 5.1, foam structures can be categorized as either open or closed cell. Open cell foams have proven to be somewhat more complicated under high rate loading due to the rate dependent contribution of the air contained within the foam to the stiffness of the material. When a foam has no material present on the front face (open faced), high pressure air may flow into the foam cells before compression begins. Later, as the foam becomes more compressed, the air may escape out of the front face as the air pressure within the foam exceeds the pressure at the front face.

In open cell foams, when struck by a blast wave, the surface struck by the air blast allows air to flow both in and out of it. The result is initially that the reflected pressure builds up gradually rather than instantaneously, as high pressure, shocked, air flows into the foam during initial loading.

The second effect is as the foam becomes compressed, eventually the air pressure within the cells exceeds that of the loading on the front face, and air begins to escape. This problem does not apply when a foam is faced with a non-permeable material (Figure 5.9).

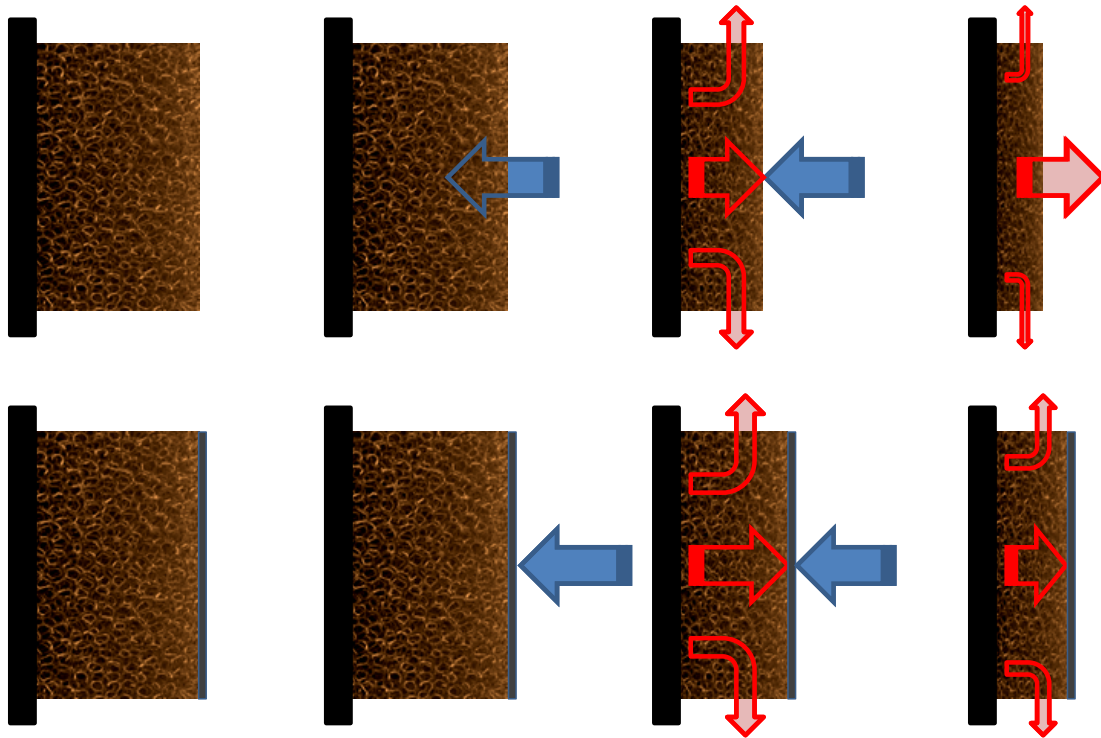


Figure 5.9 - Differences in air flow in and out of a foam under air shock wave loading with and without an impermeable front face

A study by [Lagutov, 1997] included shock tube loading of an open celled foam, in open faced and closed face configurations. A sheet of mylar was used to block the foam pores in the closed face configuration. An increase in back wall pressures was observed when the front face of the foam was made non-penetrable by air.

5.2.2 Blast Loading Experiments on Foams

Studies of foam behaviour under blast loading have been conducted with and without high density materials in front of the foam.

Studies of closed cell foams under blast loading have been undertaken by Nerenberg and Makris [Makris, 1996; Nerenberg, 1998; Nerenberg, 1997] in order to determine the amplification and attenuating characteristics of LD45 (Low density polyethylene foam with a density of 45kg/m³) and HD80 (High density polyethylene foam with a density of 96kg/m³) closed cell foams. It was found that foams have the potential to both amplify and attenuate blast loading. It was also found that increasing the foam thickness would decrease the peak pressure behind the foam. Note this trend is opposite of that seen under (effectively) infinite duration shock tube loading.

Work by Ouellet [Ouellet, 2006] included blast loading of various foams. The foam with the lowest plateau stress of 200 kPa was shown to amplify the transmitted pressure, while the foam with the next lowest plateau stress (900 kPa) was able to attenuate the blast load. The last foam had a plateau stress which was higher than the peak applied blast pressure, and actually amplified the blast wave. The plateau stress of the foam was 2000kPa, while the peak applied blast pressure was only 1600kPa. The amplification in this last case was likely the result of impedance mismatch. The results of the study show the importance of foam selection for blast wave attenuation.

Work by these researchers shows that foam which amplifies pressure can also produce pressure attenuation by changing the foam's thickness or the severity of blast loading; likewise, a foam which can attenuate a given blast wave may amplify a blast of higher severity, or a blast of the same severity if the thickness of the foam is decreased.

Blast tests conducted by Nerenberg and Ouellet were conducted at the Canadian Explosives Research Laboratory (CERL, Ottawa, Ontario). The experiments were conducted in a blast chamber at the facility. C-4 charges were suspended above an experimental test fixture in both studies (Figure 5.10). Details of each fixture vary between Ouellet and Nerenberg, however both

utilize foam samples mounted on a flat rigid surface. The surface was instrumented in both experiments with flush mounted pressure transducers. It was assumed in these studies that the pressure measured by the flush mounted pressure transducer was equivalent to the stress at the back of the foam sample.

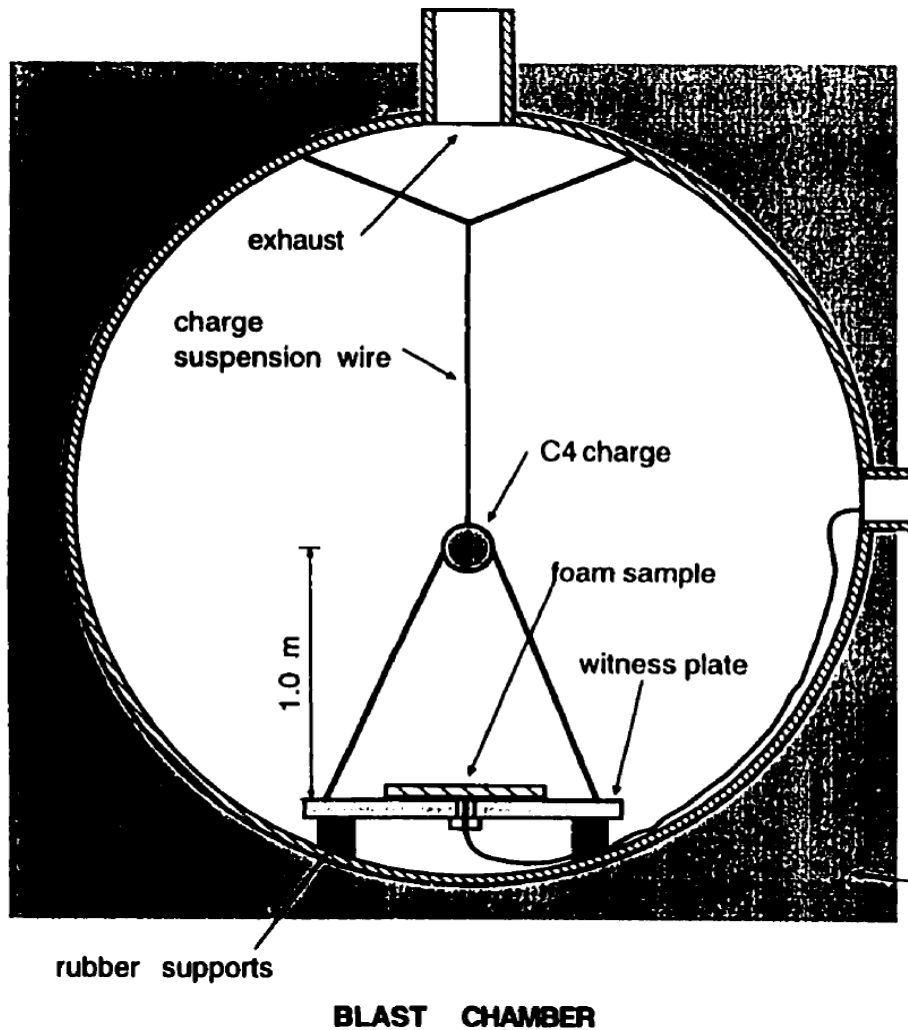


Figure 5.10 - Blast chamber used by both the Nerenberg and Ouellet studies [Nerenberg, 1998]

5.2.3 Experiments on Foam and Rigid Plate Decouplers

The work by Ouellet [Ouellet, 2008] utilized a single thickness of foam, however plates of varying areal density, (mass per unit area) were placed in front of the foam to observe the effect on back

wall pressure under blast loading. This type of configuration is analogous to the “stress-wave decouplers” described in work by Cooper et al [Cooper, 1991]. The goal was to systematically change the mass of the high density component of a decoupling protection concept. Both significant amplification and attenuation were achieved by only varying the plate mass. It should be noted that a variety of materials were used for the plates in order to vary the mass, and no correlation between plate through thickness properties and amplification/attenuation were observed.

Experiments by Nerenberg [Nerenberg, 1998] included a few tests with a high carbon steel mounted in front of a low density polyethylene (LDPE) foam. While the work published by Nerenberg did not include the same level of variation in decoupling configurations that the work by [Ouellet, 2008] did, it is a useful resource and shows clearly the advantage of the addition of a high impedance layer to foam under blast loading.

5.3 Finite Element Model Development

In this study, the most relevant set of data to validate the foam model against was the data from experiments [Nerenberg, 1998] and [Ouellet, 2008]. These sets of data were used because they involved blast loading of foam samples of various thickness using varied charge sizes. The multiple cases for validation allowed for the testing of the developed material model's robustness.

5.3.1 Model Geometry

A numerical model for shock tube simulations was developed. It consisted of a single column of 3D solid elements (Figure 5.11). The boundary conditions, and associated assumptions of symmetry, were such that the simulation was representative of an infinite wall being struck by a planar shock wave. This meant that leakages from open celled foams would not be captured out of the side of the material. Pressure-time history was prescribed to elements which acted as a source for blast loading. The length of the ALE air mesh was longer for shock tube studies than blast simulations due to the effect of the air mesh length on the maximum duration of the load pulse.

The air was modelled using an ideal gas equation of state, with the constant volume and constant pressure specific heat coefficients being 718 and 1005 J/kgK, respectively.

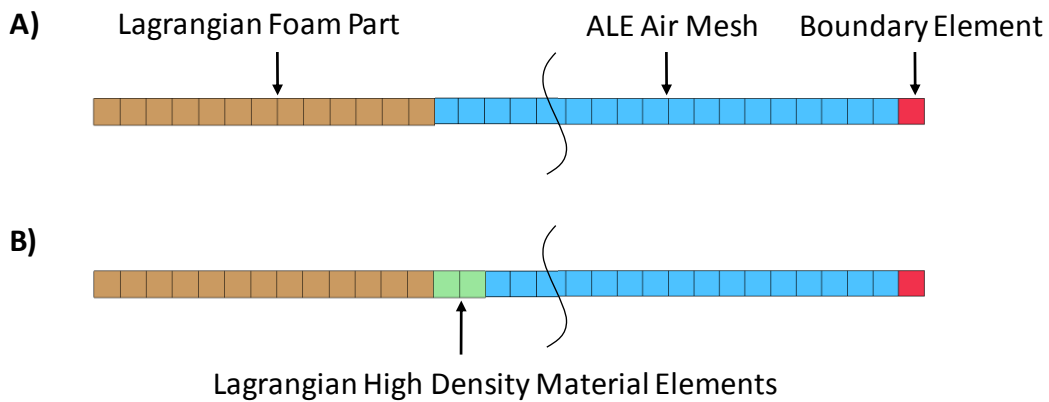


Figure 5.11 - 1D models of: A) Foam without high density material, B) Foam with high density material

A single element in width was justified by considering the low Poisson's ratio of foams [Gibson, 1988]. The assumption of uniaxial compression and a low Poisson's ratio have been utilized for most of this study and so this was consistent with the material model used. Most foam models implemented by the solver used (LS-DYNA) assume a low Poisson's ratio.

Since the Lagrangian foam part and the ALE mesh both occupied the same space, special consideration had to be made to ensure that the air did not contribute to the stiffness of the foam during deformation. As such, a vacuum is defined in the ALE mesh, in the same volume that is occupied in the foam. If this was not done, as the foam front face was accelerated towards the back wall a pressure would develop in the ALE elements (corresponding to compression of an ideal gas or Boyle's law). For higher density foams, the pressure contribution might not have been significant until high compressive strains, however for low density foams such as those simulated, it was important to remove this effect.

In simulations where it was included, the high density material was coupled to the ALE air mesh. Since the blast load was applied to the high density material, it was not necessary to couple the foam to the ALE mesh for those simulations. As mentioned previously, the ALE elements

occupying the same space as the foam were assigned a null material model which had negligible node mass and material stiffness.

5.3.2 High Density Material Model

High density materials were modelled using elastic material models. It was assumed that small strains would occur in the hard plates used for these fully planar simulations. It was also shown that the mass of the high density material in front of the foam (areal density) dominates the effect the plate has on altering blast loading. This assumption was explored by varying the young's modulus of a high density material two orders of magnitude for simulation, and observing the difference in the back wall pressure. No difference was observed in simulation results when the modulus for the ultra high molecular weight polyethylene was increased from 1.5 GPa to 15 GPa, and 150 GPa.

The density and thicknesses of the materials were determined based on information provided in [Ouellet, 2008], where the mass of plates were measured, and dimensions of the plates were provided. Thicknesses were given for all plates except for a carbon fibre composite plate. A study was also done on the influence of the plate thickness on the numerical result, and no difference was noted in simulations as long as the same areal density was maintained. A thickness of 4mm was assumed for the carbon fibre plate in the simulations for this study.

The plate properties used in the simulation of experiments [Ouellet, 2008] for model validation are listed in Table 5.1 below. Note that because limited data was available regarding the mechanical properties of the high density plates used, the Young's modulus and Poisson's ratios were estimated based on values from other literature, however the results were independent of these values.

Table 5.1 - High Density Plate Elastic Material Properties

Plate Type	Weight for 8"x8" panel (kg) [Ouellet, 2008]	Thickness (mm)	Areal Density (kg/m ²)	Density (kg/m ³)	Young's Modulus (GPa)	Poisson's Ratio
UHMWPE	0.200	5	4.8	968.8	2.5 ²	0.33
Aluminum	0.232	4	5.6	1404.7	79	0.35
Carbon Fibre	0.388	4	9.4	2349.2	9.0 ¹	0.40

¹[Huang, 2000], ²[Yan, 1997]

A need for more detailed shock-wave analysis and the use of more complicated models for high impedance materials utilizing an equation of state could be avoided due to the impedance mismatch between the high impedance material and foam. Because of the decoupling configuration, very little of the transmission of the initial shock wave was expected.

5.3.3 Low Density Polyethylene Foam (LDPE 45) Material Model

As mentioned in Section 5.1, foams are complex materials in that they show rate dependent, temperature dependent, hyperelastic, mechanical behaviour. While foams consist of two phases, it is common to model foams as a continuum. For closed cell foams this should be possible, however for open cell foams this treatment has limitations due to the ability for the air within cells to migrate from cell to cell, as well as out of the foam. While the model being discussed was a 1D model, the goal was to extend this to a 2D model of the human torso.

The assumptions made regarding the foam's behaviour had to be validated during the development of the foam material model. It was important to identify what assumptions could be made about the material behaviour in order to simplify the model, while maintaining accuracy. The approach taken during this study was to begin with the simplest model and improve assumptions until satisfactory results were achieved.

The foam itself was modelled as a Lagrangian part using solid elements. Initially, a material model for low density foam was used. In order to determine the compressive stress-strain behaviour, a modified version of Gibson's formulae for determining the stress strain behaviour of a foam was used and compared to available stress-strain data for the foam.

The stress strain behaviour of the material model utilized in the current study was considered as two parts: the stress contribution from the solid foam structure before and after buckling, and the air pressure contribution with densification being considered.

The stress contribution from the solid foam phase, as per Gibson [Gibson, 1998] was given by Equation 5.2 (behaviour before cell wall buckling) and Equation 5.1 (plateau stress after cell wall buckling). It is worth noting that this relation can be used for both open and closed cell foams.

The contribution of gas pressure up to and beyond densification is examined assuming the gas and solid phase of the foam are in series (Figure 5.12).

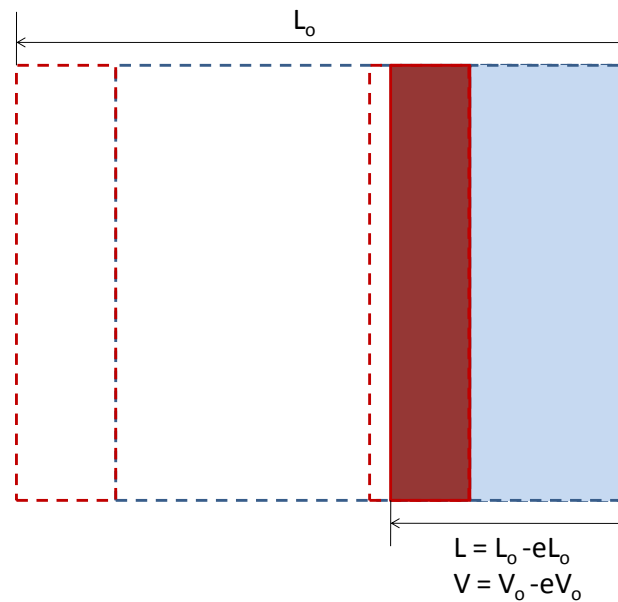


Figure 5.12 - Diagram showing cell wall material and air being considered in series

The total strain as a function of the strain in the solid and gas phases was written as:

$$e_{total} = e_{solid} \frac{\rho^*}{\rho_s} + e_{gas} \left(1 - \frac{\rho^*}{\rho_s}\right) \quad (5.12)$$

It was assumed that the solid and gas phases were in equilibrium with each and thus the pressure/stress between the two was equal.

$$\sigma = p_0 \frac{e_{gas}}{1 - e_{gas}} = e_{solid} E_s \quad (5.13)$$

By combining equations 5.12 and 5.13, and eliminating an erroneous root we can solve for the strain in the gas phase as a function of total strain and material constants.

$$e_{gas} = \frac{\left(R - 1 - e_{total} - p_0 \left(\frac{R}{E_s}\right)\right) - \sqrt{\left(\left(R - 1 - e_{total} - p_0 \left(\frac{R}{E_s}\right)\right)^2 - 4(1 - R)e_{total}\right)}}{2e_{total}} \quad (5.14)$$

Equation 5.13 can then be used to determine the stress using the strain in the gas or solid phase, and a stress-strain curve developed. The end result was very similar to the curve produced by Ben-Dor's relations, except the post-buckling domain is continuous (where Ben-Dor's equations are discontinuous at densification). At densification, the air no longer would decrease in volume, and instead an increase in total compressive strain must be through compression of the solid phase of the foam. This resulted in a very rapid increase in material stiffness at densification, and the result was nearly indistinguishable when compared to those using Gibson's theoretical relations at strains below densification.

There is solid foam material which exists in parallel, and it is accounted for in the method proposed by Gibson [Gibson, 1985]. Figure 5.13 shows how the total stress was considered the sum of the stress in the solid foam phase and cell air pressure.

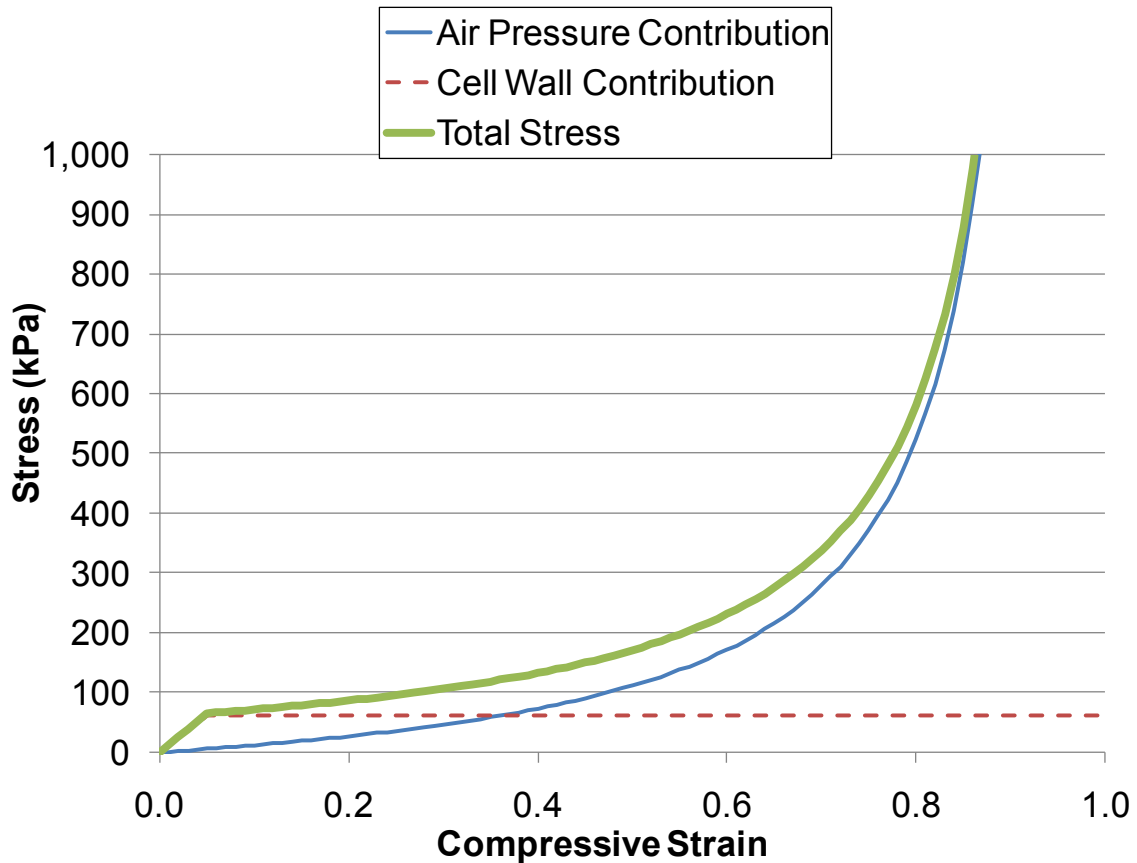


Figure 5.13 - Contribution of solid cell wall and enclosed air to stress strain behaviour of a foam

The resulting stress-strain relation was used to produce quasi-static stress-strain curves for LDPE 45 and HDPE 96 closed cell foams. The density of LDPE 45 foams is 45 kg/m^3 , and the Young's modulus and density of solid polyethylene are listed as being between 910 and 1200 kg/m^3 and 0.2 to 0.7 GPa , respectively. Equations (5.1) and (5.2) were used for pre-buckling behaviour, and Equations (5.12), (5.13) and (5.14) were used for post buckling behaviour. Material properties were selected to produce a stress strain behaviour matching experiments from Nerenberg [Nerenberg, 1998]. The solid density used was 1000 kg/m^3 and the modulus of elasticity of the solid was 0.6 GPa (note these values are within the range of values reported by Gibson and Ashby [Gibson, 1988]). The resulting fit was good as shown below in Figure 5.14.

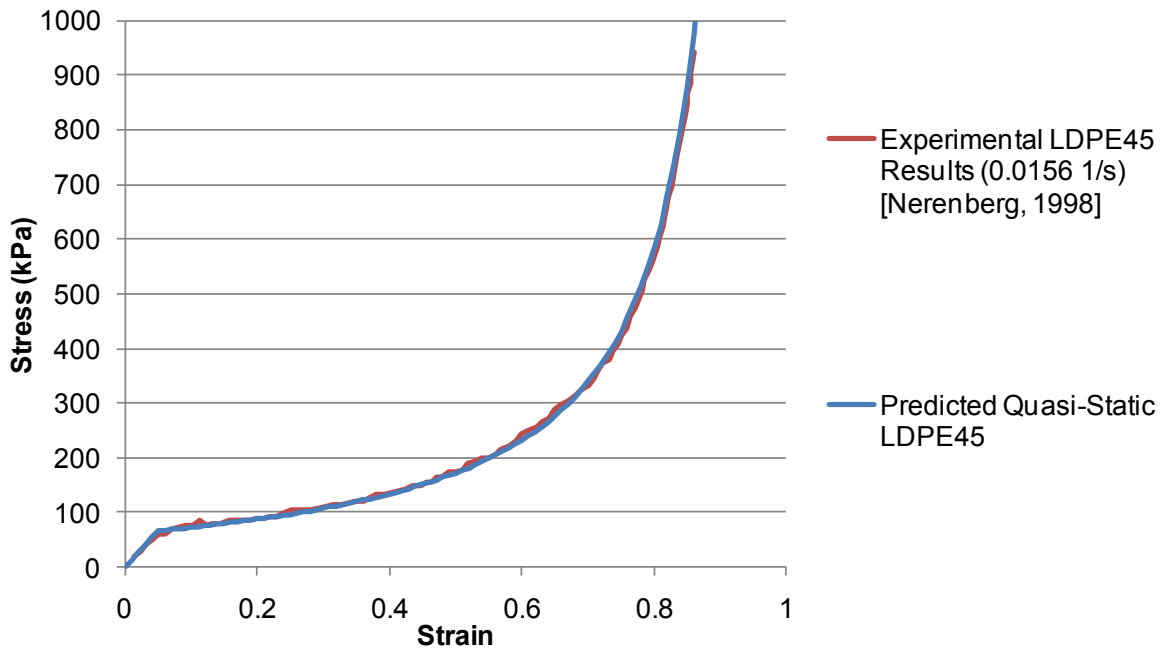


Figure 5.14 - Quasi-static stress strain behaviour for LDPE45 foam (experimental and theoretical)

Once it was shown that the relations for stress-strain behaviour of foams under quasi-static loading were well described, the dynamic properties of foams were considered.

5.3.4 Rate Dependent Behaviour of LDPE 45 Foam

The rate dependent foam material model considered was based off of work by Fu Chang [Chang, 1995]. The implementation of Fu Chang's material model allows the definition of a rate dependent model by inputting stress-strain data for various strain rates. The stress strain data was produced for the current study by using the relations used to produce quasi-static stress-strain curves, but adjusting the solid modulus (E_s) to produce a plateau stress which matched Nerenberg's dynamic tests [Nerenberg, 1998]. While this approach was simple, it reflects the explanation offered by Gibson [Gibson, 1988] that the rate dependence of foams reflects the rate dependence of the solid from which the foam was made. It should be noted that in order to cover some of the strain rates achieved experimentally, high strain rate data had to be extrapolated from Nerenberg's results. Nerenberg's high strain rate testing of LDPE 45 foam was up to strain rates as high as 140.2 per

second; the strain rates achieved with shock tube and blast loading are typically an order of magnitude higher [Ouellet, 2006].

The change in post buckling behaviour, namely the earlier onset of densification at high strain rates as noted from the studies by McArthur and Ouellet would also have been of interest; however information on this rate effect was not available for the foam of interest (namely a low density polyethylene foam with a density of 45 kg/m³).

The rate dependent model was compared to a non-rate dependent model with hysteresis and damping parameters introduced to produce unloading behaviour which was representative of the experimental results. In order to produce a stress-strain behaviour representative of a foam's increased stiffness under high strain rates, while still using a non-rate dependent model, the stress strain behaviour was assumed such that the plateau stress of the foam matched that achieved in most blast and shock tube loading of LDPE 45 foam, and the plateau stress was set to 200 kPa, which is a value representative of most of the blast and shock-tube data used in validation (Figure 5.15).

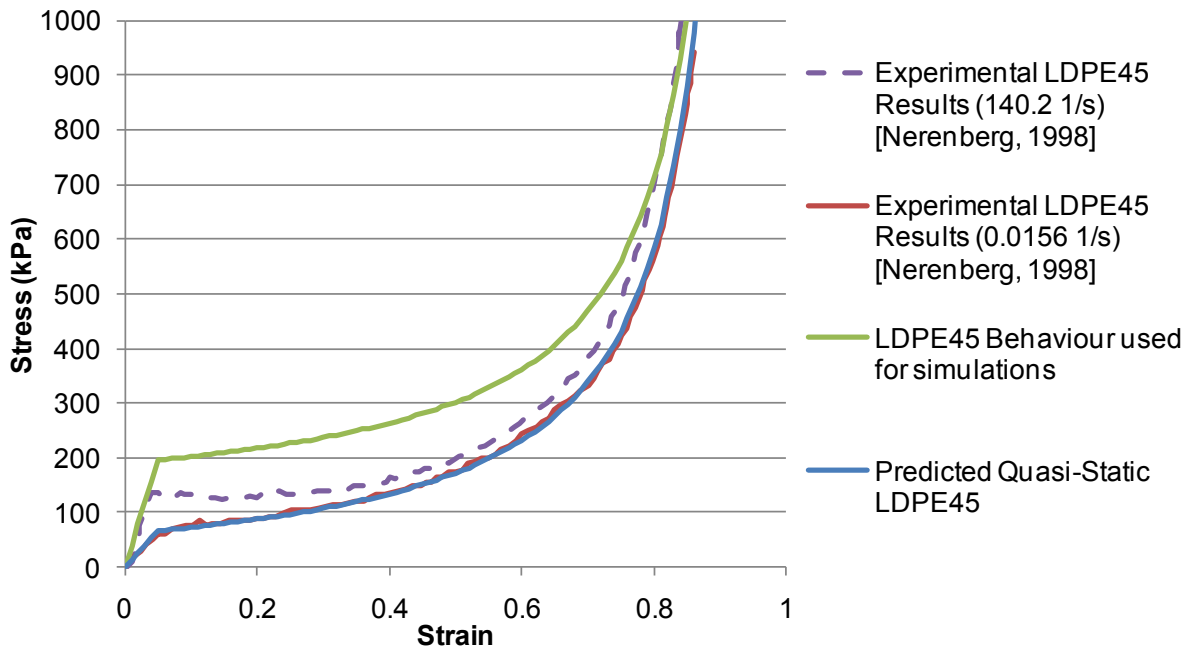


Figure 5.15 - Stress strain behaviour from experimental work [Nerenberg, 1998], compared to calculated quasi-static behaviour, and the stress strain behavior used in simulations for the non-rate dependent model

The use of a rate independent model has limitations in that it assumes the plateau stress does not vary greatly for the experiments being considered. It was found that this approach was adequate for the prediction of the pressure history behind LDPE 45 foam under blast loading, with and without the inclusion of a hard plate on the front face. It is expected that as more information regarding the behavior of foams at extremely high strain rates (on the order of 1000/s) and their dynamic properties becomes available, that the need to use pre-existing shock tube and blast data for estimation of plateau stress at these strain rates will no longer be necessary.

5.3.5 Low Density Polyethylene Foam Numerical Damping and Unloading Behaviour

This section discusses the foam damping and hysteresis parameters, which were found to influence the dispersion of the blast wave in a low density polyethylene foam. While damping is technically a part of the material's dynamic behavior, it was found to be necessary to consider the effect of

both hysteresis and damping together to obtain realistic wave dispersion behavior in the numerical model.

As mentioned in section 3.2.4, artificial bulk viscosities are utilized in numerical codes to ensure the stability of the code when shock waves are present. A limitation of the use of artificial viscosity is that soft materials (such as foam) can undergo extremely high strain rates, and extremely large deformations, as was predicted as a part of the current study. This means that this class of materials would be susceptible to extremely high artificial viscosity values, but also erroneously calculated values as a result of the use of an effective element length. This might indicate that all artificial viscous contributions should be eliminated (which is an option in many implementations of foam material models). Unfortunately, since these materials exhibit increasing stiffness with increasing strain (densification) numerical instability would result from the removal of all viscous terms. Thus, rather than eliminating the artificial viscosity terms, they are reduced an order of magnitude, or replaced with a damping parameter which can be defined for each material. The artificial bulk viscosity values were disabled for foams in this study and a damping term was used to ensure numerical stability.

Foam material models include a damping term which can be defined by the user. Including damping introduces a velocity dependent stiffness and also causes a dissipation of energy and dispersion of waves. In the context of shock loading of foams, the damping value should be chosen to be low enough that the contribution at high strain rates is minimized, while maintaining stability of the model. While the implementation of damping in these models is poorly documented, it is expected that the benefit of these over the linear artificial viscosity term is that the contribution is uncoupled in other directions, while the artificial viscosity can cause an undesired volumetric response.

Hysteresis parameters in the material model allow the definition of an unloading path which differs from the loading path and does not involve the inclusion of a viscous term to the stiffness; however energy is dissipated through unloading. In a shock-tube loading scenario, or other scenario where unloading does not occur, the effect of hysteresis is negligible. However, when blast loading is applied, unloading occurs as the blast wave travels through the foam, and thus is a source of energy

dissipation. The hysteresis factor implemented for the foam material model used requires the input of two parameters: the hysteresis and shape factor.

The damping and hysteresis factors were chosen such that unloading and wave dispersion behaviour from experiments were properly reproduced numerically. A sample of results using the same numerical model, but varied damping and hysteresis parameters is shown in Figure 5.16. Note that when both damping and hysteresis are disabled, the model predicts the formation of a shock wave in the material Figure 5.16(A). Also note that over-zealous application of damping and hysteresis can result in erroneous peak pressure and peak arrival time estimates Figure 5.16(D).

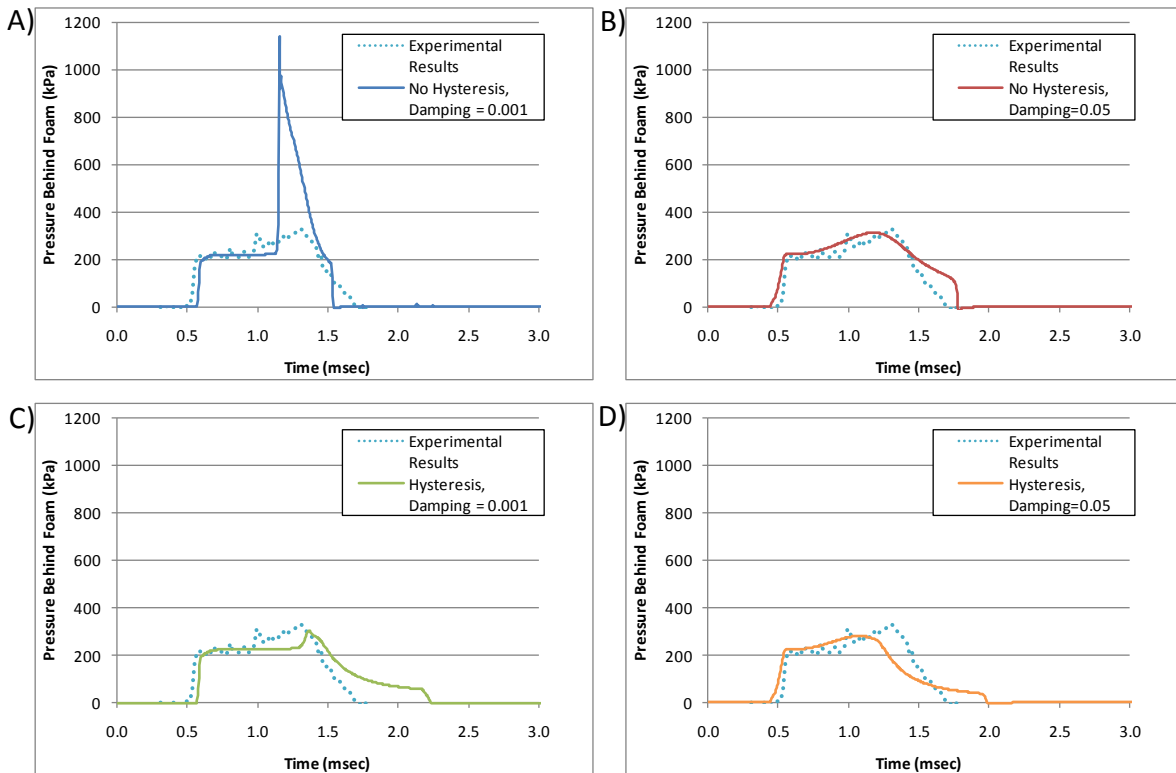


Figure 5.16 - Effect of addition of wave dispersing and energy absorbing parameters to foam material model. A) No dispersion (No Hysteresis, Low Damping); B) No Hysteresis, Damping Added; C) Hysteresis, Low Damping; D) Hysteresis and damping added. All compared against data from [Nerenberg, 1998] for 100mm of LDPE 45 foam loaded by 170g at a 1m distance.

A comparison of the simulation of two experimental cases from Nerenberg [Nerenberg, 1998] showed that while the rate dependent model does a good job of predicting the behaviour of a foam under blast loading, the non-rate dependent model with an appropriate plateau stress, damping and hysteresis parameters, does a better job of predicting the pressure time history. The damping value used in this study was 0.01, and the hysteresis and shape factors were 0.5 and 7.0 respectively.

5.3.6 Model of High Density Polyethylene Foam (HDPE 96)

A model was also developed for a high density polyethylene foam with a density of 96 kg/m³, as this was another foam used in the Nerenberg study [Nerenberg, 1998]. The same approach used for developing the model for LDPE 45 foam (Section 5.3.3 to Section 5.3.5) was used for developing the HDPE 96 foam model. This model was pursued to observe the effect of varied foam stress-strain behavior on the pressure transmitted through a foam under blast loading. The stress strain behavior of the model is shown and compared to quasi-static and high rate tests from [Nerenberg, 1998] in Figure 5.17.

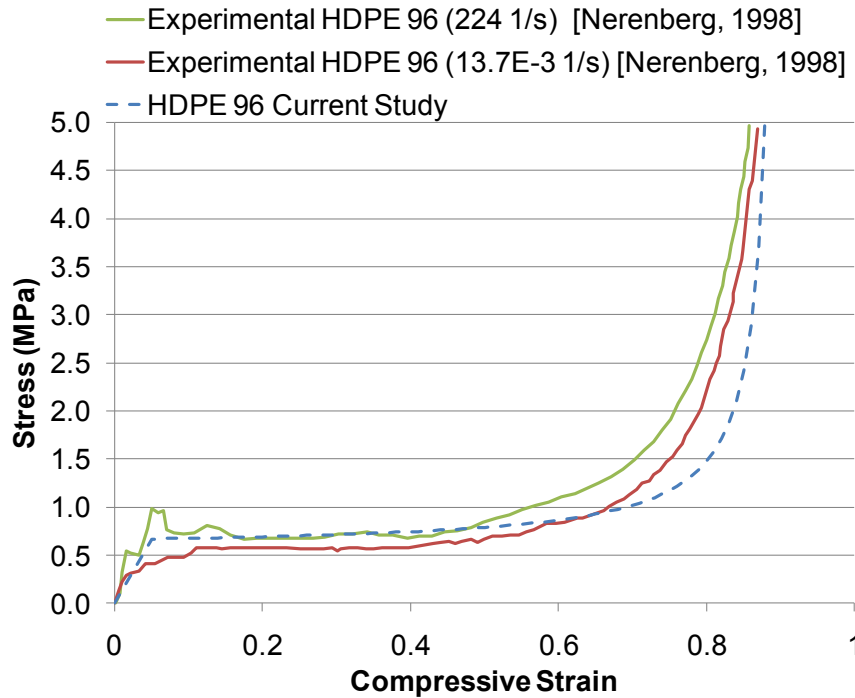


Figure 5.17 - Comparison of experimental quasi-static and high rate stress-strain data to the stress-strain behaviour predicted in the current study for HDPE 96 foam

The behavior post densification is different between the experimental and predicted values; this can be attributed to the lack of consideration given to the contact of the cell walls after buckling has occurred. This discrepancy emphasizes the need of an empirically based approach for defining post buckling behaviour such as that suggested (but improperly presented) by [Gibson, 1985]. Despite the discrepancy between the predicted behavior and experimental data from [Nerenberg, 1998], the predicted behavior was utilized for consistency. A damping constant of 0.028 was used with this material model, as well as hysteresis and shape factors of 0.1 and 7.0.

5.3.7 Wave Speeds in LDPE 45 and HDPE 96 Material Models

The sound speed was estimated using the relation proposed by [Gibson, 1995]. A density of solid polyethylene of 1000 kg/m³ was used as this was consistent with the value used in determining the

behavior for the numerical model. The air density was assumed as 1.27 kg/m³ and the speed of sound in air was assumed as 330 m/s. Sound speeds for an LDPE 45 and HDPE 96 foam were calculated as 56 m/s and 40 m/s respectively. The sound speed versus apparent bulk density for a porous material with a solid phase density of 1000 kg/m³ is shown in Figure 5.18 below.

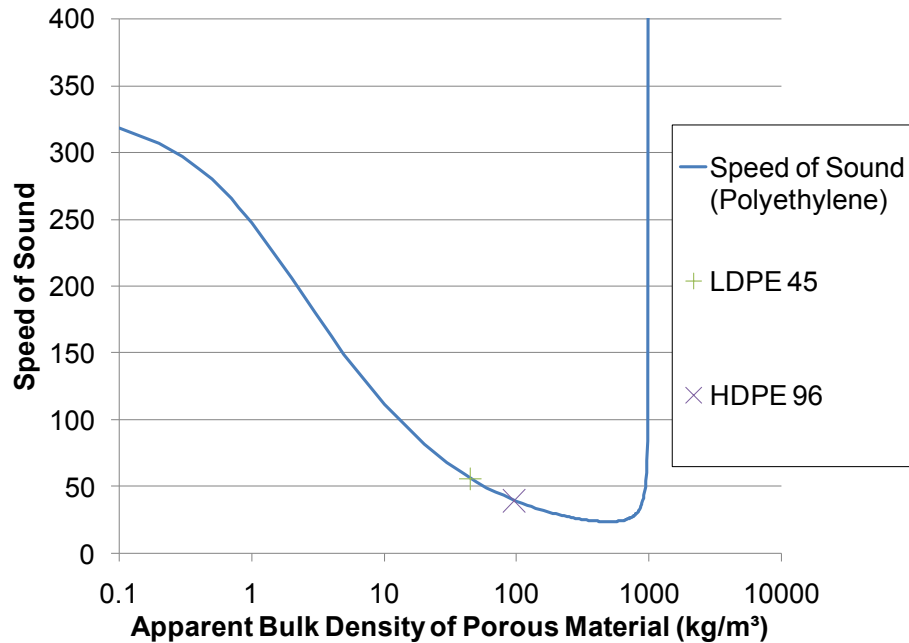


Figure 5.18 - Sound speed versus apparent bulk density for a porous material (polyethylene)

It should be noted that the above sound speeds are representative of the post buckling behavior of the foams. Prior to buckling, however, the materials exhibit a linear stress-strain relationship and thus the elastic wave speed in this region is calculated as:

$$c = \sqrt{\frac{E^*}{\rho^*}} \quad (5.15)$$

From the material curves used for the numerical models, the expected elastic wave speeds prior to buckling for LDPE 45 and HDPE 96 were 295 m/s and 374 m/s respectively.

The stress strain behaviour of foams, and the two wave speeds calculated above suggest that in foams, two waves can be propagating through the material at once. The elastic wave speed prior to buckling will be relevant regardless of load level, while the second wave speed calculated will only be relevant when the plateau stress is reached and exceeded. The extremely low post buckling wave speed means that under high rate loading, a foam material is extremely prone to the formation of shock waves (though they may dissipate quickly). The formation of shock waves can be mitigated by reducing the velocity of the foam front face under blast loading. This can be done by mounting a plate of high density material to the front face of the foam.

5.4 Model Validation Results

The models used in this study for Low Density Polyethylene foam of density 45kg/m^3 (LDPE 45) and High Density Polyethylene foam of density 96 kg/m^3 (HDPE 96) were validated using data from both Nerenberg [Nerenberg, 1998] and Ouellet [Ouellet, 2008]. The tests by Nerenberg involved blast loading of various thicknesses of closed cell LDPE 45 while the tests by Ouellet involved blast loading of a single thickness of open cell LDPE 45 (enclosed preventing air escape) with plates of varied mass placed in front of the foam.

5.4.1 Foam with Varied Thickness Under Blast Loading

Experiments conducted by Nerenberg consisted of various thicknesses of closed cell LDPE45 and HDPE 96 foams loaded by varied charge sizes at 1 meter stand-off. The results from tests where the foam was loaded by 170g and 325g of C4 were chosen for use in validation efforts because the results show the transition from amplification of the peak pressure to attenuation (Figure 5.19). The baseline pressure history (without foam) can be seen in the presented data. The peak pressure of the unmodified blast wave is quoted in [Nerenberg, 1998] as being 1.16 MPa above atmospheric for 170g of C4, and the duration was approximately 0.6 ms.

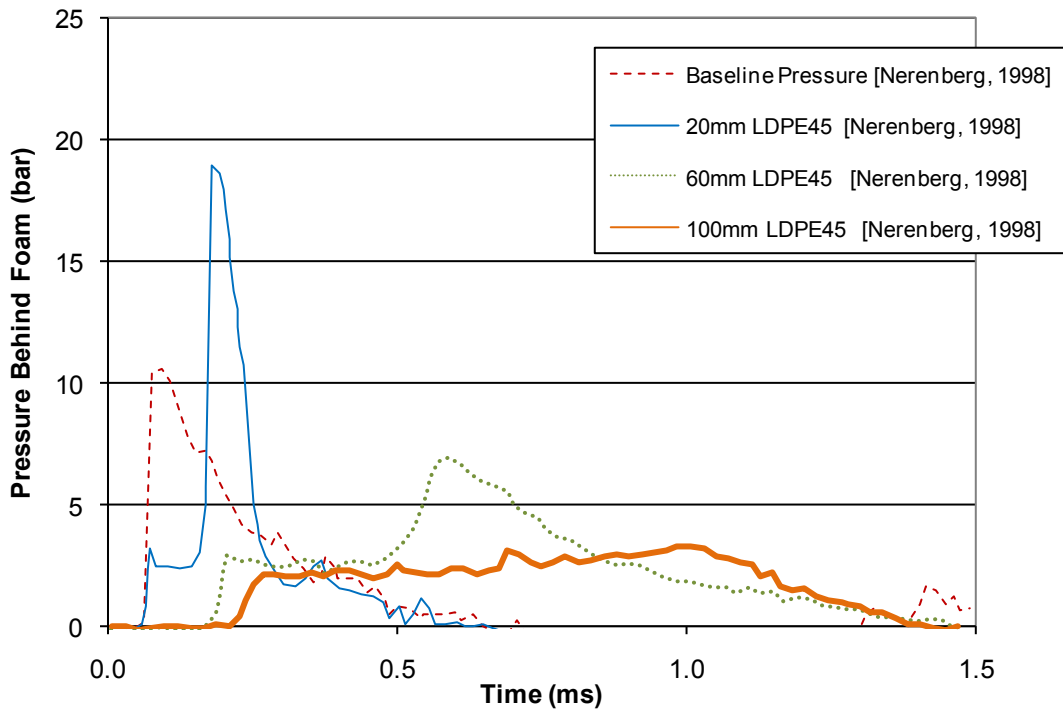


Figure 5.19 - Experimental pressure histories for various thicknesses of LDPE 45 foam loaded by 170g of C4 at 1m [Nerenberg, 1998]

In the case of 20mm of LDPE 45 foam, the thickness of the foam was not adequate to prevent densification. In the densification regime, the stiffness of foam is much higher and thus rapid increases in pressure could occur. As the thickness was increased, the energy imparted to the foam by the blast wave could be better managed; the foam is kept at pre-densification strains for a longer time. It was observed that 60mm of foam yielded a modest attenuation, while increasing thickness further to 100mm resulted in further attenuation of the peak pressure. It was noted that while the peak pressure was reduced, the duration of loading was reduced. The 100mm of LDPE 45 appears to be approaching the limit of the attenuation possible with this material, as the attenuation would be limited by the plateau stress of the foam. The author would also like to draw the reader's attention to the relatively constant plateau stress shown in the experimental data.

Results from the previously described 1D foam model were compared to experimental results.

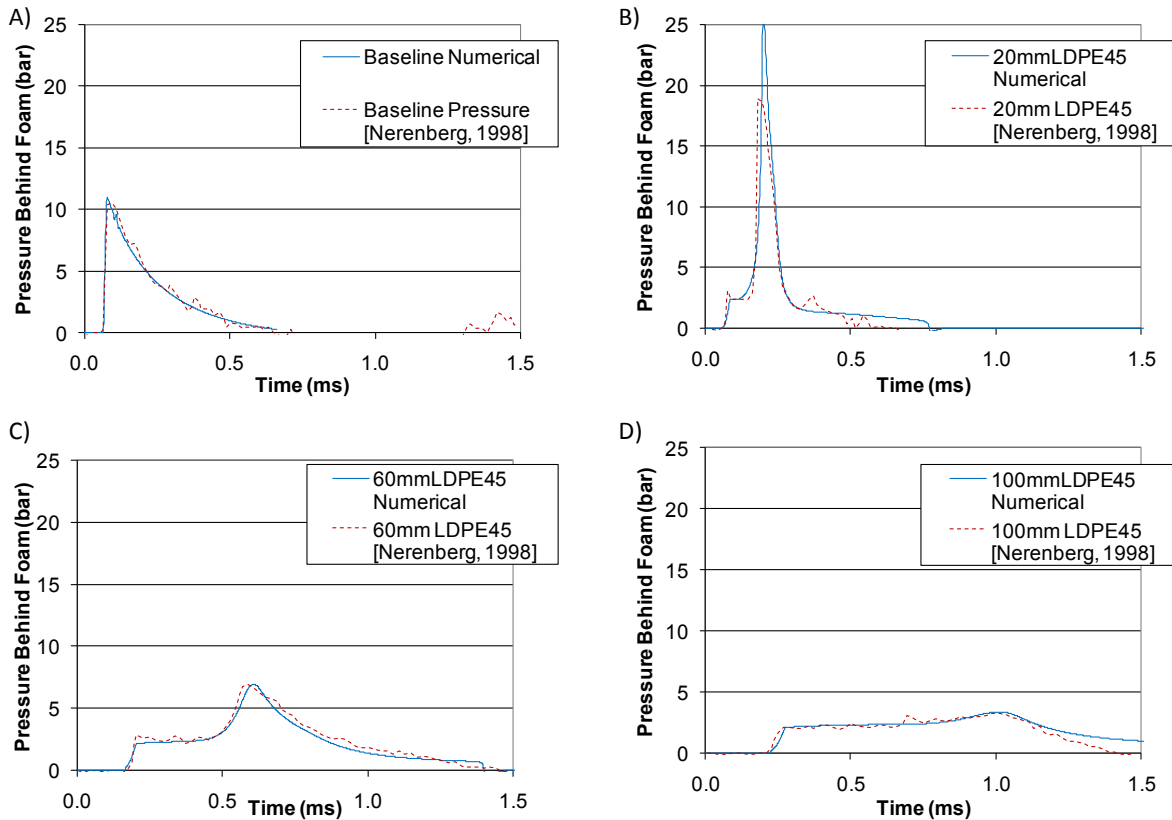


Figure 5.20 - Comparison of experimental results from [Nerenberg, 1998] and numerical results from the current study for: A) Baseline loading without foam, B) 20mm LDPE 45 foam, C) 60mm LDPE 45 Foam, D) LDPE 45 Foam. All loaded by 170g of C4 at 1m.

The numerical results matched the experimental results very closely. A significant deviation in peak pressure was observed for the 20mm case, with 35.8% error being calculated between numerical and experimental results (Table 5.2). The error could have been the result of the approximations in stress strain behaviour, as well as assumptions (such as zero Poisson's ratio) resulting in an overly stiff behaviour at high strain. Measurement error could also be a possibility. In spite of error in peak pressure for the 20mm foam case, the general shape of the pressure transmitted through the foam was close to experimental results. Since the primary purpose of the model was to evaluate protective (attenuating) concepts, the error in the case showing amplification was considered acceptable.

Table 5.2 - Comparison of peak backwall pressures from Experiment [Nerenberg, 1998] and Current Study

LDPE 45 Foam Length	Peak Pressure from Experiment (bar) [Nerenberg, 1998]	Numerical Peak Pressure (bar)	Percent Difference
20mm	19.0	25.8	35.8%
60mm	6.9	6.5	5.1%
100mm	3.3	3.3	1.7%

A large part of the success in recreating experimental results was the use of unloading and damping parameters. Figure 5.21, below, shows the position-time history of 100 points for the 100mm foam struck by the blast wave produced by 170g of C4 at 1m. It is possible to make out two distinct waves. The first which arrives is the wave which travels at the velocity determined by equation (5.15), 295 m/s (indicated by a solid blue line in Figure 5.21). The second wave begins as a compaction wave which disperses and smears rapidly (indicated by dashed lines). The tests with 20mm, 60mm and 100mm of foam allow us to observe how the compaction wave has dispersed at these distances in the material. For example, at 20mm, the compaction wave has not dispersed greatly (Figure 5.21), resulting in a very rapid rise in pressure for this case (Figure 5.20B). The compaction wave speed was calculated as being 56 m/s previously in the chapter, and the maximum velocity of the front face of the foam was determined to be 136 m/s in the case shown.

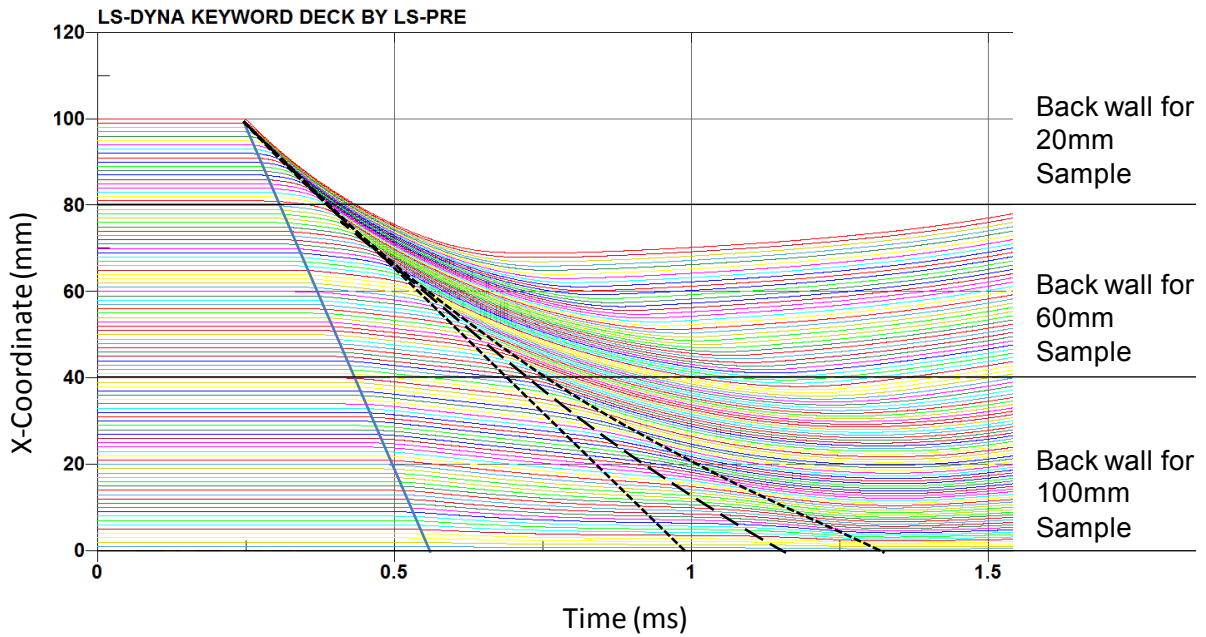


Figure 5.21 - Wave diagram for 100mm of LDPE 45 foam under blast loading from 170 g of C4

The same loading was simulated for 20mm of HDPE 96 foam (Figure 5.22). The resulting pressure profile behind the foam deviates considerably from the experimental result because of the use of a non-rate dependent model, or possibly the choice of a plateau stress that was too high for the material model. In the material characterization tests [Nerenberg, 1998] it was observed that at extremely high strain rates, the plateau stress dropped rather than continuing to increase. This phenomenon was not investigated in great depth as a part of the work by Nerenberg, and was beyond the scope of the current study.

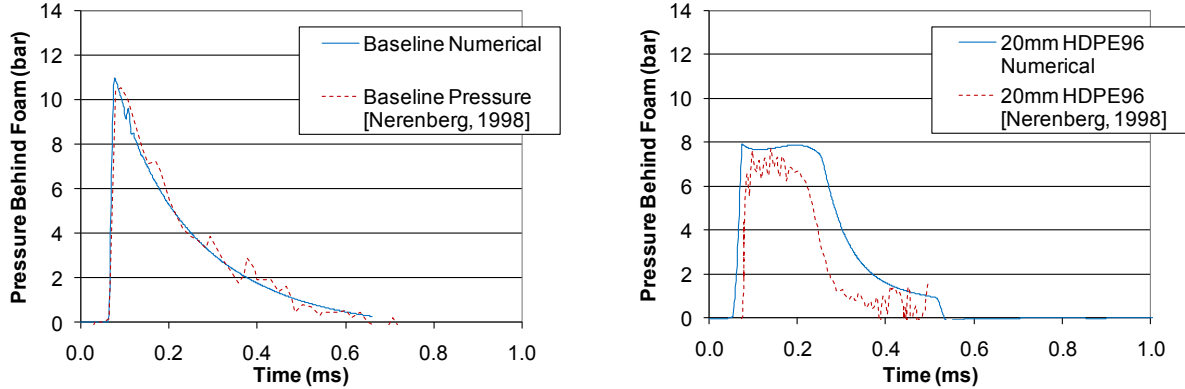


Figure 5.22 - Comparison of experimental results from [Nerenberg, 1998] and numerical results from the current study for: Baseline loading (left) and 20mm HDPE96 foam (right). Both loaded by 170g of C4 at 1m

Experiments were also carried out by Nerenberg where a 1.5mm thick high carbon steel plate was mounted in front of a 20mm LDPE45 foam sample in order to decouple the incident shock wave from the foam. This experiment was simulated as a part of the study. The peak pressure was well predicted, however the overall shape of the numerical result deviated from the experimental result due to the use of a non rate dependent model (Figure 5.23). The steel plate in front of the sample greatly reduced the velocity of the face of the foam loaded by the shock wave and prevented the formation of shock waves within the foam. The strain rate with the hard plate in front of the sample is below the regime where it can be assumed that the plateau stress is relatively constant. In spite of this shortcoming of the material model, the resulting pressure history was quite representative of the experimental result, albeit somewhat conservative during the loading phase.

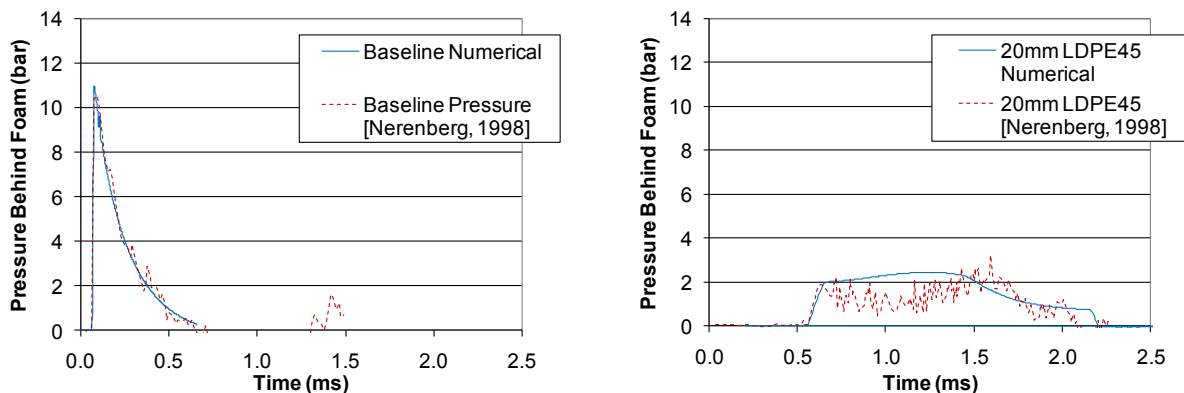


Figure 5.23 - Comparison of experimental results from [Nerenberg, 1998] and numerical results from the current study for: Baseline loading (left) and 20mm LDPE45 foam with 1.5mm steel plate (right). Both loaded by 170g of C4 at 1m.

Experiments with a larger charge of C4 (325g) at a stand-off of 1m undertaken by Nerenberg were also simulated. These were simulated in order to further validate the model and show it can predict the back-wall pressure behind a foam under varied loading.

20 and 40mm of LDPE45 foam loaded by 325g of C4 were simulated and compared to experimental results (Figure 5.24). The 20mm case matches very well to the experimental result, with the exception of some deviation in the “knee” of the pressure history, where the discontinuity was smeared for stability in the numerical case through use of a damping parameter. The 40mm simulation matched well with experimental results, except for delay in the arrival of the compaction wave.

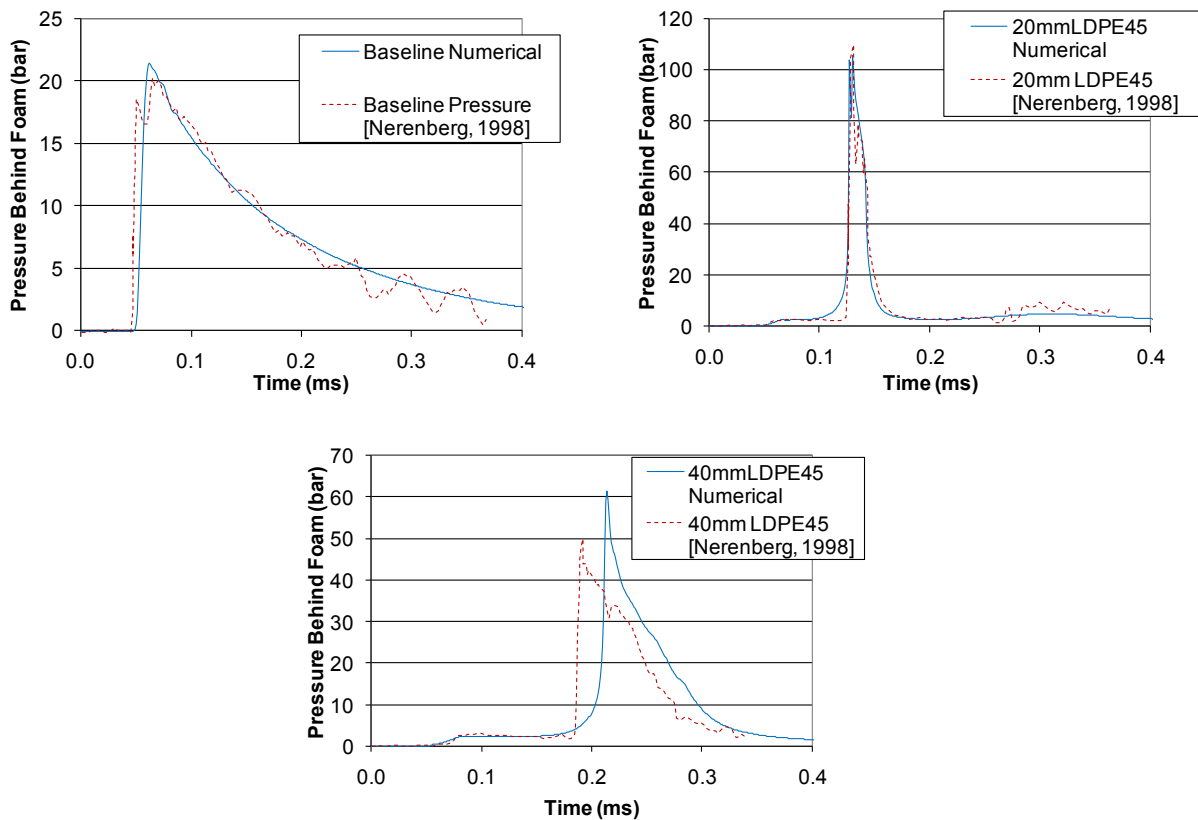


Figure 5.24 - Comparison of experimental results from [Nerenberg, 1998] and numerical results from the current study for: Baseline loading (top left), 20mm LDPE45 foam (top right), and 40mm LDPE45 (bottom). Both loaded by 325g of C4 at 1m.

Simulations of 20 and 60mm of HDPE96 foam loaded by 325g of C4 were also undertaken (Figure 5.25). The results matched well with experimental work by Nerenberg, though some deviation in the shape of the pressure pulse was observed, which was a result of deviation of the numerical model stress-strain behaviour from that shown experimentally by Nerenberg. It is likely that an empirically based stress-strain curve would have yielded more representative results.

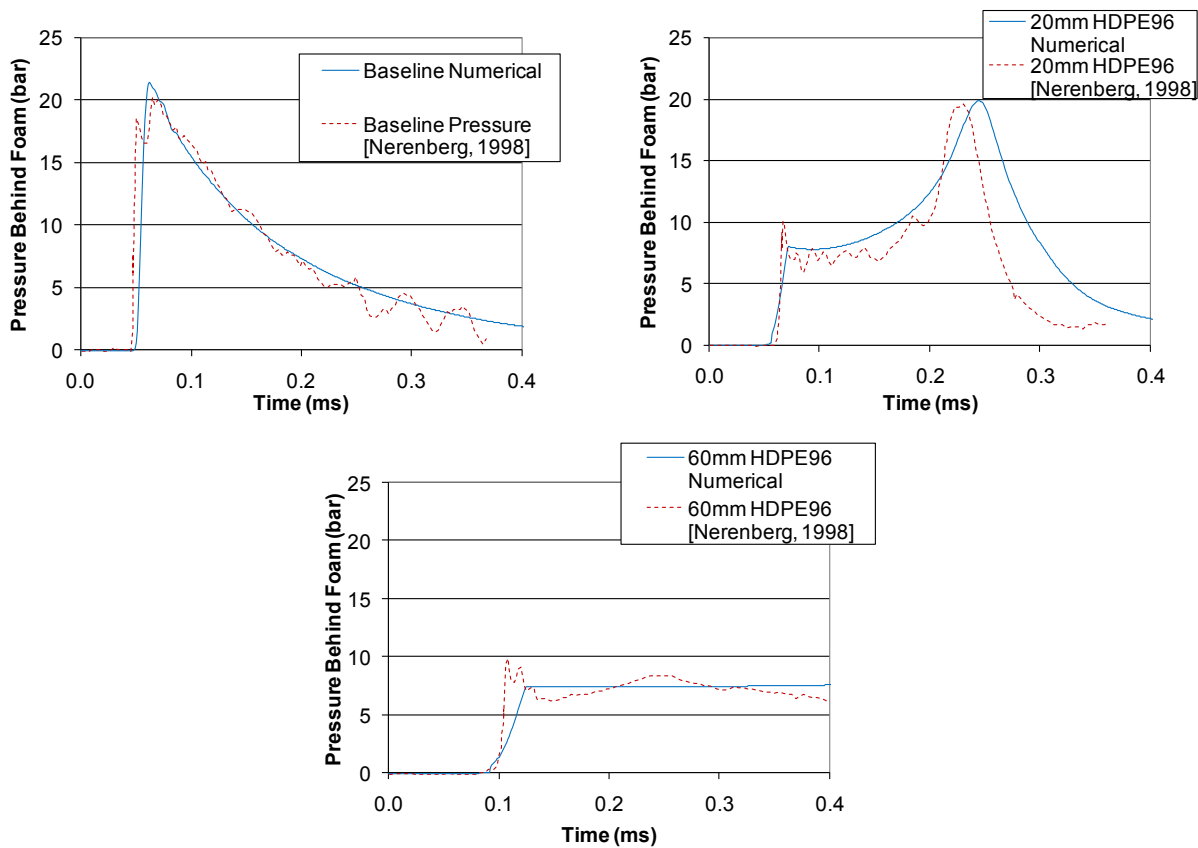


Figure 5.25 - Comparison of experimental results from [Nerenberg, 1998] and numerical results from the current study for: Baseline loading (top left), 20mm HDPE96 foam (top right), and 60mm HDPE96 foam (bottom). Both loaded by 325g of C4 at 1m.

Finally, a 325g charge was used to load a 20mm thick sample of LDPE45 foam with a 1.5mm high carbon steel plate mounted on the loaded surface of the foam. This experiment undertaken by Nerenberg was simulated in order to validate the model’s ability to capture this “decoupling” effect at higher loading. The results matched very well between experiment and numerical result (Figure 5.26) with the exception of the deviation due to the non rate dependence of the model (also observed for the same material combination loaded by 170g of C4).

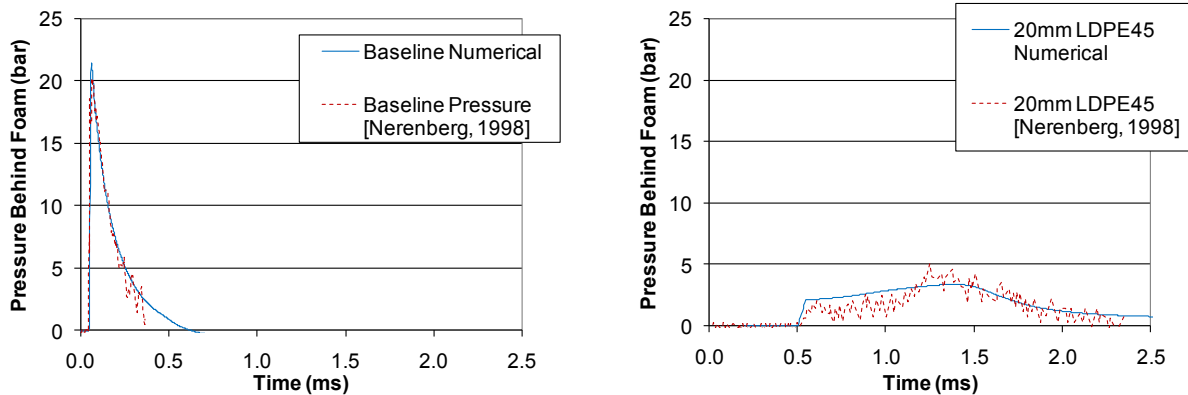


Figure 5.26 - Comparison of experimental results from [Nerenberg, 1998] and numerical results from the current study for: Baseline loading (left) and 20mm LDPE45 foam with 1.5mm steel plate (right). Both loaded by 325g of C4 at 1m.

5.4.2 Foam Coupled to High Density Material

Experiments by Ouellet [Ouellet, 2008] consisted of foam materials faced with hard plates. This study was similar to some of the experiments done in [Nerenberg, 1998], however Ouellet investigated the effect of the properties of the hard plate on the attenuation of blast by these concepts, while the foam thickness and loading was kept constant. The experiments of interest to this study involved the use of an LDPE45 open cell foam (note that the foam used by Nerenberg was closed cell).

Given the complexity of open cell foams, only closed cell foams were modeled. This posed a problem in that the data acquired in the study by Ouellet et al., used open cell foams. However, the experimental set up was such that the escape of air out of the front and sides of the foam would be minimized; this discrepancy remains a likely source of error however. In the case of the experimental set up from Ouellet [Ouellet, 2008] the gas contribution still exists, however the gas would have been contained within the volume defined by the high density material and steel wedges placed around the open cell foam sample (Figure 5.27). The closed cell foam model was still used, with the assumption that leakages from the experimental set up could be neglected.

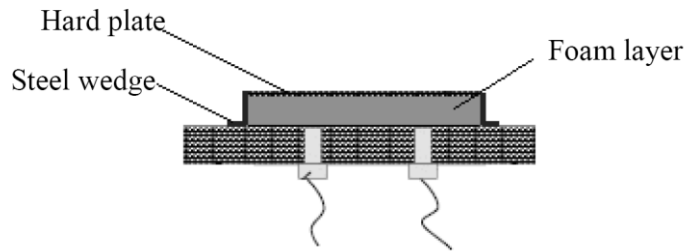


Figure 5.27 - Experimental set up for blast testing of foam decouplers [Ouellet, 2008]

The experimentally measured pressure, obtained from flush-mounted pressure transducers, is shown below for 250 grams of C4 detonated a distance of 1m from the experimental apparatus. A half inch of LDPE 45 foam was utilized in conjunction with a variety of hard plates, with the peak pressure beneath the foam being decreased with increasing plate mass (Figure 5.28).

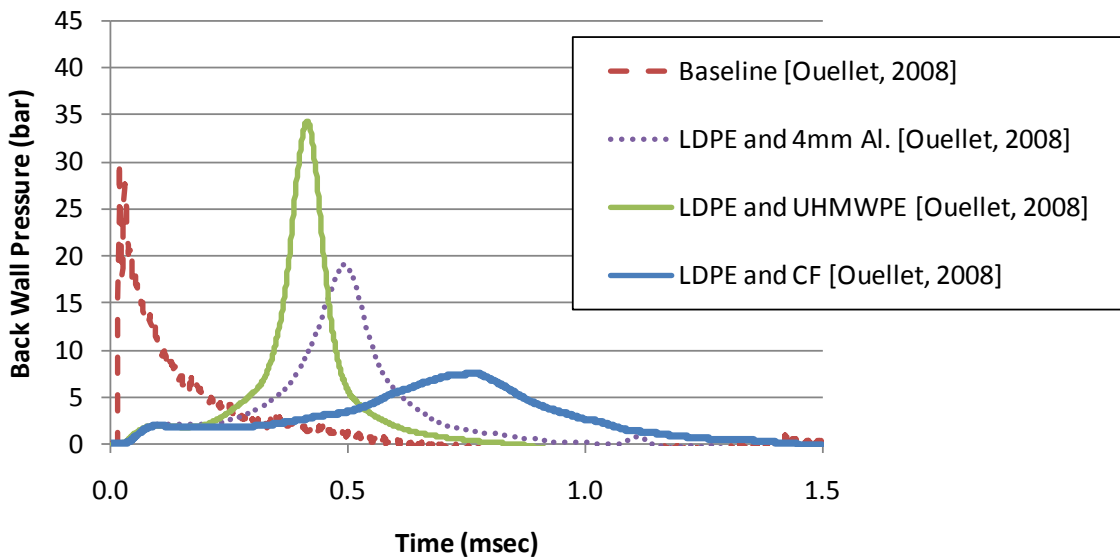


Figure 5.28 - Experimental data showing 12.7mm of LDPE45 foam with various high density materials mounted on the front face. Loaded by 250g of C4 at 1m distance. [Ouellet, 2008]

The experimental results were compared to numerical simulations of a foam of 13mm thickness (13 elements of 1mm size). The results compare very well in terms of peak pressure and general pressure history (Figure 5.29). The unloading behaviour of the numerical model does not seem to

show sufficient hysteresis in the simulation of 13mm of LDPE 45 foam with a carbon fibre plate of areal density 9.8 kg/m².

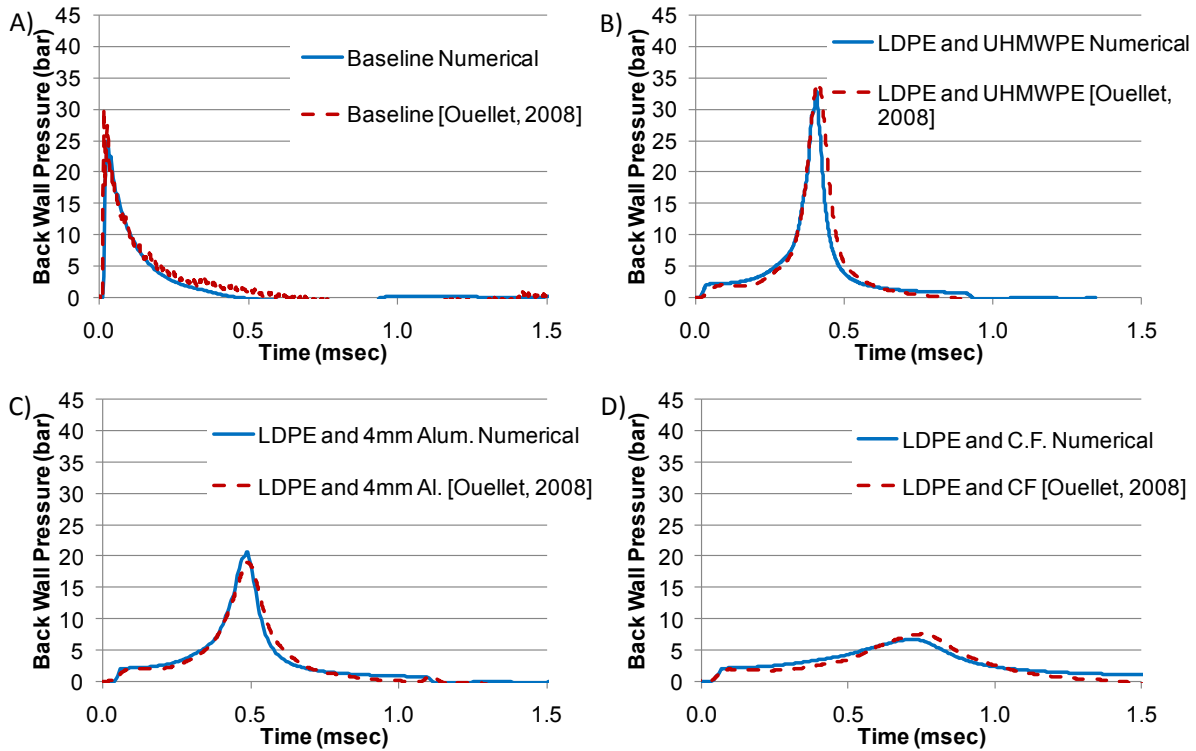


Figure 5.29 - Comparison of numerical results to experimental results [Ouellet, 2008] for A) Baseline loading (no protection), B) 12.7mm LDPE45 with 5mm UHMWPE plate, C) 12.7mm LDPE45 with 4mm aluminum plate, D) 12.7mm LDPE45 with carbon fibre plate

A comparison of the peak pressure values between experiment and numerical simulations is shown below in Table 5.3. Considering the fact that the same model was used in the simulation of experiments by both Ouellet and Nerenberg, the results are close. This is likely because the sides of the foam sample were blocked, which might minimize the error resulting from leakages.

Table 5.3 - Comparison of Experimental [Ouellet, 2008] and Numerical Peak Back Wall Pressures behind 13mm of LDPE 45 Foam Faced with Various Plates

Plate Type	Areal Density (kg/m ²)	Experimental Peak Pressure (bar) [Ouellet, 2008]	Numerical Peak Pressure (bar)	Percent Difference
UHMWPE	4.8	34.3	33.0	3.8%
4mm Aluminum	5.6	19.0	20.7	8.7%
Carbon Fiber	9.4	7.6	6.7	11.3%

Solutions for the Ultra High Molecular Weight Polyethylene (UHMWPE) case were also obtained with the elastic modulus of the UHMWPE being decreased and increased two orders of magnitude from the original value. No difference in pressure-time history at the back wall was observed.

A wave diagram for the case of the 12.7mm LDPE 45 and 4mm aluminum decoupler is shown in Figure 5.29 below. Note that the deformation is uniform throughout the thickness of the sample. The maximum velocity of the 4mm aluminum plate (and thus the foam front face) was calculated to be 34.7 m/s, below the compaction wave speed calculated as being 56 m/s. Note the blue line indicates the elastic precursor wave corresponding to the pre-buckling behaviour of the foam.

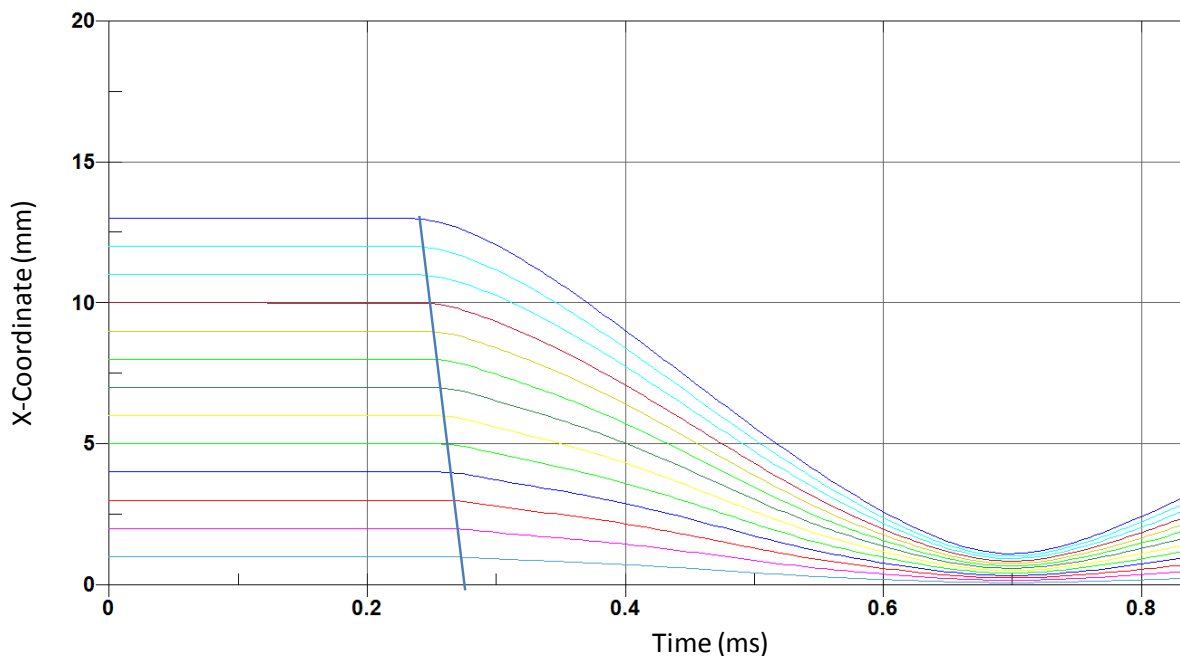


Figure 5.30 - Wave diagram for a 4mm Aluminum and 12.7mm LDPE 45 sample Loaded by 250g C4 at 1m

5.5 Foam Parametric Study with Finite Element Model

A parametric study was undertaken to gain further understanding into the effect of the various parameters on blast amplification or attenuation. The validation study already contained a study of the effect of high density plate mass. Additional parameters that were varied for this study were: foam thickness, foam stress-strain behaviour (through foam density) and blast loading.

The plate areal densities were consistent with those used in the experimental study and for validating this model [Ouellet, 2008]. Additionally, in some cases plates of higher areal density (15 and 20 kg/m²) were modelled. These areal densities approach those of hard ballistic plates used for protection against projectile threats at time of writing. The blast loading used in the validation study was carried over to the parametric study. The LDPE 45 foam used in the previous validation study was used. Additionally, a higher density HDPE 96 foam was simulated. These variations were meant to show the effect of foam plateau stress and densification on results. The thickness of foam of 12.7mm (1/2 in.) was used in this parametric study. Additionally, 25mm and 7mm thick foams were simulated.

In total this yields 28 test cases which were simulated and analysed. The study provides insights into the attenuation of blast by fabrics. This understanding can be used to predict the effect of further changes to the various parameters.

5.5.1 Effect of Plate Mass

For all cases examined, an increase in plate mass resulted in a decrease in the peak transmitted pressure. This is consistent with results from Ouellet, against which a part of the model validation was conducted in the previous section. A sample of results from the HDPE 96 simulations with a thickness of 13mm is shown below in Figure 5.31.

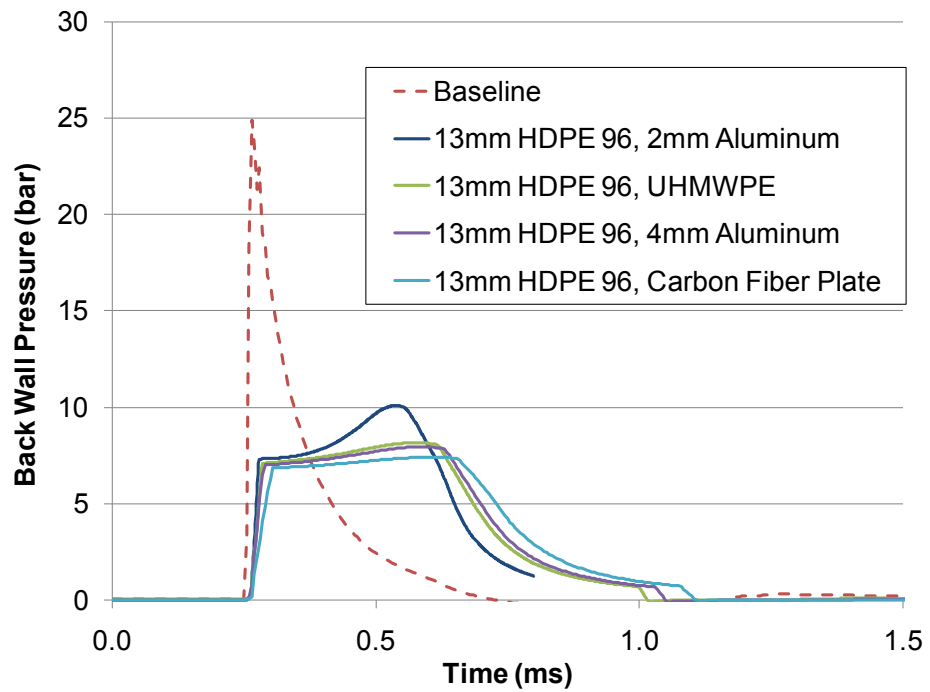


Figure 5.31 - 13mm of HDPE 96 foam faced with plates of varied areal density

A sample of results from LDPE 45 simulations with a thickness of 25mm are shown in Figure 5.32. Note that for the simulation with 2mm of Aluminum (AD: 2.8kg/m² based on mass from [Ouellet, 2008]) the wave within the foam reflects back and forth between the aluminum plate and back wall.

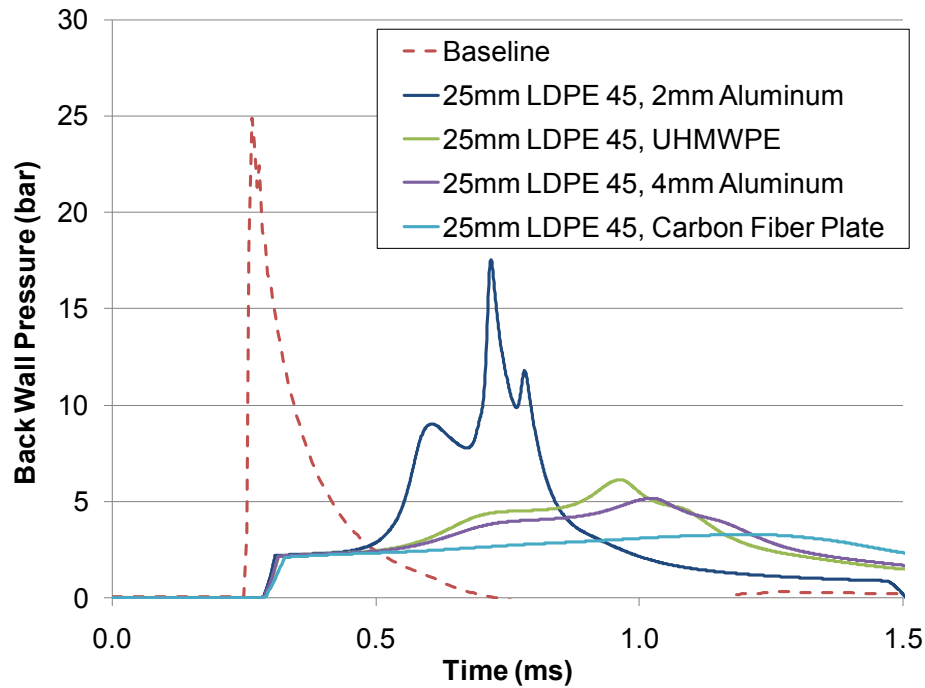


Figure 5.32 - 25mm of LDPE 45 foam faced with plates of varied areal density

5.5.2 Effect of Foam Thickness

The effect of foam thickness (without high density plate) was investigated by [Nerenberg, 1998]. The parametric study undertaken as a part of the current research allowed an investigation into the effect of foam thickness on pressure wave attenuation/amplification when a high density plate was included. The effect of increased thickness is as expected, with an increase in thickness causing a reduction in peak pressure. A sample of results of various thicknesses of HDPE 96 with a 4mm aluminum plate is shown in Figure 5.33, and results from various thicknesses of LDPE 45 with a 4mm aluminum plate are shown in Figure 5.34.

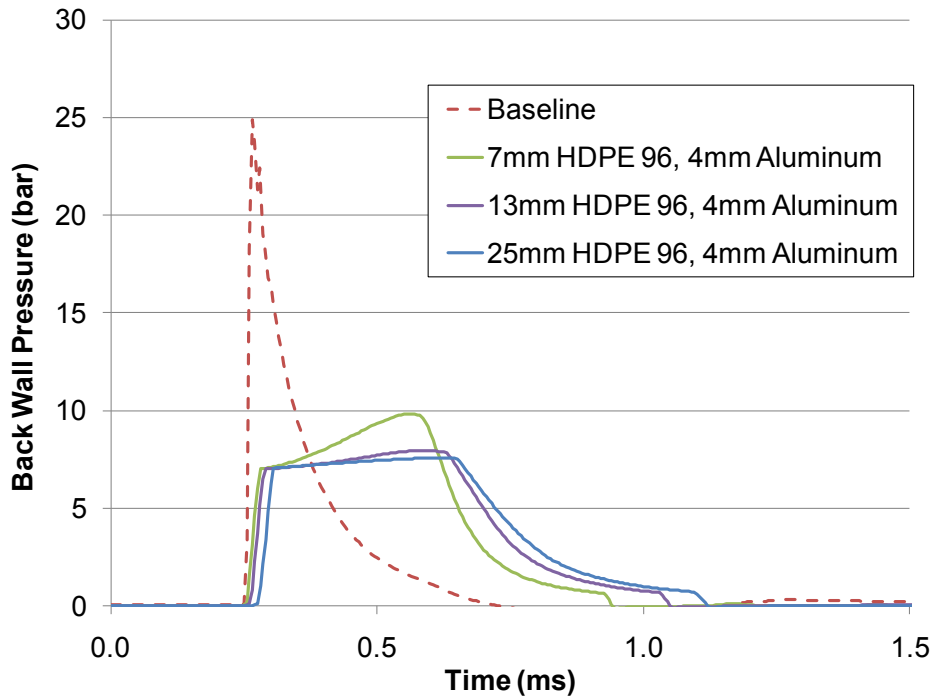


Figure 5.33 - Varied thicknesses of HDPE 96 foam faced with 4mm of aluminum ($AD = 5.6\text{kg/m}^2$)

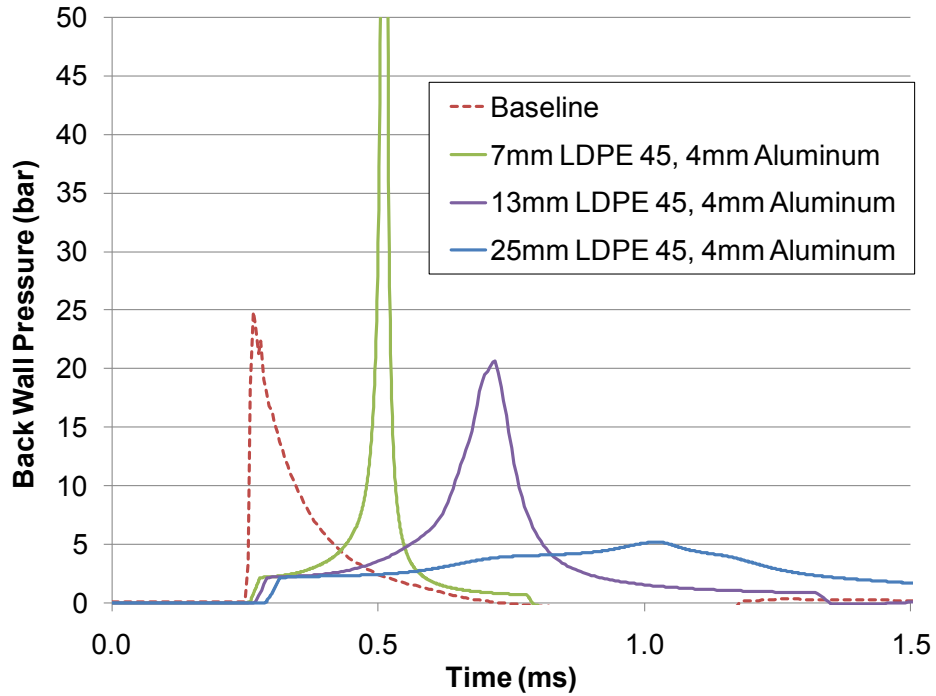


Figure 5.34 - Varied thicknesses of LDPE 45 foam faced with 4mm of aluminum ($AD = 5.6\text{kg/m}^2$)

The peak pressure results from both LDPE 45 (Figure 5.35) and HDPE 96 (Figure 5.35) simulations were plotted against areal density for the various thicknesses simulated. It can be seen that it was possible to produce attenuation of the peak pressure for any thickness of foam by selecting an appropriate areal density for the plate mounted to the foam. As the thickness was reduced, the areal density of the plate had to be increased to produce attenuation.

Note that despite being what would be referred to as a "decoupling" arrangement, the low thickness foams with lower areal density plates are fully capable of amplifying blast loads.

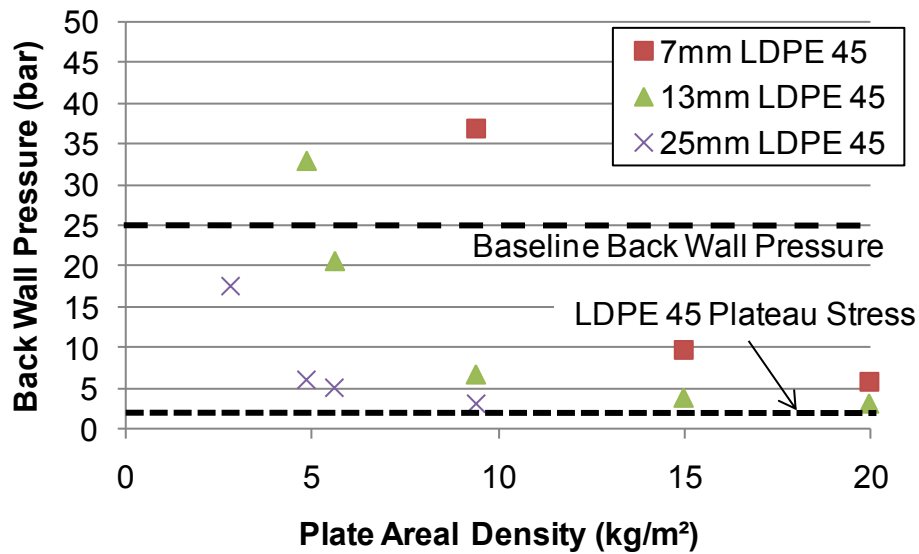


Figure 5.35 - Peak back wall pressure vs. plate areal density for various thicknesses of LDPE 45

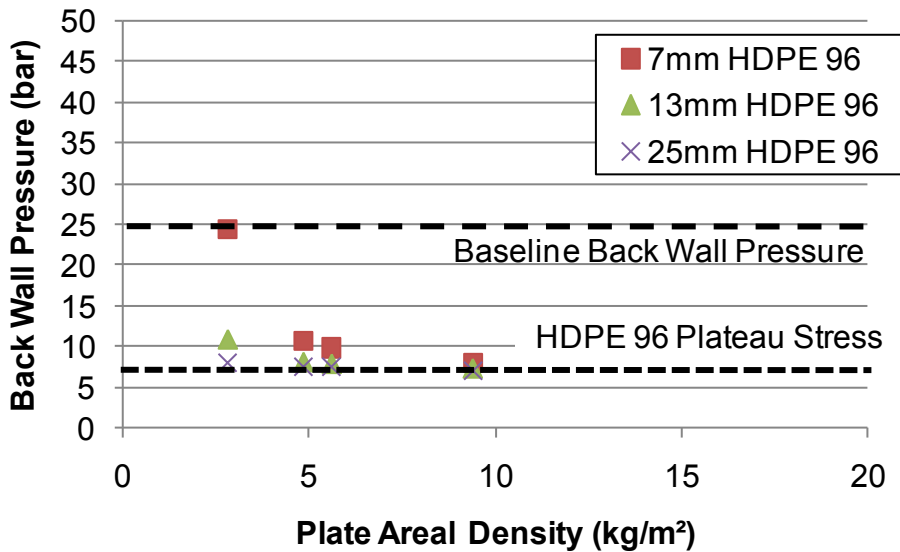


Figure 5.36 - Peak back wall pressure Vs. plate areal density for various thicknesses of HDPE 96

It was observed both in experiments and numerical simulations that higher density foams have a greater ability to manage energy. This is due to the higher plateau stress of the higher density foam. The disadvantage of high-density foams is that the minimum attainable stress/pressure is limited by the plateau stress (unless the energy imparted to the foam is insufficient to cause buckling of the solid cell phase), so although they can store more energy before reaching densification, they are not necessarily the best choice for blast protection. Ideally the foam selected would have a plateau stress which is below the human threshold for injury at long durations.

5.6 Foam Implementation with the Modified Axelsson Model To Investigate Injury

For foam with a high density material on the front, the mass of the high density material is treated as a lump mass, and the mass of the foam is split and added to the high density material mass and the back wall (however since the back wall remains stationary this mass does not appear in the equations defining the system). The system is shown in Figure 5.37 below.

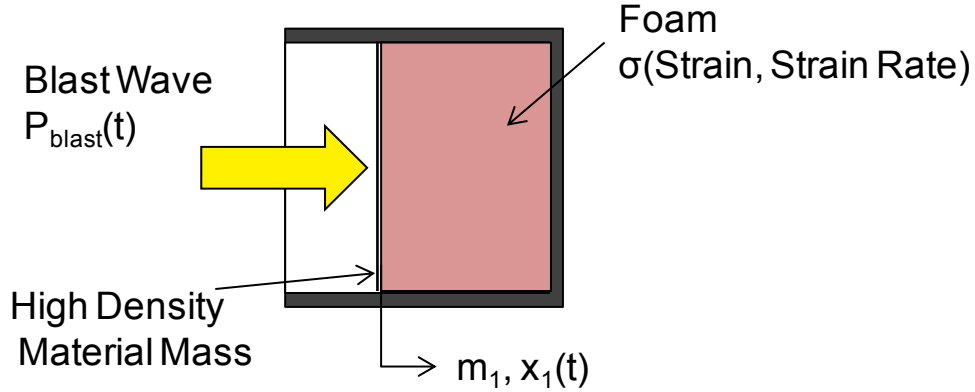


Figure 5.37 - Foam and high density material model diagram

The behaviour of foams is complicated, but has been characterized in and previously discussed in this chapter.

$$m\ddot{x}_1 = P_{blast}(t) - \sigma(e, \dot{e}) \quad (5.16)$$

$$e = x_1/x_0 \quad (5.17)$$

$$\dot{e} = \dot{x}_1/x_0 \quad (5.18)$$

The effect of strain rate was initially considered as had been done with the finite element model, however, as with the finite element model, not enough information on the high rate/high strain behaviour of foams was available to justify using a rate dependent model. Ultimately, the same behaviour as described in Section 5.3.3 was implemented in the mathematical model. Unloading was not implemented. The implementation of an unloading behaviour should not affect the peak pressure result, due to the assumption of uniform deformation through the thickness of the foam. If the deformation is uniform, unloading does not occur until the peak pressure value is reached. As has been discussed previously, the assumption of uniform deformation throughout the foam is only valid if the foam face is compressed at a velocity below the compaction wave speed of the material.

5.6.1 Validation of Foam Mathematical Model

The mathematical model of foam with a hard plate was validated against data from Ouellet [Ouellet, 2008]. This data was also used in evaluating the 1D finite element model. A prescribed load was applied based on results from the experimental work by Ouellet. The results are shown below in Figure 5.38, and indicate a good fit to experimental results. The same limitations of the finite element model apply to the mathematical model, namely the inability for the mathematical model to account for leakage of the air out of the open cell foam.

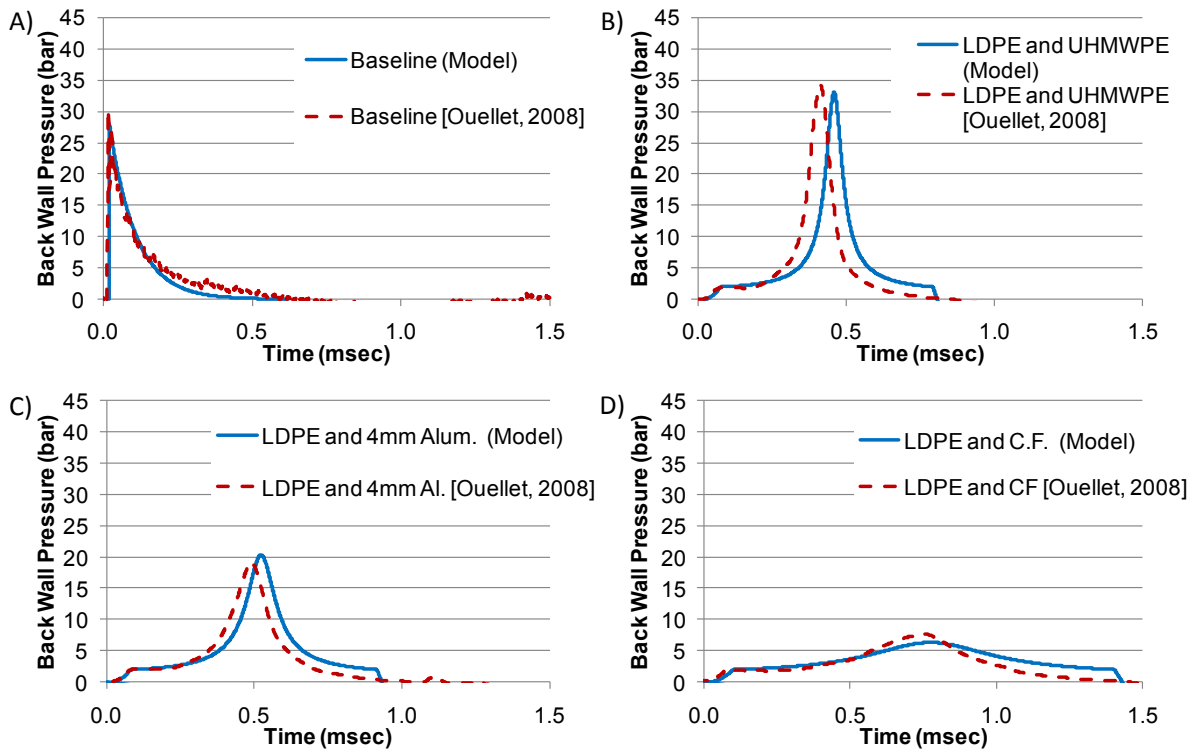


Figure 5.38 - Validation against experimental data [Ouellette, 2008] for 1D model of foam with high density materials with an A.D. of: A) Loading; B) 4.8 kg/m²; C) 5.6 kg/m²; D) 9.5 kg/m²;

The success in reproducing experimental results with the mathematical model helped confirm that it could be a useful tool in the estimation of pressure modification by protection concepts. It should be noted that all of the velocities calculated were below the compaction wave speed of 56 m/s, thus the assumption of uniform deformation was appropriate.

Due to the simplicity of the mathematical model, there are some limitations. Since the foam and air are treated as a single “element”, it is assumed that velocity, displacement and acceleration change linearly through the thickness of the material, and mass is distributed evenly through the thickness of the material, meaning wave effects or other discontinuities were not accounted for. This model assumes that the blast wave is planar, and the torso and protection are semi-infinite. The significance of the assumption of an infinite plane is that edge effects (such as leakages of air from the foam) were not accounted for. In spite of these limitations, it will be shown that there were valuable (and accurate) results produced from these models.

5.6.2 Evaluation of the Differences in Behaviour Between Shock Tube and Blast Loading

It was observed when examining the simple mathematical models used in this work, that when the impulse per unit area of the original, unprotected, back wall pressure time history was compared to the impulse seen when protection was present, an intersect occurs, which coincided with the maximum deflection of the front face of the protective concept, and thus the maximum compressive strain.

Figure 5.39 below shows the pressure and integral of pressure versus time for both the applied blast load as well as the predicted back wall pressure for 12.7mm of LDPE 45 foam with a 4.8 kg/m² plate on the loaded face. The two pressures histories shown below (Figure 5.39A) were acting on the plate in opposite directions, thus when their integrals (Figure 5.39B) were equal, a maxima in displacement had been reached.

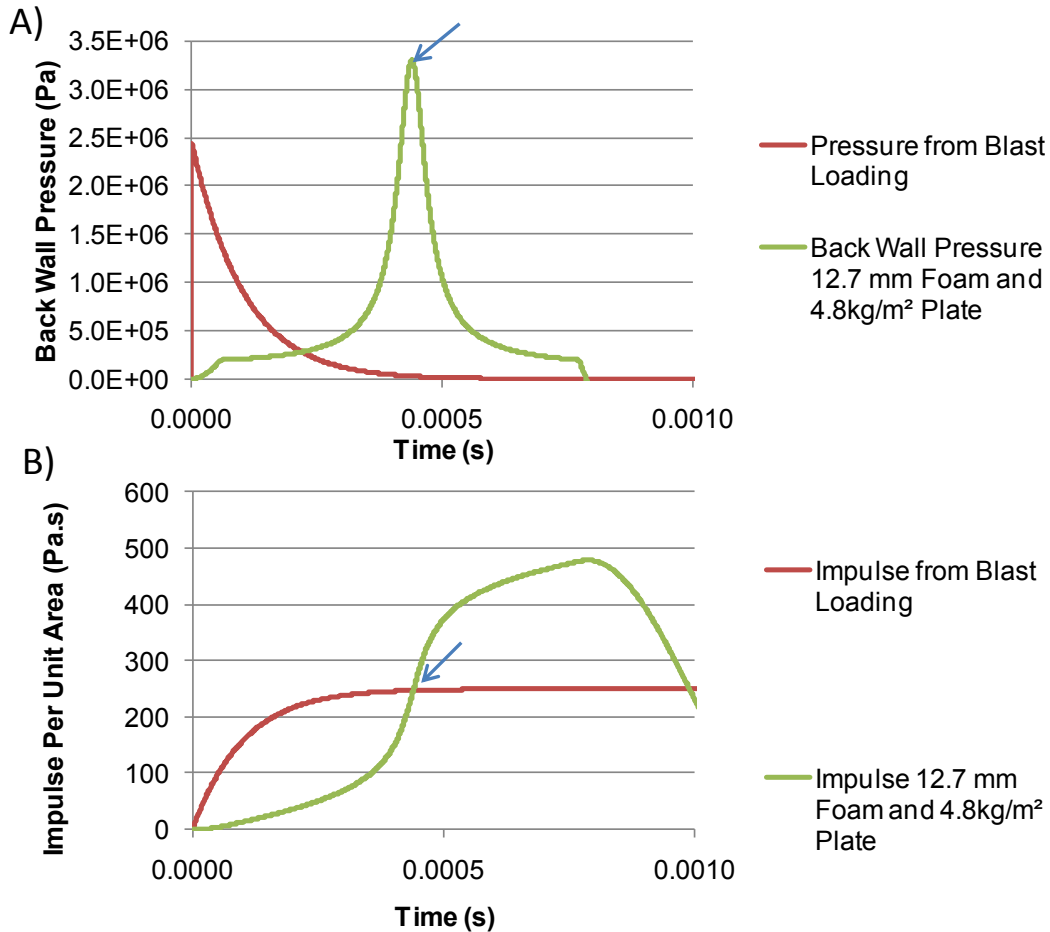


Figure 5.39 - Pressure and integral of pressure (impulse per unit area) for 12.7mm LDPE 45 foam faced with a 4.8kg/m² plate; loaded by 250g C4 at 1m

Examining the integral of blast pressure over time, it can be seen that at times above the blast duration, the impulse no longer increases. This is significant, because if the peak pressure/protection deformation occurs at this time or later, the contribution to the total impulse from blast loading does not change. By increasing the thickness or mass in front of the protection concept, the time to peak pressure could be increased, but as shown in Figure 5.39B, the impulse per unit area from blast loading will not change, thus, the integral of pressure/stress over time must be the same within the protection concept. Because this integration is taking place over a greater time, the pressure or stress within the protection will not be as high. In order to increase the time to peak

pressure, the thickness of the soft material can be increased (or the size of the air gap can be increased in the case of fabric with an air gap). Another alternative would be to increase the areal density of any high density materials used in the protection. The effect of doubling the high density material or material thickness under blast loading is shown in Figure 5.40 below.

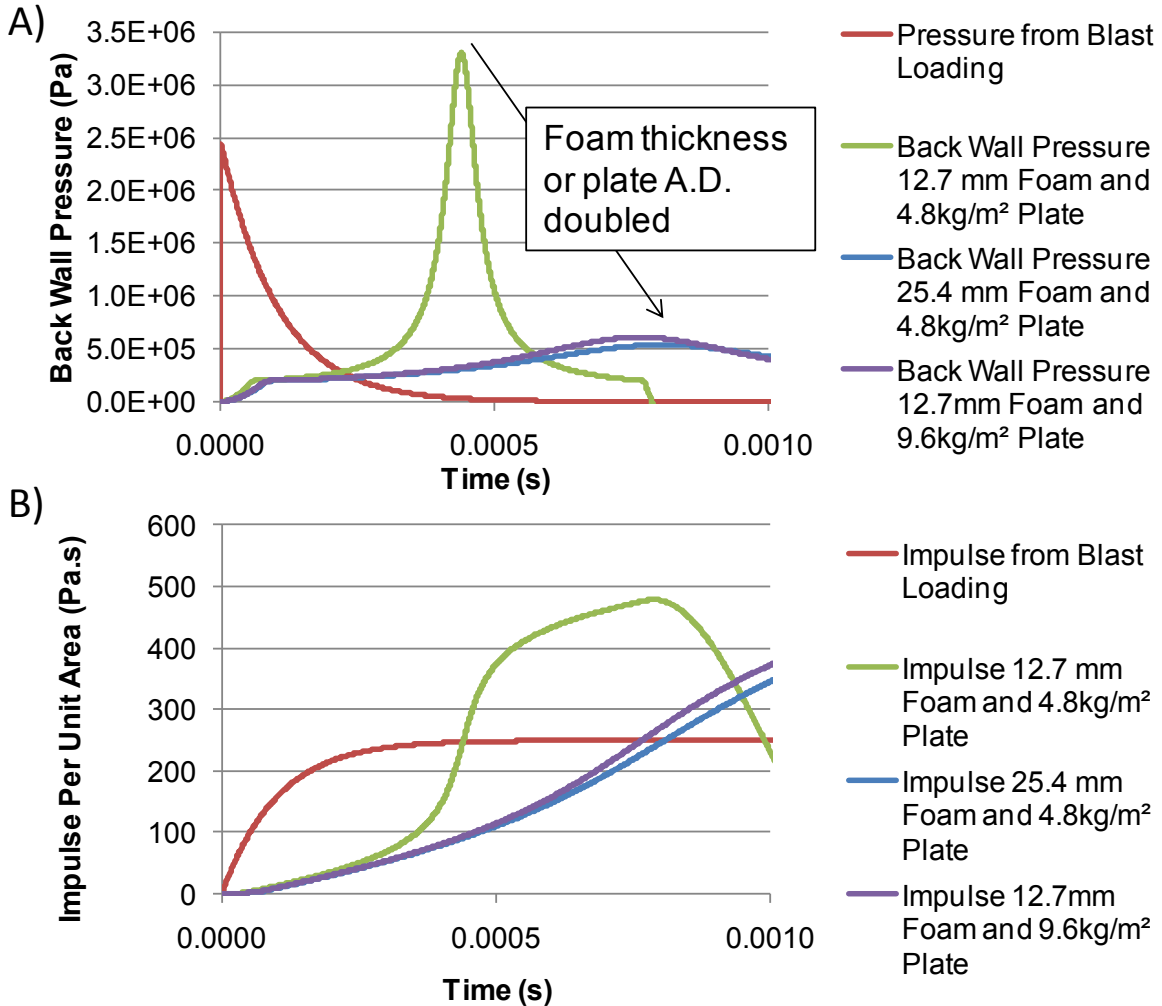


Figure 5.40 - Effect of increasing foam thickness or plate areal density on pressure and integral of pressure (impulse per unit area) for 12.7mm LDPE 45 foam faced with a 4.8kg/m² plate; loaded by 250g C4 at 1m

For shock tube loading, the behaviour of impulse was different. Since the applied shock loading was a step increase in pressure, its integral, the impulse per unit area, increased linearly with time.

This meant that as the time to peak pressure behind the protection increased, more impulse was being applied (in fact the increase in impulse was proportional to increase in the time to peak back wall pressure). This explains how for increased thickness, under shock tube loading, the peak pressure would plateau (Figure 5.41A). The time to peak was increased by the same methods described previously for blast loading.

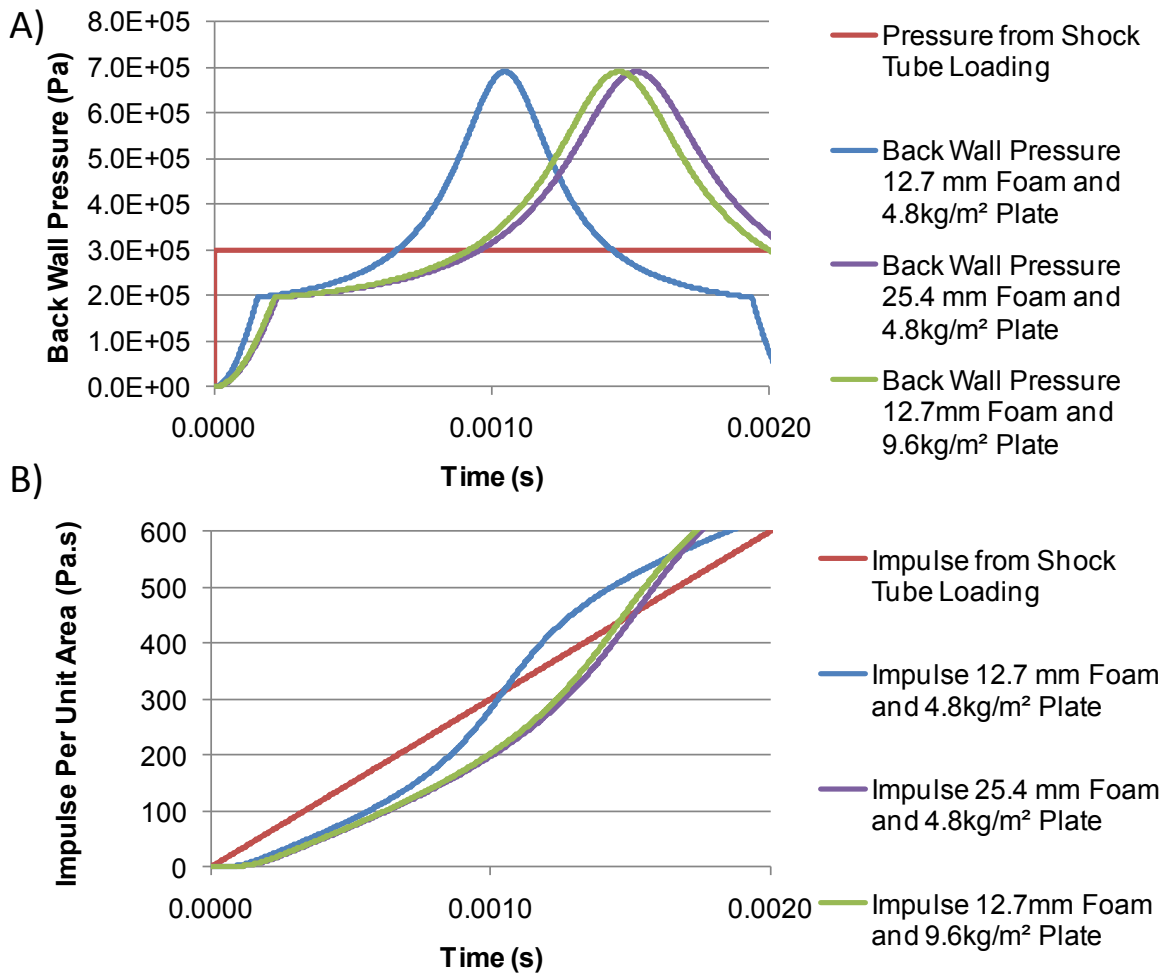


Figure 5.41 - Effect of increasing foam thickness or plate areal density on pressure and integral of pressure (impulse per unit area) for 12.7mm LDPE 45 foam faced with a 4.8kg/m² plate; loaded by a 3 bar pulse wave.

While the above discussion explains the effect of increased thickness or mass in front of a protective concept, the results could not be used to predict through analytical, back of the envelope,

calculations, the qualitative effect of these changes. The mathematical model used in this work, which determines the pressure history underneath a protective concept through numerical integration, was likely the simplest form of analysis that could be used to estimate the effect of protection. Relations proposed by Gibson [Gibson, 1988] could have potentially been used, except they both required estimates of the “time to peak”, and energy to be absorbed; the energy to be absorbed could have been taken as the reflected blast impulse, but the time to peak depends on both the loading and the material mechanical behaviour.

5.6.3 Foam and Axelsson Model LD50 Predictions

By coupling the foam and high density material described in the Section 5.6.2 with the modified Axelsson model described in Section 4.1, a tool was developed which could help predict the threshold between amplification and attenuation.

A diagram of the model is displayed below in Figure 5.42.

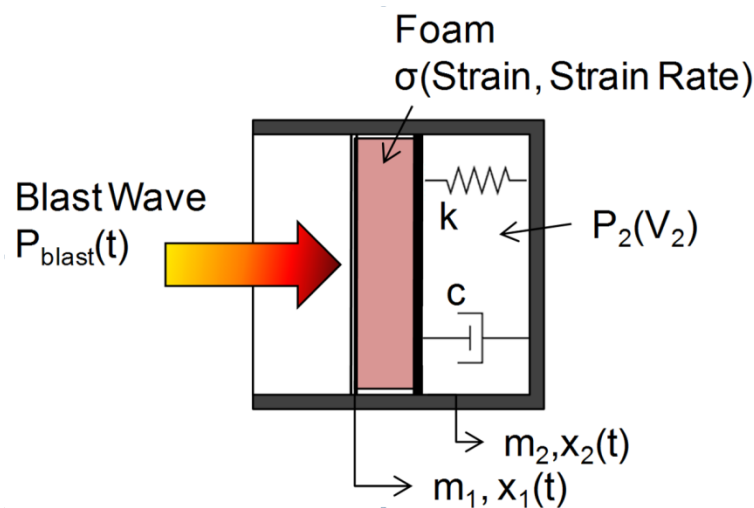


Figure 5.42 - Foam model combined with Axelsson torso model

The approach taken for examining the foam and hard plate concepts was to maintain the same thickness of the foam sample, and increase the mass of the hard plate. The plate mass was changed

such that results ranged from a predicted amplification of peak pressure and injury, to an attenuation of these values. The predicted chest wall kinematics were used as the metrics for injury prediction, using chest wall velocity (as suggested in the original work by Axelsson [Axelsson, 1996]) as well as chest wall acceleration, which has been found to be a metric of value when investigating protection concepts [Ouellet, 2008 ; Cooper, 1996].

The loading applied was equivalent to LD50 loading from [Bass, 2006], with a duration of 2ms and peak reflected overpressure of 18.8 bar. The curve was compared to that obtained from ALE calculations to ensure consistency of loading between the mathematical model and the finite element of the torso.

A summary of the cases examined and results is given in Table 5.4 below.

Table 5.4 - Summary of Modified Axelsson Model Results for Foams

Loading	Protection	Plate AD (kg/m ²)	Peak Pressure Behind Protection (bar)	Chest Max Inward Velocity (m/s)	Chest Peak Acceleration (m/s/s)
LD50 T2	None	-	18.8	21.3	7.67E+04
LD50 T2	30mm LDPE45 and Plate	7.5	130	30.9	5.06E+05
LD50 T2	30mm LDPE45 and Plate	15	11.9	23.3	3.97E+04
LD50 T2	30mm LDPE45 and Plate	30	3.20	12.2	1.14E+04
			Baseline	Amplified	Attenuated

Based on the results above, it was expected that finite element simulations of the foam with the 7.5 kg/m² plate would amplify blast, and the case with the 30 kg/m² plate would attenuate the injury. The 15 kg/m² case could result in either amplification or attenuation, depending on the metric which best represents the response. It will be shown that a slight attenuation was predicted for the 15 kg/m² case with the finite element torso.

5.7 Foam Implementation with Torso Model

While material property effects were investigated as a part of 1D model analysis, the effect of protection geometry could not be examined as a part of 1D studies, and is only briefly examined as a part of this research. In general, a flat plate struck by a planar wave would yield conservative results, while a convex plate would result in some deflection of the blast loading and reduced injury. While the material models were kept the same when implemented with the torso model, the geometries had to be altered to accommodate the 2D nature of the torso model (Figure 5.43).

Based on results from the mathematical model developed as a part of this study, a 30 mm thick plate of LDPE 45 foam was simulated with varied areal densities of rigid plates mounted on the front surface as a “decoupler”. The thickness of the rigid plate was maintained as 10mm for all simulations. The densities were selected to show a transition from injury amplification to attenuation, as predicted in the previous section. The areal densities of rigid plate simulated were 30kg/m², 15kg/m² and 7.5 kg/m². Densities were varied by reducing the material density, while maintaining the same geometry and young’s modulus.

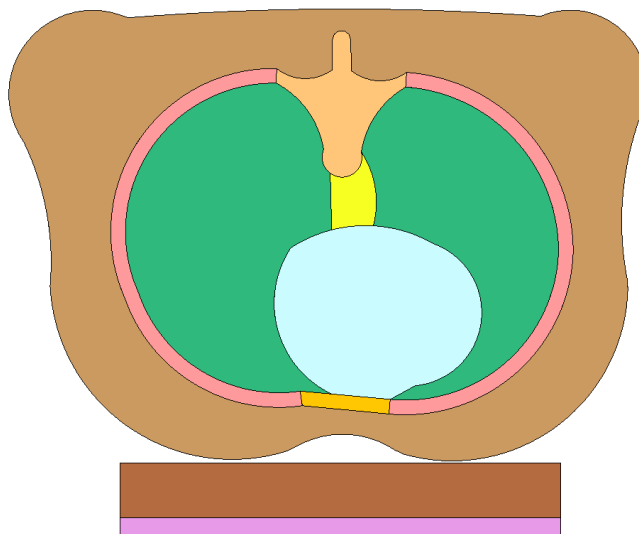


Figure 5.43 - Torso model with 30mm of foam and 10mm hard plate protection

Contact was implemented utilizing a penalty stiffness formulation very similar to the Lagrangian/Eularian coupling of an ALE algorithm, where a force proportional to nodal penetration is applied to the node penetrating node and penetrated surface. It was noted that when

the ALE implementation was used some “sticking” of the protection concept to the torso was observed in tension (during unloading the protection would fail to release from the torso). This was attributed to both the torso and protection being coupled to the same ALE mesh. The responsibility of the ALE coupling for this phenomenon was investigated by both: comparing the same run using both ALE and CONWEP (prescribed loading) implementations, as well disabling the ALE coupling prior to unloading. Both of these methods allowed the release of the protection concept after unloading, suggesting the problem was ALE related.

In all cases, unless otherwise specified, the protection was modelled as a flat plate with a width of 24 cm.

5.7.1 Finite Element Torso Model Predicted Injury with Foam Protection

As was expected based on mathematical model results, the various areal densities of hard plates used in the study show a transition from amplification of lung injury, as predicted by peak dynamic pressure, to a reduction of predicted lung injury.

The metric used for estimating injury from the torso model was percent lung volume above a threshold pressure. Four threshold pressures were defined as: 60 kPa, 100 kPa, 140 kPa and 240 kPa. The results are presented using both bar graphs and a visual topology of the 2D lung. These methods provided information in a way which could be easily compared to the baseline result (loading of the model without protection).

The baselines results for LD50 loading (2ms duration, 4.27 bar peak incident pressure, 18.8 bar peak reflected pressure) are shown along with the foam protection simulations results below in Figure 5.44.

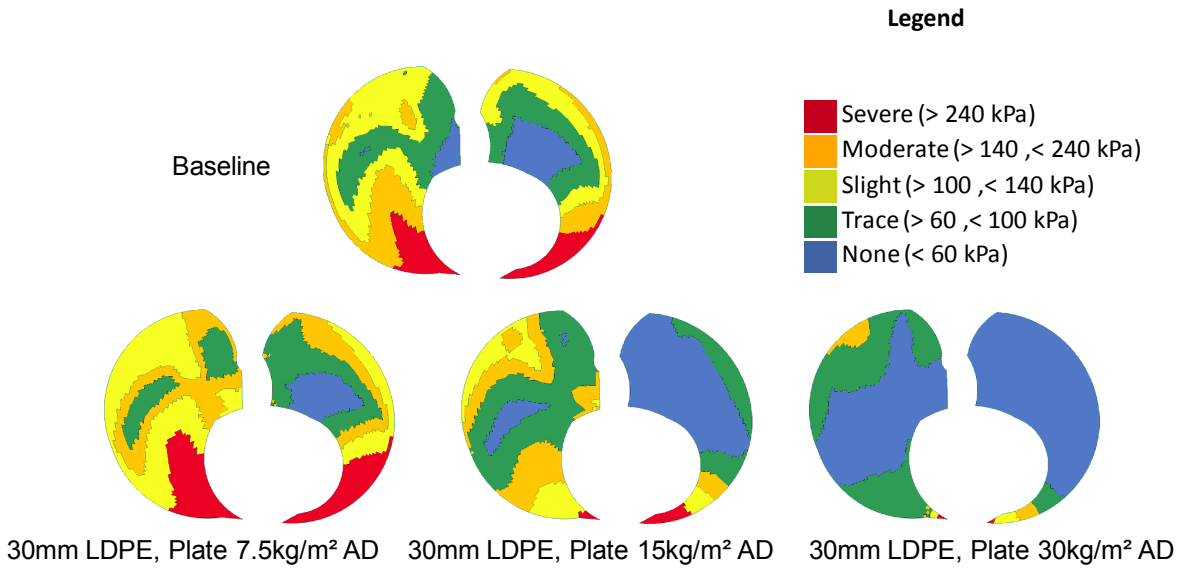


Figure 5.44 - Predicted lung injury results from the finite element torso model with various foam and high impedance material protection concepts.

The above results are summarized below in Figure 5.45, where the percentage volume of lung elements which had a peak pressure above 240 kPa is compared between cases.

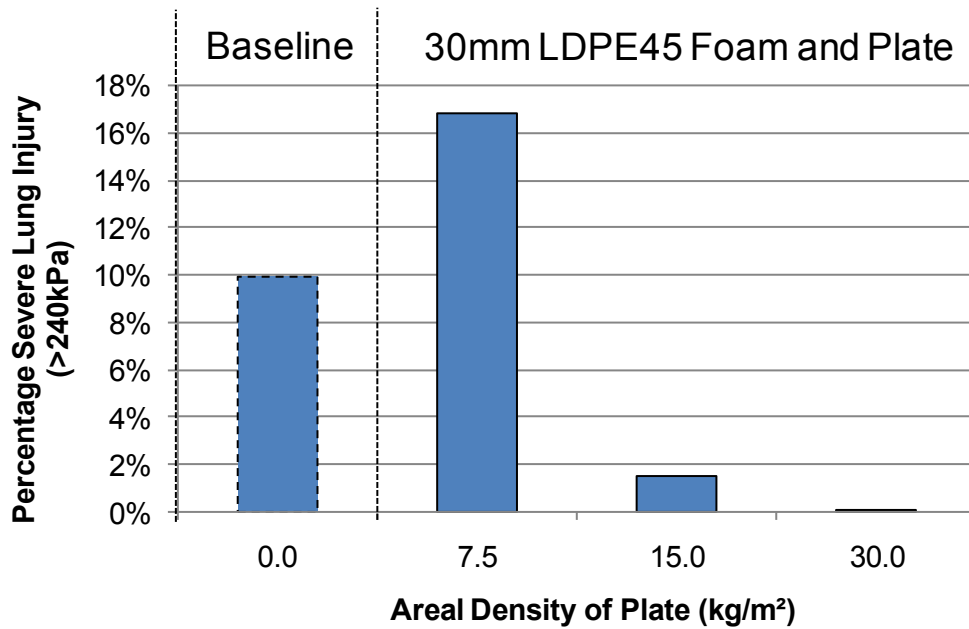


Figure 5.45 - Percentage severe lung injury for foam protection concepts

The injury was significantly attenuated by the 30kg/m² plate and 30mm of LDPE 45 foam (from 10% severe injury to 0.1%). Interestingly, the 7.5 kg/m² plate and 30mm of foam actually resulted in a fairly significant amplification of injury, predicting an increase from 10% severely injured lung without the protection, to 16% with the foam and 7.5kg/m² plate.

5.8 Discussion of Foam Results

The implementation of the 1D finite element models of foams and foams with hard plates was validated against experiments by [Ouellet, 2008] and [Nerenberg 2006]. In most cases the predicted results matched very well with experimental results, despite the fact that in some cases a closed cell foam model was used to predict results from cases where a open celled foam was used.

The results from simulations illustrate the importance of proper selection of both damping and unloading behaviour for simulation of limited duration blast loads. The foam behind the shock wave would undergo unloading before the wave had reached the back wall. The importance of unloading and damping was reduced when a high impedance material was added, because the material began to deform uniformly through thickness.

A parametric study was conducted to illustrate the effects of varied plate areal densities mounted to foams of varied thicknesses. For the range of thicknesses tested, an increase in foam thickness always yielded a reduction in peak pressure. Likewise, an increase in plate areal density always resulted in a reduction in peak pressure. The effect of the plate mass is a reduction in the rate of deformation of the foam under blast loading due to the added inertia at face of the foam loaded by the blast wave.

The results show that a protective concept cannot be evaluated based only on the simple impedance mismatch analysis described in section 2.2.1. The motion of the high impedance material and subsequent deformation of a foam can result in an increase in peak pressure compared to the applied blast loading.

The assumption of uniform deformation of the foam allowed the use of a simplified mathematical model for predicting the behaviour of foam materials coupled to high impedance materials. The model was validated against data from [Ouellet, 2008]. The results matched experiments very well, except that the arrival time of the peak pressure was delayed compared to experiments (even compared to the 1D finite element models).

The mathematical model for a foam was implemented with the modified Axelsson model developed as a part of this study. The finite element model of the torso was also used with a foam protection model added. The modified Axelsson model, when peak chest wall acceleration was used as a metric for injury, predicted amplification and attenuation of injury in the same instances as the finite element torso model. While the modified Axelsson model, as used in this study, does not offer any prediction of the level of injury (only change relative to a baseline case), the finite element model estimated the severity and location of lung injury.

Unfortunately, the prediction of injury through use of the torso model could not be directly validated, as no controlled experiments of humans subjected to blast loading with foam protection were available. The torso model itself was validated as a part of work by Greer [2006], and the foam protection models were validated as a part of the current study.

Chapter 6

Single Layer Fabrics and their Behaviour in Blast

Single layer fabrics are commonly used in apparel, and represent a simple case for protection. While no protection concept against blast consists exclusively of single layer fabrics, almost all of these concepts will have areas where fabric or plate ballistic protection is not present, leaving only thin layers of fabric, which when struck by a blast wave may alter the loading to the torso.

6.1 Single Layer Fabric Properties

The structure of fabrics is complex, and through-thickness material properties are often not well established, due the difficulty in measuring them (particularly, determining the actual applied strain). Transverse loading of a single fibre of Kevlar fabric was undertaken in one study [Cheng, 2005] however the use of this data to determine the transverse properties of a woven fabric would require modelling of a fabric at the fibre level and be a task outside of the scope of this project. As will be shown later, the through thickness properties probably do not have a significant influence on the alteration of blast loading, as this is primarily a result of the compression of air between the fabric and reflecting back-wall, and shock wave reflections between these surfaces.

The structure of fabrics, shown in Figure 6.1, results in them having holes through which air can flow, resulting in permeability. The permeability of the fabric will depend on what type of weave is used, the tightness of the weave, and the yarn geometry.

Another property of fabrics is their areal density. This is the density of the fabric per unit area. This value is commonly used instead of density because of the difficulty in determining the thickness of fabrics.

In-plane properties of fabrics have been investigated, particularly for those used in ballistic protection. This is because the in-plane properties of these fabrics are extremely important in terms of their ability to mitigate ballistic threats [Yang, 1992]. For the cases that have been evaluated experimentally, and those that will be studied numerically, these properties are not considered to be significant, as most of the loading is uniform, and out of plane (transverse, Figure 6.1).

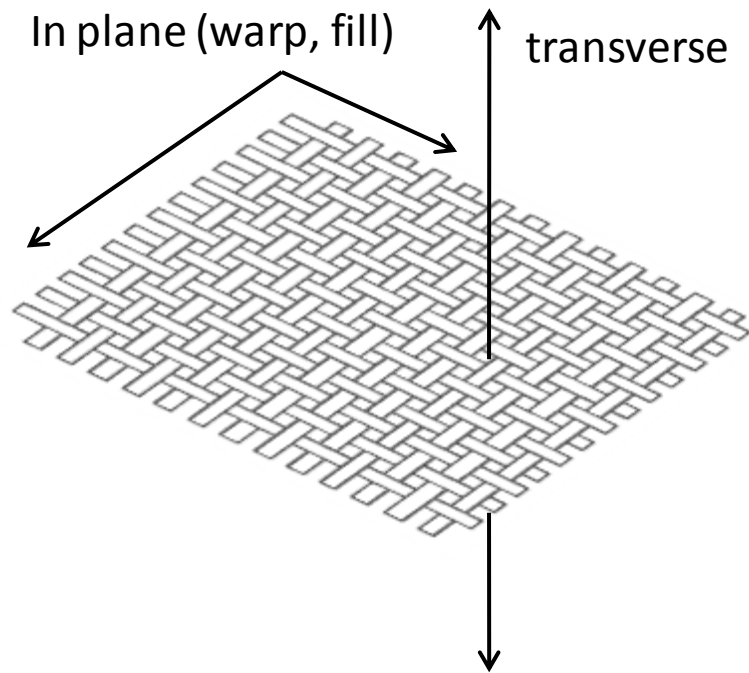


Figure 6.1 - Fabric orientation and descriptions used in current study

6.2 Experimental Work (Literature)

Skews and Hattingh et. al. [Skews,2006; Hattingh,2001] have undertaken shock tube tests to investigate fabric materials, and focused on the back wall pressure measurement (Figure 6.2) and associated amplification with single fabric samples having some stand-off from the back wall. A simple schematic of the experimental apparatus is shown below in Figure 6.2.

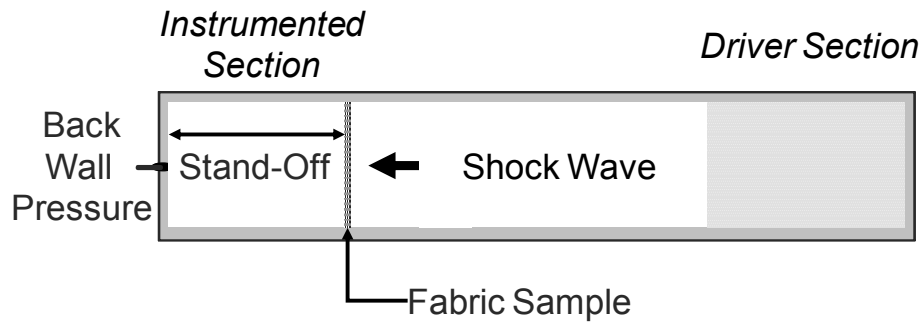


Figure 6.2 - Diagram of shock tube apparatus with fabric sample

These studies considered fabrics of varying density and porosity (muslin, cotton, and satin) and air shock waves of varying pressure ratios (the ratio of pressure of the shocked and unshocked air). In one case (Figure 6.3), muslin resulted in the lowest amplification of blast pressure (1.1 times), having the lowest density as well as the highest permeability. For the materials considered, satin had the highest amplification of blast pressure (2 times), with the highest density as well as the lowest permeability of the three samples.

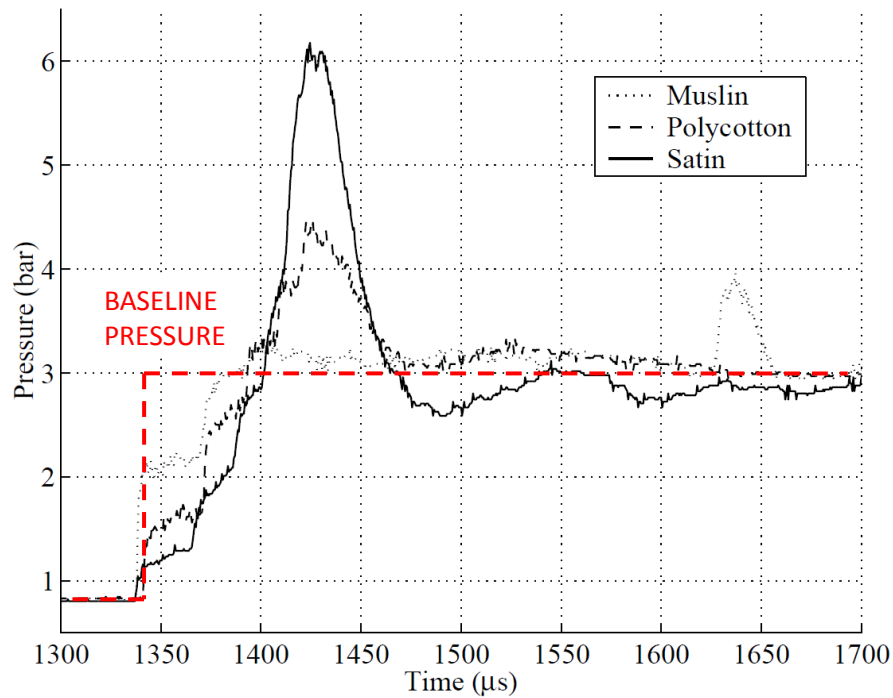


Figure 6.3 - Pressure time histories for various fabrics with 6mm stand-off, 2.21 bar baseline reflected overpressure [Hattingh, 2001]

The pressure traces for the fabrics exhibited multiple steps over time, resulting from the multiple reflections of the transmitted shock-wave between the fabric and back-wall. As the fabrics were accelerated towards the back wall, this resulted in a decreased volume between the back wall and fabric, where the fabric acts as a “moving piston” [Hattingh,2001]. The results from Naiman et al [Naiman, 2006] using permeable stationary barriers confirmed this mechanism, as their results were unable to produce amplifications observed in experiments.

The effect of varying the shock strength on the pressure amplification was also investigated. It was found that as shock strength increases, the amplification also increases, with a greater rate increase shown by the less permeable fabrics (Figure 6.4).

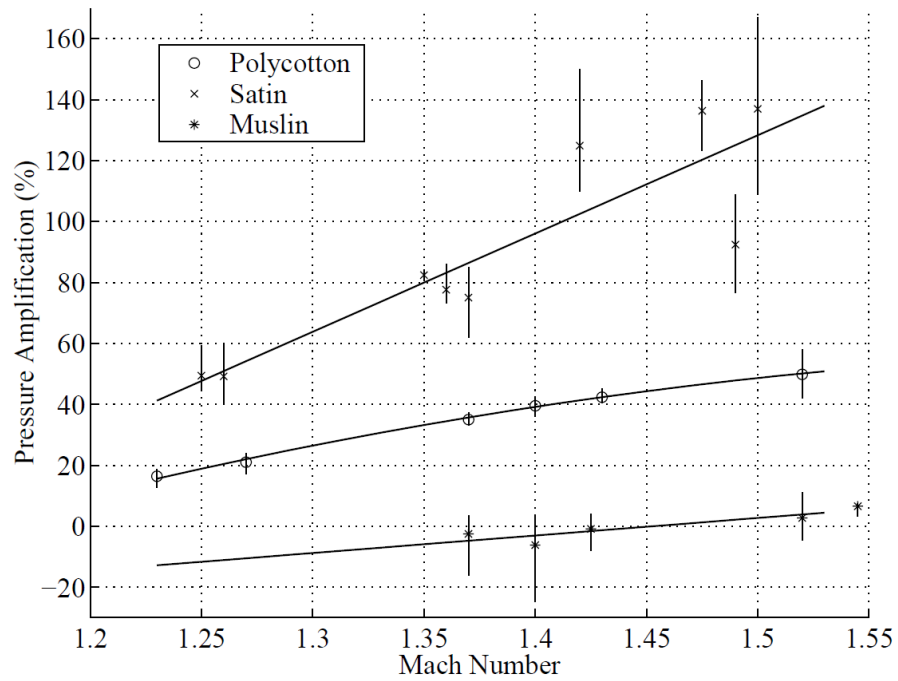


Figure 6.4 - Variation of shock strength and the resulting pressure amplification by fabrics [Hattingh, 2001]

The influence of the initial air-gap (stand-off) was investigated also. No clear trend was found in the experimental values (Figure 6.5) for the stand-off values considered.

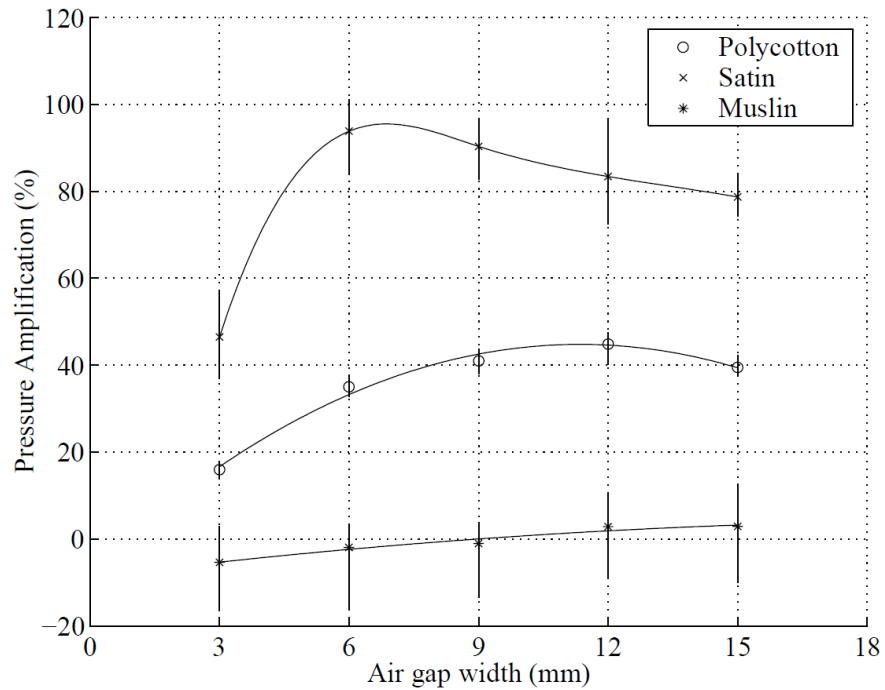


Figure 6.5 - Effect of varied air gap width (stand-off) on pressure amplification for various fabrics [Hattingh,2001]

An aramid fabric (Kevlar) was investigated in another study using a similar approach [Skews, 2006] and produced a peak pressure amplification of 4.5 times at the back wall, which was greater than any other fabric tested. This fabric was quoted as having an extremely low permeability, and was described as being essentially non-permeable.

6.3 Numerical Model of Single Layer Fabrics

To understand the phenomenon of blast amplification, experimental tests are often undertaken using a shock tube. Although this pressure loading differs from blast loading due to the relatively long duration, this type of testing is more repeatable than blast testing using explosives. A typical shock tube consists of multiple sections as shown schematically in Figure 6.2. A driver section is separated from the remainder of the tube with a rupture plate. Depending on the thickness and material, the rupture plate bursts at a particular pressure difference, resulting in a shock wave that

travels down the shock tube to the instrumented test section. The measured value of interest in this study was the back wall pressure occurring behind the sample material.

In this study, we used LS-Dyna, an explicit finite element code (Livermore Software Technology Corporation) [Hallquist, 2006], to predict the response of fabrics materials exposed to pressure waves in a shock tube environment in order to investigate the experiments by Skews [Skews, 2006] and Hattingh [Hattingh, 2001] and then evaluate a wider range of material parameters. The model was developed from a previous model used to investigate waves in a shock tube [Salisbury, 2004] and the fabric with associated permeability was integrated. This required several initial studies and developments related to model development, modeling permeability, and finite element mesh refinement.

6.3.1 Shock Tube Model for Fabrics

A shock tube model (Figure 6.6) was created with dimensions of 5 mm x 5 mm x 120 mm using 0.3125 mm cubic elements, though for some simulations this element size was further refined due to convergence issues (see convergence results in section 6.3.3). The dimensions used are smaller than typical physical shock tubes, but represents a larger effective size due to symmetry conditions. For the current study, the air in the driver and instrumented sections was modeled using an Arbitrary Lagrangian Eulerian formulation [Souli, 2004], capable of simulating the large deformation fluid flow and required structural interaction with the fabric. Symmetry boundary conditions were applied at all fluid and fabric boundaries in order to create an infinite plane of fabric. It should be noted that these boundary conditions did not allow for consideration of edge-effects resulting from leakages or material stiffness in bending. While pressure readings used from the experiments were taken from transducers near the centre of the fabric, there may have been edge effects that would lead to reduced back wall pressure. This aspect is discussed further in the results section. Larger-scale models were considered computationally prohibitive due to the high density of ALE elements required. The average pressure on the rigid back wall was used from the numerical shock tube model, and these values are the pressures reported in the results in order to avoid local pressure effects from fabric permeability.

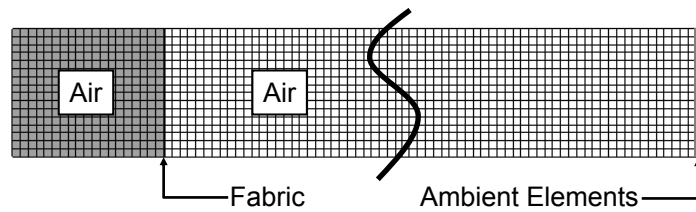


Figure 6.6 - Side view of shock tube model

The shock loading in the numerical model was generated by applying a pressure-time history at the end of the shock tube using an element (ambient element) designed to produce fluid/gas outflow. Ambient elements allow a pressure to be prescribed at a boundary, and in this study acted as a source to simulate the high pressure air reservoir of a shock tube. This approach allowed for the application of different load histories to the fabric, corresponding to the conditions used in the experiments by Skews [Skews, 2001]. For the shock tube studies documented here the pressure histories were step inputs. It should be noted that, throughout this study, all pressures were defined with reference to the reflected pressure that would be seen on the back wall without the fabric present. A shock wave resulting in a reflected pressure of 3.92 bar was the most common loading scenario considered. The initial ambient air pressure was 0.83 bar as described in [Skews, 2001]. The duration of pulse that could be achieved was limited by the length of the shock tube model such that very high stand-offs could not be considered, but was sufficient for loading scenarios considered.

The ability of LS-DYNA to simulate shock waves in a shock tube was previously investigated by Salisbury et. al. [Salisbury, 2004]. An ideal gas equation of state was assigned to the air elements, with the constant volume and constant pressure specific heat coefficients being 718 and 1005 J/kgK, respectively. In order to ensure continuity across shock fronts, LS-Dyna, utilizes a bulk viscosity for all solid elements, the magnitude of which is a function of the trace of the strain rate tensor, local sound speed, density and characteristic element length. In the study by Salisbury, it was found that the ALE formulation in LS-DYNA was able to resolve shock fronts and expansion waves with good correlation to accepted analytical solutions with an ALE element size of 5 mm for a 1 m length shock tube. It was also noted that an orthogonal mesh, oriented along the primary direction of fluid flow produced the most accurate results, attributed to the way that flow variables

are advected in the ALE algorithm [Salisbury, 2004]. The mesh orientation for the current model is shown in Figure 6.6. The initial element size was 5mm, with an element aspect ratio of 1. The element size was later reduced when the fabric was incorporated, as described below.

6.3.2 Fabric model

The fabric itself was modeled using 5mm by 5mm square Lagrangian shell elements (Belytschko-Tsay formulation) and coupled to the ALE calculation using a two-way penalty-based coupling approach [Souli, 2004]. During the calculation of the Lagrangian deformation of the fluid (ALE) mesh, before advection and remapping, the movement of the fluid relative to the structure is determined and a coupling force is applied to the fluid and structure. The force for penalty coupling is proportional to the change of the Lagrangian node location relative to the fluid mesh and the penalty stiffness. The penalty stiffness is generally kept as low as possible (to avoid numerical instability and oscillations in interface forces), while being high enough to prevent the fluid from leaking through the Lagrangian part.

Solid elements were not considered due to the mesh density that would be required to provide sufficient elements through-thickness, while maintaining the fabric thicknesses quoted in literature [Skews, 2006; Hattingh,, 2001]. It is recognized that the through thickness material properties of the fabric may be important in terms of blast response, particularly for multiple layers of fabric. While there is some data available on through-thickness properties of aramid fabrics [Raftenberg, 2004; Yu, 1985] and cotton [Taylor, 2000], the use of more complicated material models was not pursued due to limited data for the fabrics considered.

To introduce material permeability, uniform holes were created in the fabric (Figure 3) and an elastic modulus of 3.2 GPa was used with an isotropic linear elastic material model to prevent in-plane deformation and changes to the hole size or permeability of the fabric during the simulation. Initial studies showed that the in-plane modulus did not affect the results, aside from preventing unrealistic deformation of the hole used for permeability. Density of the material was varied with shell thickness to produce the desired areal densities.

Although the model scale was significantly larger and the holes used in the model were greater in size than the spacing between the weave that would lead to permeability in real fabrics, studies using multiple holes yielded similar results to a single hole, but did require significantly more mesh refinement. Values for the density and permeability of the fabrics considered were based on data from Hattingh and Skews [Hattingh, 2001; Skews, 2006]. To calibrate the fabric permeability, numerical simulations were undertaken to determine the required hole size. In these simulations, a pressure difference of 124 Pa was created across the fabric, following Hattingh [Hattingh, 2001], and the resulting volumetric flow rate of air through the hole was determined. We note that this pressure is low compared to the pressures in blast or shock scenarios, but does provide a measure of material permeability, and was used to be consistent with the experimental data. While permeability information was not given for aramid fabric (being quoted as impermeable), the experimental and predicted permeability values for satin, cotton and muslin are listed in Table 6.1 below.

Symmetry conditions, as shown in Figure 6.7, were applied such that the model was effectively an infinite plane of fabric. In the experiments by Hattingh and Skews [Hattingh, 2001; Skews, 2006] a 180mm by 76mm piece of fabric was placed in a shock tube, and taped loosely at the top and bottom corners using 12mm foam tape (the thickness of which was used to produce stand-off). The experimentalists report that, “before a test if the textile [was] pushed gently with the hand it [was] easily able to touch the back wall” [Hattingh, 2001]. Based on the dimensions of the sample, the relatively low stiffness of fabrics in bending, the loose constraint of the fabric in the experiments, and the fact that a pressure transducer on the back wall behind the middle of the fabric sample was used for experimental results, the 5x5mm fabric sample simulated numerically was allowed to accelerate unconstrained towards the back wall.

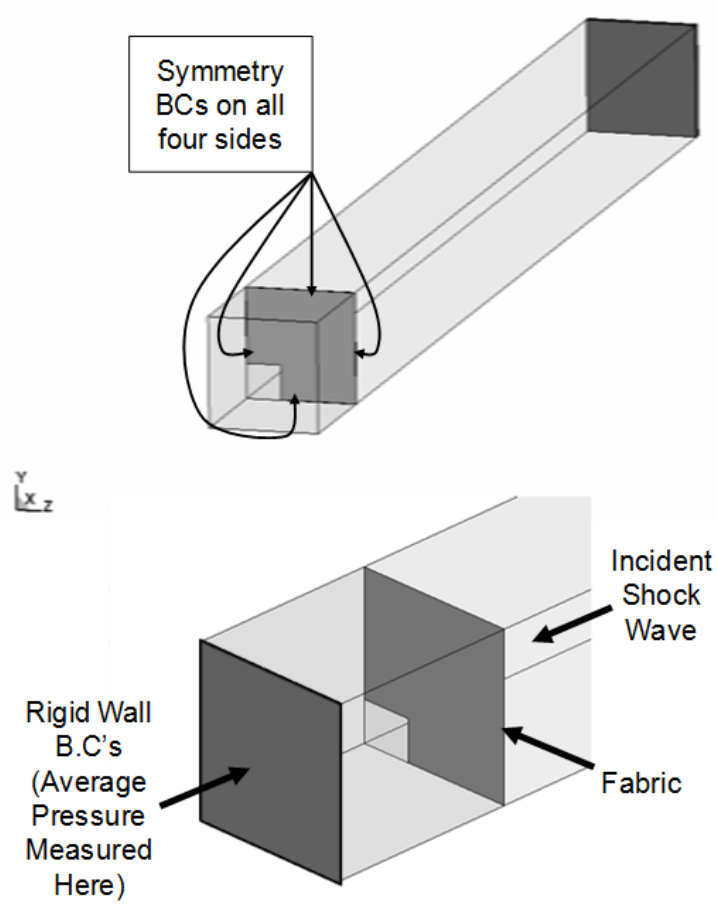
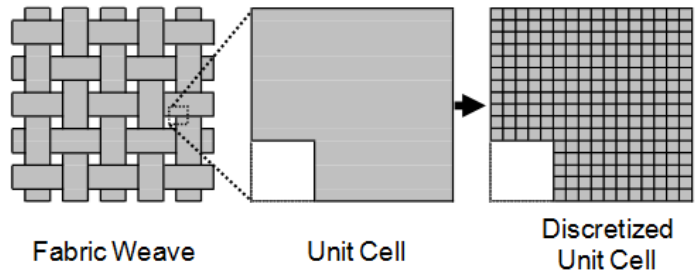


Figure 6.7 - Fabric and shock tube model

Table 6.1- Fabric parameters for experiments and numerical simulations. Experimental results from Hattingh and Skews [Hattingh, 2001].

<i>Fabric</i>	Areal Density (g/m³)	Hole Size (Elements/ [Percent])	Permeability (m³/m² per minute)	
			<i>Experiment</i>	<i>Numerical</i>
Muslin	95	9x10 [35%]	153.6	155.3
Cotton	104	4x5 [7.8%]	32.9	27.8
Satin	134	3x3 [3.5%]	6.0	7.7

The air on either side of the fabric was tracked during the simulation to ensure no unwanted leakage was occurring across non-porous sections of the fabric. A corresponding schematic of the finite element mesh is shown in Figure 6.8, with the results in Figure 6.9.

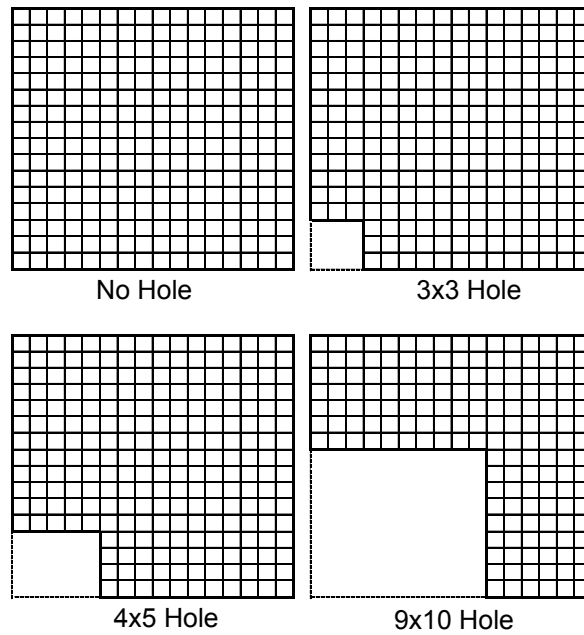


Figure 6.8 - Numerical fabric model geometries for various permeabilities

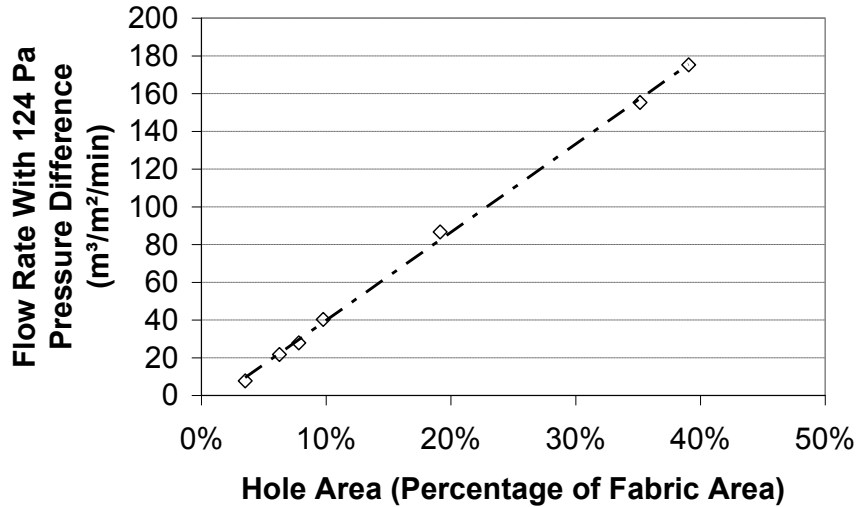


Figure 6.9 - Fabric air permeability numerical Results

This study also considered distributed fabric permeability, where multiple smaller holes were used within the small section of fabric simulated, and this necessitated a finer mesh for to accurately model the flow. Compared to a single lumped permeability, the distributed permeability provided

similar results as determined by volumetric flow rates due to pressure difference across the fabric. Furthermore, the distributed permeability was computationally expensive and required additional mesh refinement to resolve the flow through the smaller holes.

6.3.3 Finite Element Mesh refinement

Appropriate refinement of the finite element mesh must be considered in any numerical analysis. Although previous studies showed that a relatively coarse mesh (5mm elements) was required to resolve a shock wave, a finer mesh was required to predict the flow for the permeable fabrics, and to resolve wave reflections as the fabric moved towards the reflecting wall. It was found that reducing the element size below 0.3125 mm did not result in significant changes in the predicted back wall pressure at a stand-off of 6mm between the fabric and reflecting wall (Figure 6.10). It should be noted that the cases with 0 permeability (no hole) demonstrated convergence at a larger element size; however, when permeability was included a finer mesh was required. Changes in flow rate did occur when the element size was varied; however, these changes resulted in less than a 5% change in the peak pressure results from one element size tested to the next.

Richardson extrapolation [Roache, 1998] from the results of three mesh sizes (0.1563mm, 0.3125mm, 0.6250 mm) was used in order to determine the level of convergence for the permeabilities considered. An estimate of the 0 mm element size predictions determined from Richardson extrapolation are provided in Figure 6.10.

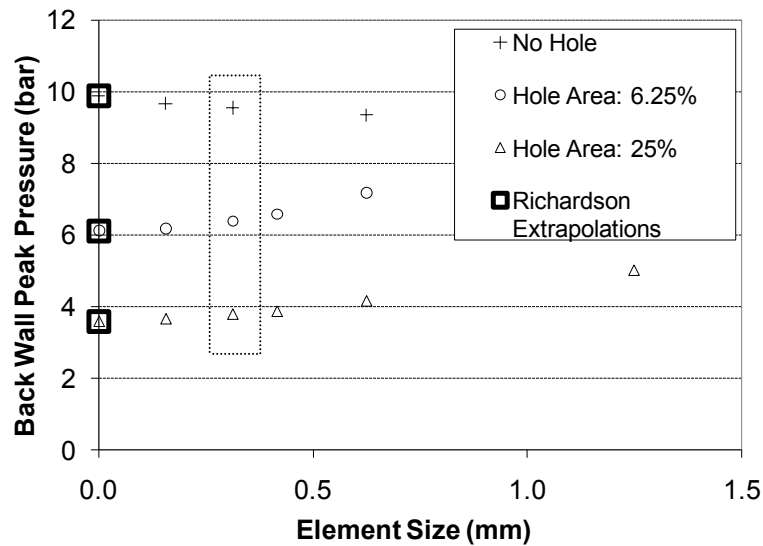


Figure 6.10 - Mesh Refinement Results, with dotted box showing element size used in most simulations

The Grid Convergence Index (GCI) has been proposed as a standard means of quantifying the level of convergence achieved with a numerical model [Roache, 1998], and for providing guidance on an appropriate mesh size. The GCI is based on mesh refinement results for the problem being considered. This value also incorporates Richardson extrapolation results, as CGI is an estimate of error bound for a given element size based on Richardson extrapolation. Table 6.2 below shows the calculated GCI values obtained from the convergence study. GCI_{12} values were used to provide an estimate of the error bound in results using a fine (0.1563mm) mesh. The GCI_{23} values (the estimated error bound for results using 0.3125mm elements) suggested less accuracy, which was expected with an increased element size. The estimated accuracy of the results at the 0.3125mm mesh size was considered acceptable for all permeabilities and this element size was chosen as the baseline element size for simulations. For more information on the calculation of the grid convergence index, see Section 3.3.

Table 6.2 – Grid Convergence Indices for permeabilities investigated in convergence study

	Permeability			Corresponding Element Size
	0%	6.25%	25%	
GCI_{12}	1.26%	1.34%	2.40%	0.1563mm
GCI_{23}	2.64%	5.21%	6.61%	0.3125mm

Peak pressure was selected for evaluation of the convergence studies, since this was the most sensitive metric to the input conditions, and ultimately of greatest relevance for comparison to the experimental results. In spite of the differences in peak pressure with varied element size, the overall behaviour was extremely consistent as illustrated in Figure 6.11 below.

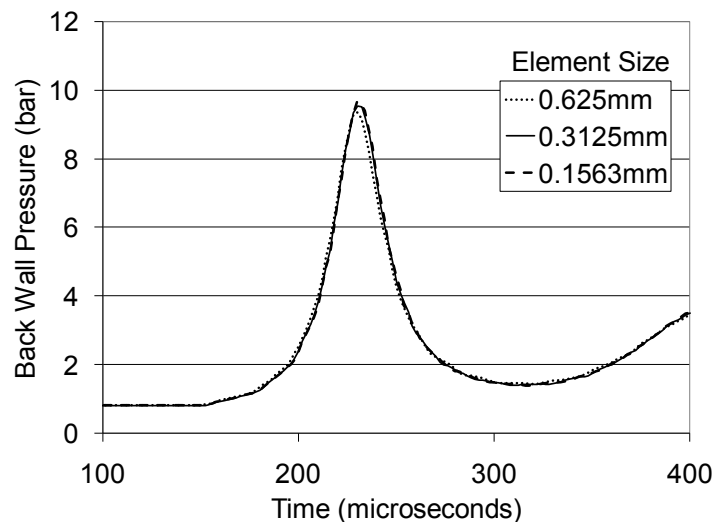


Figure 6.11 - Mesh refinement results, pressure time history behind non-permeable fabric at various element sizes

The level of refinement required for the model was also found to be dependent on the stand-off between the fabric and reflecting wall, and the loading applied to the fabric. At low stand-off and high loadings, a mesh size finer than 0.3125 mm was required to ensure a sufficient number of elements were located between the fabric and back-wall at all times during the simulation. It was found that, for impermeable fabrics with a stand-off of 4 mm or less, a mesh size of 0.1 mm was required. For permeable fabrics, the element size was not adjusted from 0.3125 mm because the minimum distance between the fabric and back-wall was not found to be critical, even at the lowest stand-off and the highest shock strength simulated.

6.4 Simulation of Shock Tube Tests

A series of experimental shock tube tests [Hattingh, 2001; Skews, 2006] were simulated using the model described above to investigate three different fabrics: cotton, muslin and satin. The fabric areal density and material permeability (volumetric flow rate for 124 kPa pressure differential) was set to the reported value in [Hattingh, 2001]. The shock loading was then applied and the pressure behind the fabric was monitored at a reflecting surface throughout the simulation. Figure 6.12 shows a cross section of the shock tube model, with air initially between the fabric and reflecting back-wall being lightly coloured, and air on the incident wave side of the fabric being a darker colour. The pressure wave rapidly applied a pressure load to the fabric surface, accelerating the fabric towards the back wall. For a non-permeable fabric, this resulted in compression of the air behind the fabric, and superposition of waves creating the ‘piston effect’. In the case of a permeable material, the air flows partially through the fabric. Later in time, the flow reverses as a result of high pressure between the fabric and wall.

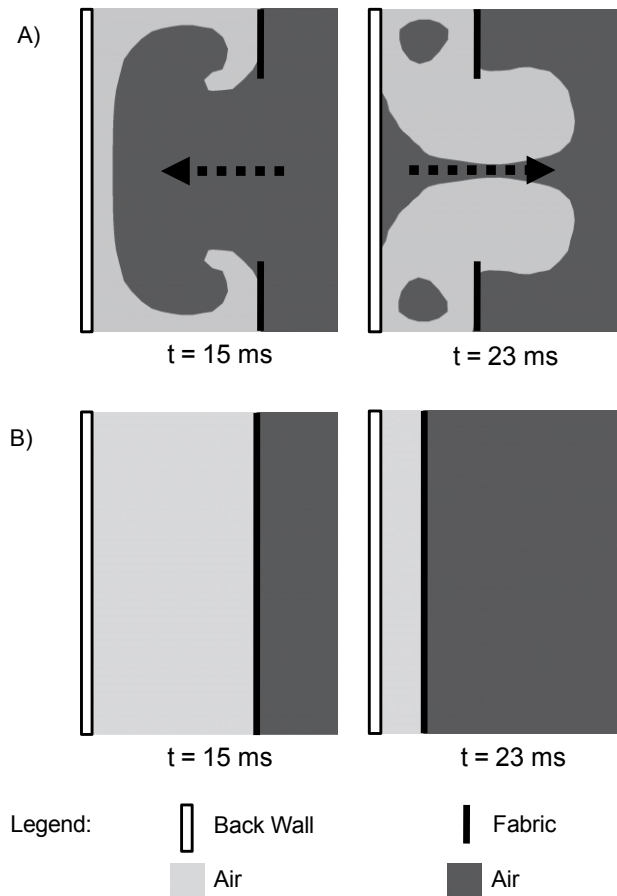


Figure 6.12 – Air flow through hole in: a) permeable fabric (muslin), b) non-permeable fabric (aramid). From numerical model with added symbols for clarity.

Figure 6.13 illustrates the effect of back wall pressure measurement position. In one extreme, if the pressure was measured directly behind the hole in the fabric there was a pronounced initial rise in pressure from air traveling through the fabric hole. In the other extreme (pressure measured in the opposite corner from the hole) the initial pressure rise was under-estimated. An averaged pressure measurement provides the most reasonable results and best reflects what the change in loading on the reflecting wall would be. The average pressure measurement in this case was close to the measurement behind the middle of the fabric, and this was due to the relatively small hole size for this simulation (3.25%).

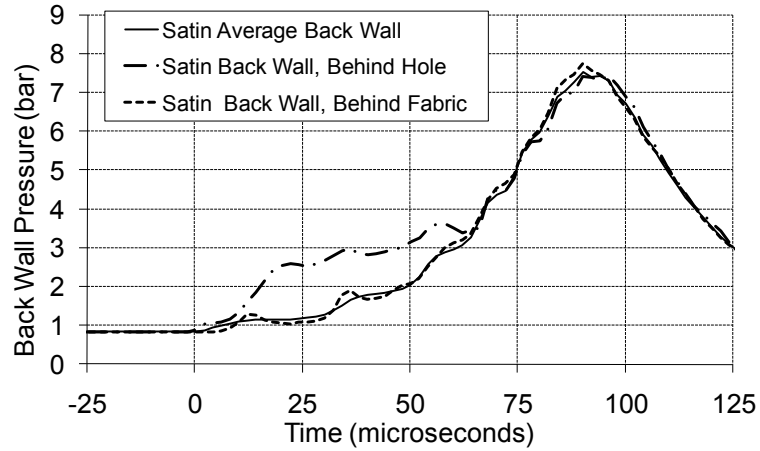


Figure 6.13 - Reflected Pressure History on Back Wall behind Satin: Averaged, Behind Fabric Hole, and Behind Fabric

The resulting time-pressure histories at the back wall for three different fabrics are shown in Figure 6.14, and the back wall pressure, and pressure 6mm from the back wall, without fabric are shown in Figure 6.15. Time history data for aramid was not available. A summary of the experimental and predicted peak pressures, along with the percent difference is shown in Figure 6.16. Please note that experimental results were digitized by hand from [Hattingh, 2001].

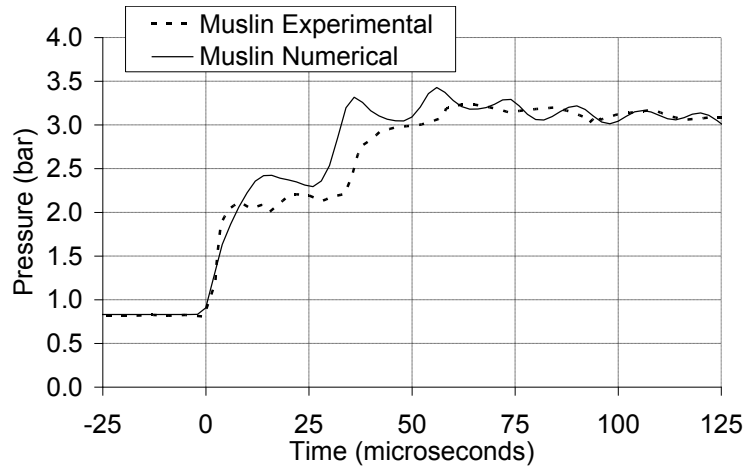
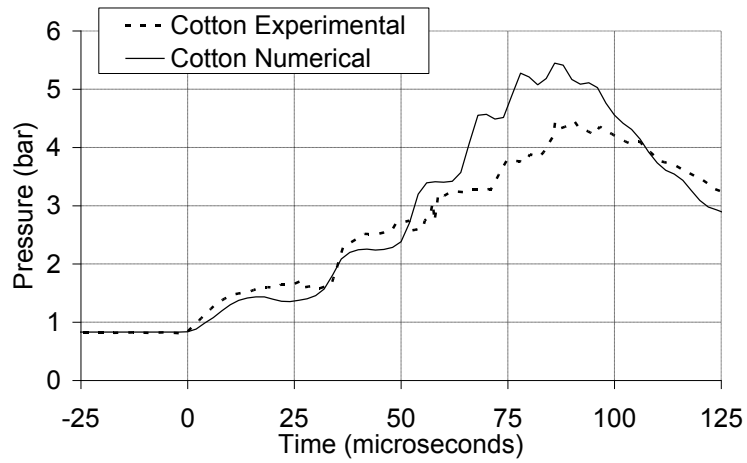
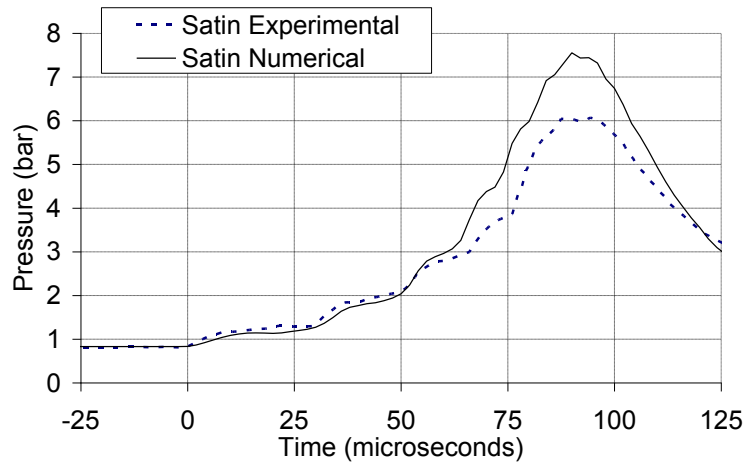


Figure 6.14 - Reflected pressure history on back wall behind satin, cotton and muslin. experimental results from Hattingh and Skews [Hattingh, 2001].

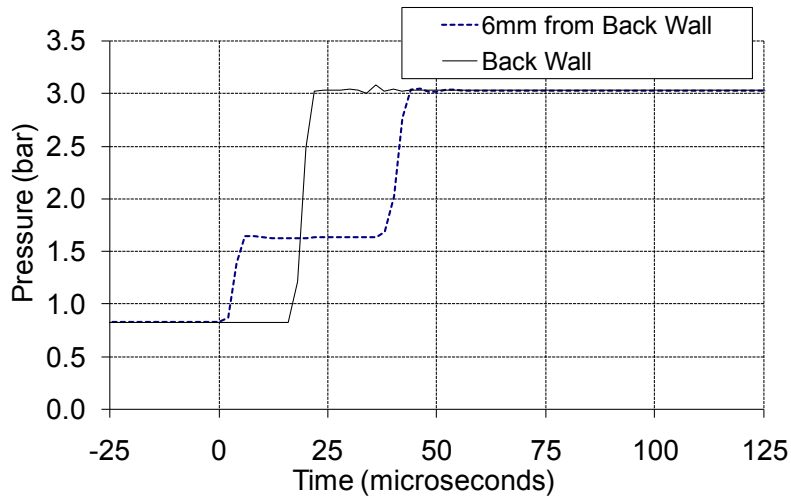


Figure 6.15 - Pressure time histories without fabric sample. Load case used for muslin, cotton and satin cases

The finite element simulations predicted times to peak pressure and the overall pressure profile, as measured behind various fabrics, reasonably well. The most significant difference was noted in terms of the predicted pressure amplification. This is shown in Figure 6.16 along with the percent error in the prediction, ranging from 5% for Muslin to 25% for Satin. It should be noted that the aramid fabric was tested under different test conditions (lower stand-off and higher shock strength), and the predicted pressure amplification was within 10% of the experimental data. For the experimental data, the number of repeat tests was not provided, so the importance of variability in the testing could not be directly assessed.

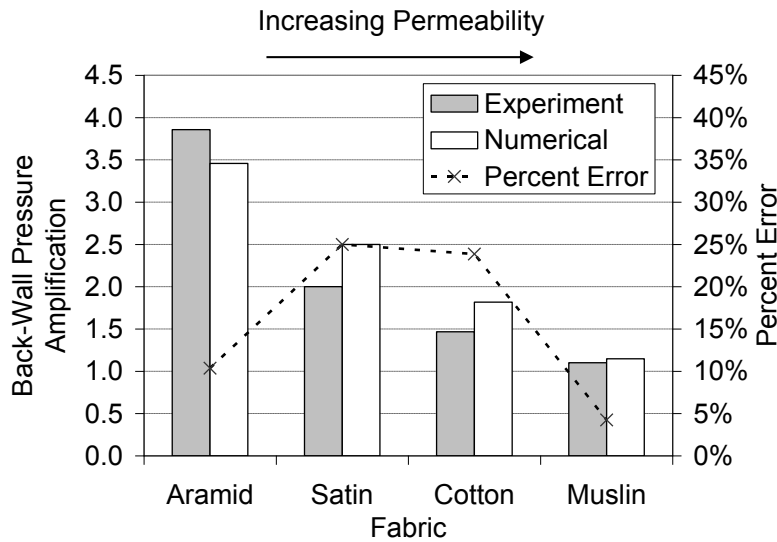


Figure 6.16 - Predicted back wall pressure amplification for various fabrics

6.4.1 Parametric Study

A parametric study was undertaken to isolate the effect of the important parameters in terms response of fabrics to blast loading. The parameters included: permeability, areal density, incident shock wave strength, and stand-off between the fabric and reflecting wall. The baseline case was: 9.8% permeability, 3.92 bar shock strength, 3mm stand-off and 150g/m² areal density. The parameters were varied around this baseline case (Table 6.3).

Table 6.3 - Range of Values for Parametric Study

	Areal Density (g/m ²)	Permeability (Percent/Number of Elements)	Stand-Off (mm)	Baseline Backwall Pressure (bar)
Max	2000	39% (10x10)	9	3.92
Min	50	0% (No Hole)	2.5	2.25
Baseline	150	9.8% (5x5)	3	3.92

The pressure measured 6mm from the back wall is provided in Figure 6.17below for the different shock strengths used in the parametric study. One can clearly see the incident pressure followed by

the reflected pressure from the back wall. Time 0 on this graph corresponds to the time at which the shock wave producing 3.92 bar reflected pressure hits the back wall.

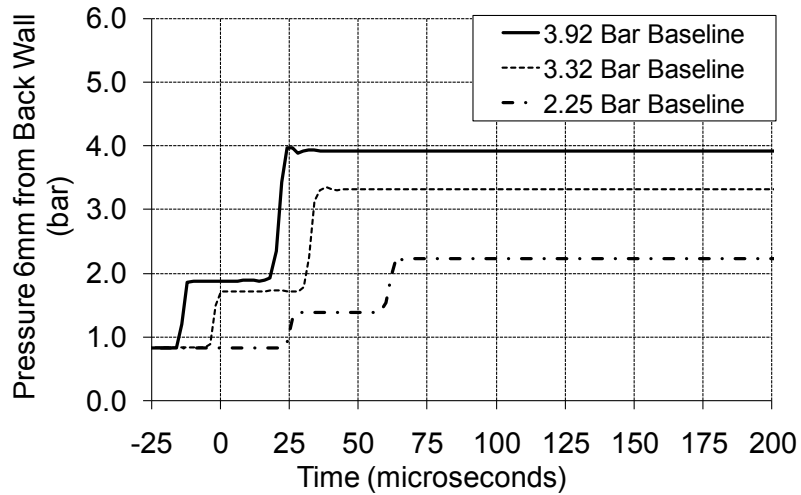


Figure 6.17 - Pressure traces 6mm from the back wall for 3.92, 3.32 and 2.25 bar reflected pressures (without fabric)

Material permeability was investigated by increasing the fabric permeability from 0% to 39%, typical values for common fabrics and ballistic fabrics with the results shown in Figure 6.18.

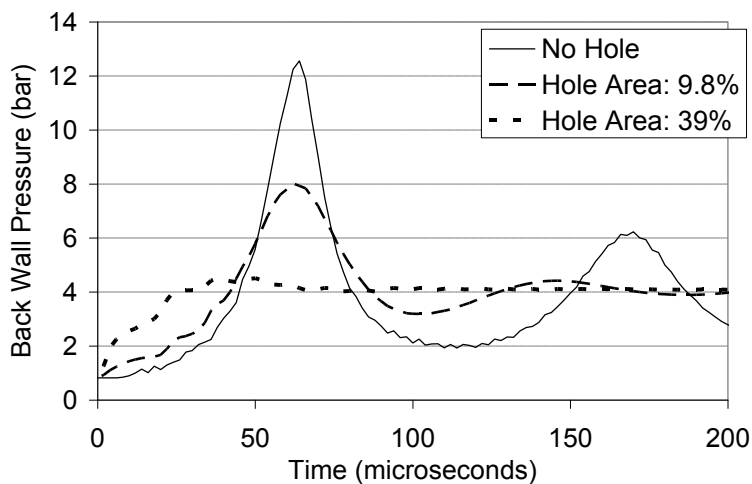


Figure 6.18 - Back wall pressure time histories for fabrics of varying permeabilities, back wall pressure without fabric: 3.92 bar (reflected), stand-off: 3mm

At a given permeability, standoff and shock strength, the material areal density was varied across a wide range as shown in Figure 6.19. In general, the rate of onset of pressure as measured at the back wall was reduced with increasing areal density.

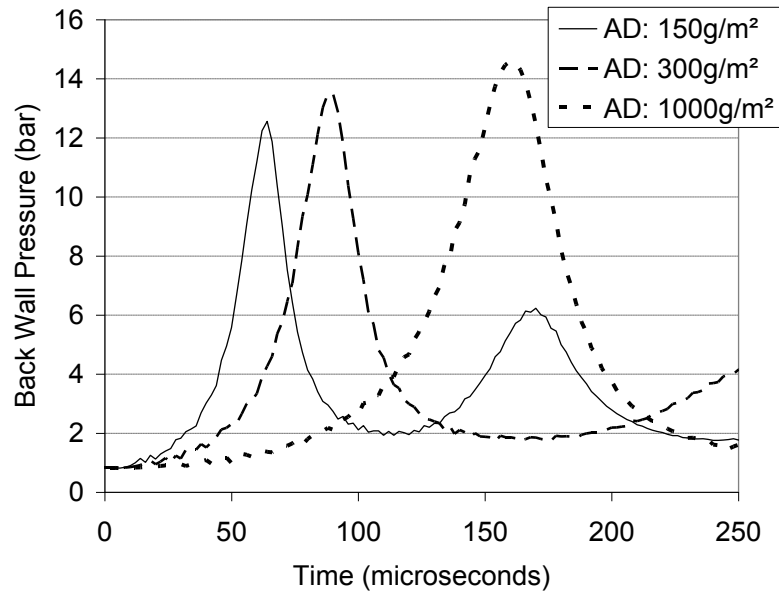


Figure 6.19 - Back wall pressure history for fabrics of varying areal densities, back wall pressure without fabric: 3.92 bar (reflected), stand-off: 3mm, no permeability

The amplification increases (Figure 6.20) with increasing areal density up to approximately 500 g/m², after which the amplification remains constant. As expected, permeable fabrics show much lower amplifications, which decrease with increasing areal density.

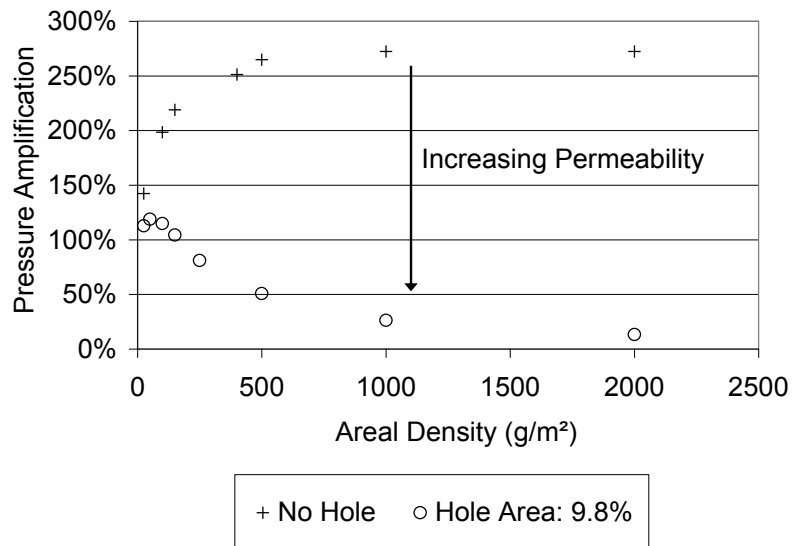


Figure 6.20 - Pressure amplification vs. areal density for fabrics with varied permeabilities, stand-off: 3mm, back wall pressure without fabric: 3.92 bar (reflected)

As reported in the literature [Hattingh, 2001], a large change in peak reflected pressure amplification has often been observed with changes in incident shock loading, and this was confirmed with the simulations (Figure 6.21).

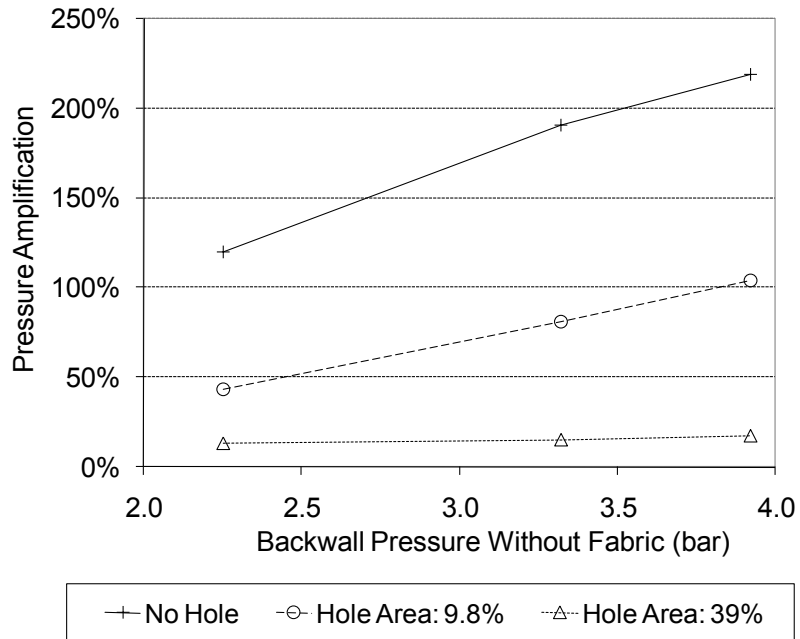


Figure 6.21 - Back wall pressure amplification for various permeabilities under varied shock tube loads, stand-off: 3mm, areal density: 150g/m²

There was no significant change in peak pressure with the stand-off in the ranges simulated (Figure 6.22). The minimum stand-off of 3mm was chosen as it was the lowest stand-off possible. Lower stand-offs would require much finer meshes which were computationally prohibitive.

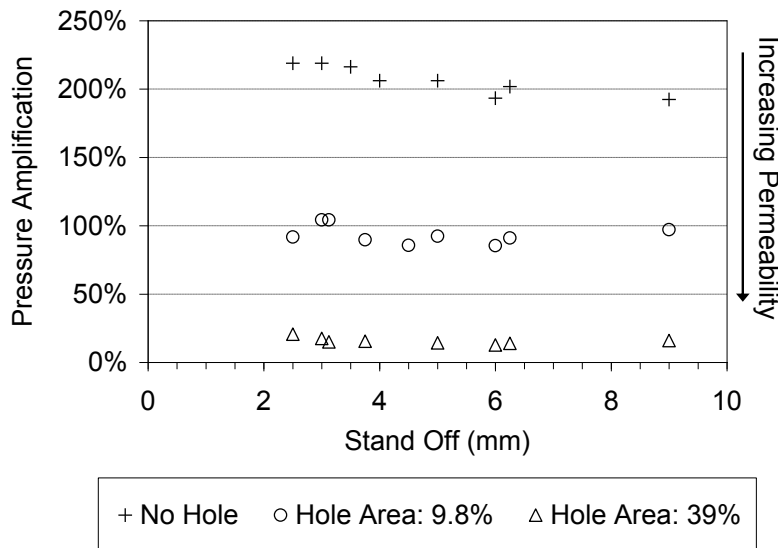


Figure 6.22 - Back wall pressure amplification vs. stand off for fabrics of various permeabilities, areal density 150g/m², back wall pressure without fabric: 3.92 bar (reflected)

6.5 Single Layer Fabric Implementation with the modified Axelsson Model

The mathematical models without the torso were meant for comparison to literature results which show the effect of protection on the transmitted pressure wave. The finite element equivalents in the current research were FEA shock tube models developed, also for comparison to experimental tests.

Some basic assumptions were used in the development of the protection mathematical models. In the case of the model for fabric with an air gap, the fabric was treated as a lumped mass. The air gap was treated such that it is assumed no air escapes. The change in pressure with change in volume was treated as described by Boyle's law. An assumption had to be made regarding the nature of compression in terms of whether it was fully adiabatic (no heat transfer out of the system) or fully isentropic (no change in air temperature). In reality the compression of air would be somewhere in between, however, detailed knowledge of the heat transfer between the air being compressed and its surroundings would be required for accurate calculation. Because the rate of

compression in the cases for this study was so high, the assumption of isentropic compression (which is commonly used at lower strain rates) would not necessarily have been valid. The assumption of adiabatic compression and isentropic compression were both investigated, and ultimately adiabatic compression was assumed. A diagram showing the model of fabric with air gap is given below (Figure 6.23).

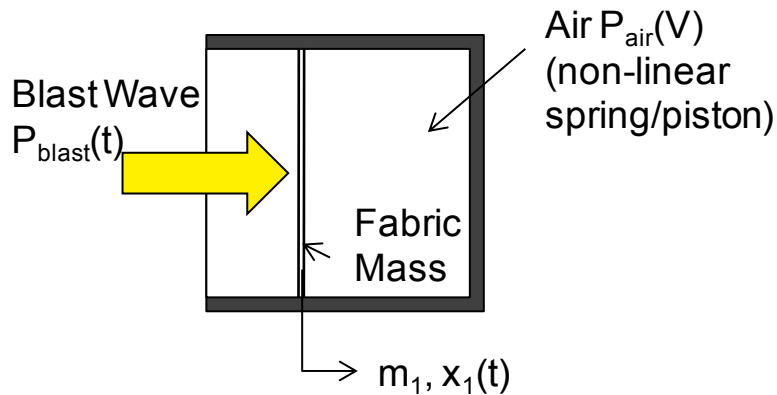


Figure 6.23 - Fabric and air gap model diagram

6.6 Validation of the Single Layer Fabric Mathematical Model

An attempt at validating the mathematical model was conducted against results from shock tube loading of an aramid fabric from [Skews, 2006]. It was found that the model over predicted the overpressure resulting from shock tube loading (reflected pressure of 2.8 bar). For one particular case considered (a single layer of aramid fabric) the experimental result from [Skews, 2006] gave the peak pressure behind the fabric as being 13.5 bar, while the result from the mathematical model was 20.7 bar. Simulation of experiments from [Ouellet, 2008], which involved the blast loading of rigid plates (aluminum and composite) with an air gap of 12.7 mm, also resulted in an over-estimation of peak pressure (Figure 6.24).

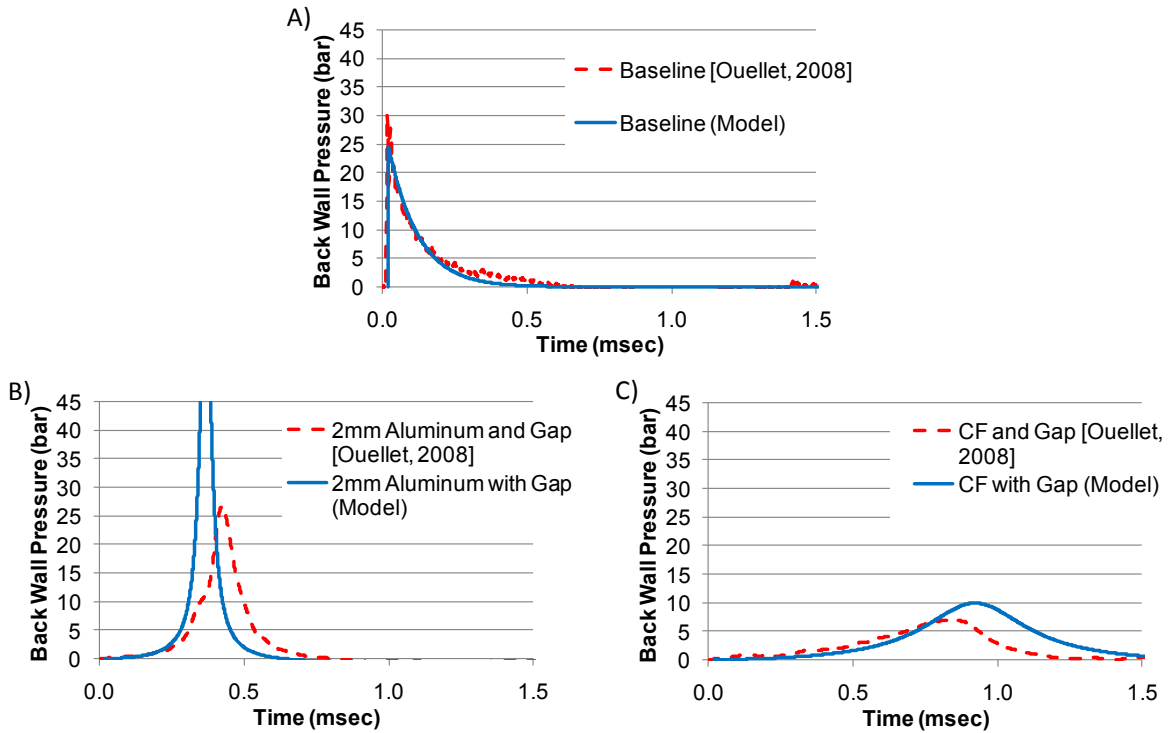


Figure 6.24 - Validation of 1D mathematical model for a plate with air gap against experimental data [Ouellet, 2008]

The error can be explained by understanding two limitations of the mathematical model. The first limitation was that it couldn't account for air leakages, as mentioned previously. The second limitation is that because the mathematical model was uncoupled, it could not account for the change in loading resulting from the motion of the fabric itself. In comparison, the coupled shock tube model described in Section 6.3 accounts for the fabric movement when determining the load. Attempts to account for the reduction of the magnitude of blast loading due to the kinematics of the fabric reduced, but did not eliminate, the error in peak pressure predicted by the mathematical model.

6.6.1 Fabric and Axelsson Model LD50 Predictions

Despite the inability for the 1D fabric and air gap model to accurately predict the amplification of a blast wave, the model was implemented with the Axelsson model (Figure 6.25), similar to the work

done in Section 5.6.3. In this case too, an LD50 blast loading of duration 2ms and peak incident pressure of 4.27 bar and peak reflected pressure of 18.8 bar was used.

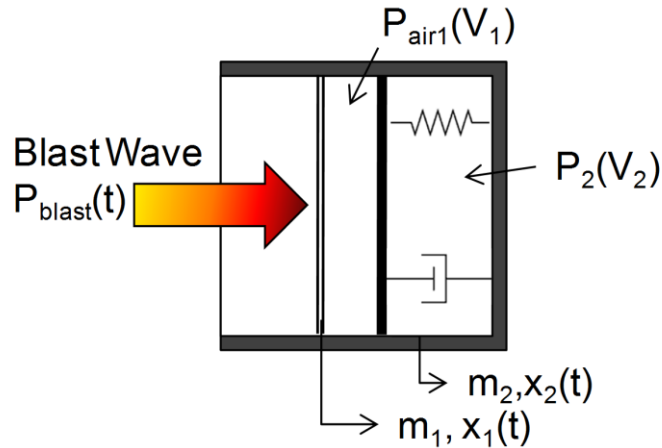


Figure 6.25 - Fabric model combined with Axelsson torso model

Using the areal density of a layer of Kevlar from [Skews, 2006], areal densities were assigned to the fabric models such that they represented 1, 32 and 64 layers of Kevlar fabric. The cases and results are provided below (Table 6.4). Due to the lack of success in the validation of the fabric and air gap model, the results are presented with little confidence in the results, but are provided for comparison against the more detailed finite element simulations which follow.

Table 6.4 - Summary of Modified Axelsson Model Results for Fabric with an Air Gap

Loading	Protection	Plate AD (kg/m ²)	Peak Pressure Behind Protection (bar)	Chest Max Inward Velocity (m/s)	Chest Peak Acceleration (m/s/s)
LD50 T2	None	-	18.8	21.3	7.67E+04
LD50 T2	1 Layer Kevlar and 10mm AirGap	0.273	1570	22.8	6.34E+06
LD50 T2	32 Layer Kevlar and 10mm AirGap	8.74	216	25.9	8.67E+05
LD50 T2	64 Layer Kevlar and 10mm AirGap	17.5	71.8	25.1	2.85E+05
			Baseline	Amplified	Attenuated

6.7 Single Layer Fabric Implementation with Torso Model

Three various areal densities of fabric were simulated with a 10mm air gap to the torso. The fabric (modelled as a shell) was assigned varying areal densities, which were meant to simulate 1, 32 and 64 layers of Kevlar fabric (based on the areal densities from the study from [Skews, 2006]). In addition to the variation of areal density, two geometries were used for each areal density: a flat piece of width 24cm, which was representative of the geometries used in other studies, and a “wrap” of Kevlar which enclosed the torso slice completely. These geometries are shown below in Figure 6.26.

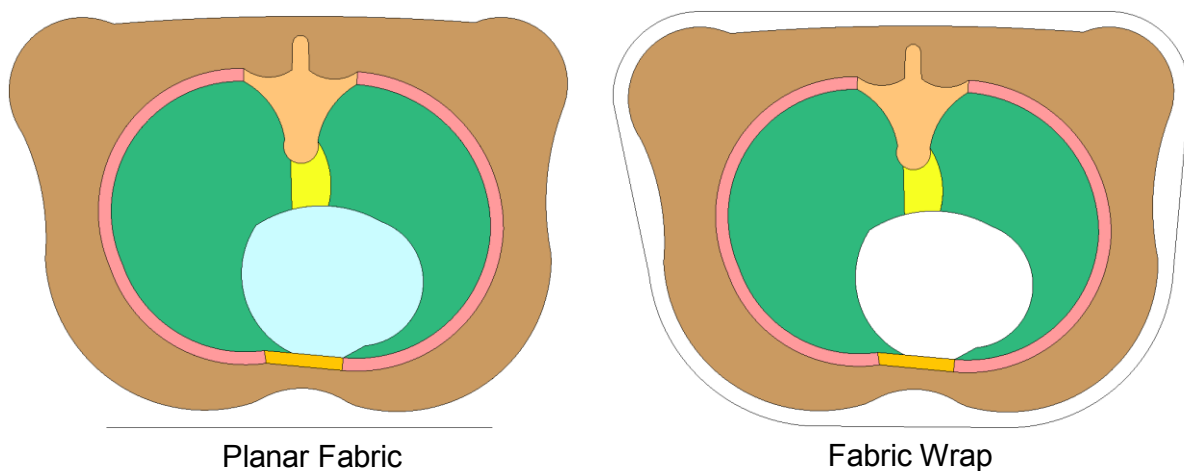


Figure 6.26 - Geometries used in torso model simulations with a fabric and air gap

In all cases, the loading applied was a 2ms duration blast, with an incident peak pressure of 4.27 bar (1.88 bar reflected). This was representative of an LD50 loading according to [Bass, 2006].

While the mathematical model from the previous section was found not to be valid due to the uncoupled nature of the loading and failure to account for leakages, the application of the fabric model to the torso model should be acceptable because the model features fully coupled fluid/structure interaction. The use of a coupled formulation should account for both the change in loading from the fabric motion, as well as the escape of air from behind the fabric.

6.7.1 Single Layer Fabric Torso Model Results

In both the planar and “wrap” configurations, the model for Kevlar with an air gap predicted an amplification of blast injury except for the highest areal density considered (equivalent to 64 layers). The Kevlar wrap resulted in higher injury levels than the planar Kevlar fabric model (Figure 6.27). This was attributed to the wrap containing the high pressure air resulting from the compression of the air in the gap between the torso and fabric, while the open edged concept allowed this high pressure air to escape without contributing further to the loading of the torso. Similarities can be drawn between this effect and the effect of fabric permeability described in Section 6.4.1.

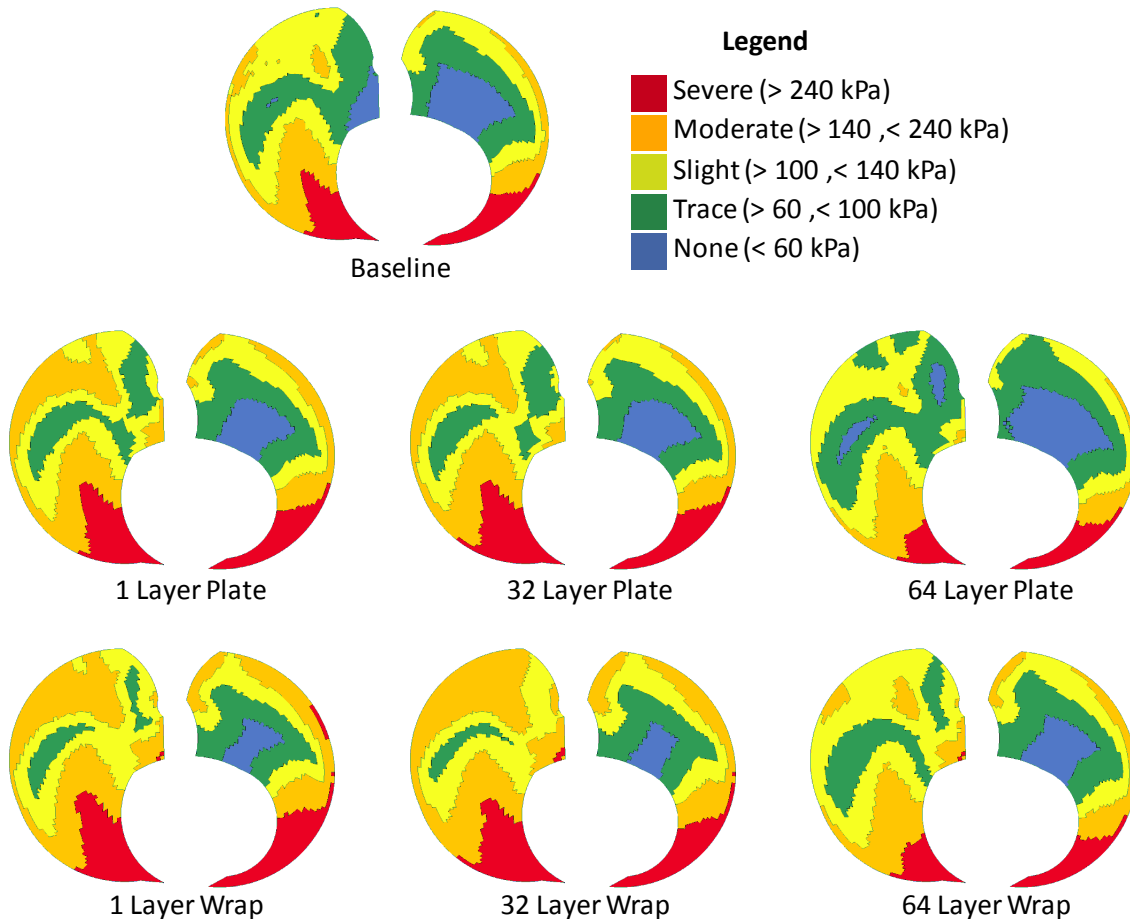


Figure 6.27 - Predicted lung injury results from the finite element torso model with fabric concepts having a 10mm stand-off.

As a summary of the above results, the percentage of elements which experienced a peak pressure above 240 kPa is shown below in Figure 6.28.

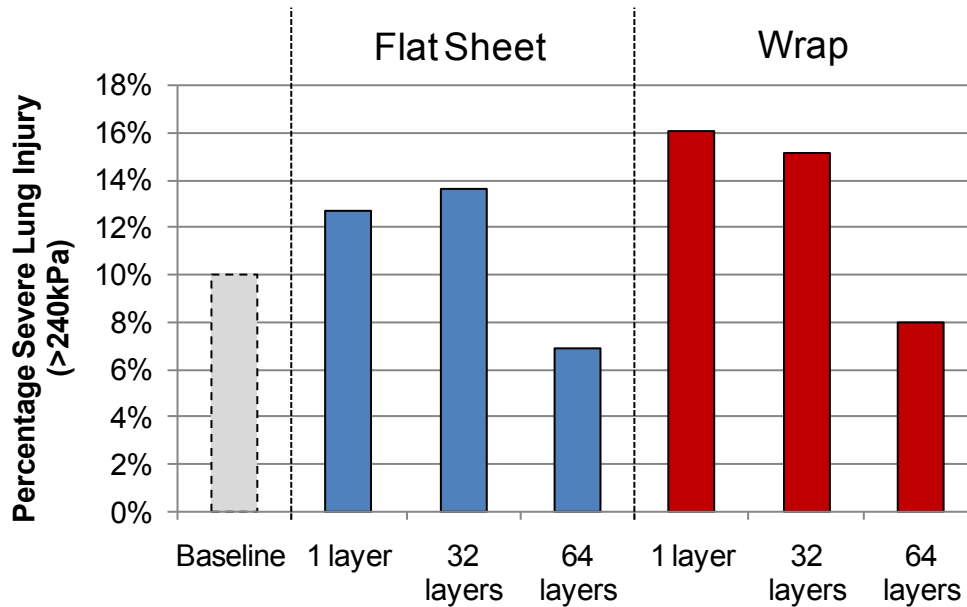


Figure 6.28 - Percentage of lung severely injured as determined by peak dynamic pressure for fabric with an air gap

6.8 Discussion of Single Layer Fabric Results

The finite element simulations of shock tube tests predicted times to peak pressure and the overall pressure profile, as measured behind various fabrics, reasonably well. The most significant difference was noted in terms of the predicted pressure amplification. The higher predicted peak pressures may be explained by the assumptions made in the model. The model boundary conditions did not allow for leakage around the edges of the fabric so air could not escape laterally in the non-permeable cases. Any edge leakage in the experiments would have led to reduced peak pressure amplification. Edge leakages may be increasingly significant as permeability is decreased and pressures between the fabric and back-wall increase. In general, the error in prediction decreased with increasing permeability.

A parametric study was undertaken to investigate the effect of fabric properties and loading on amplification of the pressure behind the fabric material. It should be noted that, although the parameters were modified individually to investigate the mechanism of pressure amplification, these parameters are typically coupled for real materials with higher permeability leading to lower areal density for a given material, for example.

Increasing the strength of the incident shock wave increased the pressure amplification, as expected. At a given areal density, stand-off and shock wave pressure ratio, increasing fabric permeability resulted in a decrease in pressure amplification (Figure 6.18) while the time to peak pressure did not change. A second peak was observed in less permeable fabrics and was attributed to the long duration loading applied in the shock tube simulation. The first peak (Figure 6.18) occurs when the fabric is accelerated towards the back-wall by the incident shock wave. In less permeable materials, the pressure between the fabric and the back-wall exceeds the reflected pressure on the face of the fabric struck by the shock wave, and the fabric begins to accelerate away from the back-wall. Eventually this pressure drops and the fabric is again accelerated towards the back wall, resulting in a second peak. The addition of permeability in the fabric damps this behavior by reducing the initial acceleration of the fabric due to less exposed area to the shock wave and a reduced pressure difference across the fabric.

Pressure amplification was found to increase up to 50g/m^2 in the case of the permeable fabrics (Figure 6.20), beyond which, increases in areal density result in a decreased amplification. Peak pressure and amplification increased with areal density (Figure 6.20) for non-permeable fabric, up to 500g/m^2 . In general, increasing areal density enhanced the piston effect and pressure amplification for non-permeable fabrics. However, at higher areal densities the fabric acceleration is reduced for a given shock strength due to the inertia of the material, resulting in a plateau. No significant change in amplification was predicted for the changes in stand-off investigated. This is explained by the counter-acting effects of the increased volume of air between the fabric and back wall allowing more compression before reaching a given pressure, and higher fabric velocity for higher stand-off

Although not investigated in the parametric study, it is expected that higher areal density materials and stand-off can be used to attenuate limited duration shock waves such as those from a high explosive; however, the amount of attenuation will depend on the duration of the wave as well as the fabric material properties. Work examining the attenuation of blast waves by hard plates [Ouellet, 2008] could be considered analogous to multiple layers of impermeable fabric with stand-off.

It was discovered during the attempt at validating the simplified mathematical implementation of the fabric and air gap model that the model systematically overestimates the peak pressure. This was attributed to the fact that the model does not account for leakages or changes in loading resulting from the kinematics of the fabric.

To remain consistent with other work done as a part of this study, the fabric and air gap model was implemented with the modified Axelsson model. For all cases considered, the modified Axelsson model predicted an amplification of injury, while the finite element torso model predictions indicated that the cases with 1 or 32 layers of fabric would amplify the blast injury, and the 64 layer cases would attenuate the injury.

Two configurations of fabrics with an air gap were considered with the torso model, a planar sheet, or plate, of fabric, and a fabric wrap. The predicted injury was higher for all fabric wrap cases due to the inability for the air to escape from behind the fabric (though air was free to move within the gap, thus was pushed to the sides of the torso after initial loading).

It must be mentioned that at the start of the finite element solutions, there were only 2 ALE elements between the torso and the shell elements used for the fabric models (10mm of stand off, in a model with a typical element size of 5mm). It was found during the validation of the finite element shock tube model that at least one ALE element should be maintained between the fabric and back wall in order to maintain convergence. This requirement was not met when the fabric was implemented with the torso model.

Chapter 7

Multi-Layer Fabric Behaviour Under Blast Loading

The work outlined in Chapter 6 had shown how fabrics with stand-off can amplify shock and blast waves. Because the amplification/attenuation effects discussed previously did not depend on through thickness properties, and assumed the existence of an air gap, it could be argued that the amplification and attenuation of shock waves by fabrics might not apply when no air gap is present between the fabric and back wall.

The work in Chapter 5 outlined how soft foams, directly against a reflecting surface, can amplify or attenuate blast waves. The foam's modification of the back wall pressure history was related to the through-thickness properties of the foam, foam thickness and foam density.

In this chapter, the transverse properties of the materials used in soft ballistic vests will be investigated to demonstrate that soft ballistic vests can amplify or attenuate blast waves when no air gap is present.

7.1 Multi-Layer Fabric Transverse Behaviour

Many studies have been undertaken to characterize the in-plane properties of fabrics, due to their influence on ballistic resistance [Yung, 1992]. Through thickness properties of soft fabric protection, however, has only been explored in a few studies.

Work by Raftenberg [Raftenberg, 2004] features results of quasi-static transverse compression of a multi-ply Kevlar vest. The vest was comprised of 28 layers of a 600 denier Kevlar KM2 plain woven fabric, though the particular weave is not specified. It should be noted that the vest was left in its Cordura case during the tests. Raftenberg suggested the constitutive relationship between second Piola-Kirchhoff stress (S_{33}) and Green-St. Venant strain (E_{33}) in the transverse direction could be described as:

$$S_{33} = \frac{aE_{33} + bE_{33}^2 + cE_{33}^3 + dE_{33}^4}{(1 + 2E_{33})^2(1 + eE_{33} + fE_{33}^2)} \quad (7.1)$$

Note that the above relation assumes that stress in the transverse direction is decoupled from strain in the warp and fill directions.

The nominal/engineering strain (e_{33}) (taken to be positive in compression) and Green-St. Venant strain are related by:

$$E_{33} = -e_{33} + \frac{e_{33}^2}{2} \quad (7.2)$$

The second Piola-Kirchoff stress (S_{33}) and Cauchy Stress (T_{33}) are related by:

$$S_{33} = \frac{T_{33}}{(1 - \varepsilon_{33})} \quad (7.3)$$

Using the above relations it was possible to produce engineering stress-strain data for use in the numerical model based on Raftenberg's results. The constants for Equation (7.1) as reported by Raftenberg, are listed in Table 7.1 below. The significant digits are as reported in [Raftenberg, 2004]

Table 7.1 - Constants for Fabric Constitutive Model [Raftenberg, 2004]

Constant	Value
a	1.2577 MPa
b	-7.68533 MPa
c	-71.1591 MPa
d	-135.116 MPa
e	4.74248
f	6.00453

The resulting stress-strain behaviour is shown in Figure 7.1 below.

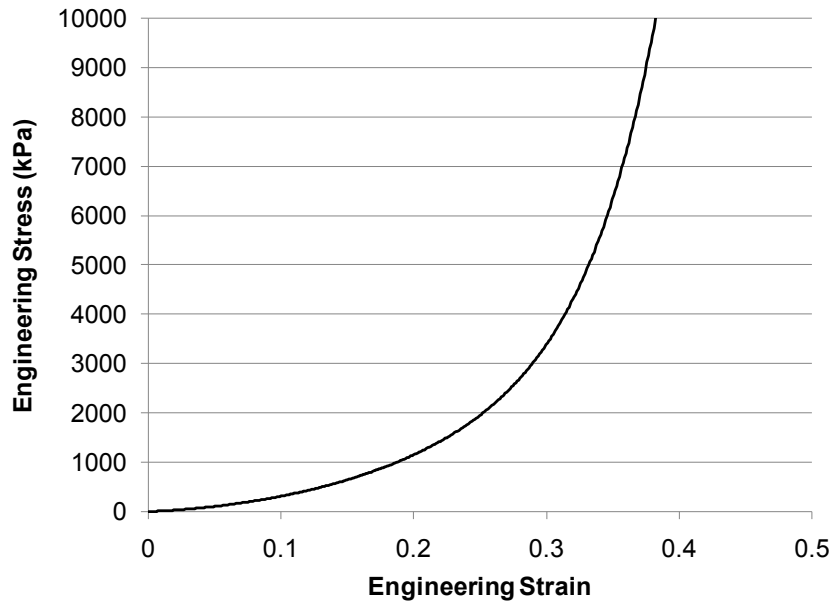


Figure 7.1 - Transverse Stress-Strain behaviour for Kevlar KM2 fabric from [Raftenberg, 2004]

In work by Jaycor/L3-Communications [Yu, 1985], the through thickness properties of a Kevlar vest were used as a part of their study. The properties were obtained from compression tests done as a part of their work. The compressive stress-strain curves for the Kevlar vests from the study [Yu, 1985] are shown below in Figure 7.2. It should be noted that while the overall results are different from [Raftenberg, 2004], the behaviour of the materials is similar; that is they both show a very low stiffness at small strains, but at larger strains the stiffness increases asymptotically.

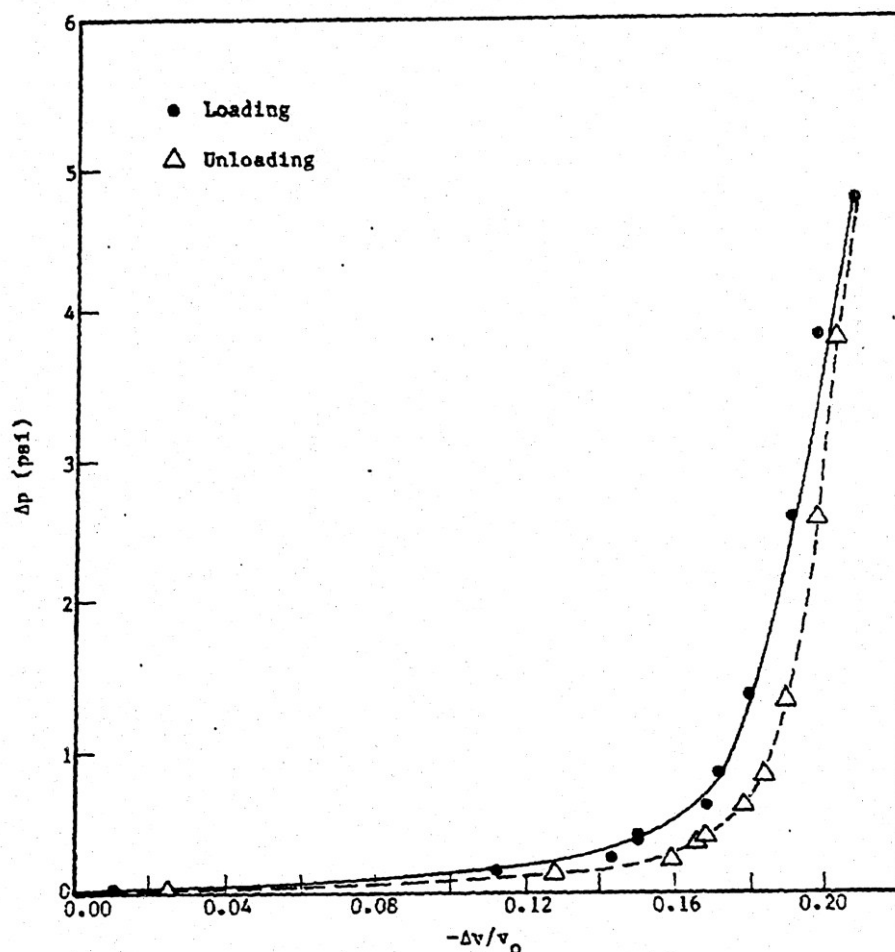


Figure 7.2 - Transverse compression test and unloading of 30 layers of Kevlar 29 fabric [Yu, 1985]

Tests of a single Kevlar KM2 fiber by Cheng et al. [Cheng, 2005] are useful in further understanding the behavior of ballistic fabrics under transverse compression. It was found that Kevlar fibers in transverse compression exhibit non-linear stress-strain behaviour, and plastic deformation. As such, when the fiber was reloaded after initial loading and unloading, the 2nd load curve follows the unloading curve. This is to say that Kevlar KM2 fibers behave differently after they have been significantly loaded once. This could have implications for protection systems utilizing Kevlar under complex blast loading.

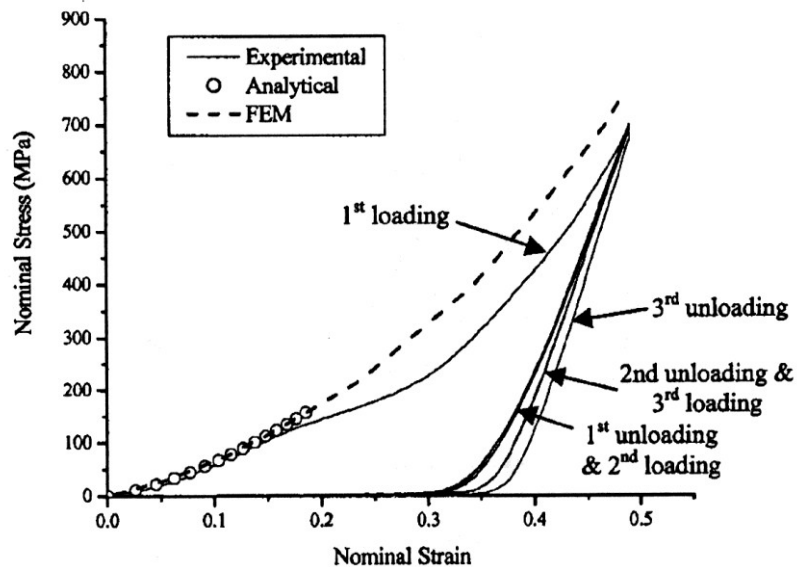


Figure 7.3 - Transverse loading and unloading of a single Kevlar fibre [Cheng, 2005]

The behaviour of fabrics in compression could be considered similar to that of foams. The primary difference (besides the density and ratio of solid and gas phases in each material) is the lack of a plateau stress in fabrics. The reader is reminded that the plateau stress-strain behaviour results from pre-buckling stiffness of cell walls. No such buckling behaviour is seen (or expected) in fabrics, and thus the behaviour is dominated by the gradual densification of the fabric.

7.2 Shock Wave and Blast Loading of Multiple Layers of Fabric

In order to better understand why soft ballistic vests can increase lung injury under blast loading, some researchers have investigated the change in the transmitted pressure when soft fabrics are placed on a surface. The experiments carried out are similar to those done for foams and single layer fabrics, as discussed in Chapters 5 and 6, respectively.

Experimental work by Gibson [Gibson, 1995] has focused on the effect of the bulk density of a porous material, such as a foam or fabric, on the equilibrium sound speed in that material, as well

as correlations between apparent bulk density, sound speed in the porous material and pressure amplification.

Gibson found that the average peak pressure ratio increased with decreasing apparent bulk density of fabric material (Figure 7.4). This also corresponded to an increase in average peak pressure ratio with decreasing average areal density, as each fabric type was tested with the same number of layers.

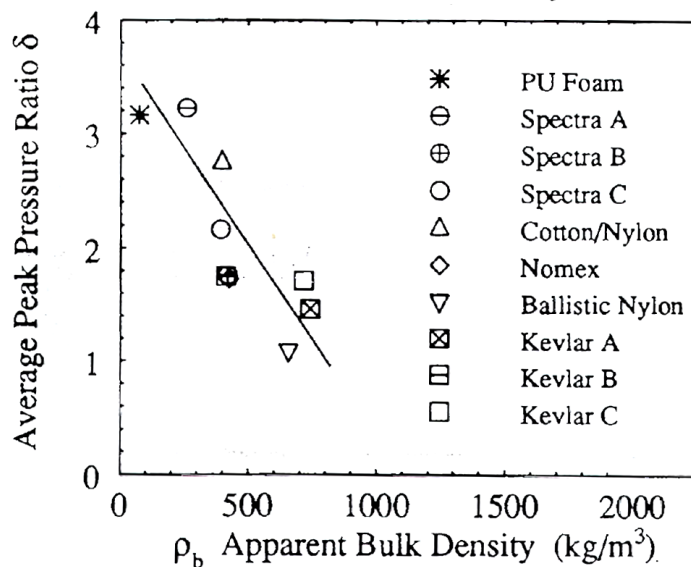


Figure 7.4 - Average peak pressure ratio [Gibson, 1995]

An interesting observation made by Gibson was that some materials would show increased blast pressure amplification with increased thickness/numbers of layers, while others would show decreased blast pressure amplification. Gibson tested 4, 8, 12, 16 and 20 layers of each of the fabrics described in Figure 7.4. It was found that materials with an apparent bulk density less than that at the minimum sound speed would increase the amplification with increasing thickness, while materials with an apparent bulk density greater than that at the minimum sound speed would show reduced amplification with increasing thickness. Examples are shown below in Figure 7.5. The peak pressure ratio δ is defined as the ratio of the measured reflected pressure under the test sample to the baseline pressure measured without a sample.

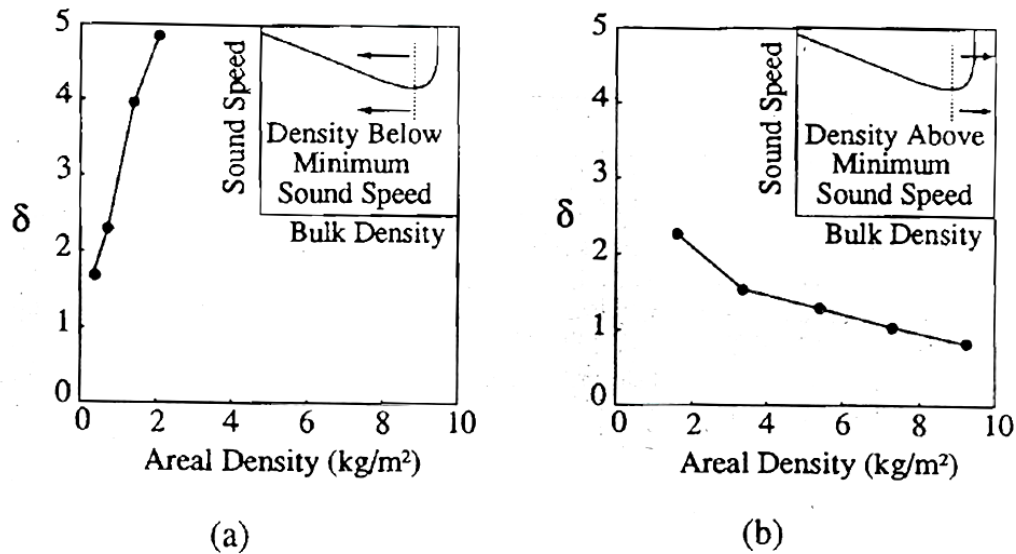


Figure 7.5 - Overpressure amplification for two different fabrics: A) Fabric with density below minimum sound speed; B) Fabric with density above minimum sound speed [Gibson, 1995]

Unfortunately, the author did not increase the areal density (through increased thickness) of the low density material so that its range of areal densities would overlap, thus it is unclear whether the material with a density below the minimum sound speed (Figure 7.5a) would have eventually shown reducing amplification with increasing sample thickness. Work conducted by Yu [Yu, 1985] has shown the expected trend in pressure amplification with changes in thickness for Kevlar 29 fabric (Figure 7.6). Specifically, it was observed in experiments that some critical thickness of protection (or number of layers) existed, at which the pressure amplification by multiple layers of fabric was maximized.

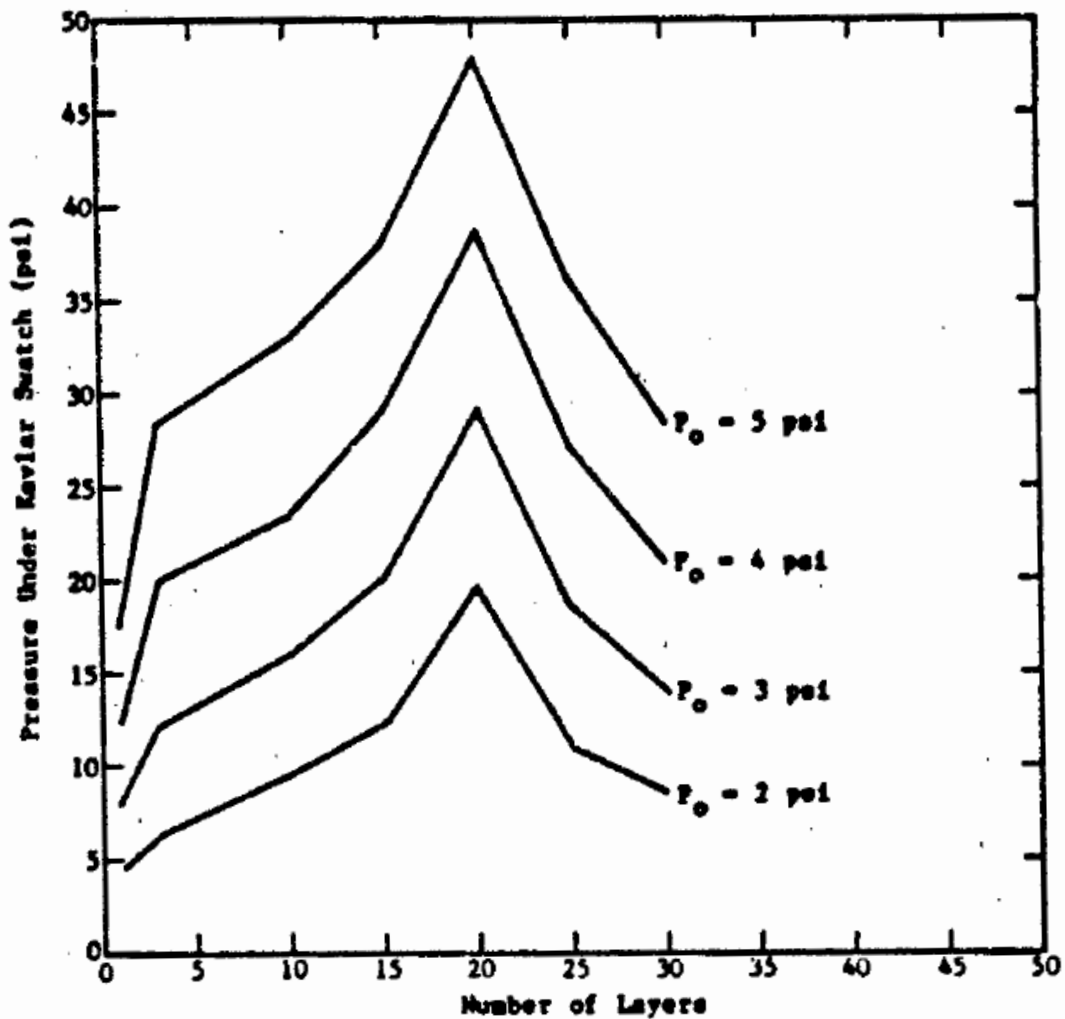


Figure 7.6 - Change in pressure amplification for various load cases and varied number of layers of Kevlar 29 [Yu, 1985]

The tendency of an increase of peak pressure with increased thickness was also observed for foams as discussed in Section 6.2. This observation was made for shock tube loading, however when one compares the amplified pressure response compared to the baseline results for the Gibson study, the response time of the fabric is extremely small compared to the blast duration (Figure 7.7), thus some comparisons could be drawn between this kind of loading and shock tube loading.

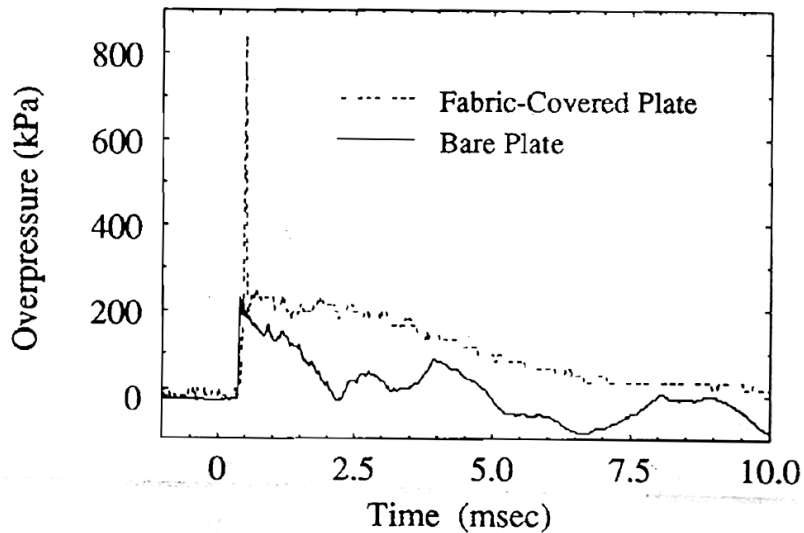


Figure 7.7 - Effect of multi-layer fabric on transmitted blast pressure [Gibson, 1995]

Work by Nerenberg [Nerenberg, 2000] focused on comparing various protective concepts designed for mitigating both secondary and primary blast injury. Included in their experiments were varied layers of soft ballistic material, as well as a flak jacket. It was found that soft ballistic fabrics and vests amplified the peak pressure transmitted to the torso, as well as the peak acceleration of the chest wall of Hybrid III test dummies, for all but the smallest charge sizes. It was found that increasing the thickness of ballistic material would reduce the peak pressure, and in some cases attenuation of the peak pressure compared to the baseline pressure was achieved. It is worth noting that the durations involved with the tests by Nerenberg were of much shorter duration than those examined by Gibson [Gibson, 1995], on the order of the duration of the amplified pressure spike when soft ballistic vests were tested (Figure 7.8). The digitization of the data from [Nerenberg, 2000] shown in the below figure is poor because the original graph had a scale of 2.5 ms.

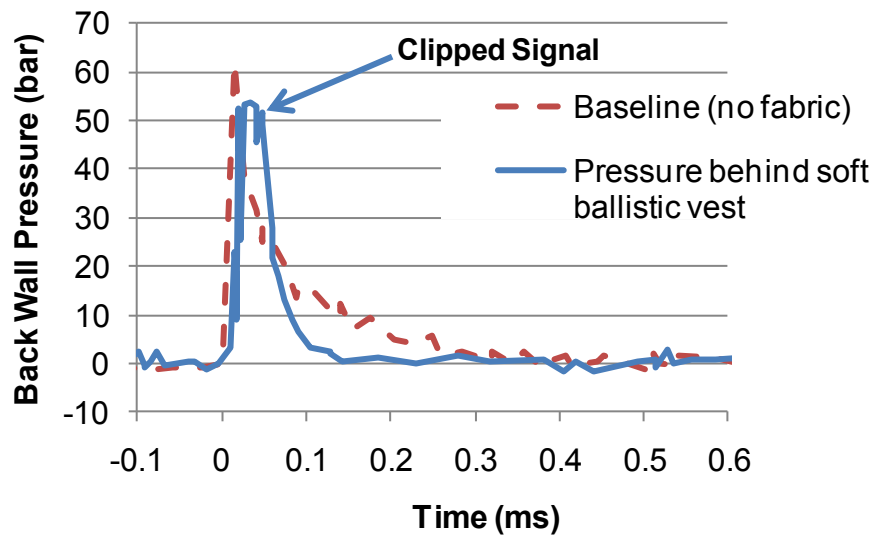


Figure 7.8 - Effect of a soft ballistic apron on peak pressure when loaded by 250g of C4 at 0.65m. digitized from [Nerenberg, 2000]

7.3 Shock Wave Loading of Live Subjects Wearing Soft Ballistic Vests

As mentioned in Section 2.5, experiments on both human volunteers [Young, 1985] and sheep [Phillips, 1988] have shown that soft ballistic vests can increase the risk of lung injury due to air blast. In humans, peak pressure as measured in the esophagus was found to increase under low magnitude shock loading. The loading, which was applied by standing volunteers in front of the open end of a shock tube, applied was a triangular pulse with 18 kPa peak pressure and a 4.8ms duration. The peak intrathoracic pressure (ITP) recorded for the volunteers wearing a soft ballistic vest (weighing 2.9kg) was 8.7 kPa on average (± 1.2 kPa); For volunteers wearing only fatigues, or fatigues with a "ceramic vest" (6.4kg), or Kevlar vest with a ceramic flak vest over top, the peak intrathoracic pressure averaged 7.4 kPa. The 8.7 kPa ITP for the soft ballistic vest was considered to be a significant increase over the fatigues only results ($7.4\text{kPa} \pm 0.7$), suggesting an amplification of the load. Only the masses of the protective ensembles were reported, with no details reported regarding the size, areal density, the number of layers of Kevlar, or thickness of the vests. The study reports that none of the clothing/protection combinations significantly reduced ITP, however the ballistic vest caused a significant increase.

Animal tests on sheep by Phillips [Phillips, 1988], utilizing the same protective concepts as the above work [Young, 1985], but involved higher loading, with peak reflected pressures ranging from 113 to 427 kPa, and durations ranging from 13.5 to 15.6 msec. Mortality and lung weight of the sheep was found to increase when a soft ballistic vest was used. Under the shock tube loading of 420 kPa magnitude, two out of six animals without ballistic vests died, while five out of six of the animals with ballistic vests died under the loading. With pressure waves with a peak of 232kPa, 299 and 427 kPa, an increase in lung weight was observed when ballistic vests were placed on animals compared to control tests; only the lowest blast strength with a peak of 113kPa failed to show an increase in average lung weight compared to the control (it remained the same). This study shows that whatever the effect of soft ballistic vests is on pressure transmitted to the thorax, it results in an increased lung injury and mortality under shock loading.

7.4 Multi-Layer Fabric Finite Element Model

The implementation of the 1D finite element model, used for parametric studies with multiple layers of fabric, was nearly identical to the model developed for foams in Chapter 5.3. While the geometry (Figure 7.9) and method of load application remained the same, the material model had to be changed to be representative of a soft ballistic fabric. The stress-strain behaviour, damping and hysteresis values also had to be estimated.

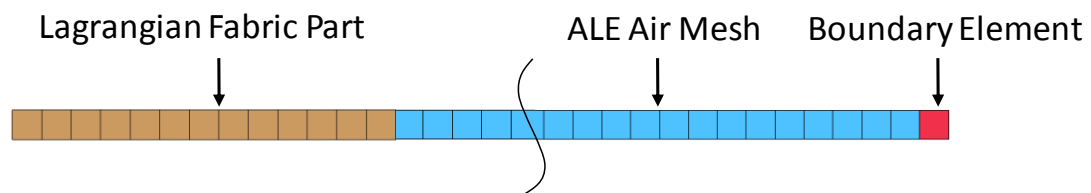


Figure 7.9 - 1D multi-layer fabric model configuration

7.4.1 Multi-Layer Fabric Material Model

A similar approach to that taken with foams was used with multi-layer fabric modeling. The relative lack of data on multiple layers of fabric under air shock loading compared to foams makes validation of the numerical model impossible, and thus some of the approaches used for the determination of damping and unloading properties used for foams could not be applied to multi-layer fabrics.

The model developed for this study was based on the transverse compression tests conducted by Raftenberg [Raftenberg, 2004], because the stress strain data reaches higher strains than the study by Yu. Equations (7.1)(7.3) and constants from Table 7.1 were implemented in both the finite element and mathematical models.

The hyperelastic behaviour of multiple layers of fabric, along with the assumption of uncoupled isotropic behaviour made by Raftenberg was consistent with the implementation of the low density foam material model (used in Section 5.3.3 for evaluating foams as a part of this study). The model also allowed for modelling of hysteresis, which multiple layers of fabrics have been shown to exhibit [Yu, 1985].

The study by Raftenberg did not include unloading results, and as such the hysteresis behaviour had to be estimated. This was done by using the loading stress-strain behaviour from [Yu, 1985], and modifying the hysteresis parameters in the material model until single element loading and unloading tests matched the experimental results. It was found that the same parameters used for LDPE 45 foam in Section 5.3.5 (hysteresis factor of 0.5, and a shape factor of 7.0) provided an excellent fit to the experimental unloading behaviour (Figure 7.10).

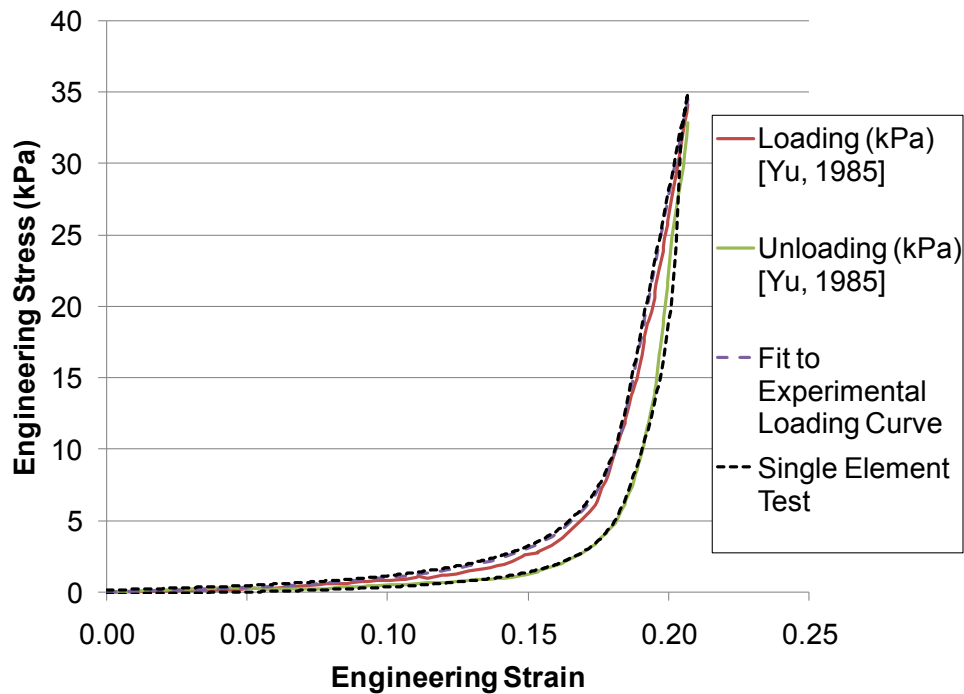


Figure 7.10 - Experimental loading and unloading behaviour for a Kevlar 29 fabric [Yu, 1985], fit to data to smooth results, and results of single element test with hysteresis implemented

The author would like to stress that the behaviour from [Yu, 1985] was obtained for a different Kevlar fibre and fabric weave than that tested in [Raftenberg, 2004] and modeled in this study. In spite of this inconsistency, the same unloading parameters obtained from fitting to the data of [Yu, 1985] were applied to the model using data from [Raftenberg, 2004].

Material density or fabric weave were not reported by Raftenberg. The fabric weave was assumed to be type 706, with a per layer thickness of 0.23 mm (a 28 layer vest was reported to have a thickness of 6.35mm by Raftenberg [2004]), and an areal density of 180 g/layer [Wetzel, 2004]. This resulted in a calculated density of 794 kg/m³ for the numerical model.

Rate dependence of the transverse behaviour of Kevlar fabrics was not explored in the available literature, and thus a rate dependent model was not considered as a part of this study.

Due to the lack of data the damping parameter for the material model was left as the default value of 0.05. As a result, the dispersion of waves in the fabric material may have been over or under estimated. This should be investigated more thoroughly in the future.

Limitations of the use of the above mechanical properties are that there was limited information regarding the high strain rate, unloading and hysteresis behaviour of soft ballistic fabric vests. These are important aspects of the dynamic behaviour of the material, and thus estimating the peak pressure behind multi-layer fabrics. However, in spite of this limitation, the trends in behaviour are expected to be the same.

The speed of sound was estimated using the method described by [Gibson, 1995] (Equation (2.7)) and the above parameters. The density of solid Kevlar used in the calculation was 1440 kg/m^3 [Yang, 2000], and a compaction wave speed of 19.7 m/s was calculated. The sound speed versus apparent bulk density is shown below in Figure 7.11, with the calculated density and sound speed of the multi-layer fabric used for the current study indicated.

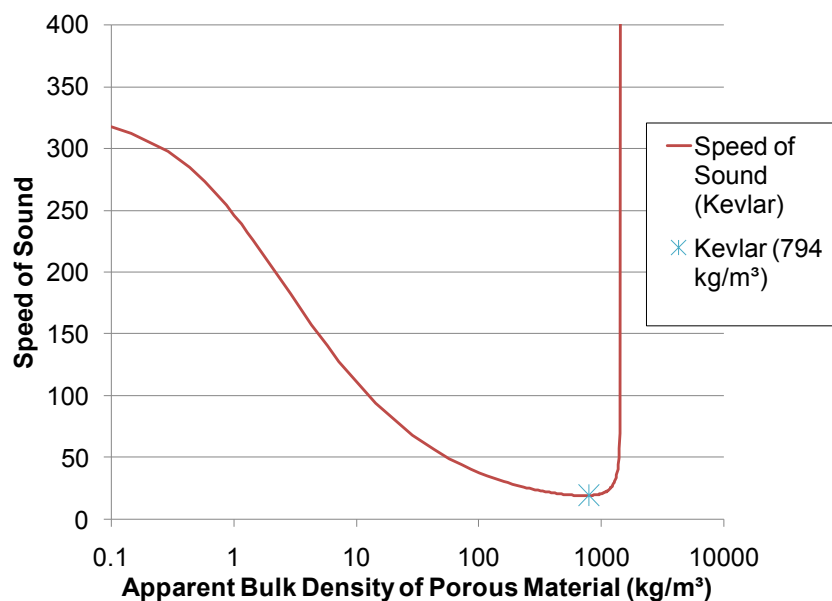


Figure 7.11 - Speed of sound versus apparent bulk density for a porous media using Kevlar parameters from the current study.

7.5 Parametric Study

A parametric study was undertaken using the material model developed for multi-layer ballistic fabric described in the previous section. The purpose of this study was to predict the behaviour of multi-layer fabrics under blast loading and compare the results to available experimental data. Shock tube loading was also investigated.

As was observed in simulations with foams, the general trend was for the peak pressure to decrease with increased thicknesses of soft ballistic cloth (an increase in thickness corresponding to increased layers of material). It was found that at low thicknesses, the peak pressure applied to the back wall began to decrease with reduced thickness of material (Figure 7.12). This was not observed with the foam materials, though they were not simulated at the very low thicknesses investigated here.

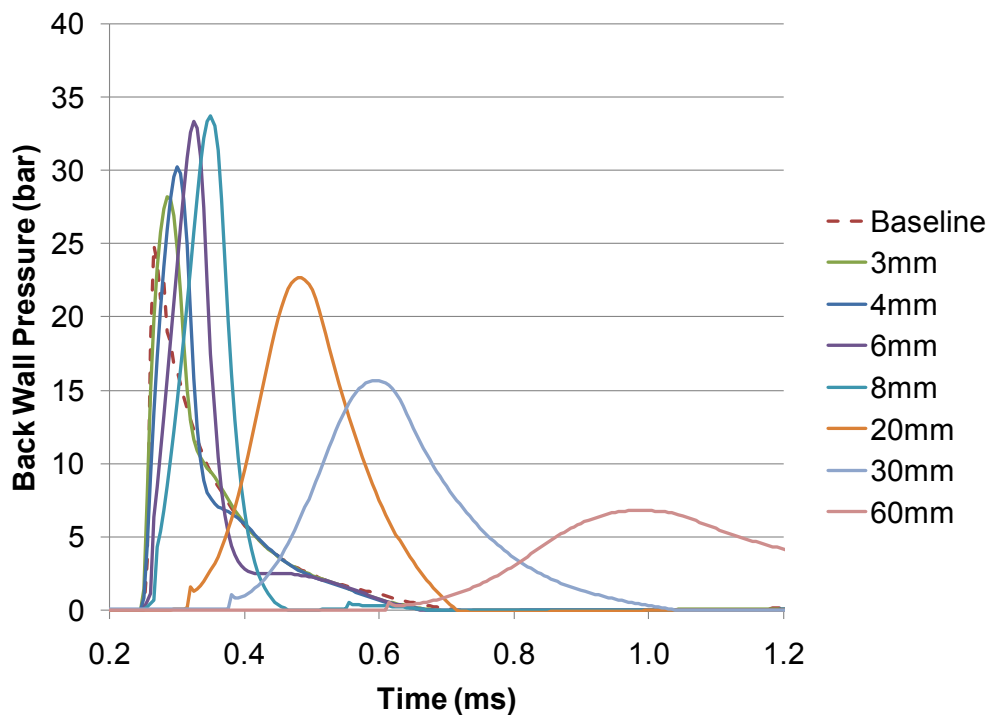


Figure 7.12 - Results from numerical simulation of various thicknesses of multi-layer Kevlar loaded by 250g of C4 at 1m (loading from [Ouellet, 2008])

Peak pressure versus material thickness are shown below in Figure 7.13. It was noted that for shock tube loading (Figure 7.13C), that no attenuation was possible (as discussed in the single layer fabric with air gap analysis in Section 6.4.1).

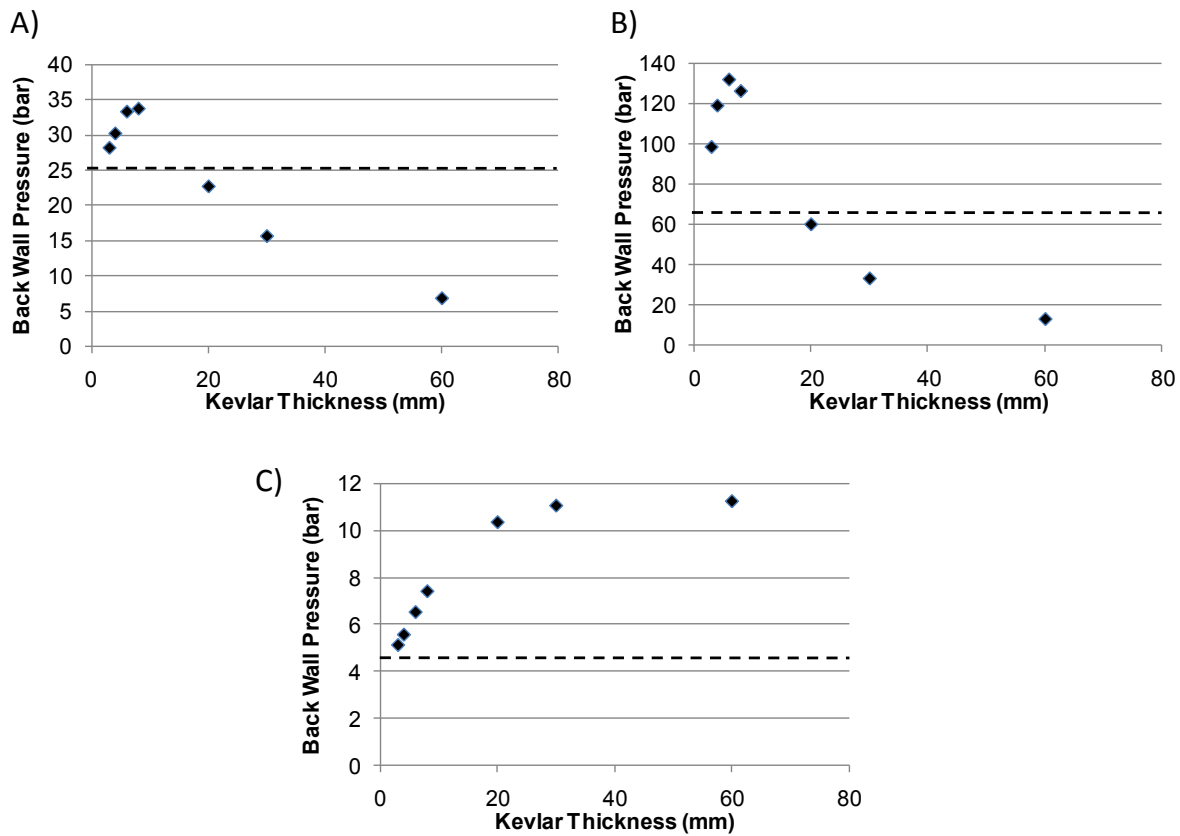


Figure 7.13 - Peak pressure results for various thicknesses of Kevlar under: A) 25 bar, 0.65 ms duration blast load (fit to data from [Ouellet, 2008]); B) 63 bar, 0.37 ms blast load (fit to data from [Nerenberg, 2000]); C) 4.5 bar Shock Tube Loading

Table 7.2 below shows the number of layers corresponding to each thickness considered in the parametric study. These values were based on the assumption of Kevlar fabric type 706, with a per layer thickness of 0.23 mm, and a density of 180 g/layer.

Table 7.2 - Number of Layers and Areal Density for the Thicknesses Examined in the Multi-Layer Fabric Parametric Study

Thickness (mm)	Number of Layers	Areal Density (kg/m²)
3	13	2.35
4	17	3.13
6	26	4.70
8	35	6.26
20	87	15.7
30	130	23.5
60	261	47.0

In all of the parametric work for multi-layer fabrics at extremely low thicknesses, reductions in material thickness yielded reductions in peak back wall pressure. Under blast loading, there appeared to be a critical thickness at which the pressure amplification was highest, between 6 and 8 mm.

7.6 Mathematical Model Implementation and Injury Prediction for Multi-Layer Fabrics

Due to the lack of available data for validation of the multi-layer fabric model, a validation case was not undertaken for the multi-layer fabric case. Instead, a few cases from the parametric study were evaluated using the mathematical model. The 20mm and 30mm results from Figure 7.12 were evaluated; however it was found that the velocity of the fabric deformation exceeded the compaction wave speed of 19.7 m/s. The resulting error in wave arrival time is visible in the results shown in Figure 7.14.

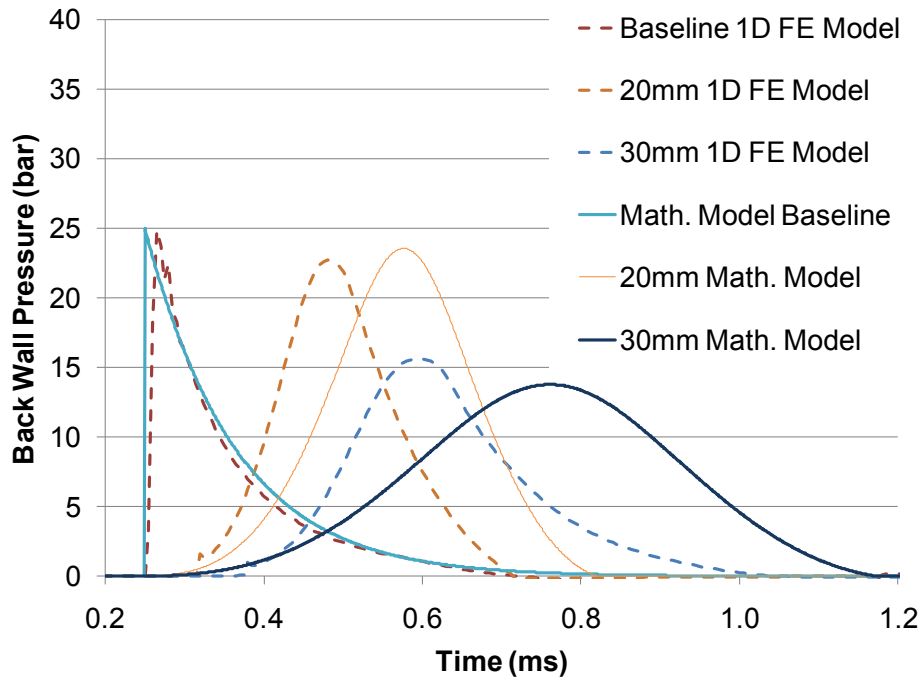


Figure 7.14 - Pressure time history behind 20mm and 30mm of Kevlar loaded by 250g of C4 at 1m. Predictions from 1D finite element models (dashed lines) and the mathematical models (solid lines)

The stress-strain behaviour of the multi-layer fabric model was made the same as described in Section 7.4.1. Unlike the finite element model, unloading behaviour was not considered. Aside from the use of Kevlar transverse stress-strain behaviour, the implementation was nearly identical to that used for foams (Section 5.6). The option was included (as was done with the foam model) to specify an areal density for a hard plate in front of the Kevlar.

Only two cases were considered for injury prediction under LD50 (2ms duration) loading. One case was where 10 mm of Kevlar was combined with a 10mm Plate with an areal density of 30kg/m². The other case considered was 20mm of Kevlar only. The results are shown in Table 7.3 below.

Table 7.3 - Summary of Modified Axelsson Model Results for Multi Layer Fabric Concepts

Loading	Protection	Plate AD (kg/m ²)	Peak Pressure Behind Protection (bar)	Chest Max Inward Velocity (m/s)	Chest Peak Acceleration (m/s/s)
LD50 T2	None	-	18.8	21.3	7.67E+04
LD50 T2	10mm Kevlar and 10mm Plate	30	16.9	14.6	5.28E+04
LD50 T2	20mm Kevlar	-	37.4	19.2	1.12E+05
			Baseline	Amplified	Attenuated

Based on the above results, the 10mm Kevlar with a 30kg/m² plate should attenuate the blast injury. The 20mm Kevlar could either amplify injury if peak pressure and chest acceleration are appropriate metrics, or attenuate the injury if chest wall velocity correlates better to the finite element torso model. The peak velocity of the side of the fabric struck by the blast wave was calculated to be 31.7 m/s for the 20mm Kevlar case, which was higher than the compaction wave speed (19.7 m/s). This violates the assumption of uniform deformation of the material, and thus the results were not necessarily representative of what was calculated with the more detailed finite element model.

7.7 Multi-Layer Fabric Torso Model Implementation

The same approach used in modelling the foam protection was used for modelling the combination of multi-layer fabric and high density material, however the emphasis was on showing possible attenuating concepts rather than the transition from amplification to attenuation of blast loading. The results are presented, however, it should be noted that the Kevlar material model was not qualitatively validated and thus while the results are representative of this class of material, they are by no means definitive estimates of the injury resulting from this loading/protection combination. More on the assumptions and limitations of the validation can be found earlier in this chapter. Similar to the models used for foam protection, a flat plate 24 cm wide was modelled with the thicknesses described in Section 7.6. The mutli-layer fabric and torso model is shown in Figure 7.15

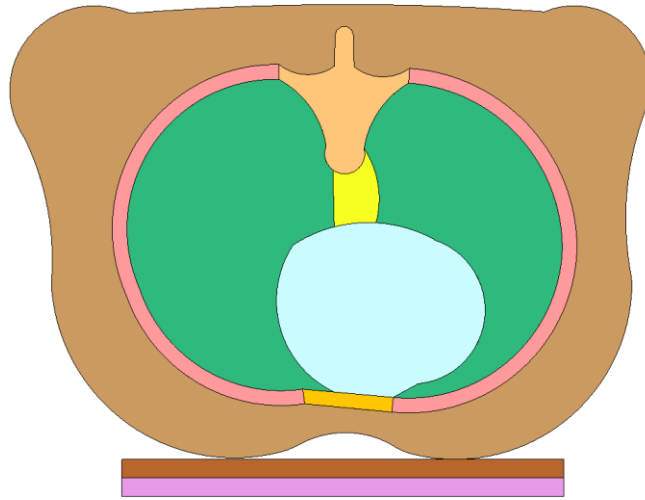


Figure 7.15 - Model used in multi-layer fabric protection simulations

7.7.1 Multi Layer Protection Results

The torso model results predict a reduction in injury, similar to that predicted by the mathematical model under the same loading conditions. a comparison of the baseline and protected cases is given in Figure 7.16

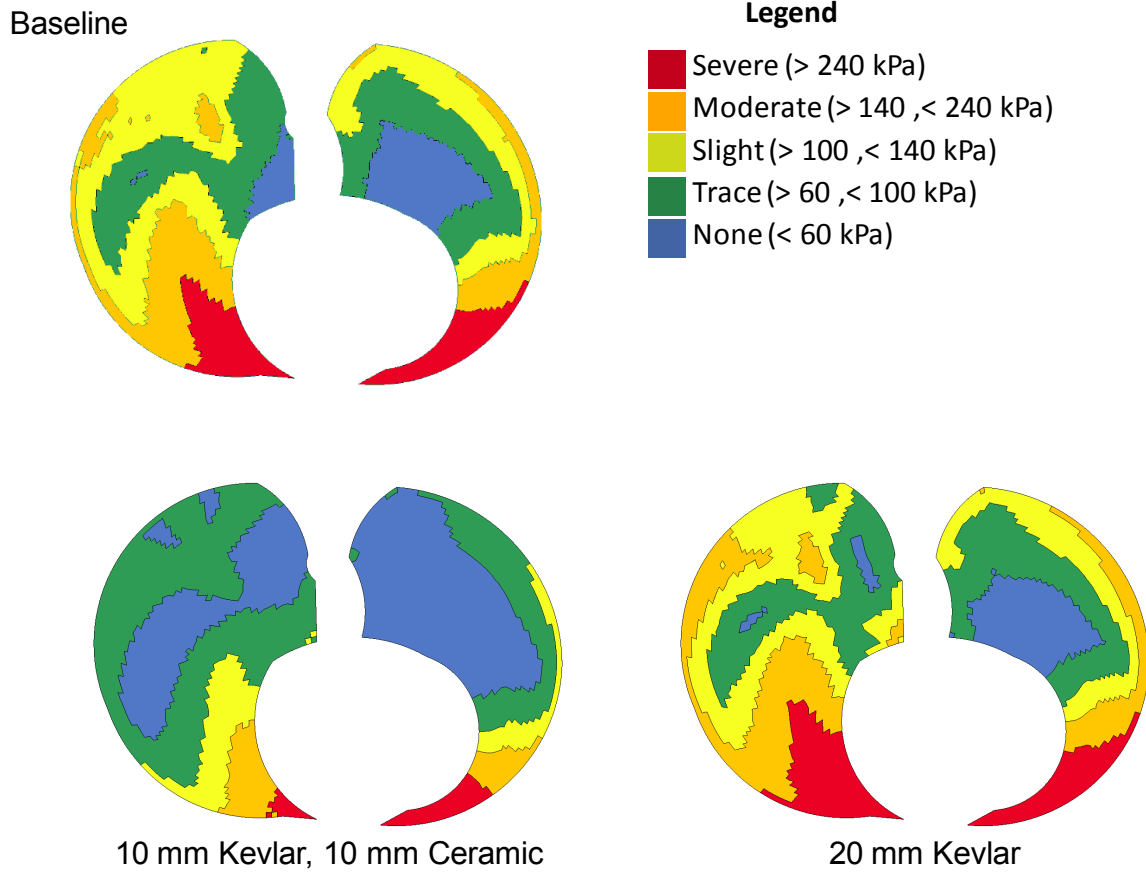


Figure 7.16 - Predicted lung injury results from the finite element torso model with multiple layer soft ballistic protection.

The above results are summarized below in Figure 7.17, where the percentage volume of lung elements which had a peak pressure above 240 kPa are compared between cases.

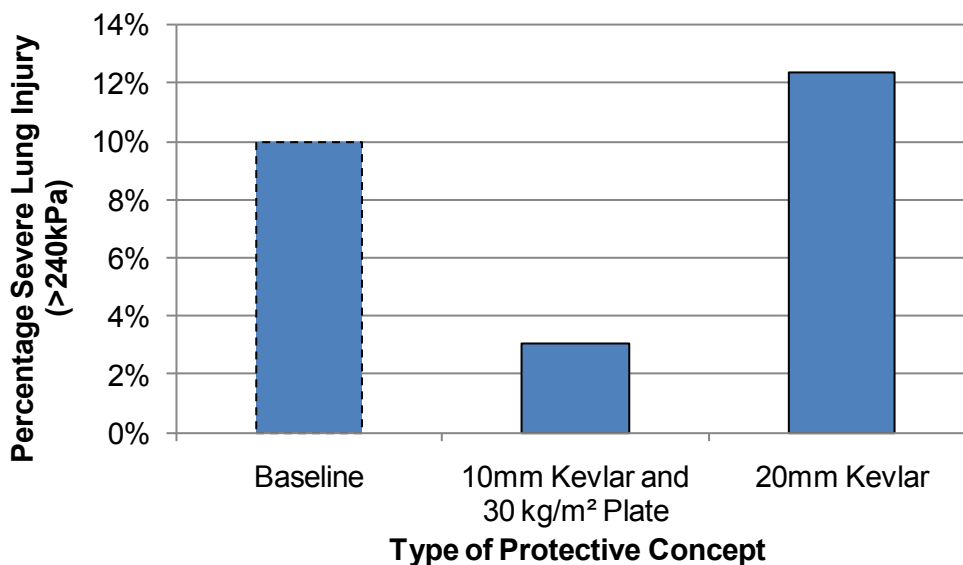


Figure 7.17 - Percentage of lung severely injured as determined by peak dynamic pressure for multi-layer fabric concepts

The results from the torso model predicted an amplification of injury with 20mm of Kevlar (equivalent to 87 layers). While this was a lot of layers, it was not considered reasonable to simulate a thinner "fabric only" concept, as this would have brought the number of elements through the thickness of the fabric material below 4, and it was already determined that the deformation would result in the formation of a compaction wave. The 10mm Kevlar case was considered acceptable due to the fact that the fabric would not be deformed quickly enough to exceed the compaction wave speed of 19.7 m/s, thanks to the 30 kg/m² plate between the fabric and blast wave. The decoupler concept resulted in a reduction of predicted injury, from the 10.0% baseline case to 3.0%.

7.8 Discussion of Results

Validation of the model was difficult in that most published literature regarding blast loading of Kevlar was obfuscated, revealing little information as to the exact material used in testing. In one

case a variety of parametric results were published, however the axis of pressure history data were unlabeled and unnumbered. A qualitative evaluation of the model was possible, showing that the numerical model produces behaviour consistent with that reported in the available literature.

The work by Nerenberg et al. [Nerenberg, 2000] states that under loading by the same charge mass and stand-off, when the number of soft ballistic vests was increased by 3 times (thus yielding a thickness of soft ballistic fabric three times higher), the vests, which originally amplified the peak pressure, were able to attenuate the blast. The numerical study showing the effect of increased thickness shows a transition from amplification to attenuation. Unfortunately, a quantitative comparison to the experiment is not possible for the reasons mentioned previously.

In work by Yu [Yu, 1985] it was found that there was a critical number of layers of Kevlar at which the pressure amplification was at its maximum; above or below this thickness of ballistic fabric the amplification would not be as great. Unfortunately no data was available regarding the duration of the loading, limiting the usefulness of this data for quantitative comparison. However, the parametric simulation results show that for the blast loading examined, the existence of a critical thickness was also observed. This occurred between 6-8mm (26-35 layers) in simulations, while in the work by [Yu, 1985] the maximum amplification was observed when the multi-layer fabric was 20 layers thick. It should be noted that the material model used in the current study was not representative of the fabric used in the study by [Yu, 1985].

The implementation of the mathematical model for Kevlar was not validated against experimental data due to the limited information provided in the literature. A comparison of mathematical model results to results from the 1D finite element model revealed that the arrival of the pressure waves lagged the finite element results for both 20mm and 30mm cases. This was attributed to the fact that the fabric deformed faster than the 19.7m/s compaction wave speed. The low compaction wave speed of the Kevlar material reduced the confidence in most of the results from the mathematical model. The exception was when a 30 kg/m² plate was put in front of 10mm of Kevlar for the Axelsson model implementation; the wave speed was kept below 19.7 m/s in that case.

The Kevlar model was able to show both amplification and attenuation of blast loading, as expected based on work by [Phillips, 1988] and [Young, 1985]. Kevlar by itself amplified the blast loading to the torso, while the Kevlar and high impedance material combination resulted in a drastic reduction of predicted injury.

The Kevlar model was found to behave unrealistically in tension, and an unrealistic deformation of the Kevlar model was observed after it underwent unloading. This was considered acceptable because the unrealistic behaviour occurred after the transmission of blast pressure to the torso model, and was not likely to have affected the injury prediction results.

Chapter 8

Conclusions, and Recommendations

This study covered a variety of materials. As a form of blast protection, soft materials were investigated for their ability to attenuate and amplify blast waves. Fabrics with air gaps, foams, foam/high density material decoupling concepts, and multi-layer fabrics were all examined as common elements of protection.

Air, Foam and multi-layer fabrics all show very little resistance to compression initially, however the compressive stiffness can increase rapidly for these materials at high strains. This stress-strain behaviour allowed the materials to both amplify and attenuate blast wave loading, depending on the thickness of the material and whether there was any mass added by incorporating high density materials in front of these low impedance materials. As long as the thickness or added mass was sufficient to keep the stress generated in the material below the peak applied pressure, an attenuation was seen. This could all be described as “Energy Management”, as the loading was not eliminated in these concepts, but changes to the shape of the load pulse were made. Generally, it was ideal to keep the strains in the soft material low enough to avoid the eventual “densification” which sometimes occurred in experiments and numerical simulations.

8.1 Foam Conclusions

Models of foams and foams with hard plates were created based on available literature data and validated against available experimental work. In most cases the predicted results matched very well with the experiments used in validation, despite the fact that in some cases a closed cell foam model was used to predict results from cases where a open celled foam was used.

The process of model development illustrated the importance of proper selection of both damping and unloading behaviour for simulation of limited duration blast loads. The importance of

unloading and damping was reduced when a high impedance material is added, because the material began to deform uniformly through thickness at lower rates.

A parametric study was conducted to illustrate the effects of varied plate areal densities mounted to foams of varied thicknesses. For the range of thicknesses tested, an increase in foam thickness always yielded a reduction in peak pressure. Likewise, an increase in plate areal density always resulted in a reduction in peak pressure. The effect of the plate mass is a reduction in the rate of deformation of the foam under blast loading due to the added inertia at face of the foam loaded by the blast wave. The results also indicated that the motion of the high impedance material and subsequent deformation of a foam can result in an increase in peak pressure compared to the applied blast loading.

8.2 Fabric Model Conclusions

A numerical model of fabric materials subjected to shock waves was created and verified using published experimental test results. In general, the trends and response as measured by pressure amplification were in good agreement; however, the peak pressures were over-predicted for lower permeability fabrics, due to leakage around the edge of the fabric in experiments.

Blast amplification can occur when a non-permeable fabric is accelerated towards a reflecting surface and the pressure behind the fabric increases due to reflecting waves and compression of the air behind the fabric. Amplification may also occur with permeable fabrics, but to a lesser degree. All other parameters being kept constant, an increase in permeability reduces pressure amplification under shock tube loading.

A parametric study showed that fabric areal density and permeability were the most influential factors in terms of blast amplification. It was found that the amplification increased greatly with incident shock wave strength and reductions in permeability. Amplification increased with areal density up to a threshold value, which depended on the material permeability, beyond which no

additional amplification was observed. Changes in stand-off did not affect the amplification for the range of values considered.

8.3 Multi-Layer Fabric Model Conclusions

A preliminary model of a Kevlar fabric was developed based on available literature. While the lack of complete material characterization and blast test data was an obstacle for the development of the material model, a representative model of a ballistic fabric was created.

The quantitative accuracy of the model could not be verified; however, qualitative behaviour was compared to descriptions of the behaviour of ballistic fabrics under blast loading from literature. It was found that if the thickness of the material undergoing blast loading was 6-8mm (26-35 layers), the amplification of the blast wave was maximized. As with foams, it was found that blast could be attenuated when a high enough thickness (number of layers) was used. A parametric shock tube study predicted similar behaviour as was predicted for non-permeable single layer fabrics, whereby peak pressure increased with increasing material thickness under shock loading, until a plateau in amplification was reached.

8.4 Mathematical (Modified Axelsson) Model Conclusions

Protection models were implemented as non-linear spring-mass systems and the resulting differential equations were solved using numerical integration. The foam and multi-layer fabric models were implemented and the foam model was validated against experimental blast data. The lack of available data made validation of the multi-layer fabric model impossible, while the results from the single-layer fabric model consistently overestimated experimental results from the literature. The uncoupled loading method used by the mathematical model was shown to be partially responsible for the error in the single-layer fabric model.

Coupling of the mathematical protection models to the modified Axelsson model allowed the prediction of the effect of protection on chest-wall kinematics under blast loading. Peak values were calculated for: Pressure transmitted through the protection model to the torso, chest-wall velocity, chest-wall acceleration. In all cases, the results were compared against a baseline case where no protection was used. The peak pressure transmitted through to the torso and chest-wall acceleration both provided similar results. Chest-wall velocity was found to be a less sensitive metric for estimating an increase or decrease in injury. Excluding the single-layer fabric model results, peak pressure and peak chest wall acceleration both predicted amplification or attenuation for the same cases as the torso model. Overall the modified Axelsson model proved to be a useful tool in the determination of protection cases to be studied as a part of the current work.

8.5 Finite Element Torso Model Conclusions

Material models developed as a part of this study were implemented with a 2D model of the human torso developed at the University of Waterloo. All simulations were run with an LD50 loading for consistency, and injury results were compared against the baseline (no protection) to determine if amplification or attenuation was achieved. Injury was estimated using the percentage of lungs with a peak dynamic pressure above 240kPa as a metric.

The foam material model was utilized in a series of three decoupling concepts. It was shown that the predicted injury could range from amplification to attenuation, even when a high impedance material was mounted on a low impedance material. The ability for decoupler to mitigate blast loading was found to depend on the areal density of the high impedance material and the thickness of the low impedance material.

The fabric model with an air gap was implemented using shell elements, and two geometries were considered: a planar section of fabric, and a fabric wrap, which closed completely around the 2D torso model. Areal densities representative of 1, 32 and 64 layers of Kevlar were assigned to the fabric model and amplification of injury was predicted by the model for the 1 and 32 layer cases for both geometries. Similarly, the model predicted attenuation at 64 layers for both geometries.

The predicted injury levels for the planar section geometry were consistently lower than the wrap geometry, and this was attributed to the ability of the air to escape from between the torso and planar fabric section.

Two configurations, Kevlar and Kevlar with a hard plate, were both evaluated using the torso model. The predicted injury amplification for the Kevlar protection was in line, qualitatively, with results from the literature where soft ballistic vests had been found to amplify injury. The attenuation attained with the combined Kevlar and ceramic model was also expected based on published work from other researchers.

8.6 Recommendations

The following is a list of recommendations based on the outcome of the current study.

Work investigating the high rate, high strain behaviour of foams should be conducted in order to aid in the development of material models for foams which undergo high rate, gross deformation. The cause of the early onset of densification at high rates would be of particular interest.

The characterization of wave dispersion behaviour in foams would also be of great interest. While wave dispersion was adequately captured in the foam models used in the current work, a more rigorous method might be beneficial, and aid in the identification of which material parameters affect how a foam disperses waves.

For the fabric with air gap work, future studies could include numerical and experimental studies to quantify edge effects, as well as experiments showing response to a variety of shorter duration shock waves. The permeable fabric models developed as part of the current study could be used as a starting point for attempting to estimate the transverse compressive behaviour of multiple layers of permeable fabric.

There is a deficiency in the amount of information available regarding the transverse properties of multiple layers of ballistic fabric. High rate characterization as well as thoroughly documented blast and shock tube testing would be extremely useful for the development and validation of blast protection models. The same level of interest as was expressed in foam damping and unloading behaviour also applies for multiple plies of fabric.

Work could also be done towards the development of an anisotropic material model for multiple layers of fabric, allowing the definition of a hyperelastic compressive stress-strain behaviour for the transverse direction, and the appropriate behaviour in the warp and fill directions.

The techniques developed as a part of this study were not used to their full capacity, in that no attempt was made in the current study to design a protective concept. Rather, cases were selected to show the transition of the model from predicting injury attenuation to predicting injury amplification. Future work could build more on the already developed model by comparing a broader range of materials, or by considering complex blast loading scenarios. The examination of more elaborate protection concepts might also yield interesting results.

Bibliography

Adler, O.B., & Rosenberger, A. (1988). Blast injuries, *Acta Radiologica*, vol. 29, no. 1, pp. 1-5.

Argyros, G.J. (1997). Management of primary blast injury, *Toxicology*, vol. 121, no. 1, pp. 105-115.

ASME. (2006). *Guide for Verification and Validation in Computational Solid Mechanics*. ASME PTC V&V 10 - 2006. ASME Committee PTC 60.

Axelsson, H., & Yelverton, J.T. (1996). Chest wall velocity as a predictor of nonauditory blast injury in a complex wave environment, *The Journal of trauma*, vol. 40, no. 3 Suppl, pp. S31-7.

Axelsson, H., & Yelverton, J.T. (1994). *Chest wall velocity as a predictor of non-auditory blast injury in a complex wave environment*. 7th International symposium of weapons traumatology and wound ballistics, St. Petersburg, Russia.

Bannister, K. A. (1997). *Airblast Loading Model for DYNA2D and DYNA3D*. Technical Report, ADA322344. Army Research Lab, Aberdeen Proving Ground, MD.

Bass, C.R., Rafaels, K., & Salzar, R. (2006). *Pulmonary Injury Risk Assessment for Short-Duration Blasts*. Personal Armour Systems Symposium (PASS) 2006, Leeds, United Kingdom, September 2006.

- Ben-Dor, G., Cederbaum, G., Mazor, G., & Igra, O. (1996). Well tailored compressive stress-strain relations for elastomeric foams in uni-axial stress compression, *Journal of Materials Science* vol. 31, pp. 1107-1113.
- Ben-Dor, G., Mazor, G., Igra, O., Sorek, S., & Onodera., H. (1994). Shock wave interaction with cellular materials; Part II: open cell foams; experimental and numerical results, *Shock Waves*, vol .3, pp. 167-179.
- Bowen, I., Fletcher, E., & Richmond, D.(1962). *Estimate of Man's Tolerance to the Direct Effects of Air Blast*. Technical Report, DASA-2113. Defense Atomic Support Agency, Department of Defence, Washington, D.C.
- Bulson, P.S. (1997). *Explosive loading of engineering structures : a history of research and a review of recent developments*, 1st edn, E & FN Spon, London, New York.
- Chang, F.S. (1995). *Constitutive Equation Development of Foam Materials*. Ph.D. dissertation, Wayne State University.
- Chavko, M., Prusaczyk, W.K. & McCarron, R.M. (2006). Lung injury and recovery after exposure to blast overpressure, *The Journal of Trauma*, vol. 61, no. 4, pp. 933-942.
- Cooper, G.J. (1996). Protection of the lung from blast overpressure by thoracic stress wave decouplers, *The Journal of trauma*, vol. 40, no. 3 Suppl, pp. S105-10.

- Cooper, G.J., Pearce, B.P., Sedman, A.J., Bush, I.S. & Oakley, C.W. (1996). Experimental evaluation of a rig to simulate the response of the thorax to blast loading, *The Journal of trauma*, vol. 40, no. 3 Suppl, pp. S38-41.
- Cooper, G.J., Townend, D.J., Cater, S.R. & Pearce, B.P. (1991). The role of stress waves in thoracic visceral injury from blast loading: modification of stress transmission by foams and high-density materials, *Journal of Biomechanics*, vol. 24, no. 5, pp. 273-285.
- Cooper, G.J. (1990). Isolated pulmonary blast injury in rats--a new model using extracorporeal shock wave lithotripter, *Military Medicine*, vol. 155, no. 4, pp. A17-8.
- Cooper, G.J. & Taylor, D.E. (1989). Biophysics of impact injury to the chest and abdomen, *Journal of the Royal Army Medical Corps*, vol. 135, no. 2, pp. 58-67.
- Cronin, D., Salisbury, C., Greer, A. (2004). *Numerical Modeling of Blast Injuries: Phase 1 – Final Report*, Contract report for Defence R&D Canada – Valcartier, March 2004.
- Cripps, N.P. & Cooper, G.J. (1996). The influence of personal blast protection on the distribution and severity of primary blast gut injury, *The Journal of Trauma*, vol. 40, no. 3 Suppl, pp. S206-11.
- DePalma, R.G., Burris, D.G., Champion, H.R. & Hodgson, M.J. (2005). Blast injuries, *The New England Journal of Medicine*, vol. 352, no. 13, pp. 1335-1342.
- D'Yachenko, A., & Manyuhina, O. (2006). Modeling of weak blast wave propagation in the lung, *Journal of Biomechanics*, vol. 39. pp. 2113–2122.

- Freund, U., Kopolovic, J. & Durst, A.L. (1980). Compressed air emboli of the aorta and renal artery in blast injury, *Injury*, vol. 12, no. 1, pp. 37-38.
- Frykberg, E.R. & Tepas, J.J.,3rd (1988), Terrorist bombings. Lessons learned from Belfast to Beirut, *Annals of Surgery*, vol. 208, no. 5, pp. 569-576.
- Gayzik, F.S., Hoth, J.J., Daly, M., Meredith, J.W., & Stitzel, J.D.(2007). A finite element-based injury metric for pulmonary contusion: investigation of candidate metrics through correlation with computed tomography, *Stapp Car Crash Journal*, vol. 51, pp. 189-209.
- Gibson, L.J., & Ashby, M.F. (1988). *Cellular Solids: Structure and Properties*, Pergamon Press, Oxford.
- Gibson, P.W. (1995). Amplification of Air Shock Waves by Textile Materials, *Journal of the Textile Institute*, vol. 86, no. 1, pp. 119-128.
- Gubaidullin, A.A., Britan, A., & Dudko, D.N. (2003) Air shock wave interaction with an obstacle covered by porous material, *Shock Waves*, vol. 13, pp. 41-48, 2003
- Greer, A.D. (2006). *Numerical modeling for the prediction of primary blast injury to the lung*. MSc Thesis, University of Waterloo, ON
- Gruss, E. (2006). A Correction for Primary Blast Injury Criteria, *Journal of Trauma*, vol. 60, no. 6, pp. 1284-1289.

- Guy, R.J., Kirkman, E., Watkins, P.E. & Cooper, G.J. (1998). Physiologic responses to primary blast, *The Journal of trauma*, vol. 45, no. 6, pp. 983-987.
- Hallquist, J. (2006). *LS-DYNA theoretical manual*. Livermore Software Technology Corporation, Livermore, California
- Hattingh, T., & Skews, B. (2001). Experimental investigation of the interaction of shock waves with textiles, *Shock Waves*, vol. 11, no. 2, pp. 115-123.
- Huang, Z. (2000). The mechanical properties of composites reinforced with woven and braided fabrics, *Composites Science and Technology*, vol. 60, pp. 1479-498
- Ho, A.M. (2002). A simple conceptual model of primary pulmonary blast injury, *Medical Hypotheses*, vol. 59, no. 5, pp. 611-613.
- Hyde, D.W. 1988, *Microcomputer Programs CONWEP and FUNPRO, Applications of TM 5-855-1, 'Fundamentals of Protective Design for Conventional Weapons' (User's Guide)*. Technical Report, ADA195867. Army Engineer Waterways Experiment Station, Vicksburg, MS.
- Irwin, R.J., Lerner, M.R., Bealer, J.F., Brackett, D.J. & Tuggle, D.W. (1997). Cardiopulmonary physiology of primary blast injury, *The Journal of Trauma*, vol. 43, no. 4, pp. 650-655.
- Irwin, R.J., Lerner, M.R., Bealer, J.F., Lightfoot, S.A., Brackett, D.J. & Tuggle, D.W. (1998). Global primary blast injury: a rat model, *The Journal of the Oklahoma State Medical Association*, vol. 91, no. 7, pp. 387-392.

- Kingery, C.N. (1966). *Air blast parameters versus distance for hemispherical TNT surface bursts*. Technical Report, AD0811673. Army Ballistic Research Lab, Aberdeen Proving Ground, MD.
- Lagutov, Y.P, Gvozdeva, L.G., Sharov, Y.L., & Sherbak, N.B. (1997). Experimental investigation of gas percolation through porous compressible material under the effect of shock wave, *Physica A*, vol. 241, pp. 111-117, 1997
- Landshoff, R. (1955). *A Numerical Method for Treating Fluid Flow in the Presence of Shocks*, Technical Report, LA-1930. Los Alamos Scientific Laboratory.
- Makris, A., Frost, D.L., Nerenberg, J., & Lee, J.H.S. (1996). Attenuation of a blast wave with a cellular material, *Proceedings of 20th International Symposium on Shock Waves*, vol. II, pp. 1387–1392.
- Mayorga, M.A. (1997). The pathology of primary blast overpressure injury, *Toxicology*, vol. 121, no. 1, pp. 17-28.
- McArthur, J., Salisbury, C., Cronin, D., Worswick, M., & Williams, K. (2003). High strain rate characterization of shock absorbing materials for landmine protection concepts, *Shock and Vibration*, vol. 10, pp. 179-186.
- McElhane, J.H. (1966). Dynamic response of bone and muscle tissue, *Journal of Applied physiology*, vol 21, pp.1231-1236.

Mellor, S.G. (1992). The relationship of blast loading to death and injury from explosion, *World Journal of Surgery*, vol. 16, no. 5, pp. 893-898.

Meyers, M.A. (1994). *Dynamic Behavior of Materials*, Wiley, New York.

Miller, P.R., Croce, M.A., Bee, T.K., Qaisi, W.G., Smith, C.P., Collins, G.L., & Fabian, T.C. (2001). ARDS after Pulmonary Contusion: Accurate Measurement of Contusion Volume Identifies High-Risk Patients, *Journal of Trauma: Injury Infection & Critical Care*, vol. 51, no. 2, pp 223-230.

Mills, N.J. (2007). *Polymer Foams Handbook: Engineering and Biomechanics Applications and Design Guide*, Butterworth-Heinemann, Oxford, UK.

Mills, N.J., & Gilchrist, A. (1997). The Effects of Heat Transfer and Poisson's Ratio on the Compressive Response of Closed-Cell Polymer Foams, *Cellular Polymers*, vol. 16, no. 2, pp. 87-109.

Monti, R. (1970). Normal shock wave reflection on deformable solid walls, *Meccanica*, vol. 5, no. 4, pp. 285-296.

Naiman, H., & Knight, D. (2007). The effect of porosity on shock interaction with a rigid, porous barrier, *Shock Waves*, vol. 16, pp. 321-337

Nerenberg, J., Makris, A., Kleine, H., & Chichester, C. (2000). The Effectiveness of Different Personal Protective Ensembles in preventing Blast Injury to the Thorax. *Fourth International Symposium on Technology and the Mine Problem*, pp. 12–16. Monterey, California.

Nerenberg, J.G. (1998). *Blast Wave Loading of Polymeric Foams*, McGill University, Montreal, Quebec, Canada.

Nerenberg, J. G., Nemes, J.A., Frost, D. L., Makris, A. (1997). Blast wave loading of polymeric foam, *21st International symposium on Shock Waves*, Great Keppel Island, Australia, July 20-25

National Library of Medicine (NLM), The Visible Human Project, National Institutes of Health, www.nlm.nih.gov/research/visible/visible_human.html.

Ouellet, S., Levine, J., & Dionne, J.P. (2008). Parametric study on rigid plates, compressible foams and air gaps combinations for mitigating blast in personal protection applications, *Personal Armour Systems Symposium*, Royal Military Academy, Brussels, Belgium, October 6th-10th, 2008

Ouellet, S., & Williams, K. (2008b). Characterisation of Defence Research and Development Canada's Mannequin for the Assessment of Blast Incapacitation and Lethality (DRDC MABIL), *Personal Armour Systems Symposium*, Royal Military Academy, Brussels, Belgium, October 6th-10th, 2008

Ouellet, S., Cronin, D., & Worswick, M. (2006). Compressive response of polymeric foams under quasi-static, medium and high strain rate conditions, *Polymer Testing*, no. 25, pp. 731-743.

Ouellet, S. (2004). *Study of an Anti-Trauma Layer to Reduce Behind Armor Blunt Trauma in Advanced Personal Armor System*, Masters Thesis, University of Waterloo, Canada

- Phillips, Y.Y., Mundie, T.G., Yelverton, J. T., & Richmond, D.R. (1988). Cloth Ballistic Vest Alters Response to Blast, *The Journal of Trauma*, vol. 28, no. 1 supplemental, pp. s149-52.
- Raftenberg, M.N., Scheidler, M.J., & Moy, P. (2004). *Transverse Compression Response of a Multi-Ply Kevlar Vest*. Technical Report, ARL-TR-3343. Army Research Laboratory
- Rawlins, J.S. (1978), Physical and pathophysiological effects of blast, *Injury*, vol. 9, no. 4, pp. 313-320.
- Rudinger, G. (1965) Some Effects of Finite Particle Volume on the Dynamics of Gas-Particle Mixtures, *American Institute of Aeronautics and Astronautics Journal*, vol. 2, no. 7, pp. 1217-1222.
- Salisbury, C. (2004) *Investigation of the Arbitrary Lagrangian-Eulerian Formulation to Simulate Shock Tube Problems*, 8th International LS-DYNA User's Conference, Detroit, MI.
- Salisbury, C.P., Greer, A.D., Cronin, D.S. (2004b). *Numerical Modeling of Blast Injuries: Phase II - Final Report*, Contract report for Defence R&D Canada – Valcartier, October 22, 2004
- Salisbury, C.P., Greer, A.D., Cronin, D.S. (2004c). *Numerical Modeling of Blast Injuries: Phase III - Final Report*, Contract report for Defence R&D Canada – Valcartier, March 1, 2004.
- Seitz, M.W., Skews, B.W. (2006) Effect of Compressible Foam Properties on Pressure Amplification During Shock Wave Impact, *Shock Waves*, vol. 15, pp 177-179.

- Skews, B.W. (2006). Blast pressure amplification due to textile coverings, *Textile Research Journal*, vol. 76, no. 4, pp. 328-335.
- Skews, B.W. (1991). The reflected pressure field in the interaction of weak shock waves with a compressible foam, *Shock Waves*, vol. 1, no. 3: pp.205–211.
- Smith, P.D. & Hetherington, J.G.(1994). *Blast and ballistic loading of structures*, Butterworth-Heinemann, Oxford ; Boston.
- Souli, M. (2004). *LS-DYNA Advanced Course in ALE and Fluid/Structure Coupling*, Livermore Software Technology Corporation.
- Stitzel, J.D., Gayzik, F.S, Hoth, J.J., Mercier, J., Gage, H.D., Morton, K.A., Duma, S.M., Payne, R.M. (2005). Development of a finite element-based injury metric for pulmonary contusion part I: model development and validation, *Stapp Car Crash Journal*, vol 49. pp. 271-89.
- Stuhmiller, J.H., Bykanova, L., Chan, P., Dang, X., Fournier, A., Long, D.W., Lu, Z., Masiello, P., Ng, L., & Niu, E., (2006). *Mathematical Modeling of Physical and Cognitive Performance Decrement from Mechanical and Inhalation Insults*, Technical Report, ADA466592. Titan Corp., San Diego, CA.
- Stuhmiller, J.H. (1997). Biological response to blast overpressure: a summary of modeling, *Toxicology*, vol. 121, no. 1, pp. 91-103.

- Stuhmiller, J.H., Ho, K.H., Vander Vorst, M.J., Dodd, K.T., Fitzpatrick, T. & Mayorga, M. (1996). A model of blast overpressure injury to the lung, *Journal of Biomechanics*, vol. 29, no. 2, pp. 227-234.
- Stuhmiller, J.H., Chuong, C.J., Phillips, Y.Y. & Dodd, K.T. (1988). Computer modeling of thoracic response to blast, *The Journal of Trauma*, vol. 28, no. 1 Suppl, pp. S132-9.
- Taylor, P., Pollet, D. (2000). A preliminary study of the low-load lateral impact compression of fabrics, *Intermatonal Journal of Clothing Science and Technology*, vol. 12, no. 1, pp. 12–25, 2000.
- Treadwell, I. (1989). Effects of blasts on the human body, *Nursing RSA = Verpleging RSA*, vol. 4, no. 3, pp. 32-36.
- Trudeau, D.L., Anderson, J., Hansen, L.M., Shagalov, D.N., Schmoller, J., Nugent, S. & Barton, S. (1998). Findings of mild traumatic brain injury in combat veterans with PTSD and a history of blast concussion, *The Journal of neuropsychiatry and clinical neurosciences*, vol. 10, no. 3, pp. 308-313.
- Van Sligtenhorst, C.R., Cronin, D.S., Brodland, G.W., (2005). High strain rate compressive properties of bovine muscle tissue determined using a split Hopkinson bar apparatus, *Journal of Biomechanics*, Vol 39, Issue 10, pp. 1852-1858
- VonNeumann, J., & Richtmyer, R.D. (1950). A Method for the Numerical Calculation of Hydrodynamic Shocks, *Journal of Applied Physics*, vol. 21, pp. 232.

- Wagner, R.B., & Jamieson, P.M. (1989) Pulmonary Contusion, Evaluation and classification by computed tomography, *The Surgical clinics of North America*, vol. 69, no. 1, pp. 31-40.
- Wetzel, E., Lee, Y., Egres, R., Kirkwood, K., Kirkwood, J., & Wagner, N. (2004). *The Effect of Rheological Parameters on the Ballistic Properties of Shear Thickening Fluid (STF)-Kevlar Composites*, AIP Conf. Proc. 712, pp. 288.
- Wharton, R.K. (2000). Airblast TNT equivalence for a range of commercial blasting explosives, *Journal of hazardous materials*, vol. 79, no. 1, pp. 31.
- Wicky, S., Wintermark, M., Schnyder, P., Capasso, P., & Denys, A. (2000). Imaging of blunt chest trauma, *Eurpoean Radiology*, vol 10, pp 1524-1538.
- Wikipedia. (2007). *Image of Human Respiratory System*. Retrieved July 20th, 2009 from Wikipedia.org: http://en.wikipedia.org/wiki/File:Respiratory_system_complete_en.svg.
- Wightman, J.M. & Gladish, S.L. (2001). Explosions and blast injuries, *Annals of Emergency Medicine*, vol. 37, no. 6, pp. 664-678.
- Wilbeck, J.S. (1978). *Impact behavior of low strength projectiles*, Technical Report, AFML-TR-77-134. July 1978. University of Dayton Research Institute for the Air Force Materials Laboratory, Wright-Patterson Air Force Base, OH.
- Yamada, H. (1970). *Strength of biological materials*, Evans, F.G., ed. Williams and Wilkins, Baltimore.

Yan, R., Hine, P., Ward, I., Olley, R., Bassett, D., The hot compaction of SPECTRA gel-spun polyethylene fibre, *Journal of Materials Science* , vol. 32, no. 18, pp. 4821-4832.

Yang, H. H. (2000) Aramid Fibers. In T.W. Chou (Ed.), *Comprehensive Composite Materials, Volume 1, Fiber Reinforcements and General Theory of Composites*, pp. 199–229. Oxford: Elsevier Science,.

Yang, H. H. (1992). *Kevlar Aramid Fiber*, Wiley, West Sussex, England

Yelveton, J.T. (1996). Pathology scoring system for blast injuries, *The Journal of Trauma*, vol. 40, no. 3 Suppl, pp. S111-5.

Young, A.J., Jaeger, J.J., Phillips, Y.Y., Yelverton, J.T., Richmond, D. R. (1985). The Influence of Clothing on Human Intrathoracic Pressure During Airblast, *Aviation, Space, and Environmental Medicine*, vol. 56, pp. 49-53.

Yu, J., Vasel, E., Chuong, C., & Stuhmiller, J., (1985). *Characterization and Modeling of Thoraco-Abdominal Response to Blast Waves: Effect of Clothing on Thoracic Response*, vol. 8. JAYCOR Technical Report, DAMD17-82-C-2062 to Army Medical Research and Development Command, May 1985.

Yuen, K.F., Cronin, D.S., Deng, Y.C. (2008) *Lung Response and Injury in Side Impact Conditions*, Proceedings of the 2008 International Research Council on Biomechanics of Injury (IRCOBI) Conference, Bern, Switzerland, Sept. 2008

Zuckerman, S. (1940), Experimental study of blast injuries to the lungs, *Lancet, The*, vol. 2, no. 219, pp. 68.